



Publicly Accessible Penn Dissertations

1-1-2015

Near Infrared Fluorescent Choline Kinase Inhibitors for Cancer Imaging and Therapy

Sean Philip Arlauckas

University of Pennsylvania, sean.arlauckas@gmail.com

Follow this and additional works at: <http://repository.upenn.edu/edissertations>

 Part of the [Pharmacology Commons](#)

Recommended Citation

Arlauckas, Sean Philip, "Near Infrared Fluorescent Choline Kinase Inhibitors for Cancer Imaging and Therapy" (2015). *Publicly Accessible Penn Dissertations*. 1007.

<http://repository.upenn.edu/edissertations/1007>

This paper is posted at ScholarlyCommons. <http://repository.upenn.edu/edissertations/1007>

For more information, please contact libraryrepository@pobox.upenn.edu.

Near Infrared Fluorescent Choline Kinase Inhibitors for Cancer Imaging and Therapy

Abstract

Choline kinase alpha (ChoKa) deregulation is associated with a more aggressive phenotype and greater malignancy in many human cancers. Inhibitors of ChoKa induce apoptosis in tumorigenic cells, but validation of their specificity is difficult *in vivo*. Alterations in the profile of choline metabolites are detectable by magnetic resonance spectroscopy (MRS), but because of competing catabolic contributions from the phospholipases, the relative role of ChoKa is not absolutely discernable in a clinical setting. The goal of this work was to develop ChoKa-specific imaging probes to assist in the development of ChoKa as a diagnostic biomarker and therapeutic target. A series of compounds were synthesized for this purpose, and JAS239 was identified as the most promising choline-mimetic with inherent near infrared fluorescence. Attenuation of choline phosphorylation by JAS239 in human breast cancer cells was observed using ¹⁴C-choline radiotracing and high-resolution ¹H MRS. Microscopy was used to explore the interaction of JAS239 with the ChoKa protein. These *in vitro* studies, using the established MN58b as a positive control, indicated that JAS239 functions as a competitive inhibitor of ChoKa. Athymic nude mice inoculated with human breast cancer xenografts were injected *i.v.* with trace doses of JAS239 for imaging studies. *In vivo* optical imaging of JAS239 accumulation delineated breast tumor margins, and the signal intensity was capable of distinguishing both genetic overexpression and pharmacologic inhibition of ChoKa in breast xenografts. At therapeutic doses, JAS239 and MN58b reduced murine xenograft growth rates, and JAS239 was more effective than MN58b at reducing tumor total choline levels. Histological assessment found both JAS239 and MN58b reduced tumor cell density, decreased proliferation, and elicited an apoptotic response. In a parallel study, ChoKa inhibition was shown for the first time to be an effective therapeutic strategy in glioma tumors, however, JAS239 was not found to cross the blood-brain barrier. A library of derivatives were synthesized and these are being investigated to improve the potency, biodistribution, and tumor specificity. These results represent a new paradigm of multifunctional small molecules that can be used for ChoKa measurement, as companion diagnostics to validate new ChoKa inhibitors, and as therapeutically-effective inhibitors of choline metabolism.

Degree Type

Dissertation

Degree Name

Doctor of Philosophy (PhD)

Graduate Group

Pharmacology

First Advisor

Edward J. Delikatny

Keywords

Choline, Inhibitor, Kinase, Near infrared fluorescence

Subject Categories
Pharmacology

NEAR INFRARED FLUORESCENT CHOLINE KINASE ALPHA INHIBITORS FOR
CANCER IMAGING AND THERAPY

Sean Philip Arlauckas

A DISSERTATION

in

Pharmacology

Presented to the Faculties of the University of Pennsylvania

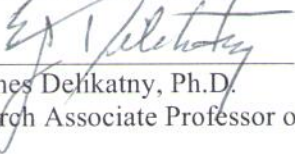
in

Partial Fulfillment of the Requirements for the

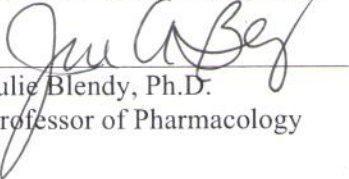
Degree of Doctor in Philosophy

2015

Supervisor of Dissertation


E. James Delikatny, Ph.D.
Research Associate Professor of Radiology

Graduate Group Chairperson


Julie Blendy, Ph.D.
Professor of Pharmacology

Dissertation Committee

Hank Kung, Ph.D., Emeritus Professor of Radiology
Emer Smyth, Ph.D., Research Associate Professor of Pharmacology
Andy Minn, M.D., Ph.D., Assistant Professor of Radiation Oncology
Aalim Weljie, Ph.D., Research Assistant Professor of Pharmacology

NEAR INFRARED FLUORESCENT CHOLINE KINASE ALPHA INHIBITORS FOR
CANCER IMAGING AND THERAPY

COPYRIGHT

2015

Sean Philip Arlauckas

This work is licensed under the
Creative Commons Attribution-
NonCommercial-ShareAlike 3.0
License

To view a copy of this license, visit

<http://creativecommons.org/licenses/by-nc-sa/2.0/>

Dedicated to my grandfather,

Philip C. Saunders

ACKNOWLEDGMENTS

Thanks is first due to Dr. Jim Delikatny, who taught me that you can quench your thirst and you can quench your fluorophores—just don't quench the magnet.

I thank my Thesis Committee members for providing expertise, volunteering resources, and staying alert during the second hour of my data analysis presentations.

I am greatly appreciative of Dr. Anatoliy Popov, whose scientific guidance, chemistry expertise, and friendship were invaluable to my graduate school experience.

I thank the members of the Delikatny lab for their help and feedback during this project. The camaraderie in this group made Monday mornings not so groggy, weeknights not so lonely, and Saturday mornings not so productive.

My professors, collaborators, and classmates in the Pharmacology Graduate Group elevated this experience beyond anything I hoped for when applying to Penn.

From this program, I met my best friend, Mansi Shinde, whose laughter, encouragement, and occasional eye-rolling continues to remind me that life's biggest challenges are always worth the effort.

I thank my family for the unconditional love and support that both motivated me and prevented me from taking myself too seriously. My Uncle Jeff has provided countless opportunities, career counseling, and crude humor. I thank my brother, Greg, who yawned loudly when I discussed my research, but always generously paid when we went out to eat.

Lastly, to my parents: You represent to me the model of success. Thank you for your patience and generosity. Everything I do is to make you proud.

ABSTRACT

NEAR INFRARED FLUORESCENT CHOLINE KINASE ALPHA INHIBITORS FOR CANCER IMAGING AND THERAPY

Sean Philip Arlauckas

E. James Delikatny, Ph.D.

Choline kinase alpha (ChoK α) deregulation is associated with a more aggressive phenotype and greater malignancy in many human cancers. Inhibitors of ChoK α induce apoptosis in tumorigenic cells, but validation of their specificity is difficult *in vivo*. Alterations in the profile of choline metabolites are detectable by magnetic resonance spectroscopy (MRS), but because of competing catabolic contributions from the phospholipases, the relative role of ChoK α is not absolutely discernable in a clinical setting. The goal of this work was to develop ChoK α -specific imaging probes to assist in the development of ChoK α as a diagnostic biomarker and therapeutic target. A series of compounds were synthesized for this purpose, and JAS239 was identified as the most promising choline-mimetic with inherent near infrared fluorescence. Attenuation of choline phosphorylation by JAS239 in human breast cancer cells was observed using ^{14}C -choline radiotracing and high-resolution ^1H MRS. Microscopy was used to explore the interaction of JAS239 with the ChoK α protein. These *in vitro* studies, using the established MN58b as a positive control, indicated that JAS239 functions as a competitive inhibitor of ChoK α . Athymic nude mice inoculated with human breast cancer xenografts were injected i.v. with trace doses of JAS239 for imaging studies. *In vivo* optical imaging of JAS239 accumulation delineated breast tumor margins, and the signal intensity was capable of distinguishing both genetic overexpression

and pharmacologic inhibition of ChoK α in breast xenografts. At therapeutic doses, JAS239 and MN58b reduced murine xenograft growth rates, and JAS239 was more effective than MN58b at reducing tumor total choline levels. Histological assessment found both JAS239 and MN58b reduced tumor cell density, decreased proliferation, and elicited an apoptotic response. In a parallel study, ChoK α inhibition was shown for the first time to be an effective therapeutic strategy in glioma tumors, however, JAS239 was not found to cross the blood-brain barrier. A library of derivatives were synthesized and these are being investigated to improve the potency, biodistribution, and tumor specificity. These results represent a new paradigm of multifunctional small molecules that can be used for ChoK α measurement, as companion diagnostics to validate new ChoK α inhibitors, and as therapeutically-effective inhibitors of choline metabolism.

TABLE OF CONTENTS

ABSTRACT.....	V
LIST OF TABLES	XI
LIST OF ILLUSTRATIONS.....	XII
LIST OF ABBREVIATIONS	XV
CHAPTER 1	1
INTRODUCTION	1
1.1 Preamble	1
1.2 Hallmarks of cancer.....	1
1.3 Choline metabolism.....	4
1.4 Choline kinase	10
1.5 Choline kinase inhibition.....	15
1.6 Carbocyanine Dyes	27
1.7 Near infrared fluorescence guided surgery	31
1.8 Scope of thesis.....	33
CHAPTER 2	35
MATERIALS AND METHODS	35
2.1 Chemistry Materials	35
2.2 Cell Culture	36
2.3 Western Blotting	37
2.4 ¹ H MRS studies of cellular extracts.....	38
2.5 ChoK activity ¹ H MRS assay	40

2.6 ¹⁴ C-choline ChoK activity assay	41
2.7 Cell viability studies	42
2.8 Epidermal growth factor stimulation.....	43
2.9 Fluorimetry analysis	44
2.10 Confocal microscopy.....	45
2.11 Animal model and tumor cell implantation	46
2.12 In vivo optical imaging	48
2.13 Ex vivo optical imaging	50
2.14 In vivo MRI	51
2.15 Animal treatments	53
2.16 Histopathology	55
2.17 Statistical analysis	57
CHAPTER 3	58
CHEMICAL SYNTHESIS.....	58
3.1 Introduction.....	58
3.2 Pyro-Choline.....	60
3.3 MN58b.....	60
3.4 WM-11	61
3.5 JAS239	63
3.6 hydro-JAS239.....	64
3.7 JAS239.5	65
3.8 JAS259	65
3.9 JAS273 and JAS274.....	66
3.10 PepTech compounds	67
3.11 Results	69
3.12 Discussion	75

CHAPTER 4	78
JAS239 CHARACTERIZATION IN BREAST CANCER CELLS	78
4.1 Introduction.....	78
4.2 Results	84
4.3 Discussion	99
CHAPTER 5	104
JAS239 CHARACTERIZATION IN BREAST TUMOR MODELS	104
5.1 Introduction.....	104
5.2 Results	106
5.3 Discussion	125
CHAPTER 6	129
CHOLINE KINASE INHIBITION AS A GLIOMA TREATMENT STRATEGY	129
6.1 Introduction.....	129
6.2 Results	131
6.3 Discussion	139
CHAPTER 7	143
CONCLUSION	143
7.1 Potential applications	143
7.2 Next generation inhibitors.....	146
7.3 Unexplored mechanisms of choline kinase inhibition	149
7.4 Future studies	152
APPENDIX 1	154
Synthesis and characterization of E,E-conjMN58b (PTC1452-01).....	154

APPENDIX 2	159
Synthesis and characterization of E,E,E-conjMN58b (PTC1452-02)	159
APPENDIX 3	167
Synthesis and characterization of TCD-717 (PTC1452-07)	167
APPENDIX 4	175
Synthesis and characterization of cycloJAS239 (PTC1452-08).....	175
APPENDIX 5	184
Synthesis and characterization of cycloJAS239.5 (PTC1452-09).....	184
APPENDIX 6	193
Synthesis and characterization of cycloHITC (PTC1452-10).....	193
APPENDIX 7	200
Synthesis and characterization of cycloHITC.5 (PTC1452-11).....	200
BIBLIOGRAPHY	207

LIST OF TABLES

Table 1. Calculated Partition Coefficients for synthesized structures.....	71
Table 2. Potency of MN58b and JAS239 in a panel of breast cancer cell lines	91

LIST OF ILLUSTRATIONS

Figure 1.1. MRS detection of elevated tumor choline levels.....	5
Figure 1.2. PtdCho catabolic and choline anabolic routes.....	9
Figure 1.3. ChoK α phosphorylates choline via an unusual ping-pong mechanism.....	12
Figure 1.4. Structures of symmetric ChoK α inhibitors.....	19
Figure 1.5. The use of ICG for NIRF-guided tumor resection	29
Figure 3.1. Class of compounds synthesized as potential ChoK α inhibitors.....	59
Figure 3.2. Colorimetric monitoring during JAS239 synthesis	62
Figure 3.3. Second generation JAS239 analogs contracted to PepTech Corporation	68
Figure 3.4. Synthetic pathway for the preparation of prototype ChoK α inhibitors	70
Figure 3.5. Optical properties of JAS239.	70
Figure 3.6. Colorimetric comparison of JAS239 before and after reduction.....	73
Figure 3.7. UV fluorescence of MN58b and JAS239 derivatives	73
Figure 4.1. Cancer cell mechanisms affecting the intracellular pool of PC	79
Figure 4.2. Templates for ChoK α -specific inhibitors.....	81
Figure 4.3. Time dependent increases in PC resonances measured in ^{31}P NMR spectra .	83
Figure 4.4. Choline metabolite and ChoK α levels in cultured cell models	83
Figure 4.5. ^{14}C -choline radiotracing assay for ChoK activity	86
Figure 4.6. ^1H NMR ChoK assay.....	87
Figure 4.7. ChoK inhibition by fluorescent choline mimetics measured by NMR	88
Figure 4.8. JAS239 is a competitive inhibitor of ChoK in MDA-MB-231 cells.....	89
Figure 4.9. Characterization of ChoK α in a panel of human breast cancer cell lines.....	90
Figure 4.10. Breast cancer cell viability in response to ChoK inhibitors	91

Figure 4.11. ¹⁴ C-choline radiotracing to distinguish choline transport from choline phosphorylation.....	92
Figure 4.12. Effect of ChoK α expression on JAS239 uptake and retention.....	94
Figure 4.13. Uptake and subcellular localization of JAS239.....	96
Figure 4.14. JAS239 colocalizes with ChoK α	97
Figure 4.15. Correlation coefficients to quantify JAS239/ChoK α colocalization.....	98
Figure 5.1. Tumor growth patterns in human breast cancer derived cell lines.....	106
Figure 5.2. Bioluminescence of 4175-Luc+ tumors delineates tumor margin for NIRF measurement.....	107
Figure 5.3. NIRF imaging for biodistribution of JAS239 in Tween-80/Tris formulation.....	109
Figure 5.4. Limitations of whole body optical imaging.....	110
Figure 5.5. NIRF imaging for biodistribution of JAS239 in ethanol/saline formulation.....	111
Figure 5.6. Biodistribution of hydro-JAS239 using NIRF imaging.....	112
Figure 5.7. Bioavailability study of hydro-JAS239 and JAS239.....	113
Figure 5.8. NIRF-guided surgical resection of breast tumors.....	115
Figure 5.9. NIRF imaging for JAS239 accumulation can detect genetic overexpression of ChoK α	116
Figure 5.10. NIRF imaging for JAS239 accumulation can detect pharmacologic inhibition of ChoK α	117
Figure 5.11. MN58b and JAS239 slow breast tumor growth.....	119
Figure 5.12. Evaluation of MN58b and JAS239-treated tumors using MRS.....	120
Figure 5.13. Renal damage associated with MN58b is not seen in JAS239-treated mice.....	122
Figure 5.14. Histological assessment of tumors reveals reduced cell density, lower proliferation, and elevated apoptosis in response to ChoK α inhibitors.....	123
Figure 5.15. Histological assessment of ChoK α -inhibited MDA-MB-231 tumor sections reveals apoptosis and overall reduction in viable cells.....	124

Figure 6.1. MTT assay demonstrating inhibition of cellular viability of F98, 9L and 9L-EGFRviii cell lines with MN58b	131
Figure 6.2. Effect of MN58b on ChoK activity in tumor cells	132
Figure 6.3. 9L gliosarcoma cell response to EGF stimulation and MN58b inhibition...	133
Figure 6.4. <i>In vitro</i> NMR of F98 cell extracts	135
Figure 6.5. <i>Ex vivo</i> NMR of glioma extracts	137
Figure 6.6. JAS239 in glioma models.....	138
Figure 7.1. Model of Theranostic Mechanism of ChoK α Inhibitors	144
Figure 7.2. Screen of ChoK inhibition in cytosolic preparations	147
Figure 7.3. Comparison of JAS239 and MN58b in MCF7 cytosolic preparations.....	148

LIST OF ABBREVIATIONS

CCT	Choline phosphate cytidylyltransferase
ChoK	Choline kinase
ChoK α	Choline kinase alpha
CHTs	High-affinity choline transporters
CTLs	Choline transporter-like proteins
DAG	1,2- <i>sn</i> -Diacylglycerol
DTT	Dithiothreitol
EGFR	Epidermal growth factor receptor
Em.	Emission
EPR	Enhanced permeability and retention
ER	Endoplasmic reticulum
Ex.	Excitation
FDG	¹⁸ F-Fluoro-D-glucose
FRET	Fluorescence resonant energy transfer
GPC	Glycerophosphocholine
GPC:PDE	Glycerophospholipase:phosphodiesterase
HC-3	Hemicholinium-3
HIF α	Hypoxia inducible factor-alpha
HREs	Hypoxia response elements
ICG	Indocyanine green
LPL	Lysophospholipase

MRS	Magnetic resonance spectroscopy
NIR	Near infrared
NIRF	Near infrared fluorescence
OCTNs	Organic cation/carnitine transporters
OCTs	Organic cation transporters
PA	Phosphatidic acid
PC	Phosphocholine
PC-PLC	PtdCho-specific phospholipase C
PCT	Phosphocholine diacylglycerol transferase
PEMT	Phosphatidylethanolamine <i>N</i> -methyltransferase
PET	Positron emission tomography
PI3K	Phosphatidylinositol-3'-kinase
PKA	Protein kinase A
PLA ₂	Phospholipase A ₂
PLD	Phospholipase D
PME	Phosphomonoesters
pRb	Phosphorylated retinoblastoma protein
PtdEtn	Phosphatidylethanolamine
PtdCho	Phosphatidylcholine
QSAR	Quantitative structure-activity relationships
RECIST	Response Evaluation Criteria in Solid Tumors
SAM	<i>S</i> -adenosylmethionine
SM	Sphingomyelin
tCho	Total choline-containing metabolites

CHAPTER 1

Introduction

1.1 Preamble

The purpose of this thesis is to explore the mechanisms surrounding choline kinase alpha (ChoK α) and its involvement in cancer progression. Past studies have suggested that ChoK α expression and activity may serve as valuable biomarkers in cancer. The goal of this work is to explore the rationale behind targeting ChoK α to elicit a response in tumors. Molecular imaging applications as well as pharmacologic studies are included in the study of ChoK α 's clinical importance.

1.2 Hallmarks of cancer

The idea of a “magic bullet” was proposed by Paul Ehrlich during his investigations of histological stains in human tissue (Ehrlich, 1911). His realization that dyes could interact with specific targets in cells led to the concept of chemotherapy, wherein molecules could be designed to bind and inactivate cellular targets at the pathological source of cancer (Strebhardt and Ullrich, 2008). The War on Cancer was declared in 1971 when scientists and legislators promised a universal “cure” for the ailment we now know to be caused by hundreds of pathologically-unique diseases (Sporn, 1996). After several decades and billions of dollars’ worth of research funding, the scientific community has dramatically tempered its expectations for universal “magic bullets” as the complexities of these diseases have become realized. The treatment options for many cancers are so limited that life extensions of one or two months can be sufficient for FDA approval of new and often prohibitively expensive drugs. There have been success stories for specific

patient populations, notably paclitaxel in ovarian cancer, cisplatin in testicular cancer, imatinib mesylate treatment in chronic myeloid leukemia and gastrointestinal stromal tumors, and bevacizumab in VHL-mutated renal and colon cancers (Chabner and Roberts, 2005). These breakthroughs are becoming increasingly possible as we continue to classify cancers by their genetic and environmental driving factors, tissue of origin, and response to therapy, understanding the pathways of each cancer type so that potential susceptibilities can be explored for therapeutic intervention (Sawyers, 2004). Certain attributes have also been identified that are common to all cancers. These have been known since 2000 as the “Hallmarks of Cancer” and include: self-sustaining growth signaling, evading growth inhibitors, resisting apoptosis, acquiring replicative immortality, inducing angiogenesis, and promoting cell motility to surrounding tissues (Hanahan and Weinberg, 2000). These hallmarks were updated in 2011 to include four additional trends: genome instability, immune system evasion, tumor-promoting inflammation, and altered cellular energetics (Hanahan and Weinberg, 2011).

As signal transduction-targeted drugs have begun to replace traditional chemotoxic agents, the need for novel therapeutic targets has left researchers scrambling to identify clinical markers of tumor malignancy that can be exploited for pharmaceutical intervention. The cancer hallmarks include a host of promising biomarkers for imaging and therapeutic intervention. Bevacizumab was developed as an anti-angiogenic agent when it was proposed that cancers grow and spread by highjacking the mechanism for blood vessel formation (Los *et al.*, 2007). The epidermal growth factor receptor (EGFR) is commonly mutated and hyperactive in tumors, leading to the identification of EGFR inhibitors to treat lung, colon, and glioblastoma multiforme cancers in which these

mutations are common (Kris *et al.*, 2003; Cunningham *et al.*, 2004). Therapies like these have made remarkable strides toward prolonged patient survival, but new agents are needed to overcome the challenges of treatment resistance, cancer metastasis, and tumor recurrence. Promising therapeutic strategies based upon the new cancer hallmarks are emerging, for instance the CAR-T therapies designed to train the immune system to recognize and kill tumor cells (Maude *et al.*, 2014). In many instances, methods of early detection would allow a therapeutic regimen to be started at an earlier pathological stage where there is a greater likelihood of tumor response (Etzioni *et al.*, 2003). Recognizing that areas of chronic inflammation are more susceptible to malignant transformation has helped guide the location and frequency of screening procedures (Mantovani and Sica, 2010). The drive to improve cancer detection led to a number of advances in our understanding of how cancers use nutrients and produce energy in ways that can provide distinction from normal tissue.

The work of Otto Warburg was first to report that tumors exhibit aerobic glycolysis, although the advantage this provides to cancer cells has only recently begun to be elucidated (Warburg, 1956; Burk and Schade, 1956; Gatenby and Gillies, 2004). Besides the immune-protective effect of microenvironment acidosis, this metabolic transformation produces glycolytic intermediates that the tumor can use for biosynthetic precursors to support the growing biomass (Kroemer and Pouyssegur, 2008). A number of the most common oncogenic mutations upregulate hypoxia inducible factor-alpha (HIF α), a transcription factor that causes global changes in gene expression and result, among other cancer-associated outcomes, in promotion of the glycolytic pathway (Semenza, 2003). It is seemingly counter-productive for cancers to switch from the more

energy-efficient aerobic ATP production in the mitochondria even in situations where oxygen levels are not low. This glycolytic shift, however, permits the shunting of carbon atoms to other important factors required for growth, including nucleosides and amino acids (Vander Heiden *et al.*, 2009). Upregulation of the glycolytic pathway enhances uptake of ^{18}F -fluoro-D-glucose (FDG), which has been useful for identification of tumors using positron emission tomography (PET) imaging (Mankoff *et al.*, 2007). The clinical success of FDG has sparked efforts to develop radiotracers derivative of many naturally occurring metabolites relevant to tumorigenesis. These metabolites include estrogens (Katzenellenbogen *et al.*, 1997), thymidine (Shields *et al.*, 1998), folate (Muller, 2013), pyruvate (Toyoda *et al.*, 1989), glutamine (Lieberman *et al.*, 2011), and, notably, choline (Hara *et al.*, 1997).

1.3 Choline metabolism

Magnetic resonance spectroscopy (MRS) provides a profile of endogenous metabolites within an MRI-selected voxel, and is complementary to PET studies of exogenous metabolite distribution. MRS is capable of detecting the density of any non-zero spin nuclei such as ^1H , ^{31}P , and ^{13}C (Glunde *et al.*, 2010). By studying cancer cell and tumor extracts, a number of biomarkers unique to malignant tissue have been reported (Daly and Cohen, 1989; Gillies and Morse, 2005). One such phenomenon that has been described in a range of cancers, including breast, ovarian, prostate, lung, bone, colon, brain, hepatic, and lymphocytic, is the concomitant increases in phosphomonoesters (PME) observed in ^{31}P spectra and total choline-containing metabolites (tCho) observed in ^1H spectra (de Certaines *et al.*, 1993; Glunde and Serkova,

2006; Podo *et al.*, 2011). PME and tCho accumulation is one way that cancer cells are able to provide the metabolic precursors necessary for proliferation, and has been linked to overall poorer prognosis in numerous cancers (Negendank, 1992). Similarly, early drops in PMEs and tCho are predictive of responsiveness to both chemo- and radiotherapies (Shukla-Dave *et al.*, 2002; Podo *et al.*, 2011). The nine chemically equivalent protons in the methyl groups adjacent to the quaternary nitrogen of choline yield a strong singlet resonance at 3.2 ppm that is detectable by ^1H MRS (Fig. 1.1). This technique can be adapted to study whole animals, perfused cell models, biopsy tissue, and cell extracts, with the capacity to resolve individual contributors to the PME and tCho peaks improving in that order (Ackerstaff *et al.*, 2003).

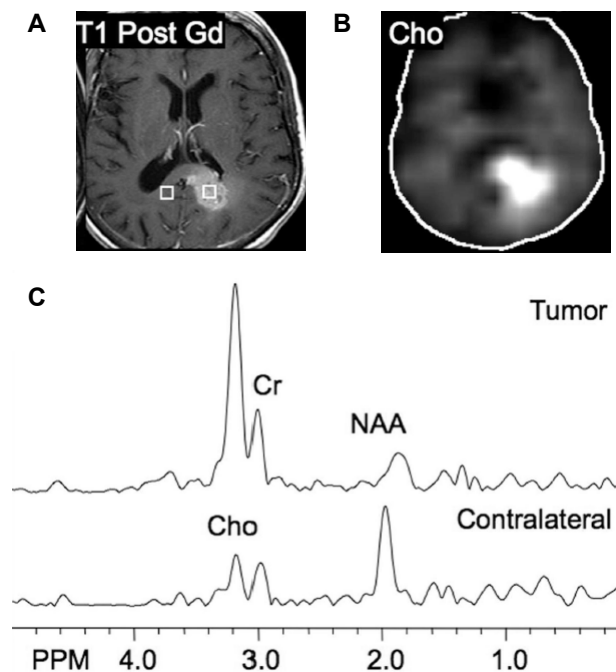


Figure 1.1. MRS detection of elevated tumor choline levels. (A) Glioblastoma multiforme tumor visible in a gadolinium-enhanced T_1 -weighted MRI image is demarcated by the right voxel. (B) Using chemical shift imaging at 3.2 ppm, a map of choline distribution (Cho) demonstrates elevated tCho in the tumor region. (C) MR spectra acquired for the tumor (right voxel) or the contralateral normal tissue (left voxel) confirm elevated tCho in cancer and diminished N-acetylaspartate (NAA) in the cancer tissue. Figure adapted with permission from *Horská and Barker, 2010*.

The tCho peak is a composite resonance in *in vivo* ^1H MRS spectra consisting of the sum of the choline-containing metabolites: free choline (3.20 ppm), phosphocholine (PC, 3.22 ppm), and glycerophosphocholine (GPC, 3.23 ppm). Tumor tissue extracts studied using high resolution MRS have revealed that the major contributor to the tCho signal is PC (Daly and Cohen, 1989). PC is an important precursor to phosphatidylcholine (PtdCho), the predominant phospholipid in mammalian cell membranes. In fibroblasts, generation of PC is required for the induction of DNA synthesis by a number of growth factors including PDGF, FGF, EGF and phorbol esters (Cuadrado *et al.*, 1993). Inhibiting PC production prior to PDGF or FGF addition eliminates activation of the Raf-1 and MAP kinase signaling cascades responsible for relaying the mitogenic growth signal (Jiménez *et al.*, 1995). Microinjection of PC itself is sufficient to induce a mitogenic response (Cuadrado *et al.*, 1993), although a different paper demonstrated that PC added to cellular media was not taken up by cells but still exhibited a pro-mitogenic response (T Chung *et al.*, 1997). Results from this paper suggest that extracellular ATP detection by the purinergic P_2 receptors induces release of mitogenically active levels of PC from fibroblasts. PC acts synergistically with ATP, insulin, and/or sphingosine-1-phosphate to stimulate phosphatidylinositol-3'-kinase (PI3K) and pp70^{s6k}, which regulate progression from the G_1 to the S phase of the cell cycle (T Chung *et al.*, 1997). PC levels have been found using MRS to increase substantially following oncogene transfection, loss of tumor suppressor function, and immortalization (Aboagye and Bhujwala, 1999; Mori *et al.*, 2004). Comparison of spectra from tumor-derived cells versus their normal counterparts has revealed elevated PC levels in breast (Aboagye and Bhujwala, 1999; Eliyahu *et al.*, 2007), glioma (Gillies *et al.*, 1994), ovarian (Iorio *et al.*, 2005), and prostate (Ackerstaff

et al., 2001) cells. Because it only measures the total steady-state pool of PC, MRS is unable to detect the relative contribution of the anabolic and catabolic pathways by which PC is generated.

Free choline can be transported across the cell membrane by a number of transporters (ChoT), which can be classified into four major groups: high-affinity choline transporters (CHTs), choline transporter-like proteins (CTLs), organic cation transporters (OCTs), and organic cation/carnitine transporters (OCTNs). Each transporter group is composed of multiple genes and splice variants (Michel *et al.*, 2006). Members of each class have been found at elevated levels in tumors, although the expression of each transporter seems to differ between cancers (Glunde *et al.*, 2011). CTL1 for example has been reported in colon cancer (Kouji *et al.*, 2009), lung cancer (Wang *et al.*, 2007), and leukemia (Fullerton *et al.*, 2006). In a study of breast cancer cells, CHT1 and OCT2 were found to be the primary choline transporters (Eliyahu *et al.*, 2007). The role of each choline transporter in each tumor type is still poorly understood, due to the complexity of the isoforms present in each transporter class.

Upon entering the cell, choline can be incorporated into a variety of important cellular components, including acetylcholine, betaine, sphingomyelin, or PtdCho (Fig. 1.2). In healthy individuals, the CHT family is primarily expressed in neurons, which take up choline and synthesize the neurotransmitter acetylcholine in a one-step pathway catalyzed by choline acetyltransferase (D Wu and Hersh, 1994). Choline can also be oxidized in the mitochondria at the hydroxyl position to form the common osmolyte betaine. Betaine:homocysteine *S*-methyltransferase transfers a methyl group from betaine to homocysteine, replenishing the methionine pool needed for the synthesis of the crucial

methyl donor *S*-adenosylmethionine (SAM) (Gonzalez *et al.*, 2004). Among other functions, SAM can be used by phosphatidylethanolamine *N*-methyltransferase (PEMT) to methylate phosphatidylethanolamine (PtdEtn) for PtdCho synthesis during choline deficiency (Cui and Vance, 1996). In humans PEMT is almost exclusively expressed in the liver (Vance, 2013). The majority of cells in the human body use choline as a head group for cell membrane lipids. The Kennedy pathway leads to formation of the diacylglycerophospholipid, PtdCho. PtdCho can then be converted to the sphingolipid sphingomyelin (SM) via transfer of PC to a ceramide by the enzyme sphingomyelin synthase (Ullman and Radin, 1974).

Anabolic production of PC occurs during the Kennedy pathway (Fig. 1.2) for PtdCho biosynthesis (Weiss *et al.*, 1956). Free choline in the cytosolic space is rapidly phosphorylated to PC by the enzyme choline kinase (ChoK) (Wittenberg and Kornberg, 1953). PC conversion to CDP-choline is the rate-limiting step catalyzed by the enzyme choline phosphate cytidyltransferase (CCT) (Kennedy and Weiss, 1956). CCT is inactive in soluble form but recruited to the nuclear membrane in a highly regulated fashion (Glunde *et al.*, 2011). Cytidine monophosphate is then replaced with 1,2-*sn*-diacylglycerol (DAG) by the enzyme phosphocholine diacylglycerol transferase (PCT) in the final step of PtdCho synthesis (Kennedy, 1957).

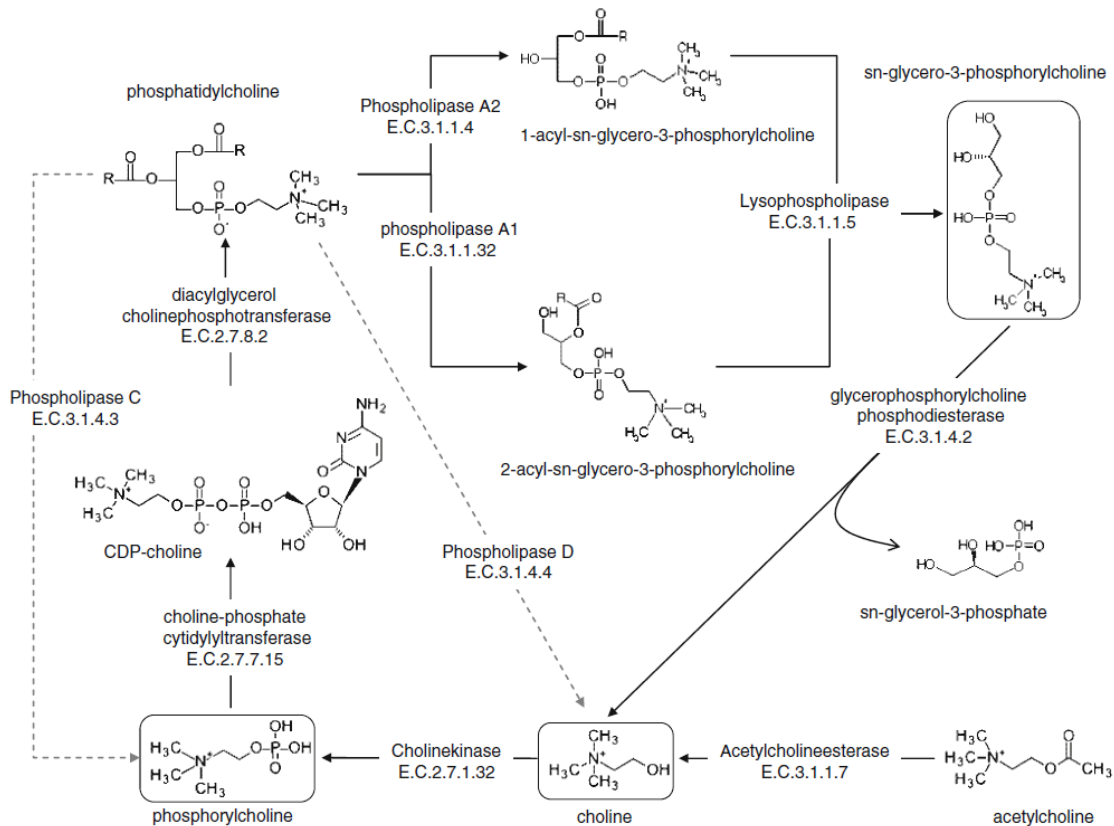


Figure 1.2. Phosphatidylcholine catabolic and choline anabolic routes. PtdCho is synthesized in most cells via the Kennedy Pathway, where choline (bottom center) is phosphorylated by ChoK, then DAG is added via a CDP-mediated two-step mechanism. PtdCho can be metabolized at a variety of cleavage sites by the phospholipase enzymes. The byproducts of both the PtdCho catabolic and anabolic steps have important signaling functions, which can go awry in diseased tissue. Reproduced from *Baykal et al., 2008*, with permission.

PC formation can also occur by a number of catabolic paths, which are mediated by a class of enzymes known as the phospholipases (Fig. 1.2). PC can be cleaved directly from PtdCho by PtdCho-specific phospholipase C (PC-PLC), releasing a DAG second messenger that can go on to activate protein kinase C. While the activation of PC-PLC at the plasma membrane and the inhibition of its activity by the compound D609 have been studied, the gene(s) encoding its protein(s) have yet to be identified (Ramoni *et al.*, 2004). PC can also be derived by phospholipases using indirect methods. These methods include conversion of PtdCho to free choline and phosphatidic acid (PA) by

phospholipase D (PLD), and the coordinated activity of phospholipase A₂ (PLA₂), lysophospholipase (LPL) and glycerophospholipase:phosphodiesterase (GPC:PDE) to render free choline. In both cases, the enzyme ChoK is again responsible for conversion of free choline to PC. These enzymes have been found to be differentially expressed in some but not all cancers, and much work is still required to fully elucidate their involvement in PC production (Podo *et al.*, 2011). A number of mitogenic second messengers are released as byproducts of PtdCho cleavage, including DAG, lysophosphatidic acid, PA, arachidonic acid, and PC itself (Agwu *et al.*, 1989; Nishizuka, 1992; Moolenaar, 1999; Du *et al.*, 2010).

1.4 Choline kinase

The primary mediator of PC levels in cancer cells is believed to be the enzyme ChoK, which is responsible for phosphorylation of free choline upon cell entry or release by a catabolic process. Enhancement of intracellular PC by Ras transformation is a ChoK-dependent process, as ChoK inhibitors have been demonstrated to halt these alterations (Ramírez de Molina *et al.*, 2001). The growth factors that rely on PC production to exert their mitogenic effects also require ChoK; ChoK inhibition in primary human mammary epithelial cells blocks EGF, insulin, and hydrocortisone-induced DNA synthesis (Ramírez de Molina, Báñez-Coronel, *et al.*, 2004). It can therefore be inferred that the production of PC as a mitogenic second messenger is regulated by ChoK and cannot be salvaged in most cases by a compensatory catabolic mechanism.

There are three different isoforms of ChoK in mammals coded by two different genes. *CHKA* encodes the protein ChoK α , which exists in two splicing variants. ChoK α variant

2 includes an 18 amino acid insertion between Met¹⁵⁰ and Gly¹⁵¹ (Aoyama *et al.*, 2004). While the importance of this splicing difference is not certain, some evidence indicates it may impact subcellular distribution (Miyake and Parsons, 2012). The *CHKB* gene encodes the protein ChoK β , which has approximately 60% sequence homology to the ChoK α isoforms (Aoyama *et al.*, 1998). ChoK is only functional in homodimer or heterodimer form, and the distribution of each isoform varies widely between tissues. While the testis and liver exhibit relatively high ChoK α expression, the heart and liver have the highest ChoK β protein (Aoyama *et al.*, 2002). Each isozyme is capable of phosphorylating choline, as well as the structurally similar ethanolamine. Only ChoK α has been found to have a link to tumor transformation (Gallego-Ortega *et al.*, 2009), but defects in ChoK β can lead to muscular dystrophy (Sher *et al.*, 2006). While the ChoK α protein is more selective for the choline substrate, ChoK β has higher affinity for ethanolamine (Gallego-Ortega *et al.*, 2009). *CHKA* but not *CHKB* deletion is embryonically lethal (G Wu *et al.*, 2008), further implicating the ChoK α variants as the crucial contributors to PtdCho biosynthesis. ChoK α/α complexes have the highest ChoK activity (higher V_{\max} and lower K_m), β/β complexes have low activity, and α/β dimer complexes have intermediate catalytic activity (Aoyama *et al.*, 2004; Gallego-Ortega *et al.*, 2009).

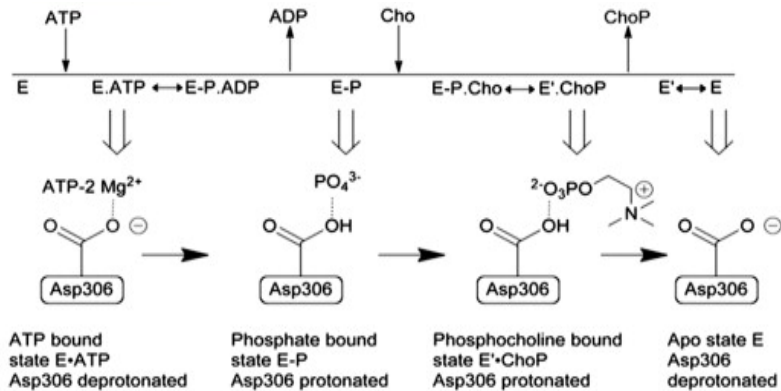


Figure 1.3. ChoK α phosphorylates choline via an unusual ping-pong mechanism. Unprotonated Asp³⁰⁶ at the active site of human ChoK α can accept a phosphate group by a Mg²⁺-coordinated reaction resulting in protonation of the amino acid and subsequent ejection of ADP. The phosphate-primed enzyme can accept choline, which induces a conformational shift in the enzyme resulting in PC exit. The deprotonated ChoK α enzyme reverts to its original conformation and is again ready for ATP binding. Adapted with permission from *Hudson et al., 2013*.

ChoK is similar to other kinases in that its N- and C-terminal lobes come together to form the ATP-binding site, but it is classified as an “atypical kinase” because there is a flexible ATP-binding loop in place of the glycine-rich P-loop found in typical eukaryotic kinases (Peisach *et al.*, 2003; Scheeff and Bourne, 2005). It has been known since its discovery that the conversion of the phosphate group from ATP to choline requires magnesium ions for reaction coordination (Wittenberg and Kornberg, 1953). It was only recently reported by Hudson *et al.* that ChoK works by an iso double-displacement mechanism, meaning that no ternary choline-ATP-ChoK complex is formed during catalysis (Fig. 1.3). Instead, ATP transfers a phosphate group directly to the enzyme at residue Asp³⁰⁶, which upon protonation causes ADP to leave (Hudson *et al.*, 2013). The protonated, phosphate-bound Asp³⁰⁶ favors the binding of choline, which causes a conformational shift in ChoK that deprotonates Asp³⁰⁶ and releases PC in a process that then makes the original ChoK conformation more favorable. This ping-pong mechanism was supported by the surprising finding that ChoK has ATPase activity even in the

absence of choline (Hudson *et al.*, 2013). The active site of ChoK is unlike the cleft-like structure of most protein kinases; the choline binding site exists in a tunnel-like pocket of hydrophobic residues with a rim of negatively-charged amino acids (Malito *et al.*, 2006). Reports generally agree on K_m values for choline between 100-180 μM , K_m values for ATP between 410-760 μM , and k_{cat} values for the enzyme of 69-83 s^{-1} (Malito *et al.*, 2006; Hong *et al.*, 2010; Hudson *et al.*, 2013).

Heightened ChoK activity was first reported in rat hepatocytes following treatment of carcinogenic polyaromatic hydrocarbons; reversal of this phenomenon by addition of transcription inhibitors (cyclohexamide or actinomycin D) suggests the increase in activity was due to an increase in ChoK protein expression (Ishidate *et al.*, 1980). ChoK α , but not ChoK β , expression can also be induced in liver cells by carbon tetrachloride (CCl_4) (Aoyama *et al.*, 2002). This hepatotoxin was later found to cause upregulation of the oncogenic transcription factor c-jun that binds to an activator protein 1 (AP1) element site in the promoter region of *CHKA* (Aoyama *et al.*, 2007). Hypoxia response elements (HREs) in the *CHKA* promoter region have linked HIF1 α activity to ChoK α expression (Glunde *et al.*, 2008; Bansal *et al.*, 2011). Inhibitors of the mitochondrial electron transport chain in neuroblastoma cells can increase ChoK α expression and phospholipase activity, leading to elevated choline metabolites (Baykal *et al.*, 2008). Additional reports have shown that the oncogene c-Myc can increase ChoK α expression ultimately leading to higher levels of PC detected using ^1H -MRS (Morrish *et al.*, 2008; 2009). ChoK α activation can be mediated by the oncogenic small GTPase RhoA and its effectors (Ramírez de Molina *et al.*, 2005). Ras mutation in NIH3T3 fibroblasts was shown to increase ChoK activity via Ral-GDS and PI3K downstream

pathways (Ramírez de Molina, Penalva, *et al.*, 2002). Treatment of human prostate and colon carcinoma cells with the PI3K inhibitor PI-103 reduced ChoK α and PC levels, indicating PI3K is regulative of PtdCho biosynthesis by promoting *CHKA* expression (Al-Saffar *et al.*, 2010). In yeast, direct phosphorylation at Ser³⁰ and Ser⁸⁵ of choline kinase (CKI) by protein kinase A (PKA) increases PC production (Yu *et al.*, 2002), although only rudimentary evidence in humans exists to suggest similar regulation of ChoK by PKA (Wieprecht *et al.*, 1994). Phosphorylation of ChoK α at the Tyr¹⁹⁷ and Tyr³³³ residues has been reported in human breast cancer cells, and these alterations increase the activity of ChoK α when in a complex with epidermal growth factor receptor (EGFR) and c-Src (Miyake and Parsons, 2012). In human breast cancer cells, extracellular calcium has been used to stimulate ChoK activity and PC formation by a Rho-dependent pathway (Huang *et al.*, 2009). This is of interest because calcium, along with other growth factors, is released in large quantities at sites of metastases to bone (Silver *et al.*, 1988; Hoey *et al.*, 2003).

The diversity of cancer-associated factors that can stimulate ChoK activity establishes the critical role this oncoprotein plays in tumorigenesis. Overexpression of ChoK α , but not ChoK β , is sufficient to drive tumor transformation (Gallego-Ortega *et al.*, 2009). Amplified ChoK α expression was first reported in breast carcinomas, and these studies found elevated ChoK activity in 39% of patient-derived tumor specimens (Ramírez de Molina, Gutierrez, *et al.*, 2002). ChoK α deregulation has since been found in 47% of colon cancer, 56% of lung cancer, and 48% of prostate cancer tissues (Ramírez de Molina, Rodríguez-González, *et al.*, 2002). ChoK α over-activity has additionally been reported in ovary (Iorio *et al.*, 2010), endometrial (Trousil *et al.*, 2014), and pancreatic

cancers (Penet *et al.*, 2015). A retrospective study of non-small-cell lung cancer patients who had received prior surgical tumor resection found that individuals with tumor ChoK α levels 1.91-times higher than healthy tissue had four-year survival rates of just 49%, compared to a survival rate of 71% in patients with ChoK α expression below this threshold (Ramírez de Molina *et al.*, 2007). ChoK α activity is clinically correlated with histological tumor grade in breast cancer, and is inversely proportional to estrogen receptor positivity in patients (Ramírez de Molina, Gutierrez, *et al.*, 2002). This is significant in that it implicates breast cancer patients resistant to the anti-estrogen tamoxifen may have pro-survival pathways mediated by ChoK. In murine models of bladder cancer, ChoK α overexpression is associated with larger, more metastatic tumors and contributes to a more aggressive carcinoma (Hernando *et al.*, 2009). HDAC inhibitors Vorinostat, LAQ-824, and belinostat provide the only example running contrary to this conventional wisdom, in that they induce differentiation and apoptosis in cancer cells but cause a rise in PC and ChoK levels (Sankaranarayananpillai *et al.*, 2006; Y Chung *et al.*, 2008; Belouèche-Babari *et al.*, 2010; Ward *et al.*, 2013). ChoK α expression and activity are otherwise described consistently as robust biomarkers for tumor aggressiveness in a growing number of cancers, with few exceptions.

1.5 Choline kinase inhibition

ChoK α suppression. There is growing clinical interest in the suppression of ChoK α activity to ameliorate the pro-growth, drug resistant, and invasive phenotype this enzyme seems to impart on cancers originating from a wide range of tissues. An siRNA screen of human kinases and phosphatases which are critical for cell survival found ChoK α knock-

down to cause a two-fold increase in apoptosis (MacKeigan *et al.*, 2005). The first study to explore RNAi knockdown of ChoK α in-depth found reduced proliferative markers and signs of differentiation in the highly-metastatic triple-negative MDA-MB-231 human breast cancer cell line (Glunde *et al.*, 2005). Chua *et. al.* performed an siRNA screen of more than 90 kinases to identify regulators of Akt, a critical molecular mediator in metabolism and cell survival pathways. In MDA-MB-468 breast cancer cells, both ChoK α and ChoK β activities were found to promote phosphorylation of Akt at Ser⁴⁷³, activating Akt in a PI3K-dependent manner (Chua *et al.*, 2009). While ChoK α RNAi silencing prevents mitotic entry and induces apoptosis in HeLa cells, knockdown of ChoK β in addition to ChoK α rescues this lethality implying that the ChoK α to ChoK β ratio is key to regulating release from G₀/G₁ arrest (Gruber *et al.*, 2012). The Lacal group used stable ChoK α knockdown by shRNA and found enhanced PARP cleavage in cervical, lung, and bladder cancer cells. This study also found ChoK α shRNA induces apoptosis in MDA-MB-231 cells and tumor xenografts, but is tolerated in untransformed human mammary epithelial cells (Báñez-Coronel *et al.*, 2008). Suppression of ChoK α expression also appears to sensitize cancer cells to chemotherapeutics (Mori *et al.*, 2007; Granata *et al.*, 2014). In 2009, a lentiviral approach to deliver ChoK α shRNA to MDA-MB-231 xenografts achieved 80% reduction in ChoK α protein and attenuated PME levels were detected noninvasively using *in vivo* ³¹P MRS (Krishnamachary *et al.*, 2009). An early study that sought to explain the observation that myo-inositol and choline addition to growth media reduces *de novo* PtdCho synthesis found this effect is due to down-regulation of ChoK α expression, rather than direct chemical inhibition of the protein (Hosaka *et al.*, 1990).

Early inhibitors. In studying the interaction between ChoK and its natural substrates, early propanol, butanol, and methyl-substituted derivatives of choline were described as ChoK inhibitors (Shelley and Hodgson, 1970). Wittenberg and Kornberg reported that ChoK activity could be stimulated by cysteine (Wittenberg and Kornberg, 1953). This early observation led Brostrom and Browning to study choline phosphorylation in the presence of the thiol group inhibitors and found ChoK inhibition by both *N*-ethylmaleimide and Ellman's reagent (Brostrom and Browning, 1973). A preliminary study as far back as 1974 linked inhibition of ChoK to membrane morphological changes in cancer cells, and demonstrated anti-tumor activity using purinyl-6-histamine to inhibit choline phosphorylation (Mayer and Werner, 1974). A comprehensive review of agents known to inhibit ChoK activity in any way includes a wide variety of Kennedy pathway intermediates (e.g. ethanolamine, PC, CDP-choline) and choline derivatives (e.g. ethyl choline mustard, acetylcholine, betaine) (Lacal, 2001). A variety of muscarinic receptor antagonists (e.g. quinacrine), ATP analogs (5'-AMP, AMP-PNP), and ions capable of displacing Mg^{2+} have also been reported, although for many of these agents it is likely that this effect is non-specific and due to action on the choline transporters, widespread interaction with ATP-binding sites in kinases, or other metal-dependent enzymes (Ishidate, 1989). Finally, ChoK is most catalytically efficient at alkaline pH ranges (8.0-9.5) and can be effectually inactivated in acidic environments (Wittenberg and Kornberg, 1953).

Hemicholinium-3. Since its discovery as a ChoK inhibitor (Ansell and Spanner, 1974), the symmetric dicationic choline-mimetic hemicholinium-3 (HC-3, Fig. 1.4) has been a prototype for ChoK inhibitors (Hamza *et al.*, 1983). Prior to its study as a ChoK

inhibitor, HC-3 was used as a research tool for its ability to inhibit acetylcholine synthesis in the nervous system (Gomez *et al.*, 1970). First discovered in 1954 (Long and Schueler, 1954), HC-3 was shown to disrupt ChoK activity in the brain by blocking sodium-dependent high-affinity choline uptake (Yamamura and Snyder, 1973; Guyenet *et al.*, 1973) and diminishing acetylcholine synthesis (Macintosh, 1961; Gardiner, 1961). While HC-3 is capable of reducing PC levels and inhibiting growth factor-induced DNA synthesis *in vitro* (Jiménez *et al.*, 1995), administering HC-3 at doses necessary for *in vivo* ChoK inhibition causes substantial off-target action on the neuronal high affinity choline transporters as well as acetylcholinesterase (Cannon, 1994). HC-3 toxicity results in a “curare-like” death due to its disruption of cholinergic neurotransmission (Boobis *et al.*, 1975). The first exploration of HC-3 derivatives took place in the late-1980s and found that hydrophobic spacer length was critical in establishing the distance between quaternary ammonium groups (Tedford *et al.*, 1986; Bhattacharyya *et al.*, 1987; Cannon *et al.*, 1988; Sheff *et al.*, 1988). A fourteen-atom spacing between the cationic head-groups yielded the most potent modulators of acetylcholine content in the caudate nucleus, one of the structures that makes up the basal ganglia and controls motor function (Bhattacharyya *et al.*, 1987). Most tertiary ammonium derivatives are inactive, however the choline-like oxazinium group can be replaced with 4-methylpiperadine, suggesting that a hydroxyl group is not essential for choline uptake inhibition (Tedford *et al.*, 1986; Sheff *et al.*, 1988).

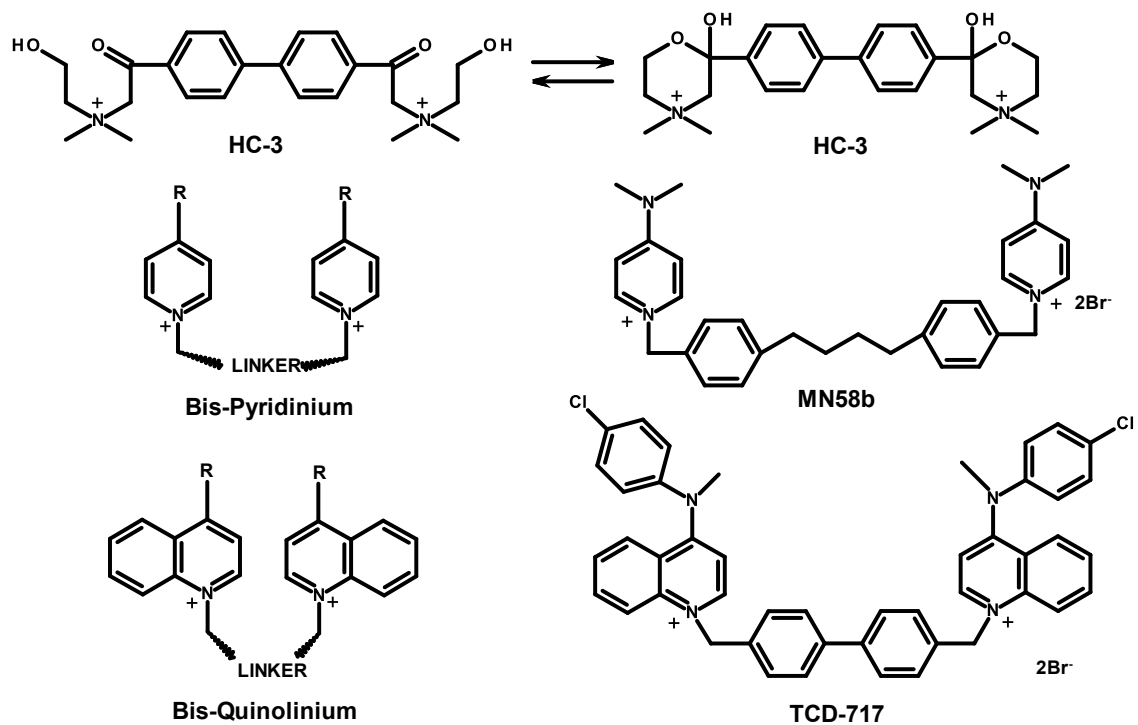


Figure 1.4. Structures of symmetric ChoKa inhibitors. The oxazinium rings of HC-3 can exist in open or ring structures, but crystallization studies indicate the closed ring is more favorable *in vitro*. Two classes of HC-3 analogs mimic the heterocyclic head-groups with either pyridinium or quinolinium moieties on each end of a hydrophobic spacer. Electron-donating substituents at the R-group improve potency against ChoKa. MN58b is a representative of the bis-pyridinium class. TCD-717 is a bis-quinolinium ChoKa inhibitor currently in clinical trials.

Bis-pyridiniums. The IC₅₀ of HC-3 against purified ChoK is 500 μM, so as new links between cancer and choline phosphorylation were discovered in the 1990s, it became clear that more selective and potent ChoK inhibitors were needed. Based upon prior HC-3 derivatives, new ChoK inhibitors were soon developed in the lab of Juan Carlos Lacal. This initial class of bis-pyridinium compounds improved the potency against pure ChoK and the growth inhibitory concentration in cancer cells by several orders of magnitude (Hernández-Alcoceba *et al.*, 1997). Quantitative structure-activity relationships (QSAR) demonstrated that electron-donating groups substituted at the C4-position of the pyridinium head-groups (Fig. 1.4) give the strongest *ex vivo* ChoK inhibition, the -NMe₂

moiety is one of the most electron-donating substituents known (Campos *et al.*, 2001). The most promising of these compounds, MN58b (Fig. 1.4), is effective against a variety of cancer cell lines, significantly retards xenograft growth, and, most importantly, is more specific for ChoK α than HC-3 (Hernández-Alcoceba *et al.*, 1999). Improved activity was found when the 4,4'-biphenyl linker of HC-3 was replaced by a 1,2-ethylene(bisbenzyl) fragment (Campos *et al.*, 2003). Although tri-pyridinium structures exhibit superior potency against purified ChoK α , the additional charge on these molecules makes them impenetrable to the cell membrane and relatively weak anti-proliferative agents (Conejo-García, 2003). Likewise, attempts to make these structures more rigid to reduce rotational bonds and conform to “drug-likeness” principles ultimately led to IC₅₀s as low as 30 nM in purified recombinant ChoK α , but these bis-pyridinium cyclophane compounds are ineffective at inhibiting growth of HT29 colorectal adenocarcinoma cells (Conejo-García *et al.*, 2003). A rigid bi-phenyl linker did yield the most potent compounds, and when paired with a 4-chloro-N-methylanilino substituent on the pyridinium moiety, gave rise to a number of promising agents (Conejo-García *et al.*, 2004). Extensive molecular modeling of these compounds with the crystal structures of ChoK α have helped to highlight the importance of the linker moiety, distance between quaternary ammoniums, delocalization of positive charge by electron-donating groups, and steric hindrance (Janardhan and Srivani, 2006).

Bis-quinoliniums. The first attempt to make HC-3 analogous ChoK α inhibitors found pyridine derivatives to be the most potent, however insights gleaned from the QSAR studies of these bis-pyridiniums suggest lipophilicity could be a major factor disconnecting *ex vivo* ChoK inhibition from *in vitro* antiproliferative efficacy (Lacal,

2001). Additionally, with a better understanding of steric and electrostatic interactions at the active site, it became attractive to substitute the pyridine moiety with a variety of substituted quinolinium or isoquinolinium fractions to improve the cell permeability (Sánchez-Martín *et al.*, 2005). The bis-quinoliniums (Fig. 1.4) have been demonstrated to have improved antiproliferative properties compared to the bis-pyridinium structures. This is due to overall greater hydrophobicity, although in both classes the same 3,3'-biphenyl linker and electron-donating substitutions have yielded the most potent ChoK α inhibitors (Sánchez-Martín *et al.*, 2005). These studies found that linker length has less of an effect on the antiproliferative properties than it does on ChoK α inhibition, and it was postulated that other mechanisms of cell death besides those induced by the interaction with ChoK α may exist for these compounds (Campos *et al.*, 2006). Nonetheless, there have been excellent ChoK α inhibitor candidates derived from this class, which have sub-micromolar IC₅₀s and GI₅₀s (Gómez Pérez *et al.*, 2012). One clinical candidate, known as RSM-932A or TCD-717 (Fig. 1.4) has recently completed Phase I clinical trials for advanced solid tumor treatment (Lacal and Campos, 2015).

Assymmetric inhibitors. The importance of symmetry was questioned even at the early stages of this field. However, when half-inhibitor fragments were found to be poor inhibitors and highly toxic, it was proposed that the dimeric form of ChoK α must allow each di-cationic inhibitor head-group to interact with a unique catalytic site (Lacal, 2001). With the crystal structures of inhibitors docked at the ChoK α active site having since been elucidated, the distance between catalytic units is now known to be too great for these inhibitors to span between bound ChoK α dimers, although the possibility that the unbound cationic head-group can bind to the choline-binding site of a free ChoK α

monomer or to the ATP-binding site on the same protein was never excluded (Hong *et al.*, 2010). In fact, two separate efforts have been made to design asymmetric ChoK α inhibitors which link pyridinium head-groups with ATP-like structures (Trousil *et al.*, 2013; Schiaffino-Ortega *et al.*, 2013). In each of these cases, there is little correlation between the potency of ChoK α inhibition and the antiproliferative effect, most likely due to toxicities linked to disruption of ATP binding to other critical targets. Use of the ChoK α structure for *in silico* screening led to the discovery of N-(3,5-dimethylphenyl)-2-[[5-(4-ethylphenyl)-1H-1,2,4-triazol-3-yl]sulfanyl] acetamide (referred to as CK37) (Clem *et al.*, 2011). Modeling of the active site for structure-directed discovery is now underway at Vertex Pharmaceuticals, and has already yielded incredibly potent and kinase-selective ChoK α inhibitors (Falcon *et al.*, 2013; Hudson *et al.*, 2013). These have proven to be useful tools for studying ChoK α mechanism and how it relates to tumorigenesis.

Attenuation of enzymatic activity. There are several pharmacodynamic markers of ChoK α inhibition, which have been identified using a combination of RNAi and small molecule chemical inhibitors. The earliest studies with bis-pyridinium ChoK α inhibitors found they are tolerated by untransformed NIH3T3 cells and only cytotoxic following oncogenic (Ras, Raf, Src, or Mos) overexpression (Hernández-Alcoceba *et al.*, 1997). It was presumed at this time that ChoK α 's involvement in cell cycle signaling is based solely on its ability to regulate production of the mitogenic second messenger, PC, and that the anticancer effect of ChoK α inhibition is primarily due to attenuation of this growth signal and depletion of substrates required for PtdCho biosynthesis (Lacal, 2001). Indeed, depletion of PC, tCho, and ChoK activity has been measured using both ChoK α -

targeted RNAi and small molecule approaches in both *in vitro* and *in vivo* settings (Hernández-Alcoceba *et al.*, 1999; Glunde *et al.*, 2005; Al-Saffar *et al.*, 2006). While this is a rational conclusion, it does not explain why normal cells are resistant to apoptosis under the same conditions.

Cancer cell sensitivity. In 2004, it was discovered in primary lymphocytes that the ChoK α inhibitor MN58b causes dephosphorylation of the cell cycle checkpoint retinoblastoma protein (pRb), driving these cells into a reversible quiescent state until drug removal (Rodríguez-González *et al.*, 2004). Due to defunct cell cycle regulation in lymphoma cells, the inability to dephosphorylate pRb causes Jurkat cells to continue proliferating. The cells compensate for inhibited *de novo* PC production by cleaving the PC head-group from the abundant membrane sphingolipid, sphingomyelin (Rodríguez-González *et al.*, 2004). The accumulation of ceramides as a byproduct leads to tumor-specific apoptosis, as confirmed by cleavage of PARP due to caspase-9 activation (Rodríguez-González *et al.*, 2004). Caspase-3 activation can be detected prior to a loss in mitochondrial potential and cytochrome-c release, suggesting apoptosis by a non-intrinsic pathway (Rodríguez-González *et al.*, 2005). MN58b has no effect on other enzymes involved in the PtdCho anabolic/catabolic cycles, interference in the MAPK pathway, or DNA-intercalation (Rodríguez-González *et al.*, 2003). Although MN58b has no measurable effect of MAPK signaling, an independent study found that siRNA knockdown of ChoK α does inhibit the MAPK cascade by reducing PA levels crucial for Ras anchorage and activation (Yalcin *et al.*, 2010). To support this hypothesis, this group developed a ChoK α inhibitor known as CK37 and found disrupted actin cytoskeleton and membrane ruffling in addition to suppressed signaling pathways downstream of Ras

(Clem *et al.*, 2011). The only known relationship between ChoK α and the plasma membrane is recruitment by EGFR in a c-Src dependent manner; whether this occurs specifically at focal adhesion sites has yet to be explored (Miyake and Parsons, 2012). This remains an important area of interest, as recent studies suggest that a scaffolding role, rather than or in addition to PC production, may be responsible for ChoK α 's role in cancer (Falcon *et al.*, 2013).

Anti-proliferative effect of ChoK inhibitors. The classic understanding of the effects of ChoK α inhibition began to unravel when a highly specific ChoK α inhibitor developed in Vertex labs was discovered to dramatically decrease PC pools, but cause a panel of cancer cell lines to enter a quiescent, rather than an apoptotic state (Falcon *et al.*, 2013). This work found that reduction of ChoK α protein, not PC levels, is the crucial mechanism of cell death (Falcon *et al.*, 2013), making it unclear why some but not all ChoK α inhibitors elicit an antitumor response. The discovery that MN58b and TCD-717, but not ChoK α siRNA, elicit an endoplasmic reticulum (ER) stress response finally provided a clue to explain this discrepancy (Sanchez-Lopez *et al.*, 2013). MN58b and TCD-717 cause a distinct activation of the unfolded protein response in cancer cells by elevating protein chaperones and the pro-apoptotic transcription factor CHOP (Sanchez-Lopez *et al.*, 2013). Inhibitor-induced apoptosis in cancer cells can be marginally reversed by addition of ChoK α siRNA, suggesting the conformational changes in ChoK α elicited by these inhibitors cause the inhibited enzyme to be recognized as a misfolded protein. This is non-lethal in normal cells due to a more moderate ER-stress response triggered by the pro-survival transcription factor ATF4 and its downstream network of genes responsible for ER repair (Sanchez-Lopez *et al.*, 2013). It appears that among the

molecules capable of blocking the choline-binding site, there is a smaller subset with antiproliferative activity. This therapeutic response is dependent on an inhibitor's ability to trap ChoK α in an inactive position, prompting cancer cells toward apoptosis by provoking an overly sensitive unfolded protein response. The difference between cytotoxic (e.g. bis-pyridinium, bis-quinolinium) and cytostatic (e.g. Vertex's V-11-0711) ChoK α inhibitors may be the length of the molecule and the ability to extend from the choline-binding site to one of the adjacent clefts formed by residues which open or close depending on enzyme conformation (Rubio-Ruiz and Figuerola-Conchas, 2014). The possibility of undetected off-target binding, however, remains a concern until these discrepancies are resolved.

In vivo validation of ChoK α inhibition. The difficulty in confirming ChoK α specificity is due to the contributions from other phospholipid and choline-handling enzymes that can confound the interpretation of changes in PC levels. Most notably, drugs with known effects on phospholipase activity have been studied for oncological use (Ackerstaff *et al.*, 2007). It is known that mitochondrial complex inhibitors are capable of enhancing activity through the Kennedy pathway (Baykal *et al.*, 2008), a factor that is especially concerning considering that many ChoK inhibitors feature cationic ammonium species similar to mitochondrial-targeted agents such as metformin and carbonyl cyanide 4-(trifluoromethoxy)phenylhydrazone (FCCP). A reliable panel of pharmacodynamic biomarkers of ChoK α inhibition has not been established, due to conflicting cellular responses to ChoK α targeted RNAi and small molecule inhibitors. It is yet unknown whether inactivated ChoK α protein is more crucial than PC depletion to these inhibitors' antiproliferative activities, although there is increasing evidence which supports this

hypothesis (Falcon *et al.*, 2013; Sanchez-Lopez *et al.*, 2013). Concrete evidence relies on strategies to detect ChoK α in its native state in the absence and presence of inhibitors. Unfortunately, choline tracers are dependent on choline transporters and cannot distinguish choline transport inhibitors from choline phosphorylation inhibitors (Hara *et al.*, 2006). MRS-based studies can detect steady-state metabolite levels, but enzymes from many pathways can affect these pools. The Phase-I clinical trial for TCD-717 in advanced solid tumors had an efficacy outcome measure based upon Response Evaluation Criteria in Solid Tumors (RECIST), but two years into the trial was amended to include *in vivo* MRS-based measurements of tCho to validate patient response (ClinicalTrials.gov Identifier: NCT01215864). It is unclear how necrosis due to poor blood supply or general chemotherapeutic effect could be deconvoluted from the ChoK α inhibitory response, except with advanced chemical shift imaging or follow-up histological assessment (Horská and Barker, 2010). One approach using systemically-delivered ¹¹C- or ¹⁸F-labeled HC-3 to compare choline distribution in 9L glioma rats found a tumor/muscle ratio as high as 5, however these were subcutaneous xenografts and poor tumor delivery was observed relative to the high renal and liver signals (Zheng *et al.*, 2007). The authors developed this probe to image CHT1 transporters, but this work still represents the first effort to label a choline-like inhibitor for imaging purposes and represents an interesting strategy of ChoK α inhibitor validation if a ChoK α specific probe were identified.

1.6 *Carbocyanine Dyes*

The cyanines represent a diverse class of fluorescent molecules that share a common structure composed of one tertiary nitrogen and one quaternary nitrogen connected by an odd number of methine groups (alternating single and double bonded carbons). The terminal nitrogen on each end of this resonant polymethine structure is typically part of a larger heterocyclic system. The first cyanine was described by Greville Williams in 1865 who mixed quinolone (with an unforeseen lepidine impurity) with amyl iodide and obtained a brown oil that, when treated with ammonia, became a brilliant “corn flour blue” substance he termed “cyanine” (Williams, 1856). After investigation by many colleagues, it was realized the methyl impurity in lepidine provided the central methine carbon between the quinoline rings (Hoogerwerff and Van Dorp, 1883). As this reaction became better understood, new isoforms were described with 0 (apocyanines), 1 (true cyanines), 3 (carbocyanines), and 5 (tricarbo-cyanine) methine groups between the terminal rings. When non-similar head-groups flank the methine linker, these structures are known as isocyanines (Adams and Haller, 1920). These head-groups can be quinolinium, indolium, thio-indolium, oxa-indolium, pyridinium, imidazolium, and benzo-indolium rings with infinite substituent groups possible (Doja, 1932). The distance between the nitrogen atoms is the primary determinant of the wavelength of maximal light absorption, and it is possible to make general predictions of optimal fluorescence excitation wavelengths using particle-in-a-box theory (Autschbach, 2007). The carbocyanines are useful as a class of dyes because the optical properties can be tuned in a predictable manner and there are many potential sites for functional modifications.

While the original interest in cyanines was for textile coloring agents, it was quickly discovered that these compounds make excellent photo-sensitizers in silver halide plates, allowing photography to advance into an expanded range of wavelengths (Doja, 1932). Cyanines have since been implemented in a variety of industrial uses which include laser disk storage, solar energy, paints, and semiconductors (Mishra *et al.*, 2000). The first widespread use of a cyanine in humans followed clinical approval of indocyanine green (ICG, Fig. 1.5A) for measurement of cardiac function (Fox *et al.*, 1957). In 1966, the report of an interaction between a cyanine and DNA questioned the notion that cyanine derivatives were biologically inert (Kodama *et al.*, 1966). Changes in red blood cell membrane potential in response to valinomycin can cause quenched aggregation or fluorescent dissociation of a panel of cationic cyanine dyes (Sims *et al.*, 1974). It was even found that 3,3'-dipropyl- and 3,3'-diethyl-thiadicarbocyanine are capable of inhibiting K^+ efflux through the Ca^{2+} -dependent K^+ transporters (Simons, 1976). Cyanines with longer lipophilic alkyl chains can incorporate into the plasma membrane and were used as a stable labeling system for tracking neuronal growth (Honig and Hume, 1986). When it was discovered that carcinoma cell mitochondria selectively accumulate cationic dyes such as rhodamine (Bernal *et al.*, 1983), Oseroff *et al.* were able to accomplish similar results using N,N'-bis(2-ethyl-1,3-dioxolane)kryptocyanine and found that effective photodynamic therapy could be achieved in bladder, colon, and squamous cancer cells with no light-induced death in normal keratinocytes or kidney epithelial cells (Oseroff *et al.*, 1986). Since these reports of biological activity, however, the enthusiasm for cyanines as fluorescent tags attached to antibodies (Folli *et al.*, 1994; Ballou *et al.*, 1995; Vogel *et al.*, 1996; Ballou *et al.*, 1997), receptor ligands (Becker *et*

al., 2001; Tichauer, Samkoe, Klubben, *et al.*, 2012), and natural products (Packard and Wolf, 1985; Becker *et al.*, 2000; Licha *et al.*, 2000) has far out-weighted the concern or interest in their pharmacodynamic effects.

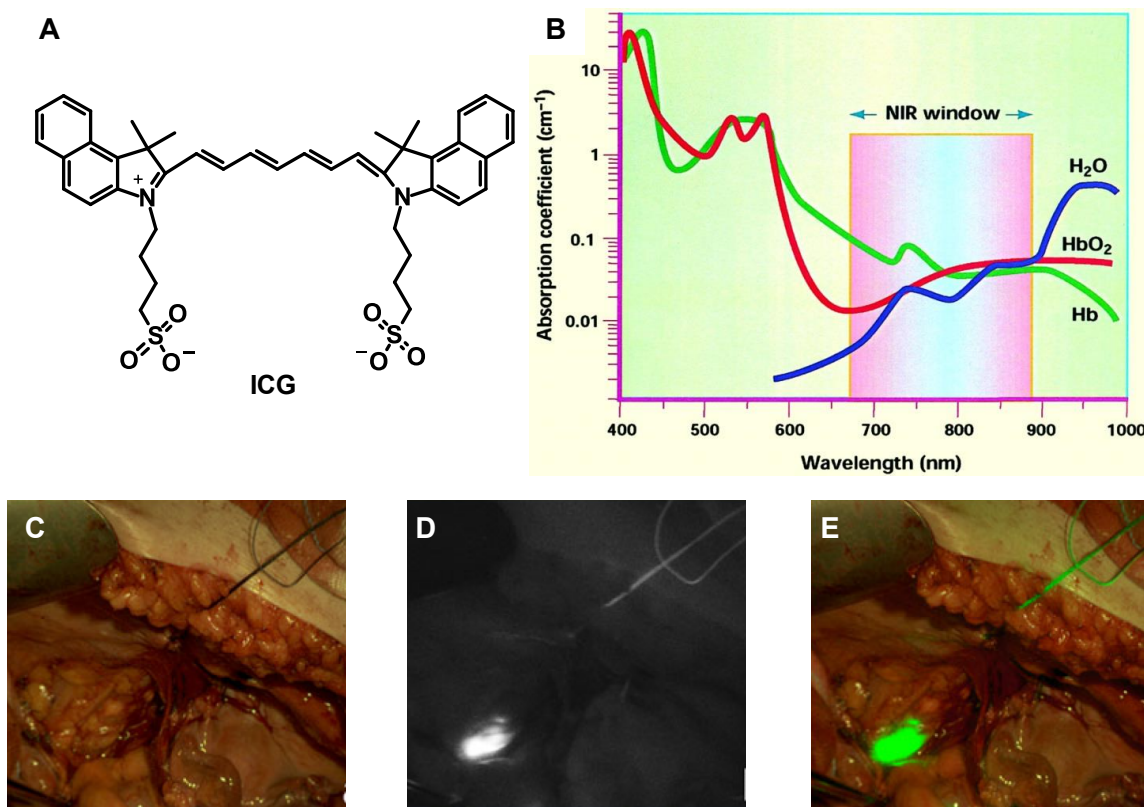


Figure 1.5. The use of ICG for NIRF-guided surgical resection. (A) ICG is a clinically approved cyanine with NIRF that binds to serum albumin and can be detected in blood vessels and lymph nodes. (B) Human tissue scatters and absorbs light in the visible range, but is relatively transparent to light in the NIR window. (C) To the naked eye, it can be difficult for surgeons to identify lymph nodes, (D) however, as a blood pooling agent ICG can be used to identify the sentinel lymph during tumor resection. (E) An overlay of the bright field and NIRF (green) channels offers a promising new intraoperative imaging tool. Panel (B) used with permission by *Mahmood and Weissleder, 2003*. Panels C-E adapted with permission from *Crane et. al., 2011*.

More often, cyanines are being used as tools to measure physiological changes as a result of disease progression. One such application is the formation of hydrocyanine derivatives using sodium borohydride to reduce cyanines on the quaternary cationic ammonium group (*Kundu et al.*, 2009). In this uncharged, non-fluorescent state,

hydrocyanines are more cell-permeable and can be returned to their charged, fluorescent state by oxidizing agents. A number of commercially-available carbocyanines were modified to their hydrocyanine form and used to detect reactive oxygen species in lipopolysaccharide-induced inflammation (Kundu *et al.*, 2009). A new class of cypate-derived carbocyanines was recently discovered in the Achilefu lab to have dichromic fluorescence with emissions at 700 nm in the symmetric state and 800 nm when asymmetry is introduced by functional group addition. This is a particularly-promising discovery because cypate-derivatives with serine-mimicking alkyl groups were shown to undergo phosphorylation by Akt, rendering a measurable alteration in fluorescence which serves as a read-out of insulin-activated Akt activity (Shen *et al.*, 2013).

There are a number of optical, chemical, and biological properties that are desirable for a clinically suitable cyanine dye. The observed brightness of a fluorophore is the product of two factors. The first is the extinction coefficient (ϵ), which describes the number of photons a given concentration of dye (c) can absorb. The actual absorbance (A) of a particular wavelength of light is also dependent on the path length of the beam through the medium (ℓ), and is described by the Beer-Lambert law: $A = \epsilon c \ell$. The second factor is the fluorescence quantum yield (Φ_f), which relates to the efficiency with which absorbed photons are emitted at a longer wavelength (Rurack and Spieles, 2011). These factors can be influenced by the solvent system, as can the general solubility of the probe, thus testing needs to be performed in serum prior to animal studies (SL Gibbs, 2012). The wavelength of excitation and emission is of particular importance for *in vivo* fluorescence measurements, as human tissue has many components which can absorb, scatter, and fluoresce light, creating a broad range of wavelengths unsuitable for optical imaging

(Lewis *et al.*, 2002; Mahmood and Weissleder, 2003). Endogenous molecules such as nucleic acids, fat, water, hemoglobin, and melanin limit light penetration in the UV and visible range, but within the spectral window known as the near infrared (NIR) wavelengths (Fig. 1.5B), human tissue is relatively transparent (Hale and Querry, 1973; Jobsis, 1977; van Veen *et al.*, 2005). Near infrared fluorescence (NIRF) measurement is becoming a major tool for non-invasive disease measurement, however thus far only ICG and methylene blue are approved for clinical use. Due to strong binding to serum albumin, ICG is confined to the vasculature and has been used for retinal angiography, measuring cardiac output, evaluating hepatic clearance, defining lymphatic architecture, and delineating tumor margin (Marshall *et al.*, 2010). While ICG's excitation (760-785 nm) and emission (820-840 nm) are within the therapeutic window, dye aggregation and photo-instability lead to relatively poor optical properties (Landsman *et al.*, 1976). The mechanism of accumulation within cancer tissue is non-specific and based upon enhanced permeability and retention (EPR) within the disorganized vasculature and insufficient lymphatic system of the tumor (Marshall *et al.*, 2010). Methylene blue is also a blood pooling agent but exhibits low tumor contrast due to its non-ideal optical properties (Ex. 668 nm, Em. 688 nm) (Matsui *et al.*, 2010). Methylene blue has been useful in lymph node mapping (Tuttle, 2004), but ICG remains the best clinical option for NIRF-guided tumor margin identification (Frangioni, 2008).

1.7 Near infrared fluorescence guided surgery

Surgery remains a crucial part of oncological treatment and cures an estimated 50% of cancers, despite the fact that the vast majority of tumor resection relies on visual

recognition and palpation to discern cancerous from normal tissue (De Grand and Frangioni, 2003). Without the aid of tissue contrast guidance, resection of tumor boundary tissue and evaluation by histopathology remains the gold standard for confirming cancer-free margins (SL Gibbs, 2012). This technique is labor-intensive and time consuming, but necessary to identify tumor outgrowths which can be too narrow for the naked eye to detect. The need for sentinel lymph node identification and resection for histological assessment could also be aided by a real-time contrast agent. NIRF-guided surgery is a promising new field that seeks to pair enhanced cancer-tissue contrast with the operational simplicity and safety of optical imaging (Frangioni, 2003). Currently the most advanced technology in this field is the Fluorescence-Assisted Resection and Exploration (FLARE) system, which consists of a dual bright field and NIRF light acquisition overlay on a hands-free monitor set up in the surgical suite (Nakayama *et al.*, 2002; Troyan *et al.*, 2009). With virtually no background signal, intraoperative NIRF imaging has been used to successfully identify tumor margins (Madajewski *et al.*, 2012) and sentinel-node positivity (Fig. 1.5C-E) (Kitai *et al.*, 2005; Crane *et al.*, 2011) using a variety of fluorophores and cancer models (Weissleder and Ntziachristos, 2003).

Britton Chance introduced optical imaging of the breast, using endogenous contrast in the NIR range created by oxygen levels and blood volume (Nioka *et al.*, 1994). It is now widely thought that exogenous contrast agents are required to achieve the sensitivity necessary to justify the use of imaging systems during surgery (Weissleder and Ntziachristos, 2003). The pharmacokinetics and optical properties of a probe are the two most important factors that contribute to successful tumor-specific NIRF. There are two approaches to achieving tumor specificity: target affinity and site-specific activation.

Fluorophore-conjugated ligands have been designed for a number of cancer-specific molecules, including somatostatin receptors (Achilefu *et al.*, 2000), folate receptors (Tung *et al.*, 2002), immunoglobulin proteins (Ballou *et al.*, 1995), carcinoembryonic antigen (Folli *et al.*, 1994), oncofetal fibronectin isoform (Neri *et al.*, 1997), and EGFR (Ke *et al.*, 2003). Weissleder expanded the field using fluorescence resonant energy transfer (FRET) to design quenched fluorophores that could be released upon cleavage by an enzyme or physiological activity of interest (Weissleder *et al.*, 1999). A number of enzyme-cleaved probes have since been designed to provide functional measurements of lysosomal proteases (Weissleder *et al.*, 1999), matrix metalloproteinases (Bremer *et al.*, 2001), cathepsins B and D (Tung *et al.*, 2000; Marten *et al.*, 2002), and phospholipases (Mawn *et al.*, 2011). While there are a growing number of such probes under investigation, the field of intraoperative NIRF imaging is limited by the number of clinically available imaging agents. Among the obstacles for clinical approval is tumor selectivity, *in vivo* sensitivity, barriers to intratumoral probe delivery (pore size, interstitial pressure), immunogenicity, and efficient clearance (Becker *et al.*, 2001; Torosean *et al.*, 2013). For this reason, small molecule drugs and imaging agents are still largely preferred over macromolecules/nanoparticles due to their favorable pharmacokinetics.

1.8 Scope of thesis

The focus of this work deals with improvement of the available methods to validate ChoK α inhibitors *in vivo*. The observation of structural similarity between the antiproliferative ChoK α inhibitors and the carbocyanines sparked the initial search for a

fluorescent dye capable of attenuating flux through the Kennedy pathway. The development of JAS239 as such a candidate is then described, with the *in vitro* characterization of its inhibitory and cell tracking capabilities included. Insights gleaned from JAS239 administration as a diagnostic probe and anticancer drug were then used to study the specificity of an established inhibitor. The final portion of this thesis describes the design of a library of JAS239 derivatives with structural modifications made based upon its described characterization.

CHAPTER 2

Materials and Methods

2.1 Chemistry Materials

Solvents were purchased from Fisher Scientific. 1,4-Diphenyl-butane was purchased from Pfaltz & Bauer, Inc. 3,3'-dimethyloxacarbocyanine iodide (DMOCI) and 1,1',3,3,3',3'-hexamethylindotricarbocyanine iodide (HITC) were purchased from Acros Organics. *N*-(3-Triethylammoniumpropyl)-4-(6-(4-(diethylamino) phenyl) hexatrienyl) pyridinium dibromide (FM 4-64) was purchased from Life Technologies. Hemicholinium-3 (HC-3) and indocyanine green (ICG) were purchased from Sigma-Aldrich. IRDye-800CW carboxylate was purchased from Li-Cor Biosciences. *E,E-conj*MN58b, *E,E,E-conj*MN58b, TCD-717, *cyclo*JAS239, *cyclo*JAS239.5, *cyclo*HITC, and *cyclo*HITC.5 were purchased from Peptech Corporation, Bedford, MA. All other chemicals were purchased from Sigma-Aldrich and used as received. The compounds were named with ChemBioDraw Ultra (v. 13, CambridgeSoft).

¹H NMR spectra were recorded on a Bruker DMX360 or UNI500 spectrometer in CDCl₃ or CD₃OD using tetramethylsilane (TMS) as an internal standard. Chemical shifts are reported in ppm. Mass spectra were recorded on a Bruker Microflex MALDI-TOF spectrometer. HPLC analysis was performed by Dr. Popov as described elsewhere (Kachur *et al.*, 2013). Absorbance and fluorescence spectra were acquired by diluting each fluorophore in methanol, addition of the solution to a 1 cm wide crystal cuvette, and measurement in a Molecular Devices Spectra Max M5 plate reader.

2.2 Cell Culture

Breast Cancer cell lines. The triple-negative MDA-MB-231 human-derived breast cancer cell line was obtained from American Type Culture Collection (ATCC) in November of 2011. These cells were expanded and frozen within 3 passage numbers after receipt. Cells were used within 6 months of resuscitation, and authorized by the ATCC via the COI assay, STR analysis, and BacT/ALERT 3D. The MDA-MB-231-derived cell line 4175-Luc⁺ was isolated from a murine lung metastasis and was generously provided by Dr. Andy Minn in August of 2013 (Minn *et al.*, 2005). Both cell lines were maintained in monolayer culture in DMEM (Mediatech, Flemington, NJ) supplemented with 10% FBS (HyClone Laboratories, Logan, UT), 1% penicillin/streptomycin (Mediatech), and 1% L-glutamine (Mediatech) at 37°C in a humidified atmosphere (5% CO₂). The 4175-Luc⁺ cells were maintained in 5 µg/mL blasticidin (Invitrogen), which was removed during experiments. MCF7 breast cancer cells expressing a *Chk-4* clone (MCF7-CK⁺) or the empty vector (MCF7-EV) were provided by Drs. Zaver Bhujwala and Tariq Shah of Johns Hopkins University in March 2012 (Shah *et al.*, 2010). These cells were cultured in MEM (Mediatech) supplemented with 10% FBS, 1% penicillin/streptomycin, 1% L-glutamine, and 400 mg/mL G418 sulfate selection agent (Mediatech). G418 was not included in the culture medium during experiments. All cell lines used were tested upon receipt and bi-monthly for mycoplasma. Cells were frozen in liquid nitrogen and only used at low passage numbers.

Glioma cell lines. To assess the toxicity and efficacy of MN58b on growth inhibition of gliomas, we chose three rat brain tumor cell lines F98, 9L and 9L over-expressing

EGFRviii (Kapoor *et al.*, 2007). The F98, 9L and 9L-EGFRviii glioma cell lines were maintained as adherent monolayers cultured in Dulbecco's Modified Eagle's Medium (DMEM, Sigma-Aldrich, St Louis, MO) supplemented with 10% fetal bovine serum (HyClone, Mississauga, Canada), 1% 4-(2-hydroxyethyl)-1-piperazineethanesulfonic acid (HEPES) buffer (Invitrogen; Carlsbad, CA), 200 U/mL penicillin and 200 mg/mL streptomycin sulfate at 37°C in 5% CO₂ in air. Cells were maintained in exponential growth phase by routine passage twice weekly at 3 x 10⁵ cells per T-75 flask. 9L and F98 cell cultures were tested upon receipt from the lab of Dr. J. Biaglow (Department of Radiation Oncology at the University of Pennsylvania) in 1999 using the Rat Antibody Production (RAP) Test performed by Charles River Laboratories (Wilmington, MA) and re-screened in 2005 using IMPACT III PCR profiling performed by RADIL (Columbia, MO). Cell lines were used within 6 months of resuscitation and tested bi-monthly for mycoplasma. The 9L-EGFRviii cell line was cloned from the 9L cells in the laboratory of Dr. Donald M O'Rourke, Department of Neurosurgery, University of Pennsylvania. We obtained the 9L-EGFRviii cell line from Dr. Donald M O'Rourke in 2010. No additional characterization has been performed on this cell line.

2.3 Western Blotting

MCF7-EV and CK+ cells were plated in 10-cm dishes (1.0 x 10⁶ cells) and grown for 24 hours. Proteins were extracted on ice using radioimmunoprecipitation lysis buffer (Abcam) fortified with a cComplete Mini, EDTA-free protease inhibitor cocktail (Roche) and quantified using the BCA Protein Assay Kit (Pierce). Approximately 30 µg total protein was resolved on a 10% SDS-PAGE gel, transferred to a nitrocellulose membrane,

blocked using nonfat milk, and blotted for ChoK α (Abcam) or GAPDH and imaged using Luminata Western Chemiluminescent HRP substrates (Millipore). Bands from each of three separate experiments were quantified using ImageJ software. Mansi Shinde of the Pharmacology Graduate Group, University of Pennsylvania provided technical support for electrophoresis, membrane transfer, immunoblotting, and film development.

2.4 ^1H MRS studies of cellular extracts

Breast cancer cells. MDA-MB-231, 4175-Luc+, MCF7-EV and MCF7-CK+ cells ($\sim 30 \times 10^6$) were harvested using trypsin and washed 2x with PBS. Dual-phase methanol/chloroform/water extraction was performed in a glass centrifuge tube as described elsewhere (Tyagi *et al.*, 1996; Glunde *et al.*, 2005). Cells were transferred to a glass centrifuge tube and 4 mL ice-cold methanol was added and cells were vortexed. After 10 minutes on ice, 4 mL of chloroform was added and the sample was again vortexed and allowed to settle on ice. After 10 minutes, 4 mL of water was added and the sample vortexed, and stored at 4°C overnight. Each glass centrifuge tube was then centrifuged at 20,000 x g at 4°C. The upper aqueous phase was separated, treated with Chelex beads to remove dicationic ions, roto-evaporated to remove methanol, and lyophilized to remove water. Samples were resuspended in D₂O containing 0.7 μmol of trimethylsilyl propionate (TSP, Aldrich) as a chemical shift reference and concentration standard. Fully relaxed ^1H NMR spectra were acquired with help from Weixia Liu and Stephen Pickup of the Small Animal Imaging Facility using an 11.7 T Varian INOVA high-resolution NMR spectrometer and a 90° pulse width (relaxation delay: 6 seconds; repetition time: 10.73 seconds; number of scans: 64; data size: 32 K; spectral width:

6,000 Hz; temp: 30°C; total acquisition time: 11 minutes 28 seconds).

Brain cancer cells. For consistency between *in vitro* and *ex vivo* extract preparation, the F98 cells grown in culture were prepared for MRS evaluation using perchloric acid extraction. Cells were seeded (1×10^5 /mL, 150 cm² flasks) and incubated overnight, media was aspirated and replaced with fresh media containing 0, 10, and 20 μ M MN58b. After 24 hour MN58b treatment, cells were trypsinized, washed and an aliquot was removed for viability counts. The remaining cells were pelleted and homogenized in 3 volumes of 6% PCA, transferred into an Eppendorf tube and centrifuged (13,000 rpm, 30 minutes, 4°C), neutralized with 3 M potassium hydroxide (KOH, Sigma-Aldrich, St Louis, MO) and the neutralized samples were lyophilized for 24 hours. Members of the Poptani Lab in the Department of Radiology performed the PCA extraction and samples were scanned on a 500 MHz vertical bore NMR scanner (Bruker, Billerica, MA) with the same parameters used for breast cell extracts.

Spectra were analyzed using Mnova Lite 5.2.5 software (Mestrelab Research, Santiago de Compostela, Spain) with 0.5 Hz apodization. Following Fourier transform, spectra were phase-corrected using the TSP peak, which was also used as a chemical shift reference at 0.0 ppm. Minor baseline correction was applied as needed. Metabolite peaks were identified on the basis of their chemical shifts (Evanochko *et al.*, 1984). The following choline-containing metabolites were identified from their N-trimethyl (⁺N(CH₃)₃) resonances: Cho 3.20 ppm (singlet); PC, 3.22 ppm (singlet); and GPC, 3.23 ppm (singlet). Metabolite concentrations were calculated using the signal area in the proton spectrum, which is proportional to the concentration and the number of protons contributing to the signal. The metabolite concentrations were calculated and corrected

for the number of cells in the NMR experiment using the following formula: [(metabolite peak height /number of protons) /(TSP peak height /number of TSP protons)] x (TSP concentration /number of cells). The resonances at 3.2 ppm from the choline-containing metabolites are all composed of 9 protons, as is the 0.0 ppm resonance of TSP.

2.5 *ChoK* activity ¹H MRS assay

MDA-MB-231, MCF7-EV, and MCF7-CK+ cells (~20 x 10⁶) were trypsinized, washed 2x in ice-cold PBS, and homogenized on ice in 4 volumes of 100 mmol/L Tris-HCl (pH 8.0) containing 10 mmol/L DTT and 1 mmol/L EDTA in D₂O as described previously (Iorio *et al.*, 2005). Samples were ultrasonicated 2x for 30 seconds at 4°C, centrifuged for 30 minutes at 12,000xg, and the supernatant transferred to an NMR tube. ATP (Sigma-Aldrich), choline chloride (Sigma-Aldrich), and MgCl₂ (Sigma-Aldrich) in Tris-HCl/D₂O buffer were added to the sample with final concentrations of 10, 2.5, and 10 mmol/L, respectively. ¹H MR spectra were recorded immediately at 10-minute intervals for 500 minutes (90° pulse length, relaxation delay: 6.6 seconds; repetition time 10 seconds; number of scans: 60; data size: 16 K; spectral width: 6,000 Hz; temp: 30°C; total acquisition time 8 hours, 20 min). Choline and PC peaks were fit from Fourier transformed spectra and were processed in the same manner as the extract data using Mnova Lite 5.2.5. Data were fit to the linear equation, $y = mx + b$, where x is time, y is the area of the PC or Cho peak, and m , the slope, gives the rate of conversion. To reduce the amount of JAS239 required to treat 20 x 10⁶ cells (grown in 4 x 150 cm² flasks containing 25 mL media each), treatment occurred after cells were pooled and centrifuged, thus 53 nmol of JAS239 were present in the 530 μL NMR sample,

equivalent to a concentration of 530 nmol/L if treatment were applied to the cells before trypsinization.

2.6 ¹⁴C-choline ChoK activity assay

Intact cells. Cells for breast cancer studies were plated at 1.5×10^6 cells/well in 6-well dishes and allowed to grow for 48 hours. For glioma cell studies, 5×10^5 cells/well were seeded in a 6-well plate and incubated for 24 hours at 37°C. Media was aspirated and replaced with fresh media containing varying concentrations of ChoK inhibitor or vehicle control, followed 1 hour later by treatment with 0.5 µCi/mL of [methyl-¹⁴C]-choline chloride (Perkin Elmer). At the indicated time-points, cells were rinsed with ice-cold PBS (Mediatech) and fixed in 16% trichloroacetic acid. Samples were scraped, collected in centrifuge tubes, washed 3x in diethyl ether, lyophilized, and resuspended in water for TLC separation using a solvent system of 0.9% NaCl: methanol: ammonium hydroxide (50:70:5, v/v/v). Quantification of the water-soluble choline metabolites was performed using autoradiography with a FujiFilm FLA-7000 in accordance with previously established protocols (Hernández-Alcoceba *et al.*, 1999). The R_f values for the choline metabolites were ¹⁴C- choline (0.07), ¹⁴C-PC (0.14), and ¹⁴C-GPC (0.39).

Cytosolic preps. For ¹⁴C-choline tracing studies independent of the choline transporters, cytosolic preps were made using the same procedure described in the ChoK activity ¹MRS assay, with diH₂O used in place of D₂O. Approximately 5×10^5 cells were used per sample. To each sample, drug was added directly at the required concentration. MgCl₂ and ATP were then added with the same final concentrations as in the NMR assay, whereas choline chloride levels were reduced to 200 µM. Finally, 3 µCi/mL ¹⁴C-

choline was mixed in the sample. Samples were incubated for 1 hour, then fixed lyophilized, reconstituted, separated by TLC, and analyzed by autoradiography following the same procedure used for intact cells. Due to the higher salt content of these samples, the R_f values for PC (0.08) and Choline (0.28) changed and were determined using labeled standards.

2.7 Cell viability studies

Trypan exclusion assay. MCF-7 EV and MCF7-CK+ cells were plated at 1.0×10^6 cells/well in 6-well plates. After 2 days, media was replaced with fresh media containing MN58b or JAS239 at concentrations ranging from 0-20 μM . At 17 hours, cells were gently rinsed with ice-cold PBS, trypsinized at 37°C , and a 200 μL aliquot was neutralized with fresh media containing Trypan Blue, and counted using a Neubauer hemocytometer. Counts were reported relative to untreated EV cells. In all viability and therapeutic studies of cells treated with JAS239, great attention was paid to protecting the samples from light, both to minimize probe degradation and the potential of a photodynamic therapy response.

MTT assay. The MDA-MB-231 and 4175-Luc+ cell lines were plated in triplicate in 96-well plates at 7.5×10^4 cells/well and incubated overnight. The culture medium was replaced with media containing varying concentrations of JAS239 or MN58b. After overnight incubation, 20 μL of 5 mg/mL of 3-(4,5-dimethylthiazol-2-yl)-2,5-diphenyltetrazolium bromide; thiazolyl blue (MTT, Sigma-Aldrich, St Louis, MO) in sterile PBS was added and the cells were again incubated for 2 h. The media/MTT mixture was removed and replaced with 150 μL dimethyl sulfoxide (DMSO, Fisher

Scientific, Fair Lawn, NJ), shaken, and the absorbance read at 550 nm using a Spectra Max M5 plate reader (Molecular Devices, Sunnyvale, CA). Background signal was read as absorbance at 690 nm and subtracted from each sample reading. For the glioma cell lines, the same procedure was followed. The MTT assays on the glioma cell lines were run by Sona Saksena, Ph.D. (Department of Radiology, University of Pennsylvania) under my guidance, and the raw data from each of the three trials was analyzed by me.

2.8 Epidermal growth factor stimulation

ChoK activity assay. The 9L and 9L-EGFRviii gliosarcoma lines were plated at a density of 1×10^5 cells/well in 6-well plates. After 24 hours, media was replaced with DMEM + 0.1% bovine serum albumin (BSA, Sigma-Aldrich). After overnight serum starvation, the 6-well plates were aspirated and DMEM + 0.1% BSA with and without 20 μ M MN58b was added. Epidermal growth factor (EGF, UPenn Cell Center) was immediately added to half the treatment groups at a final concentration of 200 ng/mL. The other half in each treatment group received the same volume of PBS. After 1 hour of incubation, [methyl- 14 C]-choline chloride was added to each well at a final activity of 0.5 μ Ci/mL. After a final hour of incubation, media was aspirated, cells were washed in PBS, and 16% TCA was added to fix each well. PC production was quantified using the TLC/autoradiography method described above.

MTT assay. The 9L and 9L-EGFRviii cell lines were distributed at 7.5×10^3 cells/well in 96-well plates. After 24 hours, media was replaced with DMEM + 0.1% BSA. Cells were incubated in serum-starved conditions for 2 days, at which time the media was replaced with fresh serum-free media containing either 20 μ M MN58b or

saline control, with half of each treatment group receiving 200 ng/mL EGF and the other half receiving PBS. After 24 hours, 20 μ L of 5 mg/mL MTT was added to each well, incubated 2 hours, and plates were analyzed using the MTT assay procedure described above.

2.9 Fluorimetry analysis

Uptake competition assay. MDA-MB-231, MCF7-EV, MCF7-CK+ cells were grown for 48 hours in 6-well plates (1.5×10^5 cells/well). Each well was aspirated and replaced with fresh media containing JAS239 with or without choline and incubated for 2 hours. Samples were washed in PBS, lysed in DMSO, and the fluorescence was measured using a Molecular Devices Spectra Max M5 plate reader with an excitation (Ex.) of 640 nm and emission (Em.) of 770 nm.

Cell retention assay. MCF7-EV and MCF7-CK+ cells were plated in 6-well plates (1.0×10^5 cells/well). After 48 hours incubation, cells were treated with varying concentrations of JAS239 for 2 hours. Each well was aspirated and rinsed once with PBS. DMSO (500 μ L) was added per well, plates were covered with tin foil to protect from light and shaken for 30 minutes prior to transfer of 200 μ L of sample to a black-walled clear bottom 96-well plate for measurement of fluorescence in the Spectra Max M5 plate reader (Ex. 640 nm; Em. 770 nm). To study ChoK α dependent retention, the same cell conditions were set up and cells were treated with 10 μ M JAS239 for 1 hour, rinsed with PBS, and incubated 15 minutes with fresh media over two separate cycles. After 3 rinses with PBS, DMSO was added and the same procedure as above was followed to measure JAS239 accumulation.

2.10 Confocal microscopy

Live cell analysis. MDA-MB-231 cells were plated at 1.5×10^5 cells/dish in 35-mm glass-bottom dishes coated with poly-*D*-lysine (MatTek Corp.). After 2 days of incubation, cells were treated with fresh DMEM containing no phenol red and 2 $\mu\text{mol/L}$ JAS239 and/or 5 $\mu\text{mol/L}$ of the nuclear targeting dye SYTO9 dye (Life Technologies). The cells were subsequently imaged with assistance from James Hayden of the Wistar Imaging Facility using a Zeiss LSM 510 META confocal microscope with Ex. 633 nm and Em. filter 650 to 790 nm.

Immunohistochemistry. MDA-MB-231 cells were plated on sterile 10 mm glass coverslips placed in 24-well plates and incubated 24 hours. The media was gently aspirated, the wells were washed with PBS and immersed in 4% paraformaldehyde for 15 minutes. Cells were washed 2x with PBS and incubated 15 minutes on ice in 0.2% Triton X-100 diluted in PBS. Cells were washed with cold PBS and blocked in 1% BSA diluted in PBS for 30 minutes. Coverslips were transferred to racks and 200 μM JAS239 was added evenly along the surface of three coverslips. After 30 minutes, these slides were washed 2x with PBS, 30 μL of rabbit anti-human ChoK α antibody (ab38290; Abcam) at 1:1000 dilution was added to the top of the slide, and the slides were incubated at room temperature for 1 hour. A separate batch of three coverslips were first incubated in anti-ChoK α antibody, rinsed 2x with PBS, then treated with 200 μM JAS239. A control group receiving anti-ChoK α antibody only were included to ensure that Texas Red fluorescence emission did not overlap with the JAS239 filter setting. Coverslips from each group were transferred to wells in a fresh 24-well plate, washed 2x with PBS, and incubated for 40

minutes in 200 μ L of dilute (1:500) goat anti-rabbit secondary antibody conjugated to Texas Red (Vector Laboratories; TI-1000). Each well was washed 3x with PBS then dehydrated using 50%, 70%, and 100% ethanol in successive 10-minute increments. Each coverslip was air-dried in the dark, mounted with VectaShield (Vector Laboratories) on slides, and kept at 4°C overnight. Alex Glavis-Bloom of the Yang Lab in the Department of Cancer Biology assisted with the development of this protocol. Confocal micrographs were acquired on a Zeiss LSM 510META NLC using Ex. 543 nm and Em. 565-615 nm for Texas Red and Ex. 633 nm and Em. >650 nm for JAS239. Images were acquired with help from Andrea Stout and Jasmin Zhao of the Cell and Developmental Microscopy Core. Background was subtracted from the images in each channel using the Fiji version of ImageJ. The Coloc 2 plug-in was used to assess colocalization (Dunn *et al.*, 2011) of the anti-ChoK- α antibody and JAS239 by calculating Pearson's Correlation Coefficients and Manders' Colocalization Coefficients for at least three separate ROIs.

2.11 Animal model and tumor cell implantation

Murine breast xenografts. All animal studies were approved by the Institutional Animal Care and Use Committee of the University of Pennsylvania. Six week old syngeneic female athymic nude Foxn1^{nu/nu} mice were acquired from the National Cancer Institute and housed in a temperature-controlled environment with 12 hour light/dark cycle. General anesthesia was induced using 2% isoflurane in oxygen for inoculations, injections, and imaging experiments. All cell lines were trypsinized, counted, washed 2x with cold PBS, and resuspended in ice-cold Matrigel (BD Biosciences, Bethesda, MD). For MCF7 inoculations, athymic nude mice were supplemented with 60-day release 0.36

mg 17 β -estradiol tablets (Innovative Research of America, Sarasota, FL) using a trochar in the nape of the neck. After 1 week of recovery time, 4x10⁶ MCF7-CK+ cells were inoculated into the left mammary fat pad (which appears on the right when the animal is in the ventral position) and 4x10⁶ MCF7-EV cells on the contralateral fat pad. MDA-MB-231 and 4175-Luc+ tumors were inoculated orthotopically unless specifically noted. These tumors were grown on the shoulder as subcutaneous xenografts, to allow for the kidneys to be cloaked during parallel optical imaging studies. Tumor growth was determined via caliper measurement of the longest (length) and two orthogonal dimensions (width and height) and tumor volume calculated as length * width * height * $\pi/6$.

Rat glioma model. Manoj Kumar and Ranjit Ittyerah of the Poptani lab were responsible for rat tumor inoculation, treatment, and tumor resection. These methods are described in detail elsewhere (Kumar *et al.*, 2015). Six week old syngeneic female Fisher F344/NCr (120-150 gm weight) rats (n = 13) were purchased from the National Cancer Institute and housed in a temperature controlled animal facility with a 12 h light-dark cycle. General anesthesia was induced by intraperitoneal injection of ketamine/xylazine (80/8.0 mg/kg). The animal was placed on a stereotactic frame. A small burr hole was made 3-mm lateral and 3-mm posterior to the bregma and 2-mm deep into the right cerebral hemisphere using a drill bit. F98 tumor cells (5x10⁴) in a 10- μ l suspension in PBS were inoculated over a 5-min period with a Hamilton syringe and a 30-gauge needle using a stereotactic apparatus. After injection of the cell suspension, the needle was withdrawn slowly and the wound was closed by suturing the skin. Animals were monitored periodically for 2 weeks during recovery.

2.12 In vivo optical imaging

JAS239 biodistribution in 4175-Luc+ bearing mice. One week prior to imaging, athymic nude mice bearing orthotopic 4175-Luc+ tumors were placed on a low-fluorescence alfalfa-free diet (5V02; LabDiet, St Louis, MO). Mice were anesthetized with 2% isoflurane and a pre-scan bioluminescence and NIRF (Ex. 745 nm; Em. 800 nm) image was acquired in an IVIS Spectrum with settings set to Automatic mode (Perkin Elmer, Hopkinton, MA) to be used as a reference for eliminating auto-fluorescence in later acquisitions. NIRF is measured in Average Radiant Efficiency, which is a measure of photons per second (p/sec) corrected for the area (cm²) of the region of interest (ROI) and the efficiency of the lamp at the sample distance and filter settings used ($\mu\text{Watts} \cdot \text{cm}^{-2} / \text{steradian}^{-1}$). Bioluminescence is measured in Radiance, which has the units of p/sec/cm²/sr. Each mouse was injected i.p. with 150 mg/kg of firefly *D*-luciferin sodium salt monohydrate (Biosynth, Switzerland) in saline and a time-course imaging sequence was used to establish that maximal luminescence was reached 15 minutes post-injection. No luminescence was detected in the NIR range. After 24 hours, a pre-scan bioluminescence and NIRF image was again acquired to ensure that no residual luminescence was remaining. Mice were injected via tail vein with either control vehicle or 20 nmol JAS239 in 100 μL of 0.1% Tween-80 in 50 mM Tris-HCl buffer. Mice were imaged for NIRF over a time-course of 20 minute increments. After initial hepatic clearance diminished (approximately 75 minutes), mice were again injected i.p. with *D*-luciferin and imaged for bioluminescence and NIRF 15 minutes later. ROIs with a 20% threshold were automatically drawn around the tumor using the bioluminescence image

in the LivingImage software (PerkinElmer) program, and this region was used to analyze intratumoral JAS239 accumulation in the NIRF images. Technical assistance was provided by Julie Czupryna of the Small Animal Imaging Facility.

A different formulation of JAS239 was tested in a separate cohort of mice bearing orthotopic 4175-Luc+ tumors. Approximately 4 weeks after tumor inoculation, each animal was injected i.v. with 20 nmol JAS239 dissolved in ethanol and diluted 1:100 in 0.9% saline. The tumor contrast with this 1% ethanol/saline formulation was compared to the contrast in response to 20 nmol indocyanine green (ICG) injected one week after the JAS239 was no longer detectable. A new cohort of mice was then inoculated on the back right shoulder with 4175-Luc+ subcutaneous xenografts. The location of these tumors allowed us to cloak the lower extremities of the mice and minimize background signal related to excretion. These mice were each injected with 20 nmol JAS239 in the ethanol/saline formulation after 4 weeks of tumor growth. Whole-body NIRF imaging of each mouse was used to determine the time of maximum intratumoral accumulation. Delivery of JAS239 in hydrocyanine form (hydro-JAS239) was first performed by i.v. injection in a new cohort of five athymic nude mice with subcutaneous 4175-Luc+ xenografts. Time-course images were acquired using the excitation and emission parameters for JAS239. After fluorescence in these animals diminished to undetectable levels, 20 nmol of either JAS239 or hydro-JAS239 was administered by gavage and NIRF images in the IVIS Spectrum were acquired over a span of 24 hours.

JAS239 in the ethanol/saline formulation was injected into three mice at time points 1, 4, and 24 hours prior to euthanasia by CO₂ asphyxiation. Tumor resection from these mice was then recorded in the integrated imaging device built in the laboratory of Sunil

Singhal of the Department of Surgery at the University of Pennsylvania. This device features a screen displaying the overlay brightfield image from a standard webcam with the NIRF signal detected by a charged coupled device (CCD) camera. Time-stamped images were recorded as separate files and overlay of the bright light (grey-scale) and NIRF (green) channels was performed in ImageJ with assistance from Ryan Judy of the Singhal lab.

As a preliminary experiment, a single athymic nude mouse bearing a 9L glioma xenograft on the right shoulder was injected with 20 nmol JAS239 in 1% ethanol and imaged for NIRF (Ex. 710 nm; Em. 800 nm) in a LiCor Pearl by Sona Saksena in the Delikatny Lab.

2.13 Ex vivo optical imaging

Biodistribution. Once the maximal intratumoral levels of JAS239 were determined by whole-body NIRF imaging for each vehicle formulation, animals were re-injected with the same formulation approximately 1 week later (allowing the first dose to clear entirely). Animals were euthanized 90 minutes after injection with JAS239 in Tween-80/Tris buffer or 24 hours after injection with JAS239 in ethanol/saline, as these were the times of maximal tumor/background fluorescence determined by whole-body NIRF imaging for each formulation. Tumors as well as relevant organs were resected, placed in a 24-well plate, and imaged for NIRF in an IVIS Spectrum. ROIs were drawn around each well and quantified using the LivingImage software. Tumor-to-muscle NIRF ratios were reported relative to a section of excised quadriceps muscle.

Diagnostic studies. Twenty mice bearing both MCF7-EV and MCF7-CK+ tumors were monitored until tumors reached approximately 200 μ L. Ten days prior to optical imaging, mice were switched to low-fluorescence chow. Two mice became moribund before imaging and three additional mice were excluded from these studies because their tumor inoculations missed the mammary fat pad. The remaining cohort was separated with eight mice receiving 20 nmol JAS239 in Tween-80/Tris buffer and seven receiving 20 nmol JAS239 in ethanol/saline. The cohort receiving JAS239 in Tween-80/Tris buffer was euthanized after 90 minutes, and the tumor-bearing flanks were surgically exposed. Using an IVIS Spectrum, NIRF from the tumor-bearing fat pads was subtracted from background muscle signal and the Average Radiant Efficiency reported. The same procedure in the remaining cohort was performed 24 hours following injection of JAS239 in ethanol/saline.

2.14 In vivo MRI

Animal preparation for MRI scan. Mice were prepared individually for MRI exams by induction of general anesthesia with 3% isoflurane in oxygen delivered in an induction chamber. The anesthetized animal was secured to a custom-built restraining device to minimize motion-induced artifacts. The head was positioned within a nose cone delivering 2% isoflurane in oxygen. Each limb was secured to a custom in-house restraining device to minimize motion artifacts. A respiration pillow was placed on the dorsal side of the body to monitor respiration rate, while a thermister was inserted into the rectum to measure body temperature. Both sensors were connected to a small animal monitoring device (SA Instruments Inc, NY, USA) that reported vital signs during

scanning. A slotted-tube resonator (inner diameter = 11 mm, depth = 9 mm) built in-house and tuned to 400 MHz was used for ^1H spectroscopy and imaging (Poptani *et al.*, 2003). The tumor of each animal was placed in the coil and the probe was then centered in the magnet. Body temperature was regulated at $37 \pm 1^\circ\text{C}$ by blowing warm air into the magnet bore through a hose connected to a thermostatically controlled device (SA Instruments, NY, USA). Animal preparation and MRI/MRS acquisitions were performed by Manoj Kumar of the Poptani Lab, with my assistance and processing of the data.

In vivo single voxel spectroscopy. Athymic nude mice bearing subcutaneous tumors (approximately 300 μL in volume) underwent pre-treatment MRS scans in a 9.4 T horizontal bore magnet equipped with 40 G/cm gradients interfaced to an Agilent Direct-Drive console (Agilent, Palo Alto, CA, USA) operating vnmrj 2.3.C software. Multi-slice gradient and spin echo images were used for tumor localization. T_2 -weighted spin echo anatomical images acquired using a spin echo multi-slice (SEMS) pulse sequence (TR=1000 ms, TE=10.0 ms, number of slices=20, field of view=20x20 mm^2 , slice thickness=1 mm, NT=1, matrix size=256x128) were used for voxel selection. A spectrum was acquired in a 3x3x3 mm^3 voxel using a PRESS sequence (TR=3000 ms, TE₁=12.68 ms and TE₂=10.01 ms, number of averages=128, complex points=4096, and spectral width=4000 Hz with an acquisition time of 6 min 24 sec). Water suppression was achieved using variable power and optimized relaxation delays (VAPOR) (Tkac *et al.*, 1999). An unsuppressed water spectrum was subsequently acquired with 8 averages to be used as a chemical shift and concentration reference. One week following initiation of treatment, a post-therapy *in vivo* single voxel ^1H MR spectrum was acquired for each animal. Pre and post-treatment spectra were processed and analyzed using Mnova Lite

5.2.5 software (Mestrelab Research, Santiago de Compostela, Spain). The water suppressed and unsuppressed free induction decays were processed by apodization of 10 Hz followed by Fourier transformation. The spectra were phased and chemical shift and baseline correction were performed prior to integration of the water (4.7 ppm), tCho (3.2 ppm), PUFA (2.8 ppm), and lipid (1.3 ppm) resonances. The metabolite/water ratio was determined for both pre- and post-treatment spectra. The percent change in metabolite concentration was then estimated by the formula: $[\text{post-treatment concentration} - \text{pre-treatment concentration}] * 100\% / \text{pre-treatment concentration}$.

2.15 Animal treatments

Companion diagnostic evaluation in breast model. MRS was used to establish baseline tCho levels in a cohort of ten athymic nude mice bearing 4175-Luc+ tumors. Mice were injected i.p. for 5 consecutive days with either 100 μ L saline or MN58b. Previous studies have reported that a 5 day treatment regimen of 4 mg/kg of MN58b was sufficient to lower tCho levels in mice (Al-Saffar *et al.*, 2006). However, in our experience this dose was found to be toxic, thus the MN58b dose was reduced to 2 mg/kg. A follow-up scan was then acquired 1 week after the pre-treatment scan. After post-treatment scanning, each animal was then injected i.v. with a trace dose (20 nmol) of JAS239 in ethanol/saline vehicle. After 24 hours, the mice were euthanized and each tumor was analyzed for NIRF as described above.

Breast tumor growth inhibition. A cohort of fifteen athymic nude mice were inoculated with 4175-Luc+ tumors and split evenly into three treatment groups. A 2% DMSO in 0.9% saline vehicle was used to solubilize JAS239 at concentrations required

for therapeutic injection. Beginning 3 days post-inoculation, animals received a 100- μ L i.p. injection of either control DMSO/saline vehicle, 2 mg/kg MN58b in DMSO/saline vehicle, or 4 mg/kg JAS239 in DMSO/saline vehicle daily for 5 consecutive days. Tumor volumes were assessed by caliper measurement for 30 days.

Pharmacodynamic indicators of ChoKa inhibition in breast cancer. A second cohort of fifteen athymic nude mice was inoculated with MDA-MB-231 cells, which had previously been used in the literature for MRS assessment of our positive control ChoKa inhibitor, MN58b (Al-Saffar *et al.*, 2006). When a volume of approximately 300 μ L was reached, tumors were scanned for baseline metabolite levels. Tumor volume estimates were made based upon the T_2 -weighted images. The animals were separated randomly into treatment groups, and for 5 consecutive days each group was injected i.p. with 100 μ L of control DMSO/saline vehicle (n = 5), 2 mg/kg MN58b in DMSO/saline vehicle (n = 4), or 4 mg/kg JAS239 in DMSO/saline vehicle (n = 3). Differences in cohort size are due to variability in tumor growth rate and the inability to place voxels within post-treatment tumors that were too small, resulting in the animal being removed from further study. Follow-up MRI/MRS scanning was used to assess tumor growth inhibition and changes in metabolite levels between treatment groups. Blood was collected from each animal by cardiac puncture and stored in heparin-coated tubes. Each resected tumor was embedded in Optimum Cryo-Temperature (Sakura Finetek, Torrance, CA), flash-frozen in liquid nitrogen, and stored at -80°C for histological assessment. Blood samples were submitted to the Diagnostic labs of the Ryan Veterinary Clinic for liver profiling and toxicological assessment.

ChoK inhibition in glioma tumors. The Poptani group treated ten tumor-bearing animals with MN58b at 2 mg/kg/day i.p. for 5 days (Kumar *et al.*, 2015). This dose was calculated using the FDA guidelines for cross-species equivalence, which suggests a 2 mg/kg rat dose is roughly equivalent to a 4 mg/kg mouse dose. A separate cohort of tumor bearing animals (n = 3) were treated with an i.p. injection of 1 mL saline daily for 5 days. Two animals died during the MN58b treatment resulting in post-MN58b data from only 8 animals. The death of these animals was most likely due to the tumor burden, as no overt indications of toxicity were noted as a result of MN58b toxicity: loss of weight, change in grooming or social habits, fur ruffling, or change in eye color.

The tumor bearing animals were anesthetized with an overdose of ketamine/xylazine. Following lack of deep tendon responses, the head was decapitated and the brain was removed from the skull. Tumor tissue and contralateral normal brain tissue were harvested from each animal under aseptic conditions in a laminar flow hood. PCA extractions and high-resolution ¹H NMR studies were performed on tissue samples from contralateral normal brain, saline, and MN58b-treated tumor tissue on a 500 MHz vertical bore NMR scanner (Bruker, Billerica, MA) using the same experimental protocol as described for cell extracts.

2.16 Histopathology

Tumors were kept frozen (-80°C) in Optimum Cryo-Temperature blocks for 1 week. For hematoxylin and eosin (H&E) staining, slides were first post-fixed in methanol at -20°C before staining using a Shandon Gemini automated stainer (ThermoFisher). Briefly slides were rehydrated by immersion in a series of descending ethanol dilutions (100%-

70%) then rinsed in water. Slides were stained in hematoxylin (Azer Scientific) for 1 min followed by a water rinse and dip in acid alcohol (0.1% HCl, 50% EtOH). Slides were then rinsed in tap water for 15 minutes followed by 1 minute in eosin (Azer Scientific). Slides were dehydrated in a series of ascending ethanol dilutions (70%-100%) followed by xylene before cover-slipping with Cytoseal (Fisher Scientific).

For immunohistochemistry of tissue slices, slides prepared from each fresh frozen tumor were placed directly in pre-cooled (-20°C) methanol and dried for 10 minutes at room temperature and 5 minutes at 55°C. Slides were then placed in 10% neutral buffered saline for 20 minutes, rinsed in ddH₂O, and rinsed for 5 minutes at room temperature in 0.1 M Tris Buffer. Caspase-3 (R&D Systems AF835) and Ki67 (Abcam ab16667) antibody staining was performed on a Bond Max automated staining system (Leica Microsystems) using the Bond Intense R staining kit (Leica Microsystems DS9263). The standard kit protocol was followed with the exception that the primary antibody incubation period was extended to 1 hour at room temperature. Avidin-Biotin Blocking was added to reduce non-specific binding (Vector Labs SP-2001), and a Peptide Blocking step was added (DAKO X0909). The Caspase-3 antibody was used at a dilution of 1:1000 and Ki67 was used at 1:100. Antigen retrieval was performed using E2 (Leica Microsystems) retrieval solution for 20 minutes. Biotinylated Anti-Rabbit Secondary (Vector BA-1000) was used at a 1:200 dilution. After staining, slides were rinsed, dehydrated in a series of ascending concentrations of ethanol and xylene, then cover-slipped. Cryo-sectioning and slide-staining was performed by Socrates Agrio-O'Reilly and Carly David of the CHOP Pathology Core Laboratories.

Each slide was scanned at 20X magnification using the Aperio Scan Scope OS (Aperio Technology, Vista, CA). The Image Scope viewing software and nuclear staining algorithm V.9 (version 9; Aperio Technologies, Inc.) were used to quantify Ki67 and Caspase-3 positive nuclei in representative regions of each slice. Intensity thresholds and cell segmentation parameters were optimized by Daniel Martinez of the CHOP Pathology Core Facility to ensure unbiased manual scoring. The percentage of nuclei with strong-positive staining were reported for each region of interest and averaged among treatment cohorts.

2.17 Statistical analysis

Data are reported as the mean \pm standard deviation (SD) of three separate experiments ($n = 3$), unless noted otherwise. Probability (P) values were calculated in Microsoft Excel 2010 (Version 14.0.7128.5000 32-bit) using a 2-tailed Student's t-test, except in specified cases. P -values < 0.05 were considered statistically significant.

CHAPTER 3

Chemical Synthesis

3.1 Introduction

There are a number of limitations to the current approach to identify and validate ChoK α inhibitors *in vivo*. Small molecules offer a pharmacokinetic advantage over macromolecules, but the choline-mimetic ^{11}C and ^{18}F -labeled tracers cannot distinguish choline transporter inhibition from choline phosphorylation inhibition (Zheng *et al.*, 2007). This is a limitation because choline transport inhibition can often lead to severe toxicities (Boobis *et al.*, 1975). Non-invasive MRS evaluation can measure choline metabolite pools in the steady state, but cannot distinguish ChoK α activity from the diverse anabolic and catabolic pathways that use choline as a building block. Several bis-pyridinium and bis-quinolinium small molecules that have been demonstrated to bind to and inhibit ChoK α in a specific manner (Campos *et al.*, 2006). These ChoK α inhibitors share many structural features (symmetric terminal heterocyclic groups containing quaternary ammonium groups connected by a lipophilic linker moiety) with a class of fluorescent small molecules known as the carbocyanines. In this work, a number of choline mimetic molecules were prepared, and their optical properties were characterized to identify possible inhibitors with fluorescence in the NIR range (Fig. 3.1). Three synthetic approaches were employed: 1) addition of a NIR fluorophore to choline, 2) modification of the known ChoK α inhibitor called MN58b, and 3) incorporation of choline-like moieties to a carbocyanine structure.

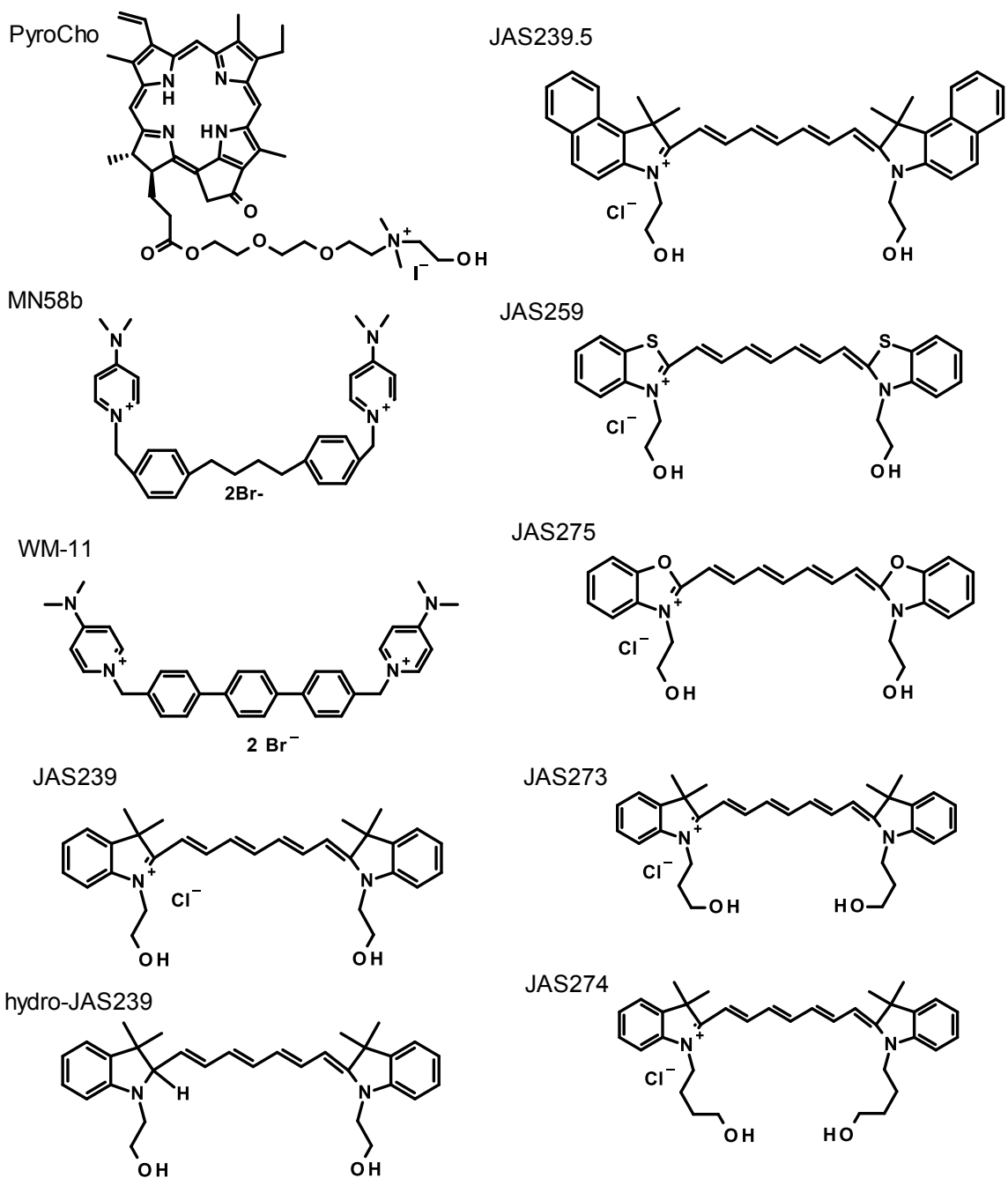


Figure 3.1. Class of compounds synthesized as potential ChoKa inhibitors. Each of the above compounds were synthesized in the Delikatny Lab under guidance of Dr. Anatoliy Popov. These structures represent derivatives of choline, bis-pyridiniums, and carbocyanines.

3.2 Pyro-Choline

A pyropheophorbide conjugated to a methyl group of choline via a polyethyleneglycol (PEG) spacer was generously provided by Dr. Anatoliy Popov of the Department of Radiology at the University of Pennsylvania. This product, named PyroCho, exists as a dark green solid. Susceptible to photodegradation, PyroCho was stored at -20°C and reconstituted in stock solutions by measuring the absorbance in a cuvette and calculating concentration using the Beer-Lambert law and the extinction coefficient value (at 665 nm) of 50,000 L mol⁻¹ cm⁻¹. There are two absorbance peaks occurring at 418 nm and 665 nm. Excitation at either absorbance peak results in fluorescence with maximal emission at 670 nm. Excitation at 660 nm also produces a second fluorescence at 725 nm that can be used for NIRF optical imaging. Above 10 μM, the fluorescence is no longer linearly-proportional to concentration due to stacking and self-quenching of the pheophorbide rings. The calculated partition coefficient (cLogP) of PyroCho is 6.24 (Table 1).

3.3 MN58b

1,4-Bis(4-bromomethylphenyl)butane. 1,4-Diphenylbutane (2 g, 9.51 mmol) was added to a mixture of 48% aqueous HBr (4.15 mL, 39.9 mmol) and glacial AcOH (50 mL), followed by 1,3,5-trioxane (0.57 g, 6.34 mmol) and hexadecyltrimethylammonium bromide (52 mg, 0.143 mmol). The mixture was stirred such that only a single layer could be seen then heated to a gentle reflux for 8 hours. The volatiles were removed under reduced pressure. The product was isolated by column chromatography (silica gel, hexane/benzene 1/1, v/v). The isolated 1,4-bis(4-bromomethylphenyl)-butane (1.959 g,

yield 52%) was a white solid, mp 119 to 121°C (from acetone). ¹H NMR (500 MHz, CDCl₃, δ ppm) 7.04 ppm (*AB*, *A* = 7.18, *B* = 6.89, *J*_{*AB*} = 9 Hz, 8H), 4.53 (s, 4H), 2.66 (m, 4H), 1.62 (m, 4H).

1,10 -((Butane-1,4-diylbis(4,1-phenylene))bis(methylene))bis(4-(dimethylamino)pyridin-1-ium) bromide (MN58b). The mixture of 4-dimethylaminopyridine (238.0 mg, 1.948 mmol) and 1,4-bis(4-bromomethylphenyl)butane (385.9 mg, 0.974 mmol) in dry ethanol (30 mL) was heated and stirred at 160°C in a 45 mL Parr autoclave equipped with a magnetic stirring bar for 3 hours. The white solid product was precipitated twice from ethanol into diethyl ether, dissolved in deionized water and lyophilized. Yield: 96%, melting point (mp) 103 to 106°C (from water). ¹H NMR (360 MHz, CD₃OD, δ ppm): 8.21 (dt, *J* = 7.6 Hz, *J* = 2.9 Hz, 4H, H-2pyr), 7.29 (dm, *J* = 7.9 Hz, 4H, Ph), 7.23 (dm, *J* = 7.9 Hz, 4H, Ph), 7.00 (dm, *J* = 7.6 Hz, 4H, H-3pyr), 5.33 (s, 4H, CH₂N⁺), 3.25 (s, 12H, N(CH₃)₂), 2.64 (m, 4H, CH₂-C₆H₄), and 1.62 (m, 4H, C-CH₂-C).

3.4 WM-11

To explore the effect of introducing a conjugated double bond network between the quaternary ammonium groups of MN58b, we replaced the 1,4-diphenylbutane linker with 1,4-diphenylbutadiene and proceeded with the same bromination step used in MN58b synthesis. After 1 hour of heating at 105°C, however, the mixture turned into a black tar. Several strategies were employed to isolate crystals from the mixture by Dr. Anatoliy Popov and a student, William Marrero-Ortiz, but these were unsuccessful and it was determined that the desired product was not present in the mixture. A more stable

resonant linker using 4-(4-(4-(hydroxymethyl)phenyl)phenyl)phenyl)methanol in place of 1,4-diphenylbutadiene has recently been proposed by Dr. Popov. The 1,4-bis(4-(bromomethyl)phenyl)benzene intermediate has been successfully purified, and will soon be dissolved in ethanol and condensed with 4-dimethylaminopyridine in an autoclave reaction to produce the MN58b derivative WM-11.

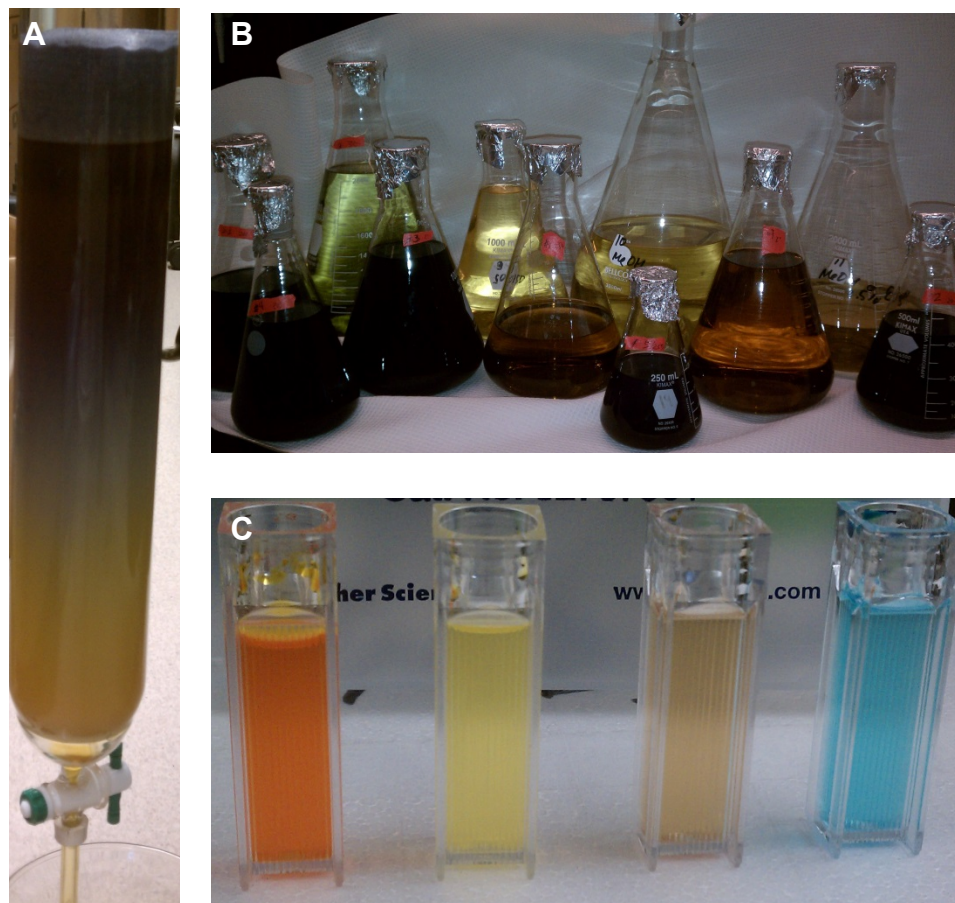


Figure 3.2. Colorimetric monitoring during JAS239 synthesis. (A) Cyanine dyes were purified by silica gel column chromatography and (B) fractions were separated by color. (C) A sample from each fraction was placed in a cuvette and analyzed for absorbance and fluorescence in a spectrophotometer.

3.5 JAS239

1-(2-Hydroxyethyl)-2,3,3-trimethyl-3H-indol-1-ium chloride. A mixture of 2,3,3-trimethyl-3H-indole (1,592.3 mg, 10 mmol) and 2-chloroethan-1-ol (1,610.2 mg, 20 mmol) in dry ethanol (15 mL) was heated and stirred at 160°C in a 45 mL Parr autoclave equipped with a magnetic stirring bar for 4 hours. The purple solid product was precipitated twice from ethanol with diethyl ether. Yield 86%. ¹H NMR (360 MHz, CD₃OD, δ ppm): 7.88 ppm (m, ¹H), 7.77 (m, 1H), 7.65 (m, 2H), 4.68 (m, 2H), 4.06 (m, 2H), 1.63 (s, 6H), labile OH and N = C–CH₃ protons are in exchange with CD₃OD. MALDI-TOF, m/z: (M-Cl)⁺ 204.35, calculated for C₁₃H₁₈NO 204.14.

1-(2-Hydroxyethyl)-2-((1E,3E,5E)-7-((Z/E)-1-(2-hydroxyethyl)-3,3-dimethylindolin-2-ylidene)hepta-1,3,5-trien-1-yl)-3,3-dimethyl-3H-indol-1-ium chloride (JAS239). A solution of acetic anhydride (112.3 mg, 1.1 mmol) in CH₂Cl₂ (2 mL) was added to a cooled (-20°C), stirred suspension of N-((1E,3E,5Z)-5-(phenylimino)penta-1,3-dien-1-yl) benzenaminium chloride (142.4 mg, 0.5 mmol) and triethylamine (222.6 mg, 2.2 mmol) in CH₂Cl₂ (10 mL). The resulting clear solution was stirred for another 3 hours at room temperature (RT) and concentrated under high vacuum. The residue containing N-phenyl-N-((1E,3E,5Z)-5-(phenylimino)penta-1,3-dien-1-yl)acetamide was dissolved in ethanol (5.0 mL) and added drop-wise to a refluxing solution of 1-(2-hydroxyethyl)-2,3,3-trimethyl-3H-indol-1-ium chloride (360.0 mg, 1.5 mmol) and anhydrous sodium acetate (200 mg, 2.5 mmol) in ethanol (100 mL). The mixture was refluxed for 5 hours and concentrated. The product JAS239 was isolated by column chromatography [silica gel, ethyl acetate–methanol (0–100%)] (Fig. 3.2A). Fractions

isolated from the column (Fig. 3.2B) were concentrated under high pressure and the fraction containing pure product (JAS239) was identified by spectrophotometric analysis (Fig. 3.2C). Yield 19.9%. ^1H NMR (360 MHz, CD_3OD , δ ppm): 7.93 [t (dd), $J = 13.1$ Hz, 2H]; 7.58 [t (dd), $J = 12.8$ Hz, 1H]; 7.46 (d, $J = 7.2$ Hz, 2H); 7.38 (td, $J = 7.4$ Hz, $J = 1.1$ Hz, 2H); 7.29 (d, $J = 7.9$ Hz, 2H); 7.23 (td, $J = 7.2$ Hz, $J = 0.7$ Hz, 2H); 6.53[t(dd), $J = 12.6$ Hz, 2H]; 6.35 (d, $J = 13.7$ Hz, 2H); 4.21 (t, $J = 5.8$ Hz, 4H); 4.92 (t, $J = 5.8$ Hz, 4H); 1.70 (s, 12H). MALDI-TOF, m/z : $(\text{M}-\text{Cl})^+$ 469.56, calculated for $\text{C}_{31}\text{H}_{37}\text{N}_2\text{O}_2$ 469.28. HPLC: one peak, retention time = 15.22 minutes.

3.6 hydro-JAS239

The hydrocyanine form of JAS239 was prepared using a procedure outlined by Kundu *et. al.* Briefly, 1.32 mg JAS239 was dissolved in methanol and a NaBH_4 solution (3 mg dissolved in 0.5 mL methanol) was added drop-wise while stirring. The solution turned from dark green to yellow in an incremental fashion. After approximately 0.25 mL NaBH_4 was added, the solution became colorless. The methanol was evaporated and 10 mL of dichloromethane and 20 mL distilled water was added to the flask. The mixture was transferred to a separatory funnel and shaken vigorously. Pressure within the reaction vessel was relieved carefully. The bottom (organic) layer was added to a fresh flask and product was extracted from the aqueous phase with two additional dichloromethane separations. The organic phase was dried over anhydrous sodium sulfate and the dichloromethane was removed under reduced pressure. The resulting product, hydro-JAS239, was used without further purification.

3.7 JAS239.5

Addition of a benzo-moiety to the indolium group is common for *in vivo* fluorophore design because this induces a bathochromic shift of approximately 30 nm, which can help reduce background autofluorescence. This modification also has the potential to increase the lipophilicity of the compound, which may make it more cell permeable. We prepared a JAS239 derivative using 1,1,2-trimethyl-1H-benz[e]indole as a starting indolium for the head groups. The same synthetic procedure for JAS239 was followed for the synthesis of JAS239.5. Yield 17.3%. ¹H NMR (360 MHz, CD₃OD, δ ppm): 8.23 (d, *J* = 8.3 Hz, 2H); 8.04 (t, *J* = 13.3 Hz, 1H); 7.98 (d, *J* = 8.6 Hz, 4H); 7.68-7.56 (m, 6H); 7.47 (td, *J* = 7.4 Hz, *J* = 1.1 Hz, 2H); 6.57 (t, *J* = 12.6 Hz, 2H); 6.38 (d, *J* = 14.0 Hz, 2H); 4.33 (t, *J* = 5.8 Hz, 4H); 3.99 (t, *J* = 5.4 Hz, 4H), 1.90 (s, 12H).

3.8 JAS259

To improve the water solubility of JAS239, replacement of the dimethyl-substituted carbon at the C3 position of the starting indolium salt with sulfur was proposed. The same procedure described for JAS239 was followed using 2-methylbenzothiazole in place of the trimethyl-indolium group. Following successful alkylation with 2-chloroethanol, the benzothiazole head group was dissolved in ethanol and heated under reflux conditions in the presence of sodium acetate and the precursor linker group (N-phenyl-N-((1E,3E,5Z)-5-(phenylimino)penta-1,3-dien-1-yl)acetamide) using the same procedure described for JAS239 synthesis. The sulfur group was found to be thermolabile at high temperatures and the desired product was not detected by spectrophotometric analysis. A previous report in the literature (Okoh *et al.*, 2014) described a similar

benzothiazole-based cyanine synthesis and found that the condensation reaction of the head group and acetylated linker could be achieved at room temperature without degradation. After this adjustment was made to the second synthetic step, 2-(2-((1E,3E,5E)-7-(3-(2-hydroxyethyl)-1,3-benzothiazol-2-ylidene)hepta-1,3,5-trienyl)-1,3-benzothiazol-3-ium-3-yl)ethanol chloride (JAS259) could be purified by column chromatography. Yield 15.7%. ¹H NMR (360 MHz, CD₃OD, δ ppm): 8.33-8.23 (m, 6H), 8.02 (t, *J* = 13.1 Hz, 1H); 7.94-7.80 (m, 4H); 6.57 (t, *J* = 12.6 Hz, 2H); 6.37 (d, *J* = 13.7 Hz, 2H); 4.93 (t, *J* = 5.4 Hz, 4H); 4.07 (t, *J* = 5.4 Hz, 4H).

With the knowledge gained from synthesis of JAS259, a derivative using oxygen in the place of sulfur was designed (JAS275). In place of the indole starting group in JAS239, a 2-methylnaphth(2,1-d)oxazole was used. Alkylation with 2-chloroethanol was carried out following a similar scheme to that reported for JAS239 synthesis. Similar to the JAS259 precursor, the reduced steric hindrance in this sulfur derivative (relative to the dimethyl-substituted carbon group in JAS239) allowed for the alkylation reaction to be run at room temperature, rather than in an autoclave. The oxygen within this heterocyclic system proved to be too reactive under these conditions, and the reaction failed to produce the desired hydroxyethylated ring structure.

3.9 JAS273 and JAS274

To explore the importance of the hydroxylated alkyl chain, two JAS239 derivatives were prepared with either hydroxypropyl (JAS273) or hydroxybutyl (JAS274) alkyl substitutions. For JAS273, preparation of the 1-(3-hydroxypropyl)-2,3,3-trimethyl-3H-indolium iodide precursor was performed in accordance with methods described previously (Darwish *et al.*, 2010). Alkylation of 2,3,3-trimethylindolenine with 3-iodo-1-

propanol in toluene was heated at reflux (130°C) for 2 hours. The color was observed to change from yellow to dark rose. The intermediate product was precipitated by addition of excess hexane. The acetylated linker group prepared for JAS239 synthesis was used for linkage of the hydroxypropyl-trimethyl-indolium head groups. The acetylated linker group, two times excess of the indolium group, and excess sodium acetate were heated in ethanol under reflux conditions (100°C) overnight while protected from light. A similar synthetic procedure was followed for preparation of JAS274 with 4-iodo-1-butanol as a precursor.

3.10 PepTech compounds

After the initial synthetic strategies for MN58b and JAS239 derivatives were designed with guidance from Dr. Popov and shown feasible, we turned to the PepTech Corporation (Bedford, MA) to synthesize a small library of analogs. These compounds, outlined in Figure 3.3, represent two major strategies. A variety of linker groups were used to make resonant MN58b analogs. In these compounds, *cis* (*Z*) and *trans* (*E*) conformations were explored. Movement of the quaternary ammonium groups from the outer ring moieties to the inner rings gave a stronger likelihood of fluorescence, as these compounds have a linker group whose structure was derived from the fluorophore viologen. As an additional positive control to be used in conjunction with MN58b, TCD-717 was synthesized. The second modification strategy involved cyclization within the linker group of JAS239. Similar “cyclo” derivatives have been described in the literature with improved fluorescence quantum yield compared to the non-cyclized counterpart (Yang *et al.*, 2010). To test the importance of the choline mimetic alkyl groups, the

hydroxyethyl moieties were replaced with methyl groups and represent the cyclized version of 1,1',3,3,3',3'-hexamethylindotricarbocyanine iodide (HITC).

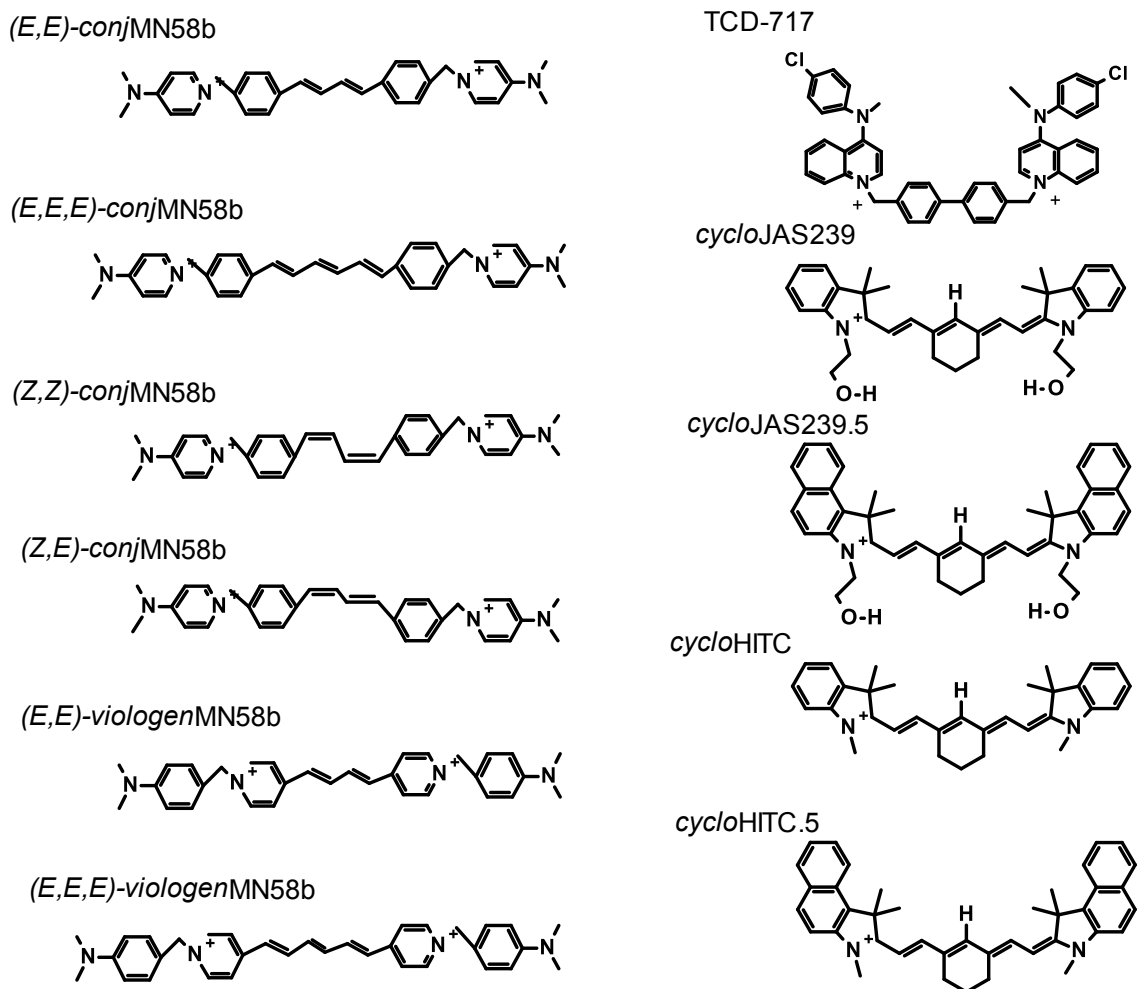


Figure 3.3. Second generation JAS239 analogs contracted to PepTech Corporation. The structures above were designed as next generation fluorescent ChoK α inhibitors. TCD-717 was also synthesized as an additional positive control. Due to unstable intermediate groups, the synthesis of Z-conformation (Z,Z and Z,E) and viologen MN58b derivatives was not feasible.

3.11 Results

The structural similarities between the bis-pyridinium/quinolinium ChoK inhibitors and the carbocyanine dyes led us to hypothesize that similar pharmacologic activity could exist between the 2 classes of compounds. To test our hypothesis, we designed a carbocyanine dye substituted with choline-like $N^+-CH_2-CH_2-OH$ moieties at the nitrogen atom of the indolium ring. The synthesis of the carbocyanine precursor, 1-(2-hydroxyethyl)-2,3,3-trimethyl-3H-indol-1-ium chloride, was performed in ethanol within an autoclave at high temperature to shorten the reaction time considerably from previous reports in the literature (Ye *et al.*, 2003). Stable 2-chloroethan-1-ol was used as the alkylating agent, rather than the unstable and more expensive bromo or iodo derivatives, to increase the yield and stability of the intermediates. In the final step, we modified a previously reported procedure for the synthesis of C7-carbocyanine (Ye *et al.*, 2003) to run at a higher temperature by replacing methanol with ethanol as the solvent. This allowed a reduction in the condensation time from 16 to 5 hours. The reaction can be supervised by colorimetric monitoring as depicted in Figure 3.4A. The final compound, JAS239, demonstrated NIR fluorescence, with an excitation maximum at 740 nm and emission at 770 nm (Fig. 3.5). As a measurement of water solubility, the cLogP was calculated in ChemBioDraw Ultra (Version 13.0.0.3015) to be 3.37 (Table 1).

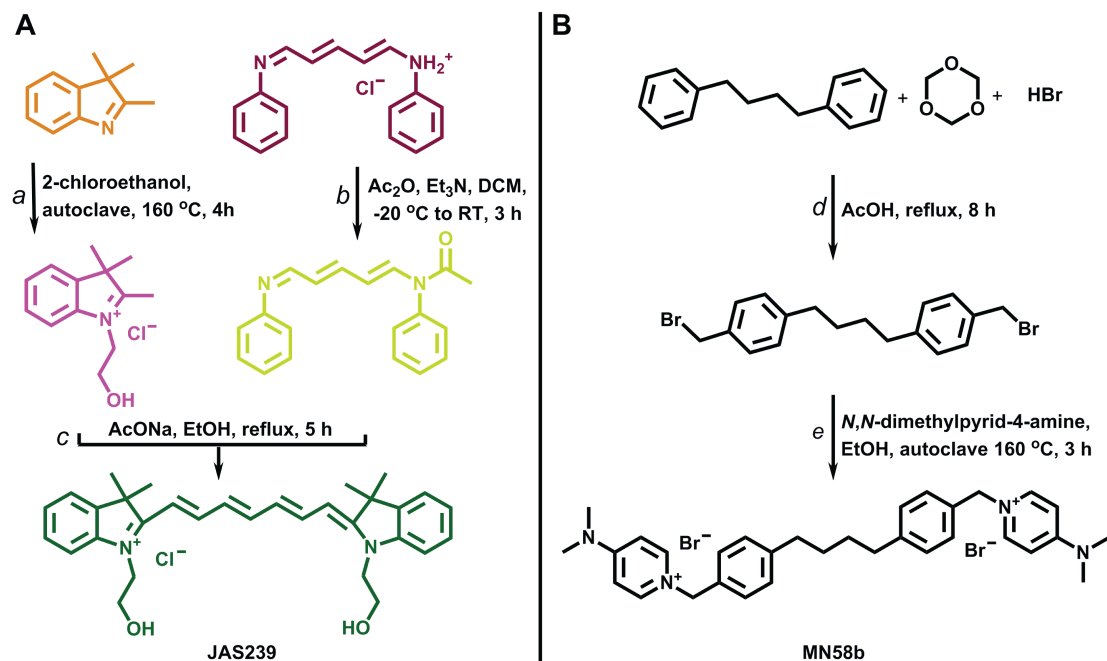


Figure 3.4. Synthetic pathway for the preparation of prototype ChoKα inhibitors. (A) JAS239 synthesis: (a) 2-chloroethanol, autoclave 160°C, 4 hr; (b) Ac₂O, Et₃N, DCM, -20°C-RT, 3 hr; (c) AcONa, EtOH, reflux, 5 hr. (B) MN58b synthesis: (d) HBr, cetyltrimethylammonium bromide [C₁₆H₃₃N(CH₃)₃Br], acetic acid, reflux, 8 hr; (e) N,N-dimethylpyridin-4-amine, EtOH, autoclave 160°C, 3 hr. Synthesis was designed and performed with guidance of Anatoliy Popov.

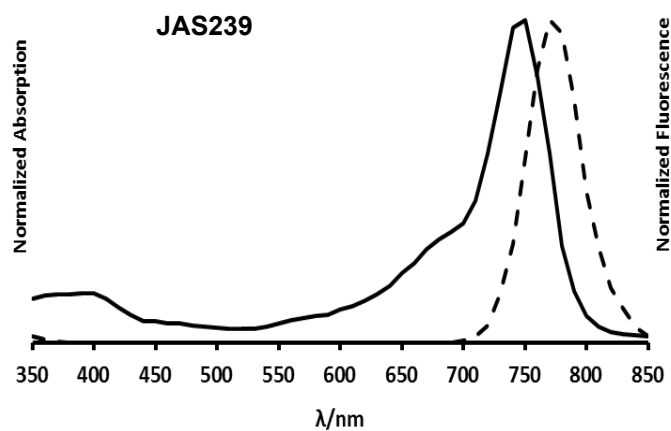


Figure 3.5. Optical properties of JAS239. Dissolved in methanol, JAS239 has maximal absorption at 745 nm and maximal fluorescence emission at 775 nm.

Table 1. Calculated Partition Coefficients for synthesized structures.

Compound	cLogP
PyroCho	6.24
JAS239	3.37
MN58b	1.24
hydro-JAS239	7.29
JAS239.5	5.72
JAS259	2.74
<i>E,E-conj</i> MN58b	0.63
<i>E,E,E-conj</i> MN58b	1.23
TCD-717	7.47
<i>cyclo</i> JAS239	4.42
<i>cyclo</i> JAS239.5	6.77
<i>cyclo</i> HITC	6.81
<i>cyclo</i> HITC.5	9.16

To compare the 2 classes of compounds, we synthesized MN58b as a positive control. The synthesis of MN58b has been reported in 2 papers where it was referred to as Compound 41 (Campos *et al.*, 2002; Conejo-García *et al.*, 2011). In this Chapter, we include a detailed description of the synthesis of the intermediate 1,4-bis(4-bromomethylphenyl)butane (Fig. 3.4B), which was not provided in the original papers (Goodson and Goodwin, 1948; Cram and Steinberg, 1951) or in either of the papers describing the synthesis of MN58b (Campos *et al.*, 2002; Conejo-García *et al.*, 2011). In addition, we have improved upon the synthesis of MN58b (Fig. 3.4B) by using an autoclave method following the phase transfer catalyzed bromomethylation (Mitchell and Iyer, 1989). This decreases the reaction time from 192 hours (Conejo-García *et al.*, 2011) to 3 hours with 50% yield and cLogP of 1.24 (Table 1). The melting point of our MN58b product differs from that in (Conejo-García *et al.*, 2011), where it is reported as 161°C to 163°C, but is consistent with the values of 98°C to 100°C when the compound was

crystallized from water (Campos *et al.*, 2002). Our attempts to make MN58b derivatives with a resonant structure, such as WM-11, have thus far failed to yield a final product.

Reduction of JAS239 by sodium borohydride eliminated the characteristic dark green color of the dye and this colorless hydro-JAS239 (Fig. 3.6) could be separated from its fluorescent parent compound by extraction in an organic solvent. The transition from a hydrophilic to a hydrophobic state was successfully predicted by its cLogP of 7.29 (Table 1). Inclusion of an additional benzyl moiety to the JAS239 head group (JAS239.5) resulted in the expected 30 nm bathochromic shift in absorbance (Ex. 775 nm) and fluorescence (Em. 815 nm) maxima. The theoretical cLogP was calculated to be 5.72 (Table 1), confirming increased hydrophobicity from the two ring additions. The indolium head group of JAS239 was replaced with a benzothiazole heterocycle, and the fluorescence spectrum of JAS259 showed maximal absorbance at 755 nm and emission at 785 nm. The cLogP was determined computationally to be 2.47 (Table 1). When the indolium head group was replaced with a naphthoxazole, however, the starting heterocyclic ring was unstable during the alkylation step, resulting in a number of impurities. A comparison of the ^1H NMR spectra from the final product mixture and the starting naphthoxazole compound revealed that this ring degradation lowered the reaction yield to less than 25% of the desired product. For JAS273 and JAS274, the absorbance and fluorescence properties of each set of reaction products were assessed by measurement in a cuvette. No bathochromic shift in absorbance was observed when product absorbance spectra were compared to the starting materials. No fluorescence was detected in the near infrared wave range for either compound.

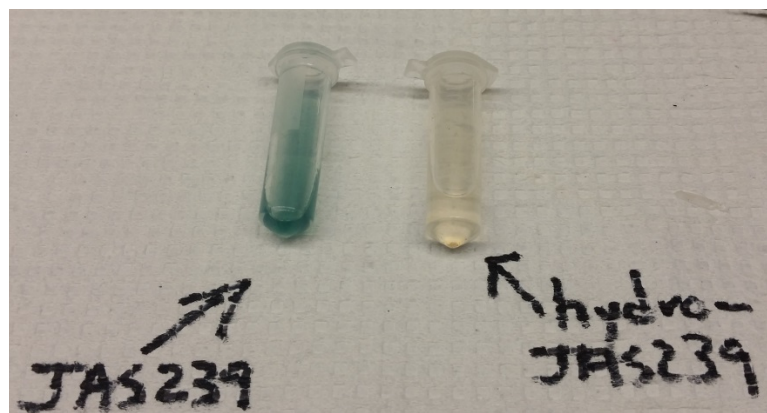


Figure 3.6. Colorimetric comparison of JAS239 before and after reduction. JAS239 dissolved in 1% ethanol is dark green (left). Following reduction with NaBH_4 , the resultant hydro-JAS239 is colorless.

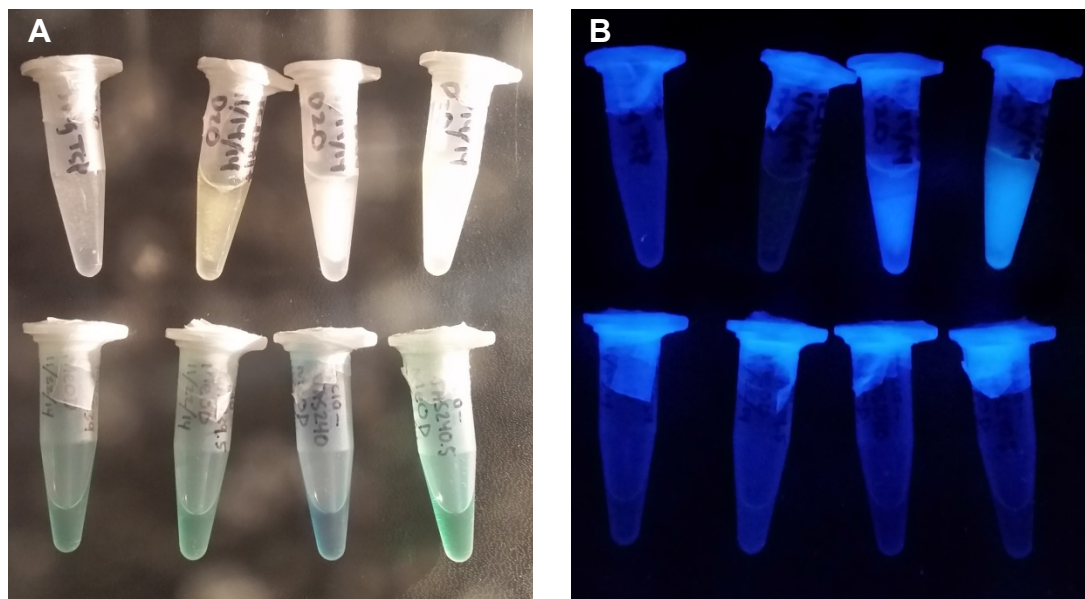


Figure 3.7. UV fluorescence of MN58b and JAS239 derivatives. Frozen vials of (clockwise from top left) water, TCD-717, *E,E*-conjMN58b, *E,E,E*-conjMN58b, cycloHITC.5, cycloHITC, cycloJAS239.5, and cycloJAS239 are pictured under (A) white light and (B) UV light. UV fluorescence is detected in the *E,E*-conjMN58b and *E,E,E*-conjMN58b vials. Background fluorescence is also observed from the parafilm wrapping.

Seven compounds in total were successfully synthesized by the PepTech Corporation, including 1,1'-(((1E,3E)-buta-1,3-diene-1,4-diylbis(4,1-phenylene))bis(methylene))bis(4-(dimethylamino)pyridin-1-ium) chloride (PTC1452-01); 1,1'-(((1E,3E,5E)-hexa-1,3,5-triene-1,6-diylbis(4,1-phenylene))bis(methylene))bis(4-(dimethylamino)pyridin-1-ium) chloride (PTC1452-02), 1,1'-((1,1'-biphenyl)-4,4'-diylbis(methylene))bis(4-((4-chlorophenyl)(methyl)amino)quinolin-1-ium) bromide (PTC1452-07); 1-(2-hydroxyethyl)-2((E)-2-((E)-3-((E)-2-(1-(2-hydroxyethyl)-3,3-dimethylindolin-2-ylidene)ethylidene)cyclohex-1-en-1-yl)vinyl)3,3-dimethyl-3H-indol-1-ium iodide (PTC1452-08); 3-(2-hydroxyethyl)-2((E)-2-((E)-3-((E)-2-(3-(2-hydroxyethyl)-1,1-dimethyl-1H-benzo[e]indol-2(3H)-ylidene)ethylidene)cyclohex-1-en-1-yl)vinyl)1,1-dimethyl-1H-benzo[e]indol-3-ium iodide (PTC1452-09); 1,3,3-trimethyl-2-((E)-2-((E)-3-((E)-2-(1,3,3-trimethylindolin-2-ylidene)ethylidene)cyclohex-1-en-1-yl)vinyl)3H-indol-1-ium iodide (PTC1452-10); 1,3,3-trimethyl-2-((E)-2-((E)-3-((E)-2-(1,3,3-trimethyl-1H-benzo[e]indol-2(3H)-ylidene)ethylidene)cyclohex-1-en-1-yl)vinyl)1H-benzo[e]indol-3-ium iodide (PTC1452-11). These will be referred to as *E,E-conj*MN58b (non-fluorescent; cLogP = 0.63), *E,E,E-conj*MN58b (non-fluorescent; cLogP = 1.23), TCD-717 (non-fluorescent; cLogP = 7.47), *cyclo*JAS239 (Ex. 748 nm, Em. 787 nm; cLogP = 4.42), *cyclo*JAS239.5 (Ex. 784 nm, Em. 843 nm; cLogP = 6.77), *cyclo*HITC (Ex. 743 nm, Em. 783 nm; cLogP = 6.81), and *cyclo*HITC.5 (Ex. 779 nm, Em. 840 nm; cLogP = 9.16), respectively. The synthesis and analysis of these compounds can be found in Appendices 1-7. *E,E-conj*MN58b and *E,E,E-conj*MN58b did not exhibit fluorescence within the NIR range, however, when frozen and imaged under a UV lamp, fluorescence could be detected (Fig. 3.7). Attempts to synthesize MN58b derivatives with the *Z*-conformation

proved untenable due to double bond isomerization during the palladium-catalyzed reduction of the alkyne groups in the precursor compound. The viologen-based MN58b derivatives failed at the final condensation step.

3.12 Discussion

The goal of this study was to develop an NIR fluorescent choline mimetic by exploiting the structural similarities between the existing bis-symmetric inhibitors and the carbocyanine dyes. Taking into consideration the structural properties established by the Lacal group for ChoK-specific inhibition (Sánchez-Martín *et al.*, 2005), we developed an autoclave Menshutkin alkylation method for carbocyanine synthesis, which successfully reduced the time required to alkylate the ammonium group of the indolium moiety by 11 hours (Arlaukas *et al.*, 2014). Choline-mimetic hydroxyethyl alkyl groups were attached at the ammonium sites within the heterocyclic head groups on either side of a 7-carbon spacer. The 7-carbon spacing is important because it imparts fluorescence in the NIR range, outside the range of autofluorescence. We then adapted the autoclave method to establish a rapid and high-yield synthesis of MN58b, the most-effective ChoK inhibitor in the literature.

A number of JAS239 derivatives were prepared in an effort to test the effect of hydrophilicity, absorbance wavelength, and alkyl chain length. The hydro-JAS239 compound was hydrophobic and colorless, consistent with our expectations for hydrocyanine modification. These properties have the theoretical potential to improve the permeability to the cell membrane and to reduce background signal from dye that is not cell-associated. However, these dyes also rely on being oxidized in cells or tissues in

order to be observed with fluorescence imaging. Similar attempts at synthesizing an oxa derivative were unsuccessful due to degradation of the reaction intermediate. A modified version of this synthesis running at -20°C is currently being explored in our group, but the product has yet to be isolated due to the time required for reaction completion. Similarly for compounds JAS273 and JAS274, where the alkyl chain of the choline mimetic was extended to 3 and 4 carbons, it is thought that impurities caused by cyclization of the alkyl group prevented the condensation reaction from occurring. Cyclization within the linker group seems to have yielded stable and bright JAS239 (cyclo) derivatives, and this minimization of rotational bonds may improve the pharmacokinetics of these probes (Lipinski, 2003).

While the syntheses of many resonant MN58b derivatives were unsuccessful, the *E,E-conj*MN58b and *E,E,E-conj*MN58b compounds are promising ChoK α inhibitor candidates. Detection of fluorescence in the solid state opens the possibility that binding of these less rigid molecules to a stable active site may stabilize the structure and impart fluorescence, albeit not at ideal wavelengths for *in vivo* imaging purposes.

The number and variety of previously reported ChoK inhibitors suggests that there exists a certain degree of flexibility in the functional groups and spacers, which can yield effective candidate therapeutics. The major concerns for analogs of HC-3 *in vivo* are that they (i) will nonspecifically target normal tissue; (ii) will disrupt choline uptake into normal cells, which can lead to neuronal toxicity; or (iii) will be prone to DNA intercalation, resulting in ChoK-independent cell death. The inherent fluorescence of a carbocyanine-based inhibitor greatly simplifies the process of excluding candidates that inhibit choline phosphorylation, but are not properly delivered to the intended tissue or

subcellular compartment. The ability to track the cellular uptake of these fluorophores using fluorimetry and confocal microscopy also permits the determination of potential interactions with choline transporters, which could affect the interpretation of the efficacy of ChoK inhibition *in vitro*. This is also important because compounds that inhibit choline transport have been shown to lead to respiratory paralysis in animals. The broad excitation range of JAS239 and its fluorescence in the NIR window wherein breast tissue is relatively transparent makes it possible to study (i) plasma half-life, biodistribution and tumor localization; (ii) cellular uptake pathways and kinetics; and (iii) subcellular localization by *in vitro* and *ex vivo* microscopy.

Chapter 4

JAS239 characterization in breast cancer cells

4.1 Introduction

Upregulation of choline kinase alpha (ChoK α) has been correlated with histologic tumor grade and resistance to antiestrogen therapies in breast cancer, ultimately indicating a poorer prognosis (Ramírez de Molina, Gutierrez, *et al.*, 2002). ChoK α catalyzes the conversion of choline to phosphocholine (PC), an important second messenger and the first step in the biosynthesis of the predominant membrane phospholipid, phosphatidylcholine (PtdCho). ChoK α activity can be enhanced by a number of clinically relevant oncogenes (Bhakoo *et al.*, 1996; Ramírez de Molina, Penalva, *et al.*, 2002; Ramírez de Molina *et al.*, 2005), growth factors (Warden and Friedkin, 1984; Cuadrado *et al.*, 1993; Jiménez *et al.*, 1995), transcription factors (Aoyama *et al.*, 2007; Glunde *et al.*, 2008), and carcinogens (Ishidate *et al.*, 1980). Furthermore, ChoK α overexpression alone is sufficient to induce malignant transformation (Ramírez de Molina *et al.*, 2005). The 9 chemically equivalent protons in choline yield a strong singlet resonance detectable by proton magnetic resonance spectroscopy (^1H MRS). MRS studies have found increasing PC and total choline (tCho) levels as breast cell lines progress from normal to immortalized, to oncogene transformed, to malignant (Aboagye and Bhujwalla, 1999). *In vivo* ^1H MRS studies have identified choline accumulation in 83% of breast lesions (Katz-Brull *et al.*, 2002). Furthermore, alterations in choline and lipid metabolism detected by MRS are predictive of tumor response to certain therapies (Negendank, 1992; Delikatny *et al.*, 2011).

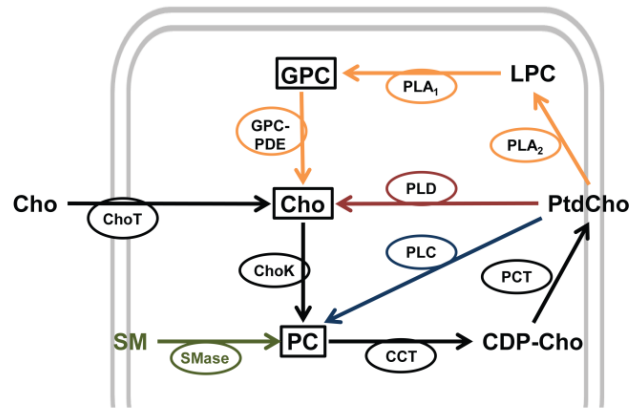


Figure 4.1. Cellular mechanisms affecting the intracellular pool of PC. Choline (Cho) uptake via Cho transporters (ChoT) and entry into the Kennedy pathway of PtdCho biosynthesis (black) by which Cho is phosphorylated by ChoK (EC 2.7.1.32), then converted to CDP-Cho and PtdCho by choline phosphate cytidyltransferase (CCT; EC 2.7.7.15) and phosphocholine diacylglycerol transferase (PCT; EC 2.7.8.2), respectively. The four catabolic routes: (ii) membrane sphingomyelin (SM) hydrolyzed by sphingomyelinase (SMase; EC 3.1.4.12; green) to PC and ceramide; (iii) PtdCho deacylation to lyso-PtdCho (LPC), GPC, and Cho (yellow) by phospholipase A2 (PLA2; EC 3.1.1.4), and lysophospholipase (EC 3.1.1.5) or phospholipase A1 (PLA1; EC 3.1.1.32), and GPC: phosphodiesterase (GPC:PDE; EC 3.1.4.2), respectively; (iv) PtdCho hydrolysis directly to Cho and phosphatidic acid by phospholipase D (PLD; EC 3.1.4.4; red); (v) PtdCho hydrolysis directly to PC and diacylglycerol via PtdCho-specific phospholipase C (PLC; EC 3.1.4.3; blue). ^1H MR-visible Cho metabolites that contribute to the composite tCho peak are in boxes.

In vivo ^1H MRS is limited by spectral resolution, with the tCho peak representing a composite resonance consisting of free choline, PC, and glycerophosphocholine (GPC). Phosphorus (^{31}P) MRS is capable of distinguishing the phosphomonoester PC from the phosphodiester GPC, but ^{31}P -MRS is relatively insensitive requiring large voxels *in vivo*. In addition, direct PC measurements are not always accurate descriptors of ChoK α activity because of the catabolic formation of PC by the phospholipase and sphingomyelinase enzymes (Fig. 4.1). There have been efforts to hyperpolarize choline with the intention of monitoring ChoK α activity (Gabellieri *et al.*, 2008; Sarkar *et al.*, 2009); however, this approach is limited by the polarization lifetime of ^{15}N and has yet to be demonstrated feasible in intact cells or *in vivo* tumor models. Radiolabeled ^{11}C -choline

(Contractor *et al.*, 2011) and ^{18}F -choline (Bansal *et al.*, 2008) are proving to be useful for positron emission tomography (PET) imaging in tumors that are not FDG avid, such as the prostate. However, isotope-labeled choline analogs are also dependent on the complex families of proteins responsible for choline transport (ChoT: high-affinity choline transporters, choline transporter-like proteins, organic cation transporters, and organic cation/carnitine transporters). Upregulation of these proteins has been demonstrated in some cancers but their involvement remains, for the most part, poorly understood (Eliyahu *et al.*, 2007; Glunde *et al.*, 2011). An alternative method to noninvasively detect ChoK α status would be useful to aid in clinical tumor assessment.

ChoK α has garnered clinical attention as a biomarker of tumor malignancy, leading to its study as a treatment target. Silencing ChoK α via RNAi has been shown to reduce cell proliferation (Glunde *et al.*, 2005), enhance the sensitivity of aggressive cell lines to 5-fluorouracil (Mori *et al.*, 2007), and reduce tumor growth rates (Al-Saffar *et al.*, 2006) in breast cancer models. The choline mimetic, hemicholinium-3 (HC-3), has long been known to inhibit ChoK α , but also interrupts neuronal choline transport and acetylcholinesterase activity (Ansell and Spanner, 1974). Its neurotoxicity at doses relevant for ChoK α inhibition (Cannon, 1994) led to the development of molecules capable of blocking choline phosphorylation without causing respiratory paralysis (Hernández-Alcoceba *et al.*, 1997). The most potent and specific ChoK α inhibitors to date have been established by the Lacal lab and were identified from quantitative structure–activity relationship studies of bis-pyridinium (Campos *et al.*, 2001) and bis-quinolinium (Sánchez-Martín *et al.*, 2005) HC-3 mimetics (Fig. 4.2). These studies found that lipophilicity enhances antiproliferative activity but must be optimized because of

trade-offs in solubility. The top candidates identified were symmetric and featured 2 aromatic heterocyclic head groups, containing quaternary ammonium elements, attached by a linker of optimized length (Campos *et al.*, 2006). Many of the bis-pyridinium and bis-quinolinium structures feature electron-donating functional groups, which stabilize the positive charge and increase activity (Campos *et al.*, 2001). Effective inhibitors have been identified from compounds with aromatic or aliphatic linkers, which can be used to optimize the antiproliferative properties.

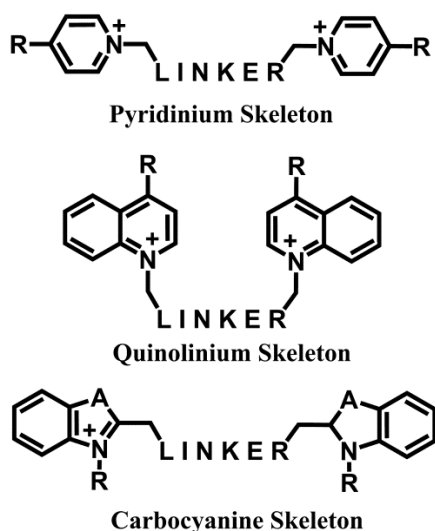


Figure 4.2. Templates for ChoK α -specific inhibitors. The bis-pyridinium (top) and bis-quinolinium (middle) structures with electron-donating functional groups (R) and aromatic or aliphatic linkers. A novel template for ChoK inhibitors is proposed based upon the carbocyanines (bottom), whose fluorescence properties are determined by linker length and are substitutable at the A and R positions.

1,10-((Butane-1,4-diylbis(4,1-phenylene))bis(methylene)) bis(4-(dimethylamino)pyridin-1-ium) bromide (MN58b) is the best-characterized bis-pyridinium ChoK α inhibitor, having been demonstrated to be effective against breast, colon (Al-Saffar *et al.*, 2006), bladder (Hernando *et al.*, 2009), and cervical cancer, as well as squamous cell carcinoma, histiocytic lymphoma, and chronic myeloid leukemia

models (Hernández-Alcoceba *et al.*, 1999). As part of their transformation, cancer cells are thought to acquire an addiction to PC, which sensitizes them to ChoK α -targeted inhibition. MN58b treatment causes a temporary cell-cycle arrest in normal cells because of dephosphorylation of the checkpoint protein pRb. Active (unphosphorylated) retinoblastoma protein (Rb) prevents G₁ to S-phase transition. Tumor cells are often insensitive to this growth arrest and attempt to bypass ChoK α blockade by excising the PC group from sphingomyelin for further PtdCho production, releasing ceramides as a by-product (Rodríguez-González *et al.*, 2004). The accumulation of ceramides, in addition to attenuation of the proliferative PC signal, leads to tumor-specific apoptosis (Kolesnick, 2002). TCD-717, developed by TCD Pharma, is the best candidate among the bis-quinolinium compounds and has completed a phase I dose escalation clinical trial for solid tumor treatment (Ramírez de Molina *et al.*, 2011).

We sought to test the hypothesis that carbocyanine-derived HC-3 mimetics could be adapted to the established criteria for effective ChoK α inhibition (Fig. 4.2). The carbocyanine dyes contain a number of structural similarities to existing ChoK α inhibitors, including symmetric heterocyclic head groups containing quaternary ammonium moieties connected by an aliphatic spacer. A preliminary experiment run by Daniel Leung in our lab used ³¹P MRS to demonstrate that the addition of either HC-3 or dimethyloxacarbocyanine iodide (DMOCI; also abbreviated as CyDy) was capable of attenuating the conversion of choline to PC in a perfused cell model of prostate cancer (Fig. 4.3). This provided early evidence that this strategy is feasible and led to a search for fluorophores with better optical properties that could inhibit PC production.

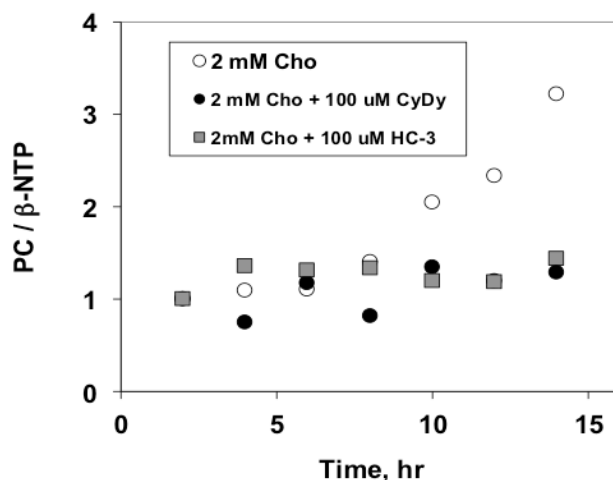


Figure 4.3. Time dependent increases in PC resonances measured in ^{31}P NMR spectra. DU145 cells grown on Biosilon beads were perfused in the presence of 2 mM choline (open circles). Time-dependent changes in PC concentration relative to beta-nucleoside triphosphate (β -NTP) were measured in real time in live cells following addition of hemicholinium-3 (HC-3, black circles) or DMOCl (CyDy, grey squares) to the perfusion media. Both the prototypical choline mimetic, HC-3, and the carbocyanine, DMOCl, are capable of attenuating choline phosphorylation ($n = 1$). Experiments were carried out by Daniel Leung of the Delikatny Lab.

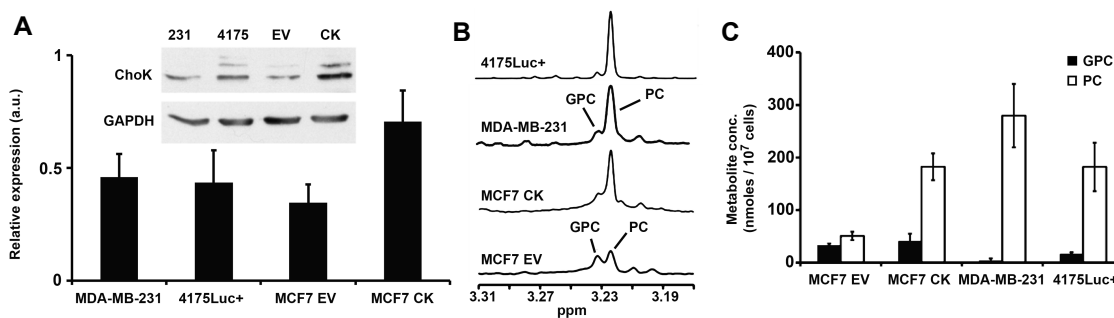


Figure 4.4. Choline metabolite and ChoK α levels in cultured cell models. (A) Western blots (insert) and quantification confirm that higher levels of PC are accompanied by increased expression of ChoK α . (B) MR spectra and (C) quantification of aqueous extracts of the cell lines. MDA-MB-231 and 4175-Luc+ have higher levels of PC than MCF7-WT. Overexpression of ChoK α leads to an increase in PC levels. Assistance with Western blots provided by Mansi Shinde of the Klein Lab, and technical support for MRS experiments provided by Weixia Liu of the Small Animal Imaging Facility. Preparation and MRS of 4175-Luc+ extracts performed by Michael Chiorazzo of the Delikatny Lab.

We report here the development of a new prototype ChoK α inhibitor, JAS239, with both potent antiproliferative activity as well as fluorescence in the near-infrared (NIR) range. The optical properties of NIR fluorophores are ideal for *in vivo* optical imaging, as human tissue (water, hemoglobin, fat) has minimal absorbance in this wavelength range (650–900 nm). Although fluorescent kinase inhibitors in the visible range have been reported (Kim *et al.*, 2010; Yenugonda *et al.*, 2011; Kim *et al.*, 2011), our approach using NIR fluorophores potentially allows for the imaging of kinase expression and function *in vivo*.

4.2 Results

The levels of ChoK α expression and choline metabolite concentrations were determined in a panel of breast cancer cell lines. Western blots (Figure 4.4A) show that the estrogen-receptor positive MCF7-EV cell line has a lower expression of ChoK α than the triple-negative and metastatic MDA-MB-231 cell line. Figure 4.4B shows ^1H MR spectra of the aqueous fraction of chloroform:methanol:water extracts prepared from the 4 cell lines. As previously reported (Shah *et al.*, 2010), the non-metastatic MCF7-EV cells show lower levels of PC, the enzymatic product of ChoK α , compared to the metastatic MDA-MB-231 cells. The ChoK α overexpressing cell line, MCF7-CK+, shows a 2.3-fold increase in PC levels accompanied by high expression of ChoK α . The 4175-Luc+ cell line has slightly lower PC levels than the parent MDA-MB-231 cells (Fig. 4.4C), but comparable expression of ChoK α . ChoK α activity assays were performed using ^{14}C -labeled choline added to intact cells followed by extraction, thin layer chromatography (TLC) and autoradiography (Figure 4.5A). These assays show that

choline is rapidly phosphorylated to PC upon cell entry as a trapping mechanism, and that catabolic breakdown of PtdCho to GPC becomes detectable after 16 hours. Figure 4.5B shows that MCF7-EV cells have the lowest relative activity of the tested cell lines, and that ChoK α overexpression enhanced the production of ^{14}C -PC. ChoK α activity was also determined using an NMR-based assay on cytosolic preparations. The NMR spectra of MCF7 cell cytosolic preparations (Fig. 4.6A) demonstrate the rise in the PC peak (3.22 ppm) at the expense of the choline peak (3.20 ppm) after choline, ATP, and Mg^{2+} ions were added. The PC and choline peak integrals were plotted over time (Fig. 4.6B) and regressions were fit to the linear portion of the curve to estimate ChoK α activity (Fig. 4.6C). Both the radiotracing and the NMR assays directly measure choline depletion and the simultaneous increase in PC. Both assays show that over-expression in MCF7-CK+ significantly increased ChoK α activity to levels similar to MDA-MB-231 cells.

A screen of potential fluorescent inhibitor-like compounds was performed using ^1H NMR. Here MCF7 cells were used as a source for cytosolic ChoK α , as they have low baseline levels of PC. ^1H NMR was used to assess ChoK α activity in the presence and absence of inhibitor (Fig. 4.7). MN58b added to the NMR tube at a final concentration of 10 μM was found to reduce ChoK α activity by 57%. FM 4-64 at 10 μM caused an unexpected 50% increase in ChoK α choline phosphorylation (not shown), and doubling the final concentration to 20 μM resulted in only a 3% reduction. For DMOCI (3,3'-dimethyloxacarbocyanine iodide), addition of 100 μM caused a 50% increase in PC formation. The NIR fluorophore HITC caused a 9% increase in ChoK α activity in this cytosolic model. These values represent single trials, as this experiment is too time intensive and expensive to justify the pursuit of ineffective compounds. In the presence of

100 μ M JAS239, a 26.2% reduction in ChoK α activity ($P = 0.02$) was observed in MCF7 cells (Fig. 4.7). ChoK α overexpressing MCF7-CK+ cells demonstrated no significant change in ChoK α activity ($P = 0.20$) when exposed to the same concentration of JAS239 (Fig. 4.7). Further studies were performed on JAS239 using MN58b as a positive control.

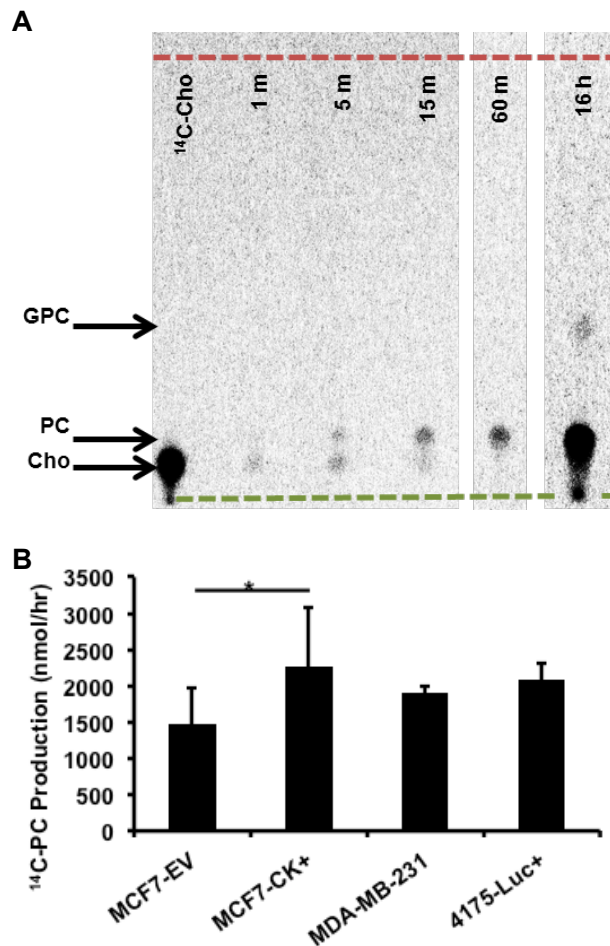


Figure 4.5. 14 C-choline radiotracing assay for ChoK activity. (A) Cells were pulsed with 1 μ Ci of 14 C choline for the times indicated. Extracts were separated by TLC and analyzed by autoradiogram. (B) Quantification of autoradiograms shows increased ChoK activity in MCF7-CK+ relative to MCF7-EV control. Mouse adaptation of the 4175-Luc+ cell line did not result in significant changes in ChoK activity when compared to the parent MDA-MB-231 cell line. Values represent \pm SEM for 3 separate experiments, $P < 0.05$.

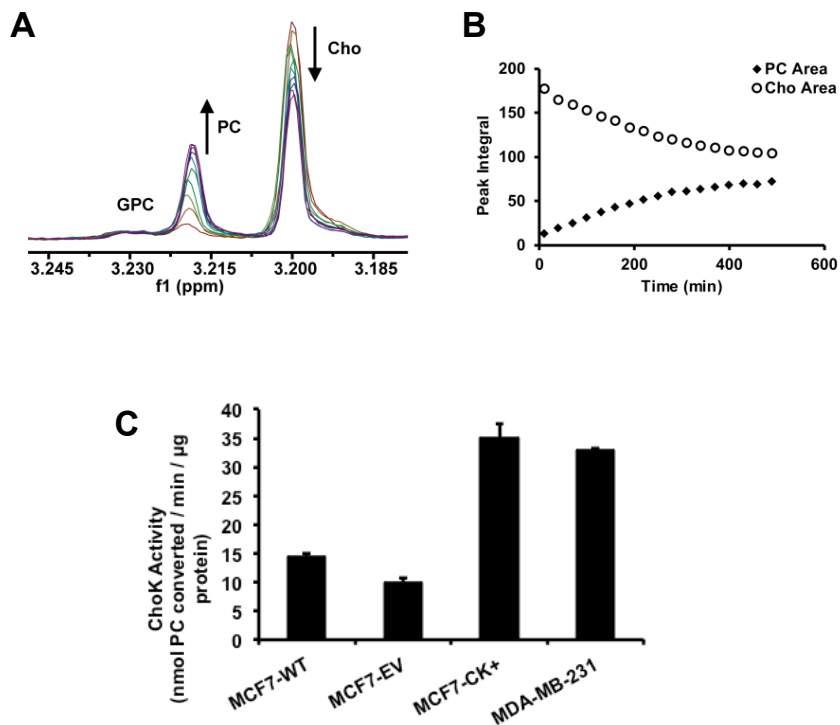


Figure 4.6. ^1H NMR ChoK assay. (A) Superimposed ^1H spectra obtained over 500 min following addition of choline, Mg^{2+} , and ATP to cytosolic extracts of MCF7 WT cells show increases in PC at the expense of choline. (B) The corresponding PC and Cho peak integrals were plotted over time and linear regression of the early portion of (B) yields an estimate of ChoK activity in the breast cancer cell panel. (C) Quantification shows that ChoK α overexpression increases activity in MCF7 cells to levels of MDA-MB-231 cells, whereas no effect was caused by expression of the empty vector (MCF7-EV). * $P < 0.05$

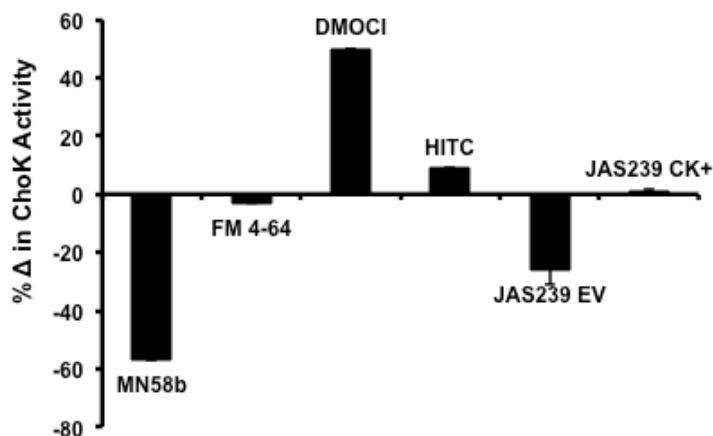


Figure 4.7. ChoK inhibition by fluorescent choline mimetics measured by NMR. PC production in cytosolic preparations from MCF7 cells was measured using ^1H NMR. Drastic reduction of PC production is observed following MN58b addition. Neither FM 4-64, DMOCl, or HITC are capable of inhibiting ChoK activity ($n = 1$). JAS239 causes significant reduction in PC production ($n = 3$) in MCF7-EV cells. Overexpression of ChoK α variant 1 reverses the inhibition by JAS239.

JAS239 was able to inhibit the phosphorylation of ^{14}C -labeled choline in MDA-MB-231 triple-negative breast cancer cells with an IC_{50} of $4.6 \mu\text{M}$ at 17 hours of treatment, comparable to the IC_{50} of $2.3 \mu\text{M}$ observed for MN58b (Fig. 4.8A). Treatment with 10 or $20 \mu\text{M}$ JAS239 for 17 hours or longer resulted in a statistically significant reduction in MDA-MB-231 viability as measured by Trypan blue exclusion (Fig. 4.8B). The antiproliferative EC_{50} of JAS239 at 24 hours is $13.3 \mu\text{M}$, as measured by the Trypan exclusion assay. Figure 4.8C shows that the reduction in choline phosphorylation occurred as early as 2 hours after treatment at 10 and $20 \mu\text{M}$, before any significant loss in cell viability was observed. By 17 hours, significant losses in both ChoK α activity and cell viability were found (Fig. 4.8D). Addition of 2 mM exogenous non-labeled choline to MDA-MB-231 cells was able to rescue the inhibition of ChoK α by JAS239 ($10 \mu\text{M}$), whereas 0.2 mM had no effect (Fig. 4.8E). By 17 hours, exogenous choline at 0.2 and 2 mM was unable to outcompete JAS239 (Fig. 4.8F).

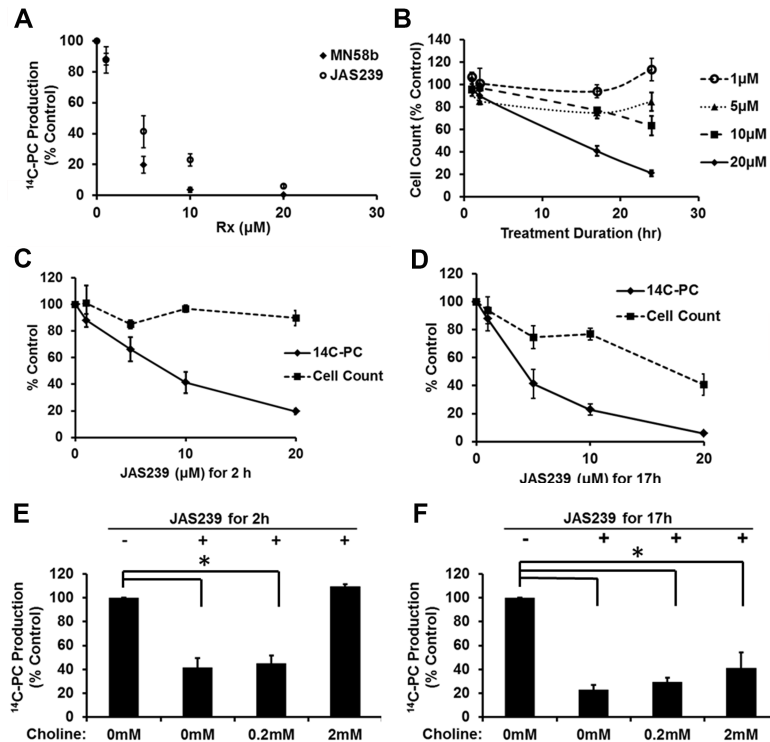


Figure 4.8. JAS239 is a competitive inhibitor of ChoK in MDA-MB-231 cells. (A) Cell treatment for 17 hr with MN58b or JAS239 inhibits ^{14}C -choline phosphorylation with an IC_{50} of 2.3 and 4.6 μM , respectively. (B) Cell viability determined by Trypan blue exclusion in response to JAS239, where \ddagger indicates cell reduction ($P < 0.05$) versus untreated control at 2 and 17 hr and $\#$ indicates cell reduction ($P < 0.05$) versus untreated control at 17 and 24 hr. (C) 2-hr exposure to JAS239 causes inhibition of ^{14}C -choline phosphorylation with no effect on cell viability. (D) After 17 hr exposure to JAS239, both inhibition of ^{14}C -choline phosphorylation and reduction in viability is observed. (E) Exogenous choline addition at high concentrations rescues ^{14}C -choline phosphorylation in cells treated with 10 μM of JAS239 for 2 hr. (F) By 17 hr, exogenous choline addition does not significantly change ^{14}C -choline phosphorylation in cells treated with 10 μM of JAS239. Data plotted as % control \pm SD for three separate experiments. $*P < 0.05$.

Direct comparison of JAS239 and MN58b in each of the 4 breast cancer cell lines was then performed. The potency of ChoK α inhibition in intact cells was assessed using ^{14}C -PC production in 1 hour. Trypan blue exclusion was used to measure cytotoxicity at 17 hours. Accelerated flux through ChoK α was observed in MCF7-CK+ cells, and MN58b normalized this aberrant flux to levels comparable to that of the control MCF7-EV cell line (Table 2, Fig. 4.9A). MN58b was more than twice as potent as JAS239 at

this early time point in both cell lines (Table 2, Fig. 4.9A,B). After overnight treatment, there was little difference in the EC₅₀s as determined by Trypan exclusion between MN58b (Table 2, Fig. 4.10A) and JAS239 in the MCF-7 EV and CK+ cell lines (Table 2, Fig. 4.10B).

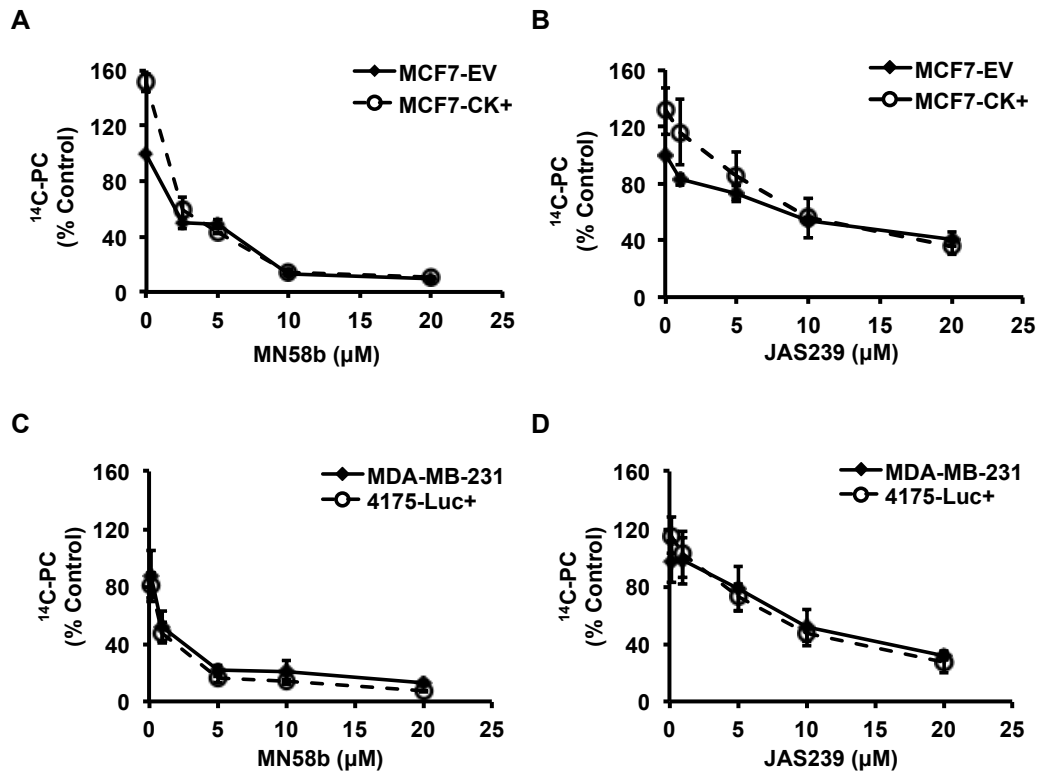


Figure 4.9. Characterization of ChoK α in a panel of human breast cancer cell lines. (A-D) Dose-response curves comparing the effect of MN58b (A, C) or JAS239 (B, D) on ¹⁴C-choline phosphorylation in MCF7-EV and MCF7-CK+ cells (A, B) or MDA-MB-231 and 4175-Luc+ cells (C, D). Values are reported as a percentage of the untreated EV group (for MCF7 cells) or untreated MDA-MB-231 group (for MDA-MB-231 and 4175-Luc+), and represent \pm SEM for 3 separate experiments.

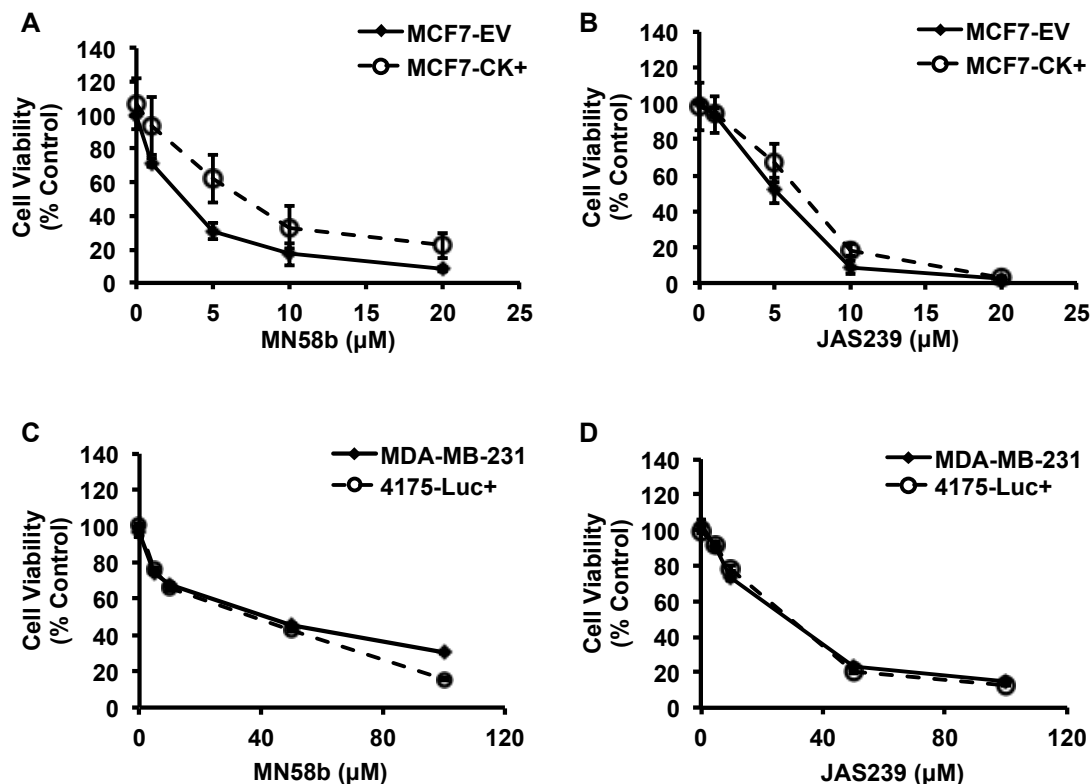


Figure 4.10. Breast cancer cell viability in response to ChoK inhibitors. (A,B) Cell viability measurements via Trypan blue exclusion demonstrate comparable cytotoxicity in MCF7-EV and MCF7-CK+ cells (A, B) exposed overnight to either MN58b (A) or JAS239 (B). MTT assays were performed on MDA-MB-231 and 4175-Luc+ (C, D) cells exposed to MN58b (C) or JAS239 (D). Values are reported relative to untreated control groups and represent \pm SEM for 3 separate experiments.

Table 2. Potency of MN58b and JAS239 in a panel of breast cancer cell lines.

Cell Line	IC50 (μ M)		EC50 (μ M)	
	MN58b	JAS239	MN58b	JAS239
MCF7-EV	3.85 ± 0.42	11.1 ± 5.64	3.29 ± 0.48	4.04 ± 0.55
MCF7-CK+	2.36 ± 0.28	10.3 ± 2.48	6.86 ± 0.43	5.33 ± 0.84
MDA-MB-231	4.36 ± 1.37	9.92 ± 0.22	14.26 ± 4.6	27.2 ± 7.9
4175-Luc+	4.59 ± 0.55	9.89 ± 0.24	20.7 ± 6.4	35.0 ± 21.6

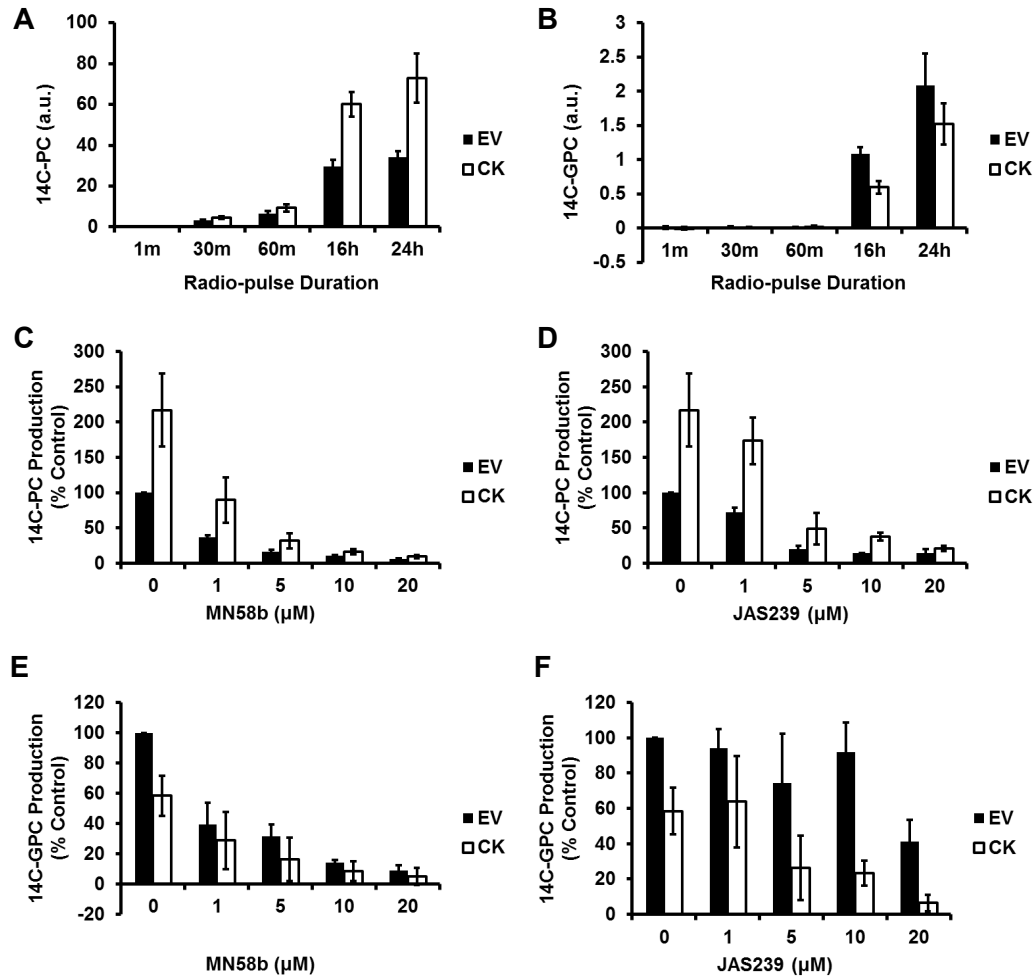


Figure 4.11. ^{14}C -choline radiotracing to distinguish choline transport from choline phosphorylation. (A) MCF7-CK+ (CK) cells have higher PC levels than MCF7-EV (EV) cells. (B) Despite higher flux through the Kennedy pathway, at 16 hr the CK cells have less GPC than EV cells indicating that GPC is rapidly converted back to PC when ChoK α is overexpressed. (C-F) MCF-7 CK or EV cells were given either MN58b (left) or JAS239 (right). ^{14}C -choline was added 1 hr after MN58b (C & E) or JAS239 (D & F) and the ^{14}C -PC (C & D) and ^{14}C -GPC (E & F) levels estimated after 16 hr. While little difference in PC depletion is observed between the two drugs, JAS239 does not deplete ^{14}C -GPC pools in EV cells. Overexpression of ChoK α rescues this effect. Values are reported relative to untreated MCF7-EV and represent \pm SD for 3 separate experiments.

No significant difference in PC production (IC_{50}) was found between the MDA-MB-231 and the derivative 4175-Luc+ cell lines following 2 hours of MN58b treatment (Table 2, Fig. 4.9C). Similarly, the mouse adapted and metastasis derived 4175-Luc+ cell line did not show altered sensitivity to JAS239 when PC production was compared to MDA-MB-231 cells (Table 2, Fig. 4.9D). The first attempt to characterize EC_{50} s in the 4175-Luc+ cell lines indicated that these cells were more resistant and required higher dosage. At high doses, it became difficult to distinguish JAS239 staining from Trypan blue during counting. For this reason, we switched assays from Trypan exclusion to the more automated MTT assay after ensuring that there was no overlap in absorbance readings between the formazan product and JAS239. As was found in radiotracing assays, MN58b was a more potent inhibitor of cell growth than JAS239 (Table 2, Fig. 4.10C). A similar, although more variable, trend existed in 4175-Luc+ cells (Table 2, Fig. 4.10D).

After 16 hours of ^{14}C -choline treatment, PtdCho breakdown could be detected using the formation of ^{14}C -GPC as an indicator of phospholipase activity (as shown in Fig. 4.5). In MCF7 cells, it became apparent that ChoK α overexpression rapidly recycled this product back to ^{14}C -PC, which helped to maintain high levels of ^{14}C -PC (Fig. 4.11A) and resulted in diminished pools of ^{14}C -GPC (Fig. 4.11B). Addition of MN58b (Fig. 4.11C) or JAS239 (Fig. 4.11D) was capable of reducing ^{14}C -PC pools after 16 hours of tracing. In MN58b-treated MCF7-EV or MCF7-CK+ cells, the ^{14}C -GPC pools were diminished to a similar degree (Fig. 4.11E). Interestingly, in the MCF7-EV cell line, JAS239 did not affect ^{14}C -GPC pools except at concentrations of 20 μ M, at which point the cells were

presumed to undergo apoptosis. This result was reversed when ChoK α was over expressed (Fig. 4.11F).

Fluorimetry was used to observe the uptake of JAS239 into MCF7 cells after 2 hours. The uptake of JAS239 was concentration-dependent, and no difference in uptake was observed when ChoK α was overexpressed (Fig 4.12A). To determine probe retention, a series of washout phases were included following JAS239 administration, however only moderate differences were found (Fig 4.12B).

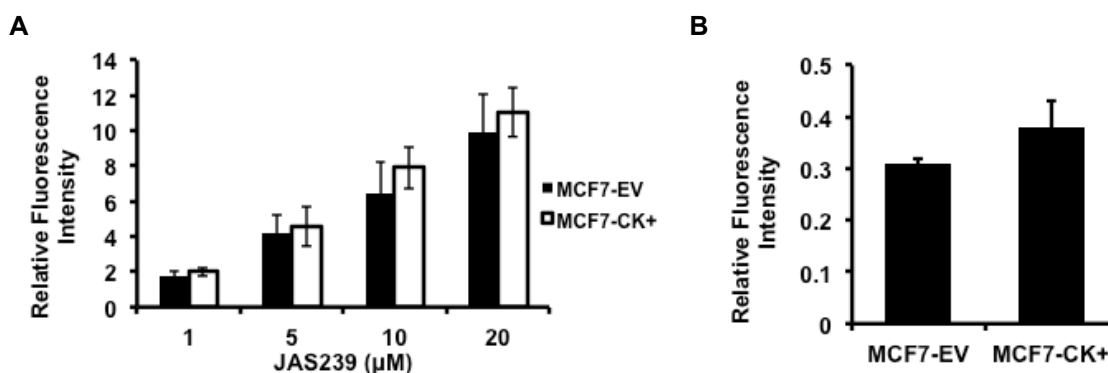


Figure 4.12. Effect of ChoK α expression on JAS239 uptake and retention. (A) JAS239 uptake over 2 hr is linear for MCF7 cells, and no change in uptake is detected following ChoK α overexpression. (B) Only moderate increases in JAS239 retention are observed in MCF7-CK+ cells compared to the MCF-EV control. Cell uptake was measured in a fluorimeter using excitation 640 nm and emission 770 nm, and corrected for cell number. Studies were performed in triplicate; error bars represent \pm SEM.

JAS239 uptake was also analyzed using MDA-MB-231 cells treated for 2 hours at varying concentrations. Fluorescence accumulation was linear within the entire therapeutically relevant dose range (Fig. 4.13A). Addition of exogenous choline did not obstruct the uptake of JAS239 into these cells (Fig. 4.13B). MDA-MB-231 cells treated with JAS239 for 2 hours and stained for 30 minutes with the nuclear stain SYTO9 were analyzed using fluorescence confocal microscopy. A distinct separation of SYTO9 (Fig. 4.13C) and JAS239 (Fig. 4.13D) fluorescence was observed, indicating that the

localization of the novel probe was confined to the cytosolic space, appearing diffusely in the cytoplasm, as well as in punctate perinuclear spots (Fig. 4.13E).

Fixed MDA-MB-231 cells were treated with a rabbit anti-human ChoK α antibody followed by a goat anti-rabbit antibody conjugated to Texas-Red. Fluorescence confocal micrographs from the Texas-Red channel and the NIR channel were acquired and merged (Fig. 4.14, top row). An average Pearson's Correlation Coefficient of -0.31 ± 0.1 was found for three experiments and confirmed that no overlap between the Texas-Red and JAS239 channels occurred (Fig. 4.15A). Confocal micrographs (Fig. 4.14, middle row) of fixed JAS239-stained MDA-MB-231 cells probed with the ChoK α -specific antibody revealed strong colocalization (Pearson's Correlation Coefficient = 0.88 ± 0.02) between JAS239 and ChoK α (Fig. 4.15A). Of the ChoK α -positive pixels analyzed, $89 \pm 9\%$ were located in pixels also positive for JAS239 (Fig. 4.15B). Likewise, $89 \pm 10\%$ of JAS239-positive pixels were also positive for ChoK α (Fig. 4.15C). When fixed cells were pre-treated with ChoK α antibody, marked reduction in JAS239 retention was detected (Fig. 4.14, bottom row). Reduced JAS239 signal relative to noise caused a lower Pearson's Correlation Coefficient (0.49 ± 0.04 ; Fig. 4.15A), although $84 \pm 4\%$ of the regions which were ChoK α -positive were also JAS239-positive (Fig. 4.15B), and $87 \pm 2\%$ of the JAS239-positive pixels were ChoK α -positive (Fig. 4.15C). This demonstrates that the JAS239 that was retained in these cells was still associated with ChoK α , although the intensities of the two channels followed a different distribution trend. These results are consistent with JAS239 being out-competed by the antibody for binding sites.

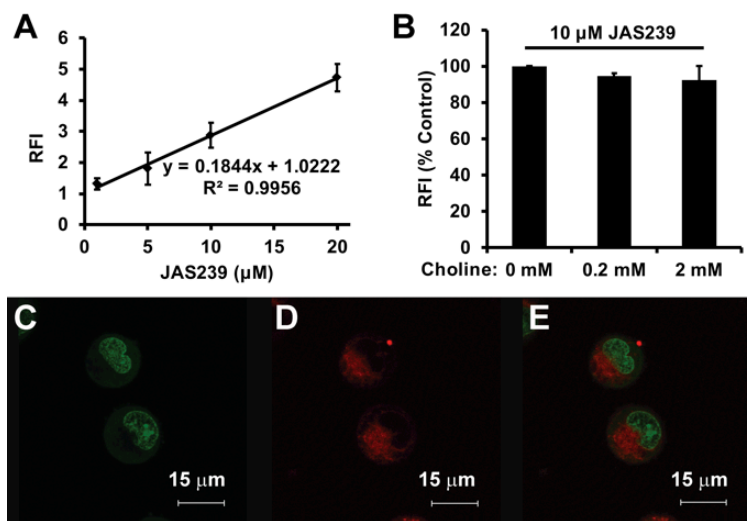


Figure 4.13. Uptake and subcellular localization of JAS239. (A) MDA-MB-231 cells treated with varying concentrations of JAS239 for 2 hr demonstrate linear increases in relative fluorescence intensity (RFI; excitation 640 nm, emission 770 nm). (B) A fluorimetry study demonstrating that addition of exogenous choline to MDA-MB-231 cells could not outcompete uptake of JAS239. Fluorescence confocal micrographs show MDA-MB-231 cells stained for 30 min with (C) the nuclear stain Syto9, (D) 2 μM of JAS239, and (E) merged images. Error bars represent \pm SD for three separate experiments. Images were acquired in the Wistar microscopy core with assistance from James Hayden.

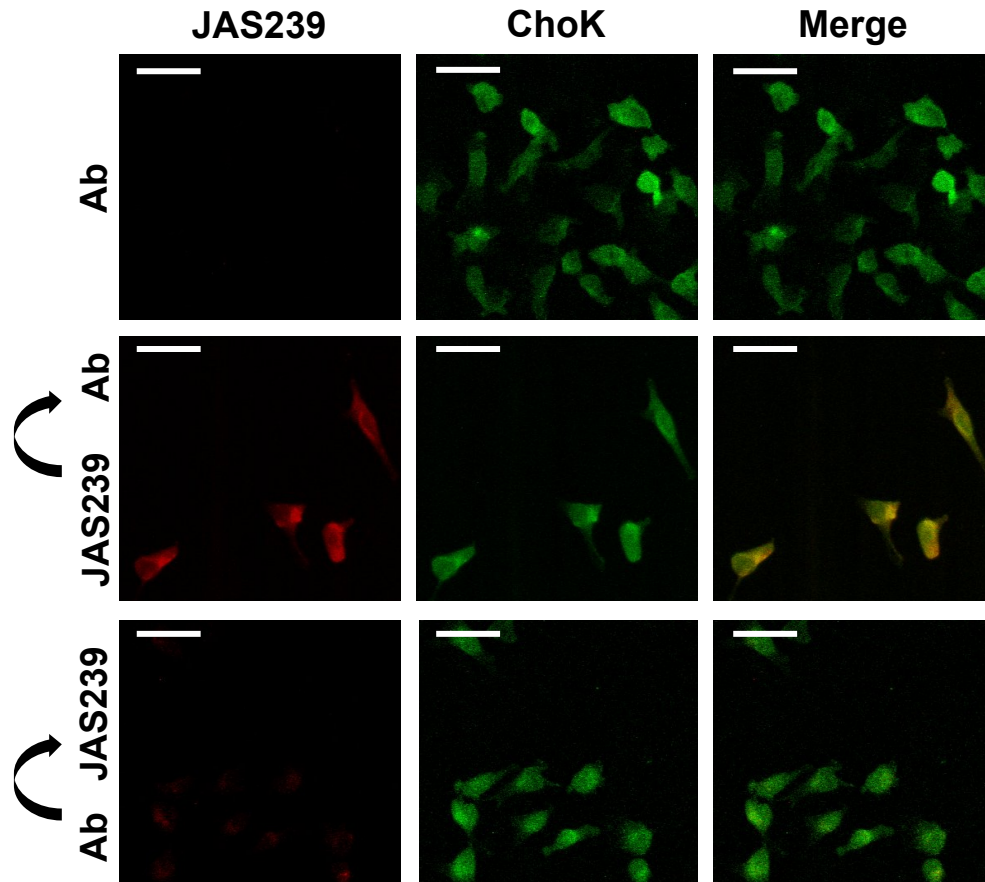


Figure 4.14. JAS239 colocalizes with ChoK α . Fixed and permeabilized MDA-MB-231 cells treated with a ChoK α -specific antibody followed by a Texas Red-conjugated secondary antibody (Ex. 543 nm; Em. 565-615) were assessed by confocal microscopy (top row). In cells stained with JAS239 followed by the ChoK α antibody (middle row), strong colocalization between the JAS239 (Ex. 633 nm; Em. >650 nm) and ChoK α is observed. Cells incubated with antibody prior to JAS239 staining (bottom row) no longer retain the NIRF probe. Scale bars represent 35 μ m. This protocol was developed with help from Alex Glavis-Bloom of the Yang Lab and images were acquired in the CDB microscopy core with assistance from Jasmin Zhao.

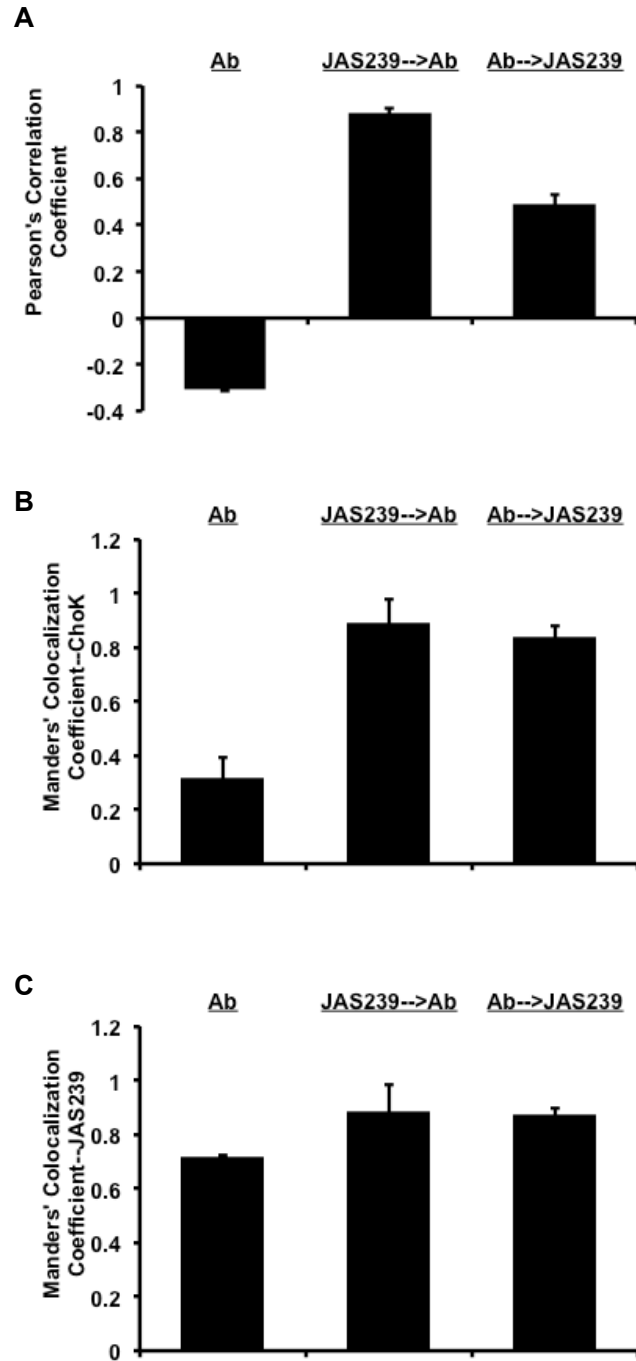


Figure 4.15. Correlation coefficients to quantify JAS239/ChoK α colocalization. (A) JAS239 is strongly correlated with ChoK α , unless fixed cells are pre-incubated with ChoK α antibody. (B) Manders' Colocalization Coefficients for the Texas-Red channel confirm the majority of ChoK α is bound by JAS239 when JAS239 is present. (C) Manders' Colocalization Coefficients calculated for the JAS239 channel indicate that the majority of JAS239 present intracellularly is co-distributed with ChoK α . Values represent \pm SEM for 3 fields of view.

4.3 Discussion

To identify a candidate NIR fluorophore capable of disrupting PC production, a panel of breast cancer cells was first characterized for ChoK α expression, activity, and native choline levels. A ^1H NMR activity assay was used to explore ChoK α kinetics in response to a pulse of choline in the presence of excess ATP and Mg^{2+} . Choline depletion in MCF7 cells was precisely mirrored by PC formation, confirming the inactivation of competing enzymes by the reducing environment of the cell lysis buffer. The enzymatic rate of ChoK α determined by this assay (6.25 nmol PC produced / 10^6 cells / hour) was consistent with estimates for ChoK activity in ovarian cancer cells (Iorio *et al.*, 2005) and the observation that ^{14}C -choline phosphorylation is nearly instantaneous upon cell entry. This assay was used to identify potential ChoK α inhibitors, because in the absence of choline transporters, phospholipases, or other members of the Kennedy pathway (Iorio *et al.*, 2005), this assay can provide a true measure of ChoK α catalytic rate.

The potent inhibition of ChoK α by MN58b reported in the literature (Lacal, 2001) was confirmed in MCF7 cytosolic preparations. DMOCI, however, was incapable of inhibiting ChoK α activity, despite preliminary studies from our lab that found a possible effect in perfused cells. This suggests choline transport inhibition may have influenced the reduction in PC observed in that model system. Neither FM 4-64 nor HITC had an inhibitory effect in the ChoK α activity assay. On the other hand JAS239 caused a significant reduction in ChoK α enzymatic rate, albeit at a higher concentration. These 530 μL samples were highly concentrated with cytosol from 20×10^6 cells. As a reference, the same molar quantity of JAS239 dispersed in the cellular media of 20×10^6

cells would be at a relatively dilute concentration of 0.53 μM . Moreover, the inhibitory effect of JAS239 in MCF7 EV cells could be rescued by ChoK α overexpression, thus confirming ChoK α to be the primary target of JAS239 that leads to the reduction in choline phosphorylation observed in this assay.

Using ^{14}C -choline as a radiotracer, JAS239 was found to inhibit ChoK α activity at concentrations higher than, but comparable to MN58b, as indicated by reduced production of ^{14}C -PC. ChoK α inhibition occurred at 2 hours, before the onset of cell death, and was reversible by addition of unlabeled choline, indicating that JAS239 acts as a competitive inhibitor. After 17 hours, choline addition was unable to reverse the effects of JAS239 on choline metabolism, suggesting that irreversible alterations to the Kennedy pathway or downstream pathways had already occurred. Because MN58b and JAS239 are charged small molecules that may be impermeable to the cell membrane, we performed the ^{14}C -choline radiotracing studies in intact cells to ensure the ChoK α inhibition observed in cytosol could be replicated *in vitro*. The improvement in JAS239 potency relative to MN58b in intact cells is presumably due to JAS239 being more cell permeable with one less cationic charge.

We next verified the efficacy of JAS239 in a panel of human breast cancer cells representing different germ lines (epithelial and mesenchymal), tumor stages (estrogen-positive and triple-negative), derivation (mouse-naïve and mouse-adapted), and ChoK α expression (low, medium, and high). ChoK α inhibition in intact cells was assessed at 2 hours of treatment, as this is sufficient time for PC formation but too early for phospholipase involvement or observable cell death. Due to the number of samples this required, we lowered the cell media volume from 3 mL per well to 2 mL per well, thus

lowering the amount of radioactive waste produced per sample. In all cell lines, MN58b was at least twice as potent. This was mirrored in the MDA-MB-231 and 4175-Luc+ cell viability data after 17 hours of treatment, however the MCF7 cell lines were more sensitive to JAS239 than would be expected from the IC_{50} s. The IC_{50} at 2 hours for the MDA-MB-231 cells doubled from 4.6 μ M to 9.92 μ M when the cell media was decreased from 3 mL to 2 mL, reflecting the reduction in total drug molecules interacting with the same number of cells per sample.

Against pure yeast ChoK α , the average reported IC_{50} s of the bis-pyridinium and bis-quinolinium ChoK α inhibitors were 37.1 and 33.9 μ M, respectively; the antiproliferative activities, EC_{50} s, in HT-29 cells were 19.7 and 3.7 μ M, respectively (Campos *et al.*, 2001; Sánchez-Martín *et al.*, 2005). Although determined in different systems, the measured IC_{50} of 4.6 μ M for JAS239 represents potency comparable or better than 85% of the reported bis-pyridinium-based ChoK α inhibitors, and 61% of the bis-quinolinium compounds. The EC_{50} values are also comparable, although determined using different assays in cell lines of different tissue origin. The action of JAS239 against MDA-MB-231 cells suggests ChoK α inhibition may be an effective strategy in triple- negative breast cancers, which are often therapy resistant. Its potency suggests that further modifications based upon the carbocyanine template, and subsequent structure-activity characterization, may yield compounds highly specific to ChoK α .

An interesting difference in how MCF7 cells respond to treatment with MN58b and JAS239 was observed after 16 hours of radiotracing. Based upon the evidence that ChoK α overexpression causes depletion of 14 C-GPC by promoting its conversion back to 14 C-PC, we hypothesized that ChoK α inhibition would reduce PC levels and not deplete

^{14}C -GPC. We found JAS239 did not deplete the ^{14}C -GPC pool in MCF7-EV cells, whereas MN58b caused depletion of both the ^{14}C -PC and the ^{14}C -GPC pools. This suggests some of the inhibitory effect of MN58b on PC formation may be due to choline transport inhibition in these cells. Further radiotracing studies with inhibitors added following ^{14}C -choline addition and measurement of choline efflux from the cells are needed to better understand this mechanism.

The uptake of JAS239 into intact MDA-MB-231 cells was analyzed by fluorimetry and was found to be both rapid and linearly proportional to the concentration of probe added; no quenching of signal intensity was observed even when high therapeutic doses were used. Moreover, the uptake into MCF7 cells was linearly dependent on concentration and independent of ChoK overexpression. Furthermore JAS239 appears to enter cells independent of the choline transporters, as exogenous choline addition had no effect on probe uptake. The ability to separate ChoK α expression from choline uptake is an advantage to using fluorescent ChoK α inhibitors. Reported observations made using MRS and PET tracers measure the effects of both choline transport and phosphorylation together. Our approach may yield a companion diagnostic that would aid in identifying patients best suited for ChoK α inhibitor-based therapies. Overexpression of ChoK α resulted in only moderate enhancement of JAS239 retention. The MCF7-CK+ cells were previously reported by Shah *et al.* to have elevated drug and dye (Rhodamine 123) efflux capabilities, which may be a confounding factor to consider when interpreting the results from this assay (Shah *et al.*, 2010).

The inherent optical properties of this small molecule inhibitor allow for study of subcellular localization by fluorescence confocal microscopy. JAS239 collects in the

cytosolic space where ChoK α is active (Hosaka *et al.*, 1990) and is excluded from the nucleus where DNA intercalation, mutagenesis, and nonspecific cell death would otherwise be confounding factors. Using confocal microscopy of fixed MDA-MB-231 cells, JAS239 staining was compared with immunohistochemical ChoK α assessment. Colocalization of the probe with ChoK α was observed, indicating a direct interaction that could be blocked when the N-terminal antibody was bound ahead of time.

Our results have indicated that JAS239 enters breast cancer cells independent of the choline transporters and competes with choline at the active site of ChoK α . The development of a small molecule kinase inhibitor with NIR-fluorescence confers the ability to noninvasively track the biodistribution of this probe with NIR optical imaging (Yang *et al.*, 2010), greatly reducing the number of animals required for detailed pharmacokinetics studies. ChoK α expression can be up to 15-fold higher in malignant compared with non-transformed breast cells (Glunde *et al.*, 2005), thus imaging agents targeted to this biomarker may benefit from substantial signal-to-noise.

We describe here a novel strategy for reporting ChoK α expression, which has been clinically correlated to histologic tumor grade and estrogen receptor status in breast cancer. As interest in ChoK α inhibition for cancer therapy expands, these compounds have the unique potential to serve as companion diagnostics to identify patients most likely to benefit from this therapy and to make ongoing minimally invasive evaluations of their response.

Chapter 5

JAS239 characterization in breast tumor models

5.1 Introduction

Choline kinase alpha (ChoK α) has become the subject of intense interest for its utility as an oncogenic biomarker as well as an anticancer therapeutic target (Rodríguez-González *et al.*, 2003). During malignant transformation, cells sequester high levels of PC which become detectable using magnetic resonance spectroscopy due to the 9 chemically-equivalent protons on the methyl groups adjacent to the quaternary nitrogen (Negendank, 1992; Aboagye and Bhujwalla, 1999). Heightened ChoK α activity has been identified in approximately 40% of human breast tumor specimens (Ramírez de Molina, Gutierrez, *et al.*, 2002).

Inhibitors of ChoK α have been developed as tools to study the involvement of this enzyme in malignant transformation. Shutting down *de novo* phospholipid biosynthesis leads to lower levels of pro-mitotic second messenger Kennedy pathway intermediates, increased ceramide levels, and a de-stabilized endoplasmic reticulum membrane. The most potent of these agents, TCD-717, is a promising anti-cancer drug (Sanchez-Lopez *et al.*, 2013) being evaluated in clinical trials (Lacal and Campos, 2015). MN58b, a dicationic ChoK α inhibitor, has been demonstrated to be lethal to lymphoma cells, but to cause a reversible cell cycle arrest in normal cells (Rodríguez-González *et al.*, 2004). Although the mechanism by which ChoK α inhibition ultimately leads to cell death may not fully be related to the enzymatic function (Falcon *et al.*, 2013), measures of tCho levels are still the primary method of validating novel ChoK α inhibitors. A limitation of

this approach is that tumor necrosis can lead to deceptive decreases in tCho in MR spectra and measurement of secondary biomarkers is required (Horská and Barker, 2010). PET and hyperpolarized choline tracers may be useful to identify ChoK α inhibition, but choline tracer accumulation can be blocked by choline transport inhibitors (Gomez *et al.*, 1970) which have known toxicities (Boobis *et al.*, 1975). Measuring ChoK α expression and inhibition remains a difficult task that is complicated further by the complex contributions of the phospholipases, organic cation transporters, and sphingomyelinases to choline metabolite levels.

Our group synthesized a small molecule choline mimetic with inherent NIRF which effectively attenuates choline phosphorylation with no observable interaction with the choline transporters (Arlaukas *et al.*, 2014). This concept originated when the observation was made of structural similarity between the carbocyanines and the symmetric, bis-heterocyclic ChoK α inhibitors. This carbocyanine derivative called JAS239 is the first described kinase inhibitor with fluorescence in the near infrared wavelength range, wherein human tissue is relatively transparent (Jobsis, 1977). For this reason, NIRF optical imaging probes can be detected through several millimeters, and under certain conditions, centimeters of tissue (van de Ven, 2008). There is a particular need for more specific agents to assist surgeons in distinguishing tumor from normal tissue (Mahmood and Weissleder, 2003), and intraoperative imaging is an expanding field for which NIRF offers a relatively cheap method of delineating tumor margin and assessing lymph node involvement (De Grand and Frangioni, 2003). In this Chapter we test JAS239 as a ChoK α targeted optical imaging probe in murine models of cancer in the breast, which in humans, is a relatively homogenous, NIRF-transparent, and compressible

tissue (Busch *et al.*, 2013). Following *in vivo* characterization of the diagnostic potential of this probe, JAS239 was then employed at higher doses, in conjunction with MN58b, to study the therapeutic potential of ChoK α inhibition.

5.2 Results

Athymic nude mice were used for inoculation with human derived breast cancer cell lines, which were injected into the mammary fat pad and monitored via caliper measurement for orthotopic tumor formation. In 30 days, tumors derived from MCF7-EV, MCF7-CK+, MDA-MB-231, and 4175-Luc+ cell lines reached volumes of 24 ± 5 , 170 ± 30 , 7.9 ± 3.1 , and $700 \pm 150 \mu\text{L}$, respectively (Fig. 5.1). Due to their rapid *in vivo* growth that could additionally be monitored with bioluminescence imaging, 4175-Luc+ tumors were the early focus of this work.

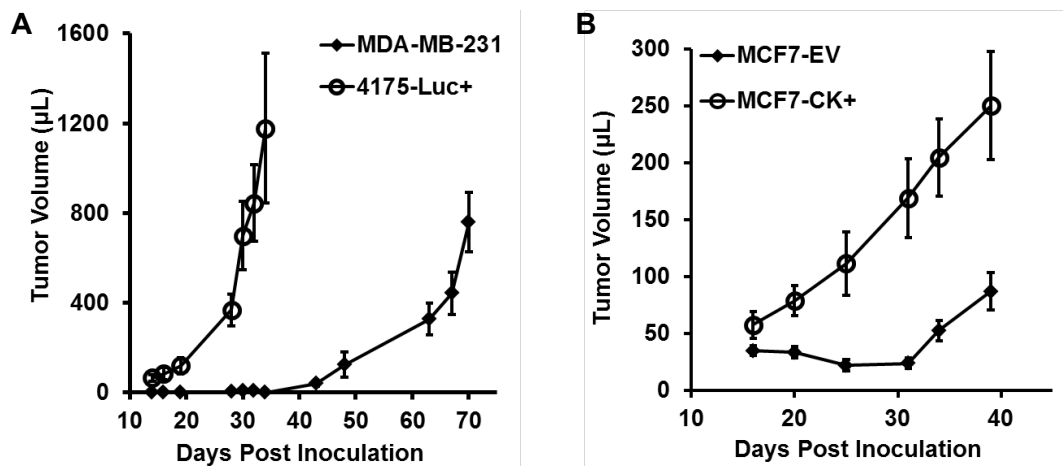


Figure 5.1. Tumor growth patterns in human breast cancer derived cell lines. (A) ChoK α overexpression accelerates tumor growth in an MCF7-derived orthotopic xenograft model. (B) Orthotopically inoculated 4175-Luc+ derived tumors exhibit accelerated growth in volume compared to orthotopic MDA-MB-231 xenografts. Values represent \pm SEM for 5 animals per cohort.

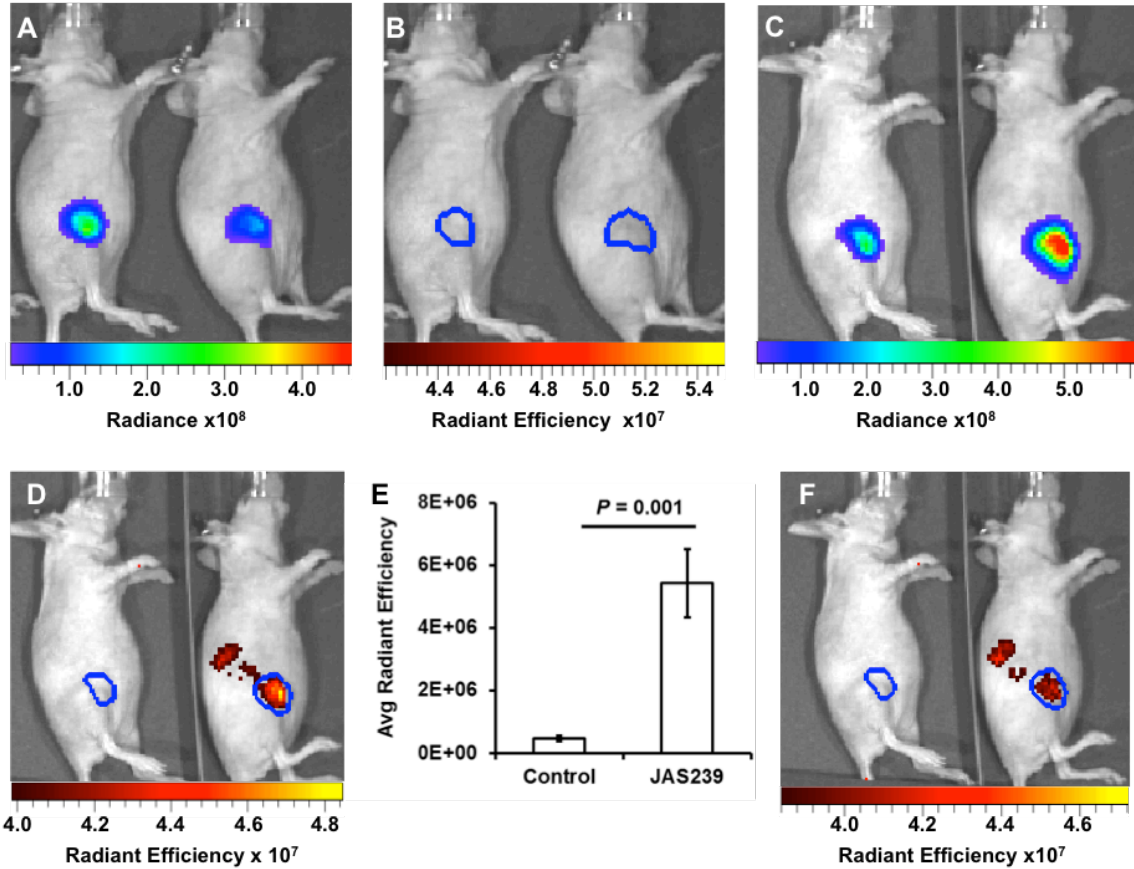


Figure 5.2. Bioluminescence of 4175-Luc+ tumors delineates tumor margin for NIRF measurement. (A) Two representative 4175-Luc+ tumor-bearing mice imaged for bioluminescent Radiance [p/sec/cm²/sr] 15 min after injection of luciferin. (B) Bioluminescence was used to draw an ROI (blue line) around the tumor margin, and was confirmed to be undetectable in the NIR filter range. (C) Mice injected with either control vehicle (left) or JAS239 were administered luciferin after 75 min and imaged 15 min later for bioluminescence to define tumor ROIs. Heightened radiance was observed in JAS239 mice presumably due to absorption of photons by JAS239 and emission at a longer, more tissue transparent wavelength. (D) Tumor margin (blue) defined by bioluminescent imaging of 4175-Luc+ tumors shows no NIRF in the vehicle-injected mouse (left) but intratumoral NIRF in the right mouse injected with Tween-80/Tris Buffer. Renal excretion of JAS239 is also seen outside the tumor boundaries. (E) Average Radiant Efficiency [p/sec/cm²/sr]/[μW/cm²] was quantified in each ROI (4 animals in JAS239 cohort). (F) The tumor NIRF (right mouse) begins to diminish relative to the renal signal 95 min after JAS239 injection.

Bioluminescence emitted by mice bearing 4175-Luc+ orthotopic tumors was measured 15 min following luciferin injection (Fig. 5.2A). This signal was used to delineate the tumor margins (in blue) using the Auto ROI tool in the LivingImage software and was used during NIRF imaging to ensure that the bioluminescent signal did not overlap with the NIR range (Fig. 5.2B). The next day, mice were treated with control vehicle (left mouse) or 20 nmol JAS239 in Tween-80/Tris buffer (right mouse). Luciferin injection and bioluminescence imaging was again used to delineate tumor margin (Fig. 5.2C), and no NIRF signal was detected in the control-treated animals (Fig. 5.2D, left mouse; $n = 5$). In the JAS239-injected animals, NIRF was emitted both from the tumor and from the kidneys (Fig. 5.2D, right mouse; $n = 4$). NIRF emission at 800 nm was over an order of magnitude stronger ($5.4 \pm 1.1 \times 10^6$ vs. $4.8 \pm 0.9 \times 10^5$ [p/sec/cm²/sr]/[μ W/cm²]) in JAS239-injected animals vs. control ($P = 0.001$, Fig. 5.2E). Maximum NIRF contrast between the tumor and background was achieved 90 minutes post-JAS239 injection, as the tumor vs. renal fluorescence diminished after this time due to probe excretion (Fig. 5.2F).

Approximately one week later, mice from this cohort were again injected with the same JAS239 formulation, euthanized 90 minutes later, and the major organs were resected and imaged for NIRF (Fig. 5.3A). The biodistribution of JAS239 is consistent with the renal signal detected in whole animals, however the signal from other internal organs (liver in particular) was higher than would be expected from the whole-body images (Fig. 5.3B). The tumor contrast seen in whole-body NIRF images probably arises because of the relative depth of these organs, compared to the surface tumor.

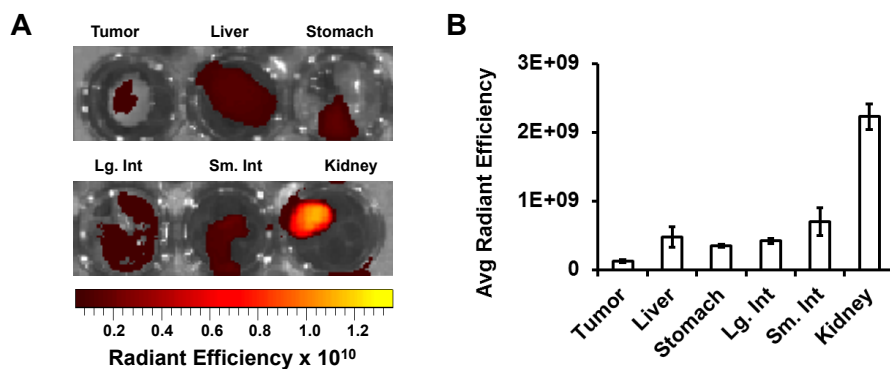


Figure 5.3. NIRF imaging for biodistribution of JAS239 in Tween-80/Tris formulation. (A) Organs from 4175-Luc+ tumor bearing mice (n = 4) were resected 90 min following injection with JAS239 in Tween-80/Tris imaged for NIRF. (B) NIRF was measured for each organ and the Average Radiant Efficiency [$\text{p/sec/cm}^2/\text{sr}$]/ $[\mu\text{W/cm}^2]$ was quantified for comparison.

A cohort of five athymic nude mice bearing orthotopic 4175-Luc+ tumors were injected with 20 nmol JAS239 dissolved in an ethanol/saline solution. NIRF imaging found that background signal from the liver and kidneys was too high to achieve optimal tumor contrast (Fig. 5.4A). After JAS239 had cleared, 20 nmol of ICG was dissolved in the same vehicle and imaged for NIRF after 15 minutes, 45 minutes, 4 hours, and 24 hours (Figure 5.4B). While tumor fluorescence was detected, cloaking the internal organs was necessary to improve contrast (Fig. 5.4C).

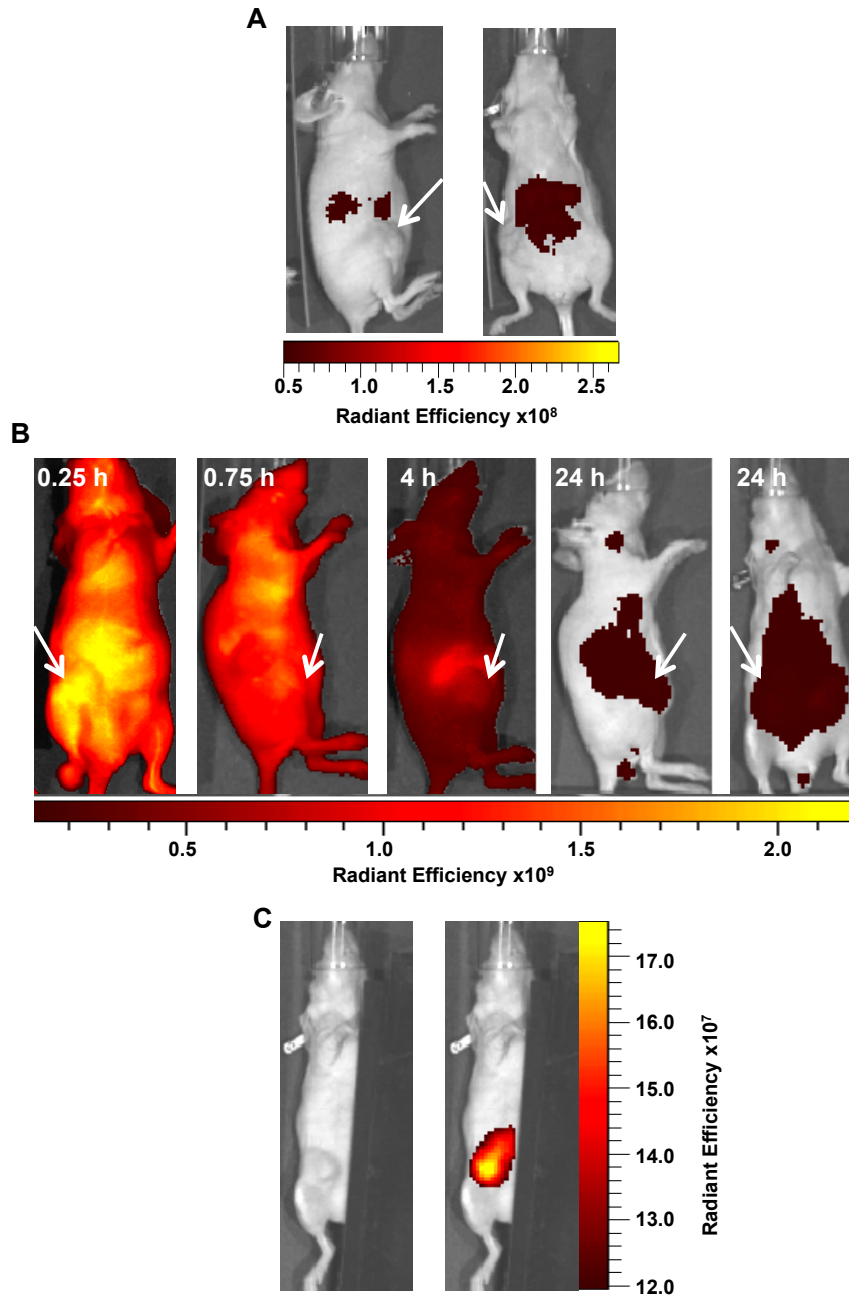


Figure 5.4. Limitations of whole body optical imaging. (A) NIRF imaging was performed on athymic nude mice ($n = 5$) 24 hr after i.v. injection with JAS239 in an ethanol/saline formulation. Poor fluorescence contrast is observed in orthotopic 4175-Luc+ tumors, due to high liver and renal signal. (B) Biodistribution of clinically-approved ICG was then imaged to confirm high fluorescence background was due to limitations of the model. The tumor (white arrow) is barely distinguishable at 0.25, 0.75, 4, or 24 hr post-injection. (C) With orthotopic breast tumors, even ICG requires cloaking of the excretory organs ($n = 3$).

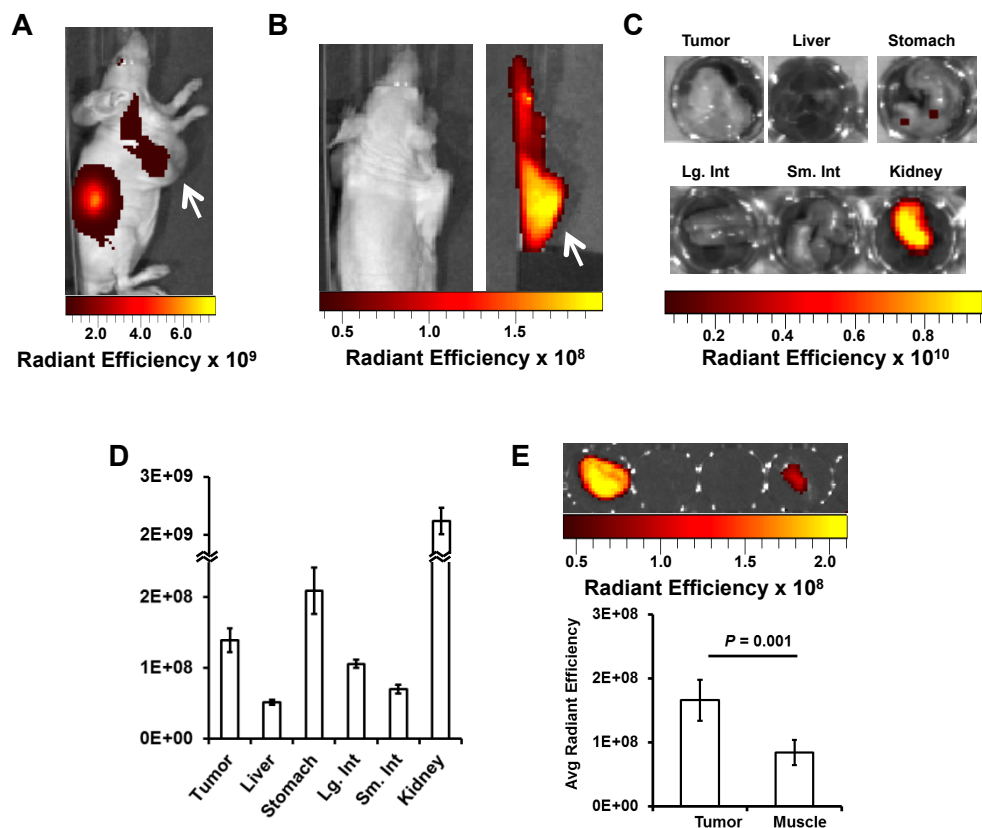


Figure 5.5. NIRF imaging for biodistribution of JAS239 in ethanol/saline formulation. (A) Delivered in an ethanol/saline formulation, maximal intratumoral JAS239 (white arrow) relative to background is achieved 24 h post-injection. (B) Tumors (white arrow) were implanted on the right shoulder to allow organs involved in JAS239 excretion to be cloaked. (C, D) Resected organs 24 hr post-injection of JAS239 were imaged for NIRF (C) and the Average Radiant Efficiency [$\rho/\text{sec}/\text{cm}^2/\text{sr}$]/[$\mu\text{W}/\text{cm}^2$] was quantified (D). (E) Tumor-to-muscle ratio was measured using quantified NIRF. Cohort size was 5 animals and values represent \pm SEM. Total JAS239 delivered was 20 nmol/animal.

We inoculated a third cohort of five athymic nude mice with subcutaneous 4175-Luc⁺ tumors high on the right flank as distant from the kidneys as possible. This cohort was injected with JAS239 in ethanol/saline. Fluorescence from the kidneys was the dominant source of NIRF signal (Fig. 5.5A). Intentional placement of these tumors on the shoulders allowed us to cloak the lower extremities and isolate the tumor for NIRF imaging (Fig. 5.5B). The tumor signal relative to noise was highest at the 24-hour time

point and the organs in these animals were resected and imaged to estimate JAS239 biodistribution (Fig. 5.5C). Compared to the Tris/Tween vehicle, the hepatic signal from this formulation dropped nearly one order of magnitude, from $4.8 \pm 1.5 \times 10^8$ to $5.4 \pm 0.3 \times 10^7$ [p/sec/cm²/sr]/[μ W/cm²], drastically reducing the background signal (Fig. 5.5D). At this time, a nearly two-fold tumor-to-muscle ratio was found (Fig. 5.5E).

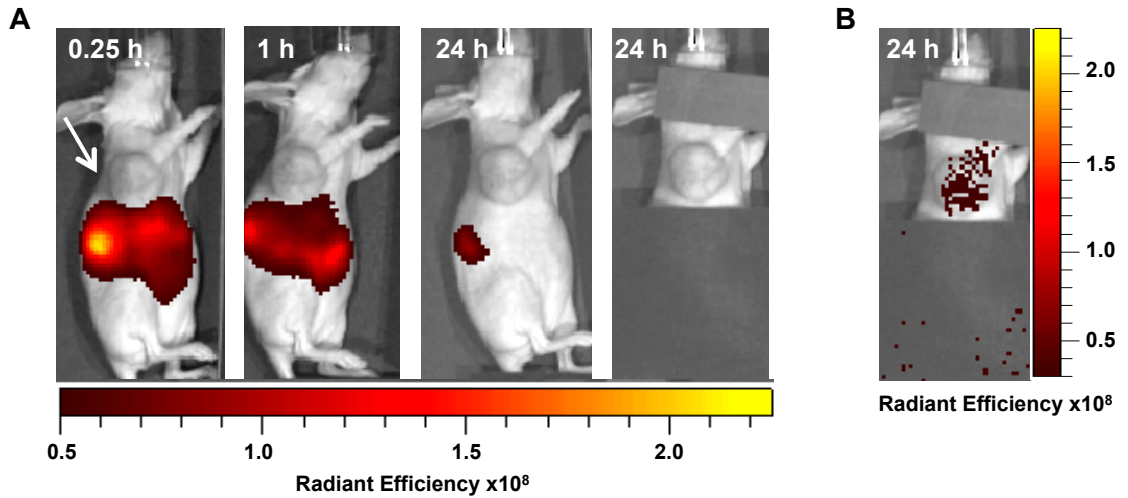


Figure 5.6. Biodistribution of hydro-JAS239 using NIRF imaging. (A) A cohort of athymic nude mice ($n = 5$) bearing 4175-Luc⁺ tumors on the right shoulder were imaged for NIRF (Ex. 745 nm; Em. 800 nm) following i.v. injection of 20 nmol hydro-JAS239. (B) Using an excitation 745 nm and emission 820 nm filter set, intratumoral hydro-JAS239 can be detected in the cloaked animals.

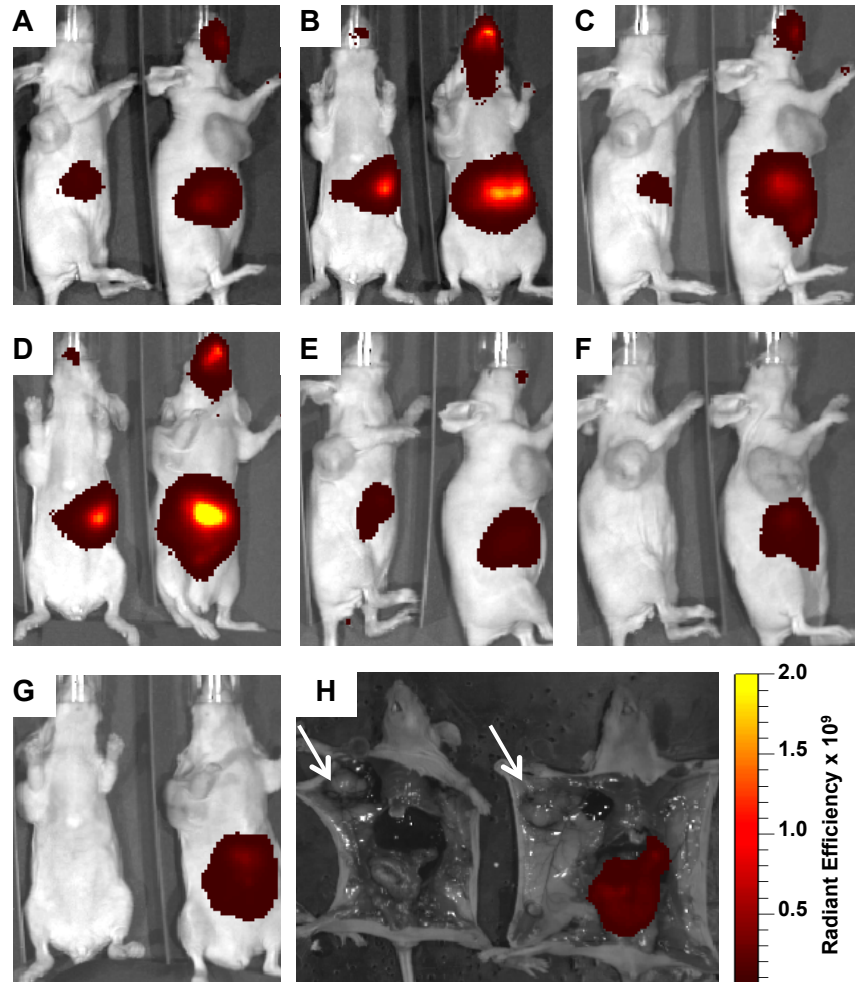


Figure 5.7. Bioavailability study of hydro-JAS239 and JAS239. Athymic nude mice bearing 4175-Luc+ tumors on the right shoulder were administered hydroJAS239 (left mouse) or JAS239 in ethanol/saline (right mouse) by gavage. NIRF images were acquired (A, B) 10 min, (C, D) 30 min, (E) 4 hr, or (F, G) 24 hr post-delivery from the (A, C, E, F) right orientation or (B, D, G) ventral orientation. (H) Animals were then euthanized and the intraperitoneal cavity was exposed to reveal that hydro-JAS239 is cleared after 24 hr, whereas JAS239 is retained in the stomach and intestines.

A modified hydrocyanine form of JAS239 (hydro-JAS239) was created in our lab. When the resonant cyanine structure is chemically reduced, the molecule is non-fluorescent and non-polar until an oxidizing agent such as a free radical is introduced. We sought to test if this non-polar variation would alter the pharmacokinetics or improve the signal-to-noise ratio. Injected intravenously, hydro-JAS239 ultimately distributed in the body in a pattern similar to JAS239 with high liver and renal accumulation early with progressively more of the total probe being directed toward renal clearance after 1 hour (Fig. 5.6A). After 24 hours, the majority of the probe was cleared by the kidney (Fig. 5.6A) and undetected in the tumor even when the animal was cloaked (Fig. 5.6B). Interestingly, when keeping the excitation wavelength constant, but increasing the emission wavelength from 800 nm to 820 nm, there was weak signal detected in the tumors (Fig. 5.6E). Administration of either hydro-JAS239 (n = 3) or JAS239 (n = 1) by gavage found neither probe to be orally available; the hydrocyanine modification did not enhance bioavailability but accelerated clearance from the body (Fig. 5.7).

A small (n = 3) cohort of athymic nude mice bearing 4175-Luc⁺ orthotopic tumors was dissected under the custom-built intraoperative NIRF imaging equipment in the Singhal laboratory. The highest background fluorescence from internal organs was found 1 hour following JAS239 injection (Fig. 5.8A). This signal, as well as reflectance from the bright-field camera, limited the distinction between and tumor and normal tissue during resection (Fig. 5.8B). The tumor was seen to have elevated JAS239 in comparison to muscle, once the two tissues were isolated (Fig. 5.8C). After 4 hours, signal from the liver diminished (Fig. 5.8D), but the tumor contrast was also reduced (Fig. 5.8E). By 24 hours, residual JAS239 could still be detected in the intact mouse (Fig. 5.8F) and in an

isolated tumor sample (Fig. 5.8G). A visualization of the equipment used for this pilot study is provided in Figure 5.8H.

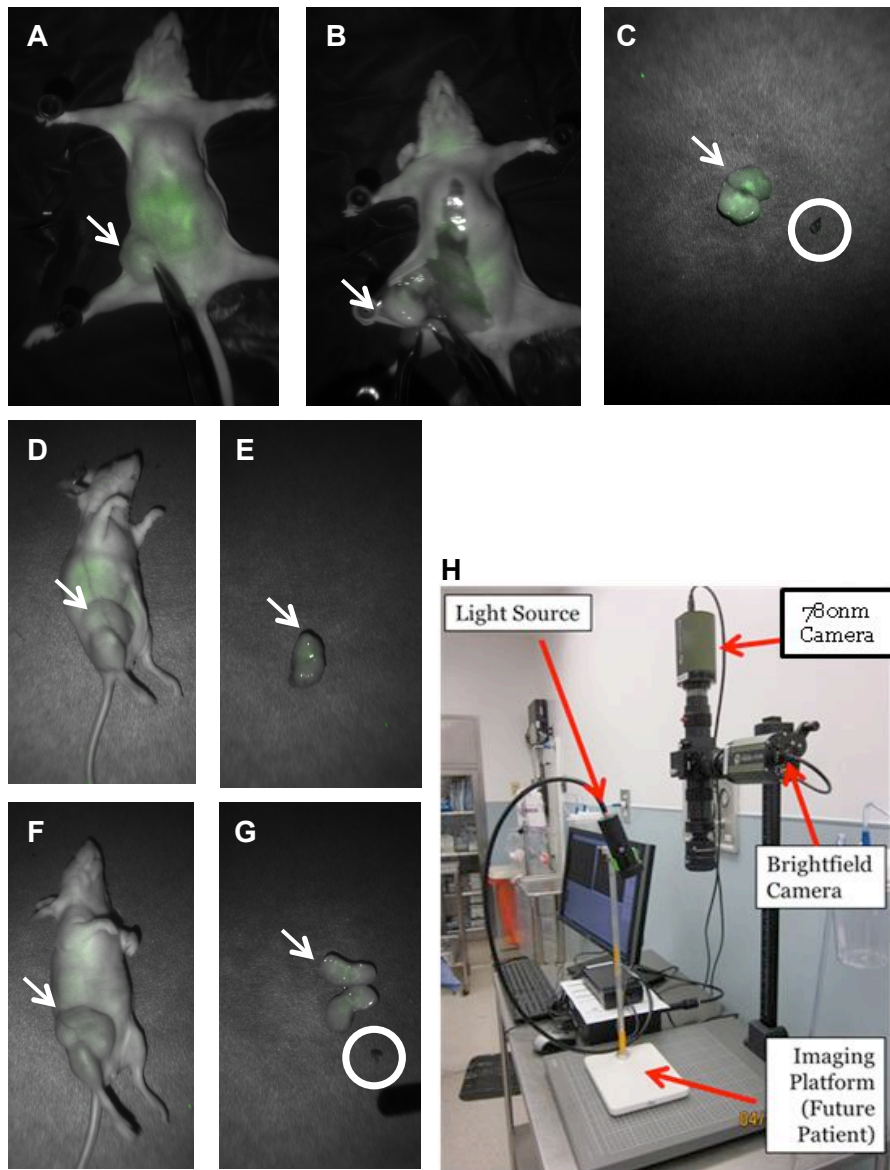


Figure 5.8. NIRF-guided surgical resection of breast tumors. Athymic nude mice with 4175-Luc+ tumors were injected with 20 nmol JAS239 (A-C) 1 hr, (D, E) 4 hr, or (F, G) 24 hr prior to euthanasia. (B) Resection of each tumor was recorded simultaneously with a brightfield camera and a NIR CCD camera. The overlay was merged with help from Ryan Judy and Jack Jiang in the Singhal Lab. The highest tumor (white arrow) to muscle (white circle) ratio is observed at (C) 1 hr, whereas this software is not sensitive enough to detect significant NIRF signal in tumors from the (E) 4 hr and (G) 24 hr time points at this trace dose. (H) A depiction of the NIRF imaging technology designed in the laboratory of Dr. Sunil Singhal is provided.

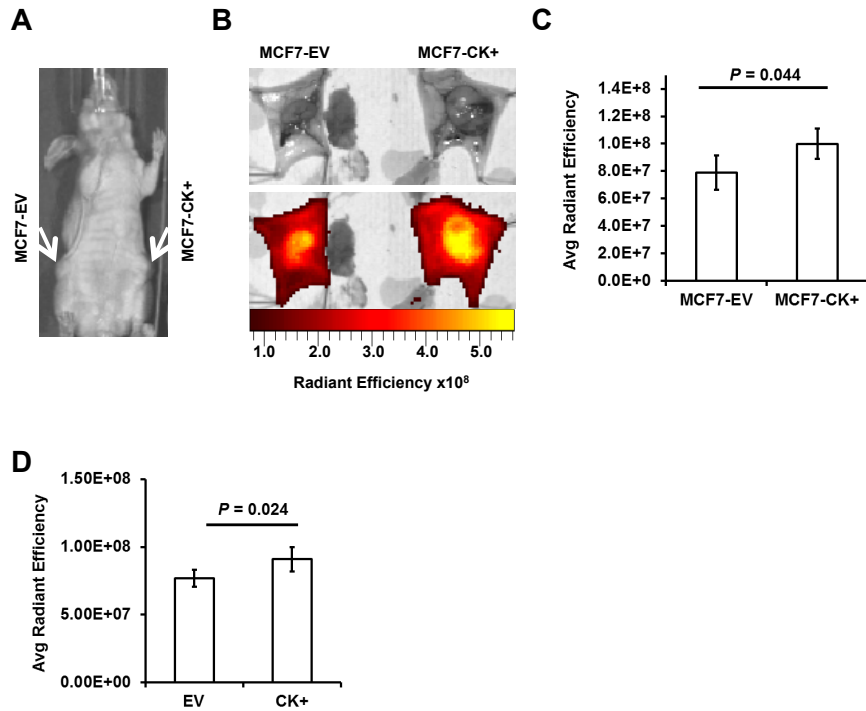


Figure 5.9. NIRF imaging for JAS239 accumulation can detect genetic overexpression of ChoK α . (A) Athymic nude mice were inoculated with MCF7-EV (left mammary fat pad) and MCF7-CK+ (right mammary fat pad) cells. (B) Tumor-bearing fat pads were surgically exposed and imaged for NIRF 24 h following JAS239 injection in an ethanol formulation. (C) Quantified Average Radiant Efficiency [p/sec/cm²/sr]/[μ W/cm²] of resected fat pads for each of 7 animals reveals enhanced JAS239 retention in ChoK α -overexpressing tumors. (D) Quantified Average Radiant Efficiency of fat pads bearing MCF7-EV or MCF7-CK+ tumors show increased fluorescence 90 min after injection of 20 nmol in a Tween-80/Tris buffer. Values represent \pm SEM for 8 animals.

The effect of genetic overexpression of ChoK α on JAS239 retention was studied in a cohort of mice bearing orthotopic MCF7-EV and MCF7-CK+ tumors (Fig. 5.9A).

Optical imaging of the surgically-exposed mammary fat pad revealed distinct JAS239-associated NIRF within the confines of the orthotopic tumor, and the tumor margins could clearly be delineated (Fig. 5.9B). JAS239 accumulation 24 hours post-injection (in ethanol/saline) was elevated 38 ± 17 % (Paired Student's t-test: $P = 0.044$) in the MCF7-CK+ tumors compared to the contralateral MCF7 EV tumors (Fig. 5.9C). JAS239 in

Tween-80/Tris buffer imaged 90 minutes post-injection yielded a similar difference in

NIRF between exposed MCF7-EV and MCF7-CK+ fat pad tumors (Paired Student's t-test: $P = 0.024$), although only a $19 \pm 8\%$ increase in radiance was observed at this 90-minute time point (Fig. 5.9D).

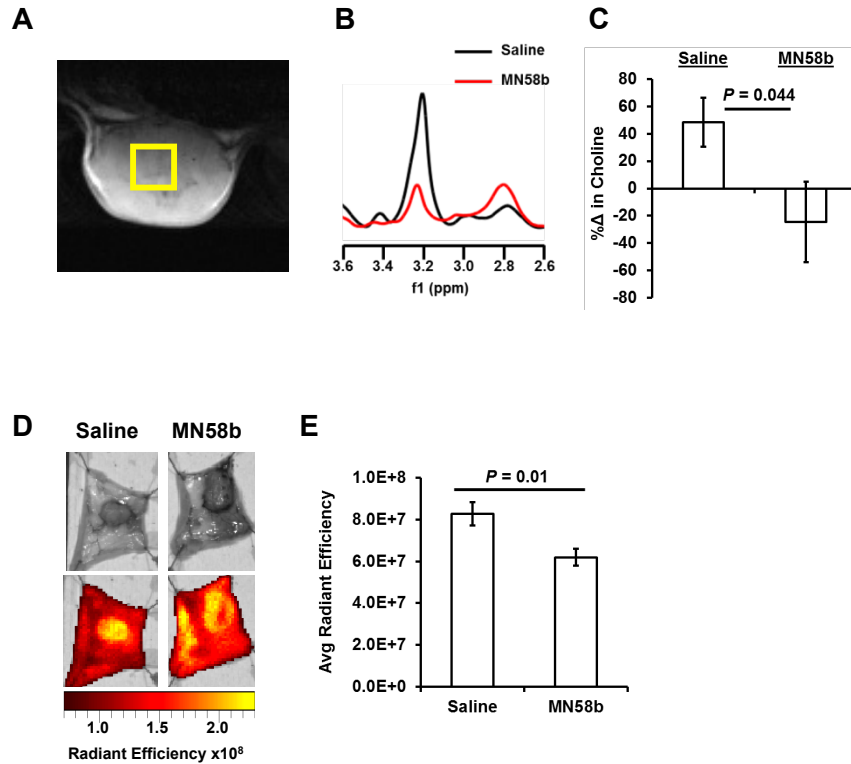


Figure 5.10. NIRF imaging for JAS239 accumulation can detect pharmacologic inhibition of ChoK α . (A) Representative T_2 -weighted MRI image of a 4175-Luc+ tumor used to plan $3 \times 3 \times 3$ mm³ voxel placement. (B) MRS spectra expanded for investigation of the choline-containing region to compare control (black) and MN58b-treated (red) tumors. (C) MN58b-treatment prevents the increase in intratumoral tCho (3.2 ppm) observed between scans in the control cohort. (D) NIRF of the exposed saline (left) or MN58b-treated (right) tumors (E) was quantified [$\text{p/sec/cm}^2/\text{sr}$]/[$\mu\text{W/cm}^2$] and prior ChoK α inhibition diminishes JAS239 retention significantly. For saline and MN58b groups, $n = 5$. Values are reported as \pm SEM. Acquisition and processing of MR data was done in collaboration with Manoj Kumar of the Poptani group.

MN58b treatment in 4175-Luc+ tumors was then used as a model for pharmacologic inhibition of ChoK α . *In vivo* MRS (Fig. 5.10A) was used to verify that MN58b caused a 25 ± 30 % reduction in tCho after a 5-day dose regimen at 2 mg/kg/day i.p. (Fig. 5.10B). The change in tCho in response to MN58b was significantly lower ($P = 0.044$) than that of the control-treated animals, which actually experienced an increase (48 ± 18 %) in the tCho resonance (Fig. 5.10C). Animals in this MRS-validated cohort then underwent JAS239 injection and follow-up NIRF imaging (Fig. 5.10D) which revealed a reduced accumulation ($P = 0.01$) of the ChoK α -targeted optical imaging probe in tumors treated with the ChoK α inhibitor MN58b (Fig. 5.10E).

JAS239 was tested for its ability to act as a therapeutic and inhibit tumor growth. Three days after orthotopic inoculation of athymic nude mice with 4175-Luc+ tumors, a 5-day intraperitoneal (i.p.) dose treatment regimen was started. Tumor volume measurements began 12 days after inoculation. Both 2 mg/kg/day MN58b-treatment ($P = 0.008$) and 4 mg/kg/day JAS239-treatment ($P = 0.009$) resulted in animals bearing significantly smaller tumors on average compared to control animals (Fig. 5.11) at this time. One week later the control cohort's tumors averaged 298 ± 40 μ L, which were significantly larger than both MN58b-treated tumors (135 ± 16 μ L, $P = 0.010$) and JAS239-treated tumors (132 ± 41 μ L, $P = 0.012$). Even by day 26, both the MN58b (372 ± 35 μ L) and JAS239 (368 ± 77 μ L) cohorts had significantly smaller ($P = 0.021$ and 0.022 , respectively) tumors than the vehicle-treated group (677 ± 96 μ L).

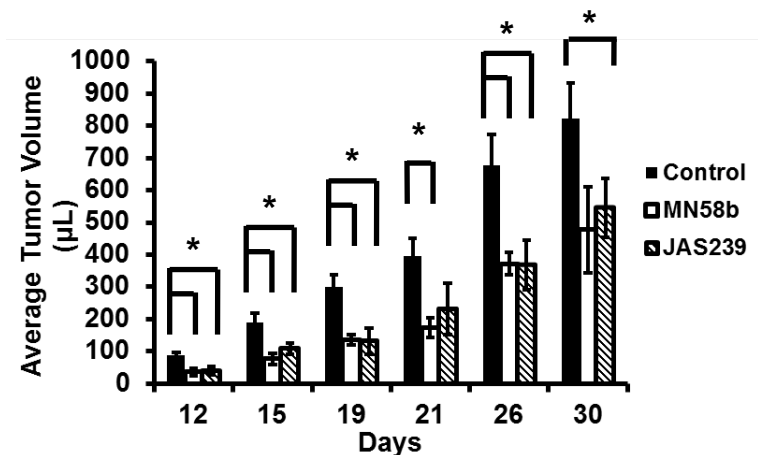


Figure 5.11. MN58b and JAS239 slow breast tumor growth. Treatment for 5 consecutive days with 2 mg/kg of MN58b (n = 4) or 4 mg/kg of JAS239 (n = 5) significantly reduced the growth rate of orthotopically-implanted 4175-Luc+ tumors, compared to control animals (n = 4).

To study the therapeutic effectiveness of JAS239 in later-stage tumors, tCho was measured as a pharmacodynamic marker of ChoK α inhibition. MDA-MB-231 xenografts were used because prior characterization of MN58b in this model (Al-Saffar *et al.*, 2006) allowed for the confident use of this inhibitor as a positive control. T_2 -weighted images were acquired and used for MRS voxel placement (Fig. 5.12A-C) in each tumor. Following baseline scans, mice were divided into treatment cohorts and injected daily for 5 days with either vehicle control (Fig. 5.12D), 2 mg/kg MN58b (Fig. 5.12E), or 4 mg/kg JAS239 (Fig. 5.12F). Post-treatment ^1H MR spectra were acquired and tCho was measured in the control vehicle-treated group to increase by $63 \pm 27\%$ during the treatment course (Fig. 5.12D&G). Significant reductions in tCho levels compared to control were measured in response to MN58b ($-25 \pm 13\%$, $P = 0.006$, Fig. 5.12E&G) and JAS239 ($-64 \pm 25\%$, $P = 0.004$, Fig. 5.12F&G).

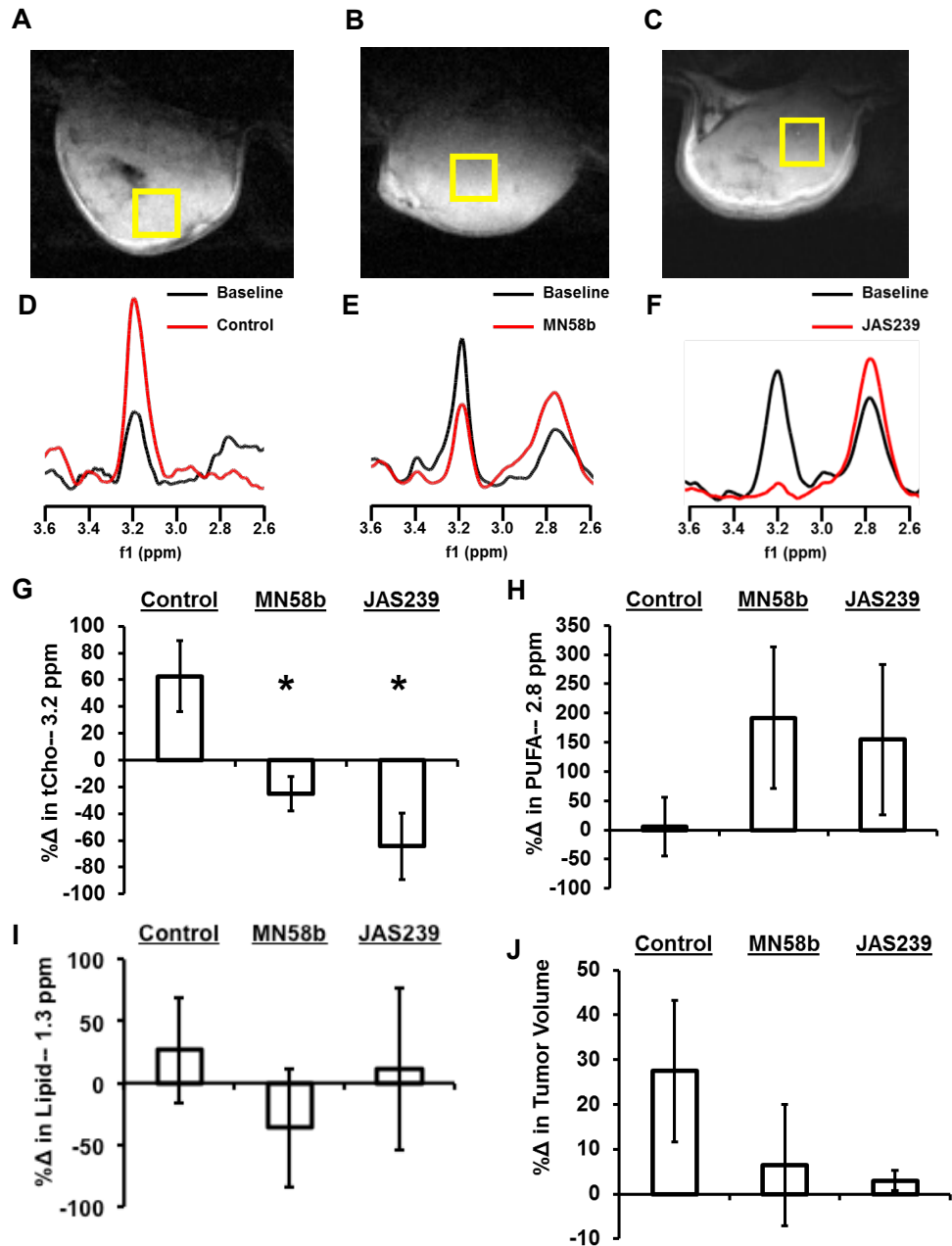


Figure 5.12. Evaluation of MN58b and JAS239-treated tumors using MRS. (A-C) T_2 -weighted images of MDA-MB-231 tumors acquired for tumor volume measurement and placement of $3 \times 3 \times 3$ mm³ voxels. (D-F) MR spectra acquired within the selected voxels before and after treatment. (G) Change in tCho (3.2 ppm) within MDA-MB-231 tumors was measured to show progressive tCho increase in (A, D) saline-treated animals (n = 5). Reductions in tCho in response to 5 days of (B, E) 2 mg/kg MN58b (n = 4) or (C, F) 4 mg/kg JAS239 (n = 3) are observed. (H) PUFA resonances at 2.8 ppm are unchanged in the control cohort and increase in response to both MN58b and JAS239, but not significantly. (I) Lipid resonances at 1.3 ppm are unchanged. (J) Vehicle-treated tumors grew during the treatment regimen, whereas both MN58b and JAS239 treated cohorts were unchanged. Values reported as \pm SEM, * indicates $P < 0.05$ compared to control group. MR data was collected in collaboration with Manoj Kumar of the Poptani group.

A trend of an elevated polyunsaturated fatty acid (PUFA) resonance, a measure of tumor apoptosis, after MN58b ($190 \pm 120 \%$, $P = 0.12$) and JAS239 ($150 \pm 130 \%$, $P = 0.21$) treatment was observed, although these values were not statistically significant compared to control ($5.79 \pm 50 \%$) due to high intra-cohort variability (Fig. 5.12H). High variability was also observed in the lipid peak at 1.3 ppm but no significant increases in lipid were found (Fig. 5.12I). MRI-based volume measurements indicated that vehicle-treated tumors grew in volume by $27 \pm 16 \%$ during the week between the pre-treatment and post-treatment MRS scans (Paired t-test: $P = 0.009$), whereas MN58b-treated and JAS239-treated tumors grew only $6.5 \pm 14\%$ and $3.0 \pm 2.3 \%$ during the same time span (Fig. 5.12J). These volume increases were not statistically significant in MN58b-treated (Paired t-test: $P = 0.44$) or JAS239-treated (Paired t-test: $P = 0.36$) tumors.

Figure 5.13 depicts a summary of the toxicological assessment of the MDA-MB-231-bearing mice from this experiment, revealing no significant effects except for an elevation of blood urea nitrogen in the MN58b-treated animals ($29.5 \pm 0.5 \text{ mg/dL}$) compared to control animals ($20.0 \pm 3.0 \text{ mg/dL}$) ($P = 0.012$). Tumors from these animals were harvested for histological assessment immediately after follow-up MRI/MRS scanning. Evaluation of H&E slides (Fig. 5.14, left column) prepared from tumor slices of the untreated cohort measured an average cell density of $8,800 \pm 200 \text{ cells/mm}^2$. Both MN58b and JAS239 caused significant reduction in cell density compared to control, with values of $5900 \pm 800 \text{ cells/mm}^2$ ($P = 0.007$) and $5600 \pm 800 \text{ cells/mm}^2$ ($P = 0.01$), respectively (Fig. 5.15A). MN58b ($55 \pm 5 \%$, $P = 0.026$) and JAS239 ($46 \pm 11 \%$, $P = 0.034$) treatment significantly reduced the percentage of Ki67-positive cells compared to the high percentage of proliferative cells ($78 \pm 1 \%$) in the vehicle treated group (Fig.

5.14, middle column). Consistent with reduced cell number and proliferation, higher Caspase-3 levels (Fig. 5.15, right column) were detected in MN58b ($72 \pm 6 \%$, $P = 0.016$) and JAS239 ($76 \pm 6 \%$, $P = 0.015$) treated tumors than in control tumors ($21 \pm 8 \%$). Ki67-positive nuclei (Fig. 5.15B) and Caspase-3-positive cells (Fig. 5.15C) were quantified in different regions of each tumor and averaged among treatment cohorts.

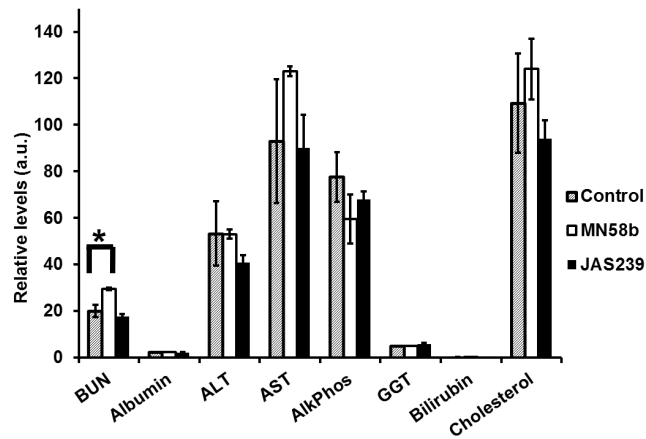


Figure 5.13. Renal damage associated with MN58b is not seen in JAS239-treated mice. A profile of enzyme function and blood metabolite levels reveals MN58b animals had elevated blood urea nitrogen (BUN) relative to control animals. No signs of elevated albumin, alanine transaminase (ALT), aspartate transaminase (AST), alkaline phosphatase (AlkPhos), gamma-glutamyl transferase (GGT), bilirubin, or cholesterol changes were found in response to MN58b or JAS239 treatment. Three animals were included per cohort and values represent \pm SEM. * indicates $P < 0.05$.

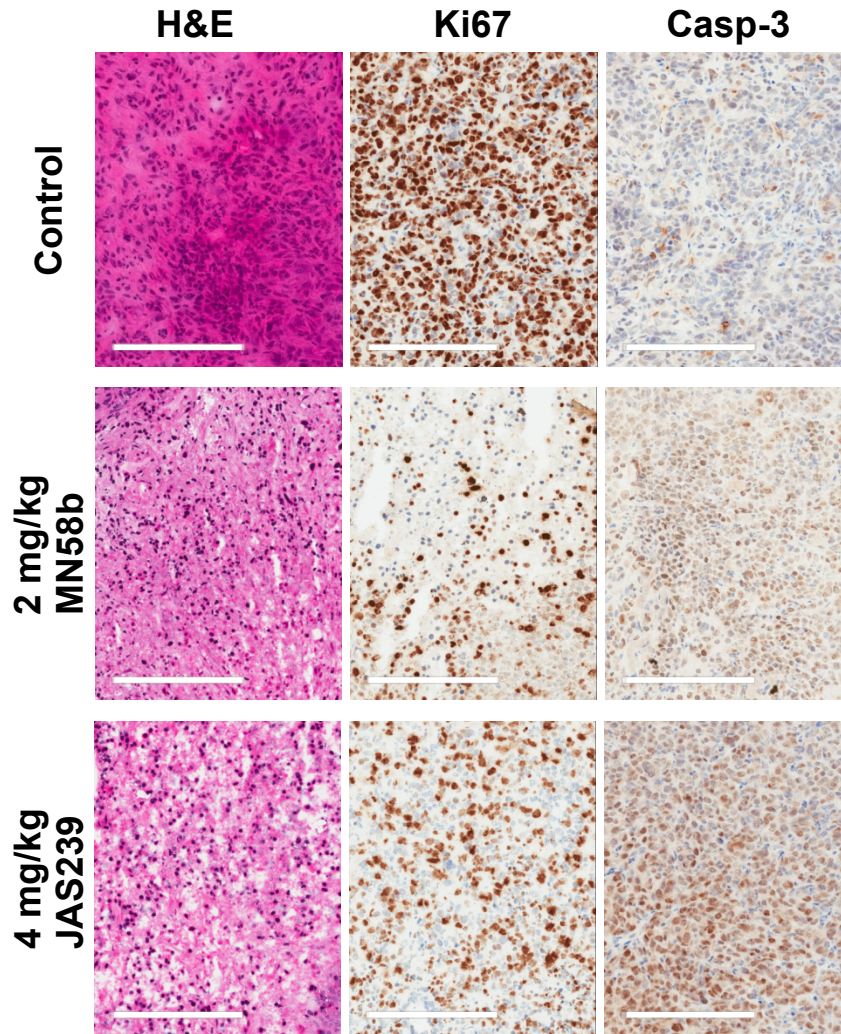


Figure 5.14. Histological assessment of tumors reveals reduced cell density, lower proliferation, and elevated apoptosis in response to ChoK α inhibitors. H&E staining (left column) of MDA-MB-231 tumor xenografts reveals lower cell density in MN58b (middle row) and JAS239 (bottom row) treated tumors compared to vehicle-treated tumors (top row). Reduced Ki67-positive nuclei (middle column) and heightened Caspase-3 positive cells (right column) are also found in MN58b and JAS239 treated tumors. Scale bars represent 200 μ m. Preparation and digital scanning of the slides were performed by members of the CHOP Pathology Core facility under direction of Daniel Martinez.

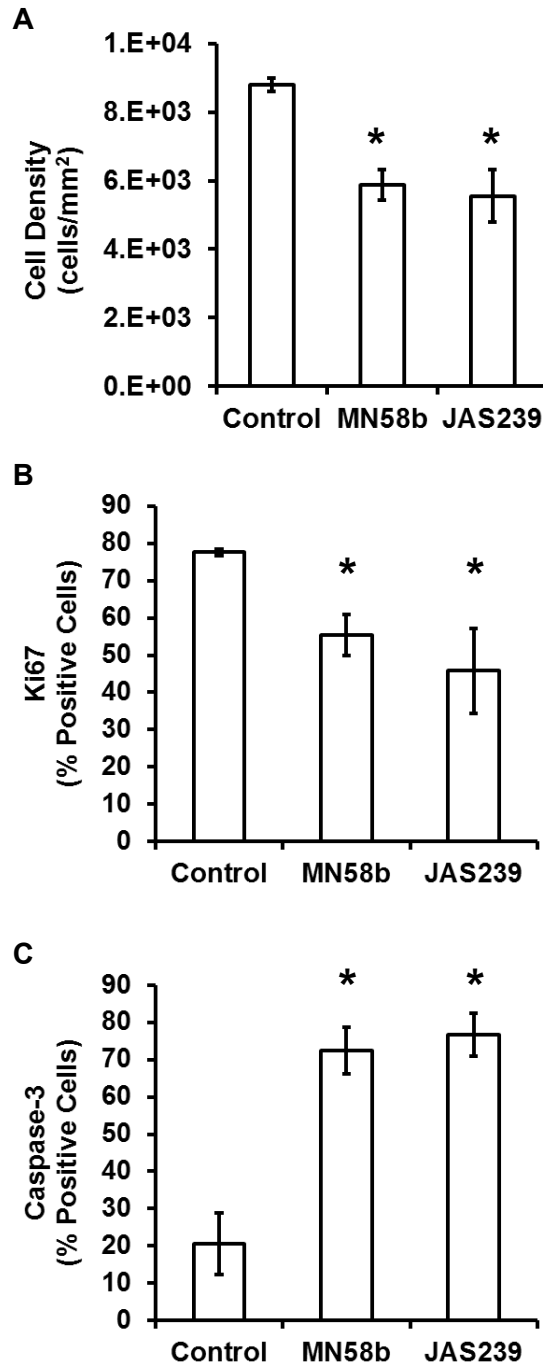


Figure 5.15. Histological assessment of ChoK α -inhibited MDA-MB-231 tumor sections reveals apoptosis and overall reduction in viable cells. (A) Significant reduction in cell density is observed in both MN58b and JAS239 treated tumors relative to control. (B) Lower Ki67 positivity is found in MN58b and JAS239 treated tumors, indicative of a reduction in proliferative cells. (C) Elevated Caspase-3 in MN58b and JAS239 treated tumors relative to control indicate apoptosis in response to ChoK inhibition. * indicates $P < 0.05$.

5.3 Discussion

In Chapter 4, we reported the development of JAS239, a ChoK α inhibitor whose inherent NIRF makes it possible to detect its interaction with cancer cells. While *in vitro* data can often be promising, translation to *in vivo* models is crucial for a true assessment of the feasibility of this technology. In this Chapter, we investigate further the utility of JAS239 to detect ChoK α expression in murine models of breast cancer. JAS239 is a cationic small molecule and this resulted in an unsurprising accumulation and clearance through the kidneys. An initial flush was observed in the liver where ChoK α is naturally abundant (Brophy and Vance, 1976) but this is also the site of first-pass metabolism. While most metabolic modifications of the probe would be expected to alter the optical properties (Shen *et al.*, 2013) and make JAS239 undetectable in the NIRF range, there is much work related to characterizing the metabolism and clearance of this probe that will be the focus of future studies.

With the guidance of bioluminescence imaging in the 4175-Luc⁺ tumor xenografts, intratumoral JAS239 NIRF was detectable but eventually drowned out by renal excretion of the intact probe. Despite its clinical utilization as a NIRF contrast agent (Marshall *et al.*, 2010), even ICG required cloaking of the internal organs to achieve optimal *in vivo* tumor contrast. By moving tumors to the shoulders away from the kidneys, intratumoral JAS239 accumulation could similarly be visualized by cloaking the internal organs. We prepared hydro-JAS239 as an activatable form of JAS239 in an effort to minimize the interference from non-specific signal, but chemical modification of JAS239 to its non-polar hydrocyanine form did not improve its tumor specificity, biodistribution, or

bioavailability. A NIRF intraoperative imaging system was capable of discriminating tumor from normal tissue, but only when isolated from the intraperitoneal organs. These results do not disparage the translational utility of JAS239, as clinical optical imaging is not a whole-body but rather a tissue or region-specific measurement.

While the biodistribution studies show JAS239 can be detected in other major organs, the tumor/muscle ratio suggests that measurements confined to the breast region are robust enough to distinguish malignant from normal tissue. This was verified when the tumor-bearing mammary fat pads of JAS239-injected mice were surgically exposed and imaged for NIRF. JAS239 accumulation was found to be a reliable identifier of ChoK α overexpressing tumors in matched MCF7-EV and CK+ tumors. As an analysis of this imaging strategy's utility in validating a previously studied ChoK α inhibitor, we treated tumor-bearing mice with MN58b or saline control. MRS evaluation before and after therapy was used as a benchmark to verify MN58b's efficacy *in vivo*. While MRS required 1 hour per mouse—including set-up, anesthesia, shimming, and scanning—before and after therapy, the optical imaging technique could be performed on up to 5 mice at a time and required a much less cumbersome procedure involving one i.v. injection and follow-up surgery 24 hours later. The parallel use of both techniques told a more complete story: that MN58b bound ChoK α (blocking JAS239 accumulation) and attenuated flux through the Kennedy pathway (lowering tCho signals). It is important to note that a greater difference in measured biomarker was observed between treated versus untreated tumors using MRS measurement, although lower variability in the optical imaging method resulted in stronger statistical confidence.

To explore JAS239's therapeutic properties, its ability to inhibit tumor growth and attenuate tCho in murine breast xenografts was determined. In orthotopic MDA-MB-231 breast tumors, JAS239 significantly reduced the tumor growth rate to the same degree as MN58b. When dosed at 4 mg/kg, MN58b showed some toxicity despite a previous report (Al-Saffar *et al.*, 2006) that this dose was used to lower PC levels in nude mice. No observable or measurable toxicity was found using 4 mg/kg JAS239, and 2 mg/kg MN58b appeared tolerable but post-mortem toxicological studies revealed evidence of elevated blood urea nitrogen indicative of impaired renal excretion in these mice. Both of these drugs were capable of reducing intratumoral tCho and increasing apoptosis-associated PUFAs (Hakumäki *et al.*, 1999). In control tumors, rising tCho was an indicator of progression during the week between pre and post-therapy scanning. Tumor status was also evaluated by histological methods that identified high cell number and proliferative index. Both ChoK inhibitors effectively reduced the cell number by reducing proliferation and inducing widespread apoptosis.

Expanding interest in ChoK α inhibitors for cancer therapy has raised the need for rapid and reliable methods to validate these therapies *in vivo*. There have been concerns expressed with the reliability of RECIST measurement alone as a marker of treatment responsiveness (Jaffe, 2006). An addendum to the first clinical trial of TCD-717 in clinic was made to include MRS evaluation of tCho levels as a supplemental response indicator (Clinical Trials identifier: NCT01215864). MRS is the current gold standard for choline measurement *in vivo* due to its specificity, non-invasive acquisition, and feasible inclusion following MRI for RECIST measurements. To understand the degree to which choline metabolites represent a real biomarker of tumor progression and response to

therapy, it would be beneficial to design secondary methods of identifying the oncogenes that contribute to heightened choline in cancerous tissue. ChoK α has been reported throughout the literature as a key contributor to aberrant choline metabolism (Hernández-Alcoceba *et al.*, 1997). Its regulative role in cell growth and division directly links the Kennedy pathway to cancer malignancy (Ramírez de Molina, Báñez-Coronel, *et al.*, 2004). To measure ChoK α in whole tumors would provide an estimate of histological tumor grade, an indicator of tumor vs. normal tissue, and a secondary validation method for evaluating ChoK α inhibitors in the clinic.

Chapter 6

Choline Kinase Inhibition as a Glioma Treatment Strategy

6.1 Introduction

Glioblastoma (GBM), the most common primary brain malignancy in adults, is an aggressive and locally invasive tumor. Despite advances in surgery, radiation, and chemotherapy, overall survival of patients affected by GBM has only marginally increased in recent decades from 6 to 14 months post-diagnosis (Candolfi *et al.*, 2007). This is partly due to a lack of effective therapeutic options and limited availability of robust and sensitive methods to assess therapeutic response. As survival with GBM is limited, it is critical to determine the efficacy of therapy early in treatment. An increased understanding of the molecular mechanisms underlying oncogenesis has led contemporary drug discovery programs to be aimed predominantly at signal transduction pathways and molecules that drive cancer initiation and progression (JB Gibbs, 2000). Elevated ChoK α activity has been associated with enhanced synthesis of PC in many cancer cell types and has been proposed as a potential target for anticancer therapy (Glunde *et al.*, 2011). ChoK α catalyzes the phosphorylation of choline, consuming ATP in the presence of Mg²⁺, yielding PC in a process mostly independent of the rate of net PtdCho biosynthesis (Kennedy, 1957; Aoyama *et al.*, 2004). Several agents such as growth factors, chemical carcinogens and oncogenes can induce ChoK α activation in malignant cells, leading to an accumulation of PC (Jiménez *et al.*, 1995; Ramírez de Molina, Penalva, *et al.*, 2002; Aoyama *et al.*, 2007).

A novel molecular therapeutic strategy focused on ChoK α inhibition has recently been developed, resulting in the characterization of a group of compounds with inhibitory activity against ChoK α (Hernández-Alcoceba *et al.*, 1997; Lacal, 2001; Ramírez de Molina, Rodríguez-González, *et al.*, 2004). The inhibition of ChoK α using small molecule inhibitors such as MN58b is a promising new treatment strategy against solid tumors (Hernández-Alcoceba *et al.*, 1999). MN58b is an anticancer drug previously reported to inhibit ChoK α activity resulting in attenuated PC levels, reduced proliferation of cancer cells *in vitro*, and growth delay of human tumor xenografts (Rodríguez-González *et al.*, 2003; Ramírez de Molina, Báñez-Coronel, *et al.*, 2004). ChoK α has recently been discovered to be activated at the plasma membrane by EGFR in breast cancer cells (Miyake and Parsons, 2012). Although the existence of a similar mechanism in brain cells is unknown, EGFR mutations are common oncogenic drivers in GBM; one of the most common mutations, EGFRviii, is constitutively active and unresponsive to ligands (Gan *et al.*, 2013). There is a strong need to obtain precise surrogate biomarkers to effectively evaluate therapeutic response in GBM.

¹H MRS provides a method of measuring changes in choline-containing tumor metabolites to serve as a pharmacodynamic biomarker of ChoK α inhibition and therapeutic response. Al-Saffar *et al.* have reported the efficacy of MN58b on subcutaneously implanted colon and breast cancer models (Al-Saffar *et al.*, 2006), however, there are no reports of MRS studies of ChoK α inhibitor-treated brain tumor tissue. In this work, the sensitivity of a brain cancer cell panel to ChoK α inhibition was measured by radiotracing and viability studies. We next carried out an exploration of ChoK α activity in a model of EGFRviii-mutated rat GBM cells, and studied the effect of

epidermal growth factor (EGF) on ChoK α activation and inhibition. Following this, rats bearing intracranial GBM tumors were treated with i.p injection of MN58b for 5 consecutive days and the resected tumors were assessed using ^1H MRS. The feasibility of JAS239-assisted NIRF detection of ChoK α was tested in pilot studies. The goal of the present study was to monitor changes in choline-containing metabolites in an intracranial model of rat glioma in response to ChoK α inhibition.

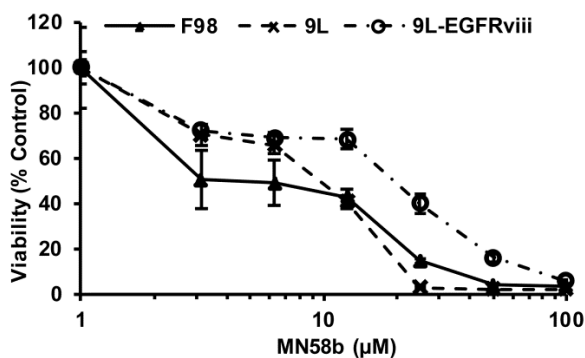


Figure 6.1. MTT assay demonstrating inhibition of cellular viability of F98, 9L and 9L-EGFRviii cell lines with MN58b. 24 hr MN58b exposure significantly reduces the viability of the F98, 9L and 9L-EGFRviii cells in a dose dependent manner. The data was normalized to untreated control cells and represents the average \pm SEM of 3 separate experiments performed in quadruplicate. Assay run by Sona Saksena of the Delikatny Lab under my guidance.

6.2 Results

MN58b was screened for its ability to inhibit the viability of a panel of rat brain tumor cell lines using the MTT assay. MN58b treatment significantly reduced the viability of the F98, 9L and 9L-EGFRviii cells in a dose dependent manner, with GI₅₀s of 20 ± 3 μM , 9 ± 3 μM and 47 ± 2 μM , respectively (Fig. 6.1). The phosphorylation of ^{14}C -labeled Cho ($R_f = 0.07$) was measured using TLC and autoradiography in cell extracts.

^{14}C -PC ($R_f = 0.14$) production in the F98, 9L, and 9L-EGFRviii cells was quantified, plotted, and fitted to determine IC_{50} s of $2.6 \pm 0.7 \mu\text{M}$, $1.8 \pm 0.5 \mu\text{M}$, and $1.8 \pm 0.3 \mu\text{M}$, respectively (Fig. 6.2A,B). No statistical difference in ChoK α inhibition was found between these groups.

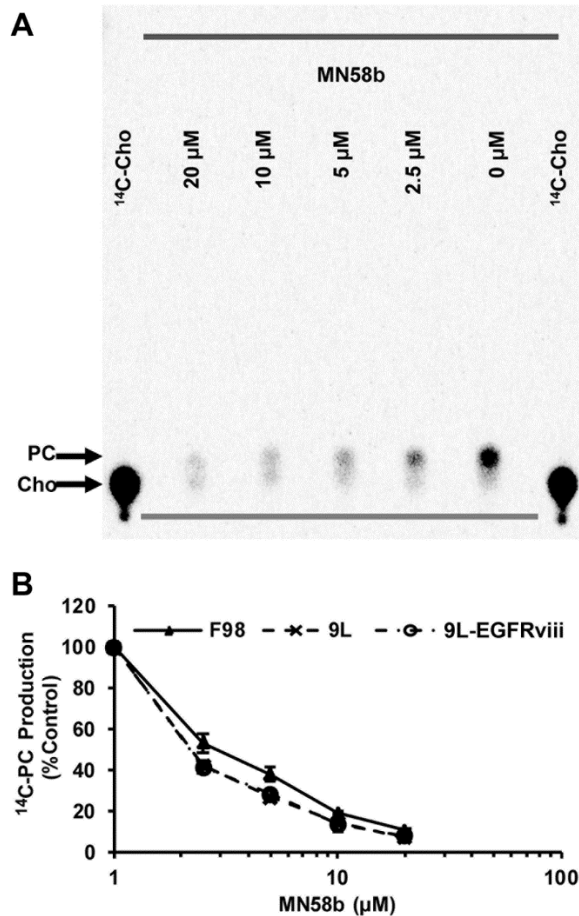


Figure 6.2. Effect of MN58b on ChoK activity in tumor cells. Autoradiography of TLC-separated ^{14}C -choline containing metabolites (A) allows for the quantification of ^{14}C -PC and demonstrates a dose-dependent reduction of choline phosphorylation in response to MN58b treatment. The graph (B) shows a dose dependent reduction of ChoK activity in the F98, 9L and 9L-EGFRviii cell lines. Error bars represent \pm SEM of 3 separate experiments.

The addition of EGF to serum-starved 9L and 9L-EGFRviii cells had no impact on cell growth (Fig. 6.3A) or ChoK α activity (Fig. 6.3B). Addition of 20 μ M MN58b dramatically reduced viability and 14 C-PC production, both in serum-starved and EGF-stimulated conditions (Figure 6.3A,B). Constitutive EGFR downstream signaling due to EGFRviii overexpression did not result in any perceivable change in ChoK α activity, and these cells were less viable than wild-type 9L cells suggesting they are more serum-sensitive.

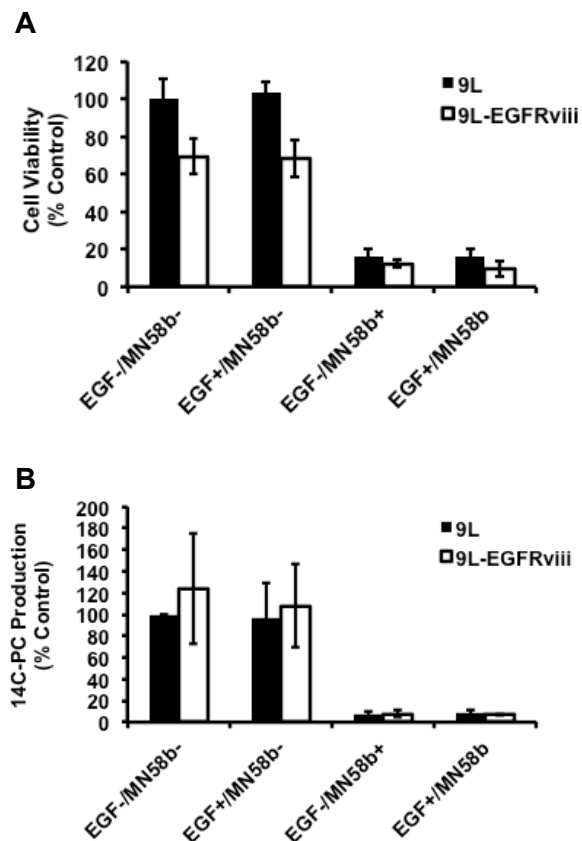


Figure 6.3. 9L gliosarcoma cell response to EGF stimulation and MN58b inhibition. (A) MTT assays show no effect of EGF in 9L or 9L-EGFRviii cells following serum starvation. MN58b at 10 μ M significantly reduces viability in each condition. (B) MN58b effectively inhibits ChoK activity in both cell lines in the presence or absence of EGF, which has no effect on ChoK activity. Error bars represent \pm SEM of 3 separate experiments.

Since ^{14}C -radiotracing demonstrated similar treatment response from all three cell lines, we chose F98 cells for further study because they most closely resemble human GBM (Bryant *et al.*, 2008). Tumors derived from the 9L cell line are a gliosarcoma and do not exhibit the necrotic areas seen in GBM (Huszthy *et al.*, 2012). 9L-EGFRviii is similar to a GBM but is not as well characterized compared to the F98 tumor model (Kapoor *et al.*, 2007). Cellular extracts were prepared from F98 cells treated with 0, 10 or 20 μM MN58b and analyzed by NMR to determine changes in PC and GPC levels (Fig. 6.4A). Analysis of the choline-containing peaks showed lower PC levels in response to MN58b compared to saline-treated cells (Fig. 6.4B). We observed significantly reduced PC concentrations in cells treated with either 10 μM MN58b ($5.9 \pm 0.7 \text{ nmol}/10^7 \text{ cells}$) or 20 μM MN58b ($7 \pm 4 \text{ nmol}/10^7 \text{ cells}$, $P = 0.049$) compared to saline-treated cells ($19 \pm 2 \text{ nmol}/10^7 \text{ cells}$, $P = 0.004$). We also observed higher GPC concentration in cells after 10 μM MN58b treatment ($6.6 \pm 2.0 \text{ nmol}/10^7 \text{ cells}$, $P = 0.911$) and a further increase after 20 μM MN58b treatment ($12 \pm 8 \text{ nmol}/10^7 \text{ cells}$, $P = 0.532$) compared to saline-treated cells ($6 \pm 2 \text{ nmol}/10^7 \text{ cells}$) but this difference was not statistically significant (Fig. 6.4B). Inhibition of the anabolic pathway of choline metabolism has been reported to increase GPC at the expense of PC (Aboagye and Bhujwala, 1999). The PC/GPC ratio was thus calculated for each treatment group, and both 10 μM (0.9 ± 0.4 , $P = 0.012$), and 20 μM MN58b-treated cells (0.57 ± 0.08 , $P = 0.007$) demonstrated significantly lower PC/GPC ratios as compared to saline-treated cells (3.0 ± 0.6) (Fig. 6.4C).

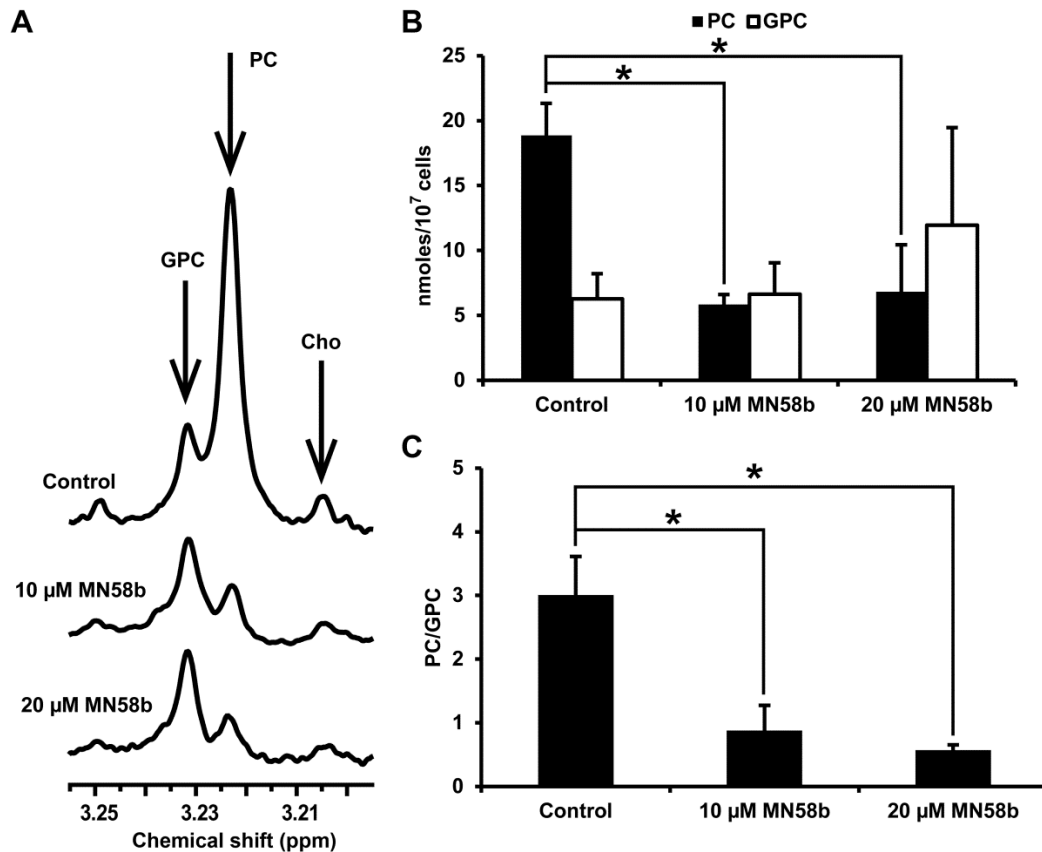


Figure 6.4. *In vitro* NMR of F98 cell extracts. (A) Untreated cells display high levels of PC (3.22 ppm) and low levels of GPC (3.23 ppm) (top spectrum); 10 μ M MN58b reduces the PC resonance relative to GPC (middle spectrum) and 20 μ M MN58b further reduces this ratio (bottom spectrum). (B) A bar graph showing the quantitation of PC and GPC from untreated, 10 and 20 μ M MN58b-treated cells (C). The PC/GPC ratio demonstrates differences between untreated, 10 and 20 μ M MN58b-treated cells. Error bars represent \pm SEM of 3 separate experiments. * indicates $P < 0.05$. Cells were treated and harvested by Ranjit Ittyerah in the Poptani Lab and spectra were analyzed with assistance from Manoj Kumar.

High-resolution ^1H NMR of F98 tumor extracts also demonstrated changes in PC and GPC values in MN58b-treated tumors (Fig. 6.5A), following the trends observed in cultured cells. Significantly lower PC levels were observed in MN58b-treated tumors (0.33 ± 0.06 nmol/mg, $P = 0.019$) compared to saline-treated tumors (0.59 ± 0.06 nmol/mg). The saline-treated tumors demonstrated significantly higher PC ($P = 0.030$) than normal brain (0.30 ± 0.09 nmol/mg). Significantly higher GPC was also observed in MN58b-treated tumors (0.44 ± 0.05 nmol/mg, $P = 0.009$) compared to normal brain (0.23 ± 0.05 nmol/mg). The GPC in saline-treated tumors (0.40 ± 0.03 nmol/mg, $P = 0.015$) was significantly higher than contralateral normal brain. However, the GPC concentration between saline-treated and MN58b-treated tumor was not significantly different ($P = 0.593$). When the PC/GPC ratios were computed, a significantly lower PC/GPC ratio was observed in MN58b-treated (0.76 ± 0.09 , $P = 0.05$) than saline-treated tumors (1.5 ± 0.3) (Fig. 6.5B). However, there was no significant difference in the PC/GPC ratio between MN58b-treated ($P = 0.124$) and normal brain (1.4 ± 0.4) (Fig. 6.5C).

In a pilot study, injection of 20 nmoles JAS239 i.v. into a mouse bearing a 9L-derived xenograft led to levels detectable by NIRF optical imaging (Figure 6.6A). Because a subcutaneous, rather than orthotopic, xenograft was used, this model does not accurately account for the major obstacle of the blood-brain barrier. A different mouse bearing an MDA-MB-231 breast tumor was injected with 4 mg/kg JAS239 in 1% ethanol for 5 consecutive days as part of a separate study. The biodistribution data from this bulk dosage of JAS239 shows no evidence of JAS239 in brain tissue (Fig. 6.6B).

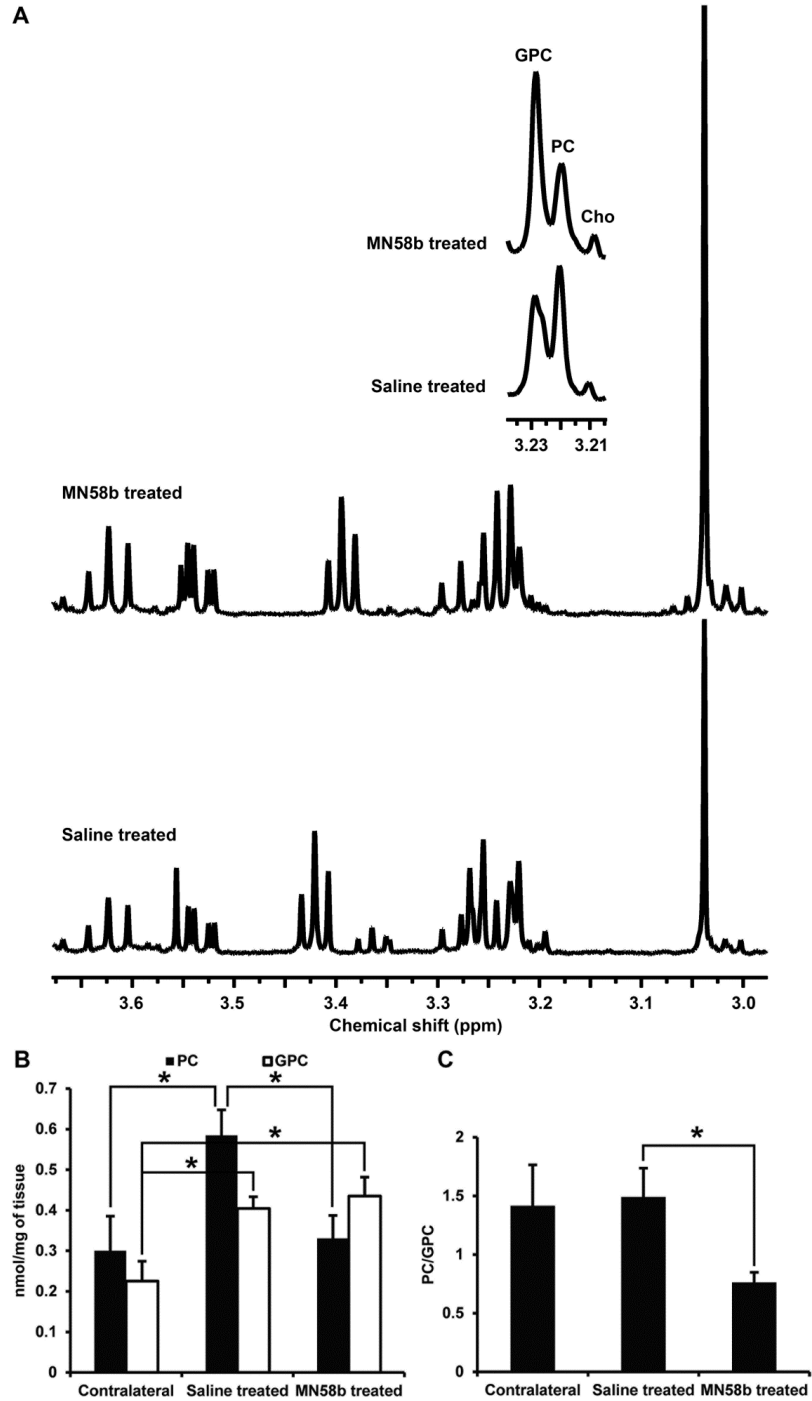


Figure 6.5. Ex vivo NMR of glioma extracts. (A) Representative *in vitro* ^1H NMR spectra from perchloric acid extracts of saline-treated (bottom) and MN58b-treated F98 tumors (top). The zoomed region (inset) is the spectral region from the choline-containing metabolites. Bar graph (B) demonstrates changes in PC and GPC levels from contralateral normal tissue, saline-treated tumors and MN58b-treated tumors. Bar graph (C) demonstrates the PC/GPC ratio in the 3 groups. Asterisk (*) represents significant differences with a P -value of < 0.05 . Error bars represent \pm SEM. The Poptani group handled all animal work for this experiment.

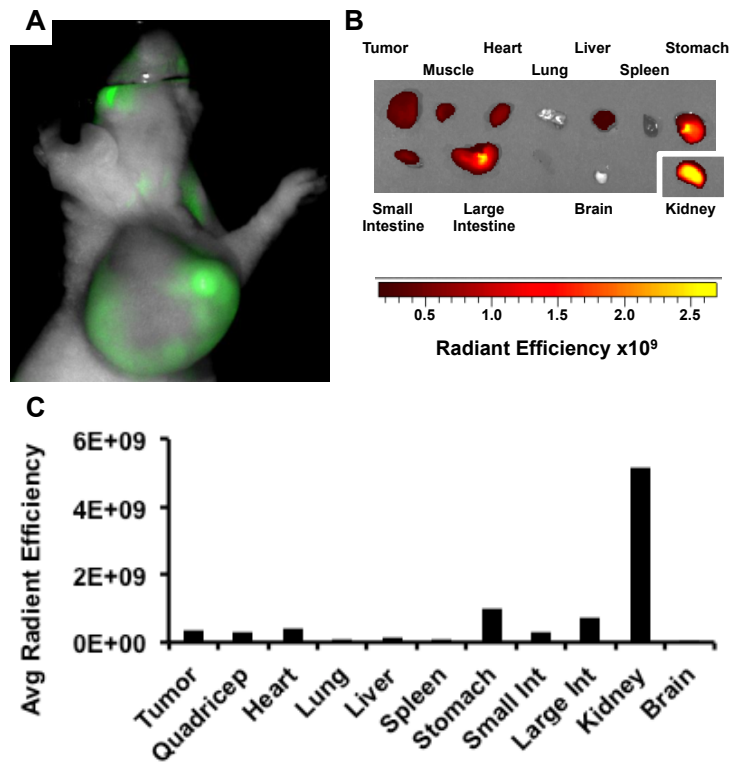


Figure 6.6. JAS239 in glioma models. (A) An athymic nude mouse with a 9L glioma xenograft was injected with 20 nmol JAS239 by Julie Czupryna of the Small Animal Imaging Core. NIR optical images were acquired by Sona Saksena of the Delikatny Lab using a LiCOR Pearl 4 hr after injection (Ex 710 nm, Em 800 nm). (B) A separate mouse with an MDA-MB-231 tumor was injected for 5 consecutive days with 4 mg/kg JAS239 and the organs were separated for NIRF imaging in an IVIS Spectrum. (C) No JAS239 accumulation can be detected in the brain.

6.3 Discussion

In this section, the effect of the choline kinase inhibitor MN58b on choline metabolism was examined in a glioma model. High ChoK α activity was found in cultured tumor cells and this corresponded with elevated PC levels found in cells and in tumor tissue extracts, confirming that PC is a viable biomarker for ChoK α -driven oncogenic transformation. The significant decrease in cellular ChoK α activity after treatment with MN58b indicates that inhibition of ChoK α may be an effective adjuvant in the treatment of gliomas.

Three different glioma cell lines were studied *in vitro* and their sensitivity to MN58b was observed via MTT and ChoK α assays. We observed the phosphorylation of ¹⁴C-labeled choline using a TLC-based ChoK α assay and found inhibition of ChoK α activity in a dose dependent manner. While MN58b inhibited ¹⁴C-PC production with similar potency in each of the three cell lines, the EGFRviii mutation imparted some resistance in terms of increased viability compared to wild-type 9L cells, which express very little EGFR. Because ChoK α has been reported to interact with EGFR in breast cancer cells (Miyake and Parsons, 2012), it was intriguing to explore the effect of the constitutively-active EGFRviii mutation found in a considerable proportion of GBM patients (Gan *et al.*, 2013). The 9L gliosarcoma line are known to be relatively insensitive to EGF stimulation (Tichauer, Samkoe, Sexton, *et al.*, 2012), but high levels of EGF (200 ng/mL) has been reported to induce a 29% increase in cell growth (Guo *et al.*, 2006). Our studies were unable to replicate the claim that EGF can stimulate 9L glioma cells, and further found no link between EGFR activity and ChoK α activation.

Higher choline levels may be suggestive of increased malignant potential, increased membrane turnover or activation of oncogenic signaling (Podo *et al.*, 2011). In F98 cell extracts high PC levels and PC/GPC ratios were seen using high resolution ¹H NMR. We observed a decrease in PC and non-significant increase in GPC in response to MN58b treatment, showing the effectiveness of ChoK α inhibition on choline metabolite levels. MN58b treatment resulted in significant reduction of the PC/GPC ratio in both cellular and tumor tissue extracts, which is consistent with previously reported results (Al-Saffar *et al.*, 2006). These results were paralleled in the *in vivo* model. A decrease in PC and in PC/GPC ratio was found in tumor extracts. Both PC and GPC were elevated in the extract spectra of tumors relative to contralateral tissue, although the contralateral PC/GPC ratio was also not significantly different from saline-treated tumor extracts even though their absolute levels were much lower. This variability was higher in tissue than in cells because gliomas are often histopathologically heterogeneous and have components of varying grades of malignancy and necrosis within the tumor.

Although the promising pilot study with JAS239 suggests that it can be detected in subcutaneous glioma xenografts, the lack of evidence that it passes the blood-brain barrier makes this only speculative at this point. Because brain cancers can often lead to permeabilization of the blood brain barrier, orthotopic GBM tumors would be an interesting JAS239 application to explore further. The ability of MN58b to inhibit the growth and metabolism of orthotopically implanted F98 tumors indicate that ChoK inhibitors can traverse the blood brain barrier, although whether this is due to a compromised barrier is yet to be determined. The advantage of an inherently fluorescent drug is the ease with which biodistribution studies can be performed, allowing follow-up

studies to be planned or modified based upon simple measurements in pilot tracer studies. These studies could be useful in detecting compromised blood brain barriers, or in aiding the delineation of tumor margins during surgical resection. At this preliminary level, inclusion of JAS239 in these expensive and time-consuming rat GBM models could not be justified, although further pursuit of this strategy is warranted.

ChoK α is particularly interesting as a therapeutic target in GBM because of its link to hypoxia. Glunde *et al.* reported increased total choline and ChoK α activity in a prostate cancer model and established a correlation between hypoxia, choline metabolites, and ChoK α activity (Glunde *et al.*, 2008). These authors also suggested that hypoxia-inducible factor-1 alpha (HIF-1 α) activation of hypoxia response elements (HREs) within the putative ChoK α promoter region can increase ChoK α expression within hypoxic environments, consequently increasing cellular PC and tCho levels within these environments. Hypoxic tumor microenvironments pose a problem for adjuvant treatments; cancer cells located in hypoxic environments undergo adaptive responses, which render them resistant to radiation and chemotherapy, resulting in recurrence (Moeller *et al.*, 2004). Such resistance to treatment contributes to the incidence of cancer recurrence. Variations in the extent and degree of hypoxia/necrosis in combination with variable angiogenic patterns represent a considerable problem in radiotherapeutics and antiangiogenic management of GBM. Thus, it is plausible to hypothesize that inhibition of ChoK α activity by a specific ChoK α inhibitor may help in reducing the survival pathways which allow GBM tumors to thrive in hypoxic microenvironments, making them more sensitive for chemo and radiation therapy. Conflicting evidence shows a

decrease in choline phosphorylation in hypoxic prostate cancer cells, although this appears to arise from other isoforms of HREs affecting ChoK α activity in human brain tumors (Bansal *et al.*, 2011). Thus, there are a number of avenues to explore regarding the link between radiation-resistance and ChoK α expression.

Chapter 7

Conclusion

7.1 Potential applications

The studies outlined in this work have led to several insights into the advantages and shortcomings of our approach to target ChoK α with small molecule theranostics.

Theranostics is an emerging field that developed out of the molecular imaging and pharmaceutical industries based upon their shared need for target specificity.

Applications of this technology for cancer imaging and therapy have previously been described, but these approaches have focused primarily on nanoparticle drug delivery agents tagged to molecular imaging contrast agents (Kelkar and Reineke, 2011). The nanoparticle revolution is promising, but has failed thus far to make a large impact in clinical applications, with the exception of liposomal formulations of some relatively insoluble anticancer drugs, such as doxorubicin (Chen *et al.*, 2011). For molecular probes and therapeutic agents, small molecules continue to be preferred, due to a precedent in industry, the well-defined pharmacokinetics of small molecules, and a relatively straightforward FDA approval process. Our approach has identified a prototype small molecule that can provide diagnostic information at low doses, and therapeutic benefit at higher doses (Fig. 7.1).

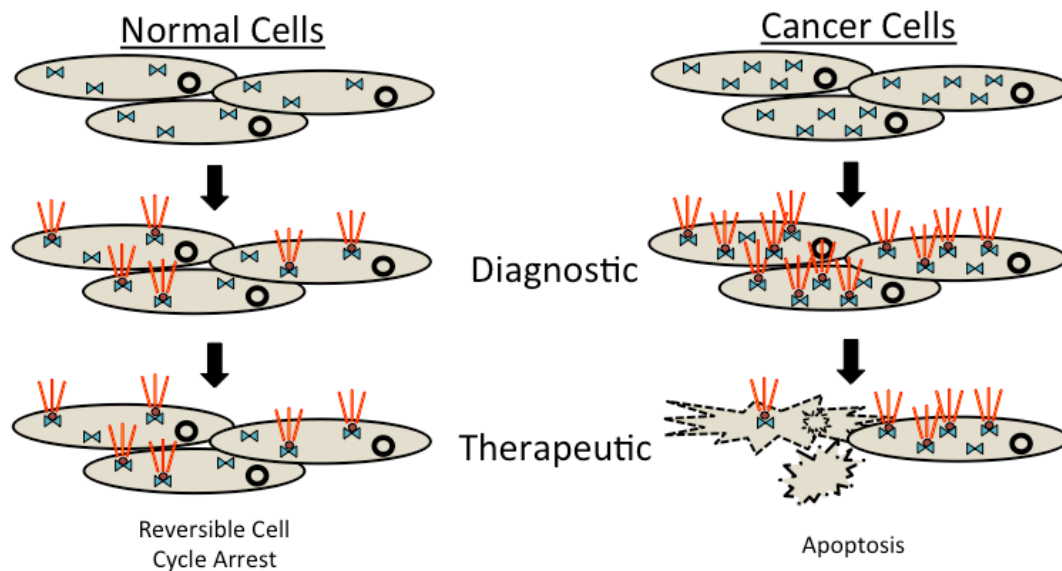


Figure 7.1. Model of Theranostic Mechanism of ChoK α Inhibitors. *Diagnostic:* Breast cancer cells are known to express higher levels of ChoK α (blue), which subsequently leads to increased accumulation of fluorescent inhibitor (red). Non-invasive optical imaging of these molecular beacons could therefore be used to detect ChoK α status. *Therapeutic:* ChoK α inhibitors cause apoptosis selectively in cancer cells, while eliciting reversible cell cycle arrest in normal cells. This is a self-reporting therapy because the level of accumulated fluorescence would diminish in response to treatment.

While the idea of fluorescent kinase inhibitors is not unprecedented (Kim *et al.*, 2010), this project represents a conceptual leap in clinical applicability because it describes the first example of a kinase-targeted small molecule whose fluorescence fits within the near infrared wavelength range required for *in vivo* detection. The original conception for this project was to design a probe capable of non-invasively reporting tumor stage based upon measurement of the fluorescence emitted from a ChoK α -retentive agent. As we became more familiar with the target and the breast tumor model, the expectations for clinical translation were augmented to better fit the capabilities of this technology. As an example, the anabolic nature of ChoK α is a disadvantage compared to catabolic targets for which a conjugated quencher-fluorophore system can

be “cleaved” by the mechanistic action of the molecular target (Mahmood and Weissleder, 2003). Designed as an “always-on” fluorophore, the expectations for JAS239 and similar probes have been tempered to account for interfering signal emitted from non-diseased tissues responsible for metabolism and excretion. In the case of the carbocyanines, the high background signal from the kidneys may have been predicted due to the cationic nature of these small molecules. By adapting our models and either cloaking the intraperitoneal organs or isolating the tumor-bearing tissue, we were still capable of making true measurements of disease status, but also introduced a new application for this technology centered around fluorescence-guided surgical aid.

For its tumor-associated fluorescence, JAS239 is being developed in our lab as an intraoperative NIRF contrast agent for delineation of tumor margin. In addition to this application, however, specific measurements of ChoK α status were also found to be feasible in these studies. Heightened NIRF was observed in tumors that genetically-overexpress ChoK α , although the difference in JAS239 accumulation may not be sufficiently robust to use this technology for determination of breast cancer tumor grade. An *in vivo* xenograft model with minimal ChoK α expression would be preferred to the MCF7-EV cell line, however such tumors have yet to be identified in the literature. Where JAS239 may be most useful is in the *in vivo* validation of new ChoK α inhibitors. Current methods rely on *in vivo* MRS to measure the composite tCho peak at 3.2 ppm, despite the complexity of pathways which contribute to choline metabolism. Alternative strategies using radiolabeled choline tracers are also being developed to mitigate these concerns, but tracer retention can be influenced by choline transport inhibition and may falsely identify agents with neurotoxic side effects. JAS239 itself has been well-tolerated

in animals and appears to be a true pre-clinical candidate capable of reducing tCho levels, inducing tumor apoptosis, and slowing tumor growth.

7.2 Next generation inhibitors

The proof-of-concept goals for this project were achieved using JAS239, however, for translation into more sophisticated breast cancer models this technology would benefit from improved potency against ChoK α . A new collaboration with Dr. Arnon Lavie at the University of Illinois at Chicago will make pure human ChoK α available for exploring new inhibitors. Additionally, this group will attempt co-crystallization of ChoK α with JAS239 to provide a better understanding of the interaction between protein and inhibitor. During this planning process, a set of next generation carbocyanines and MN58b-derivatives were designed by our group. After successful synthesis of prototype derivatives, the remaining compounds were outsourced to PepTech Corporation for synthesis. Although not all of the originally-designed structures could be produced, we are still in possession of a small compound library to screen against ChoK α .

Pilot studies are already underway to characterize the activity of these compounds. It was disappointing to not detect NIR fluorescence in solutions of the two resonant derivatives of MN58b (*E,E-conj*MN58b and *E,E,E-conj*MN58b), however, detection of fluorescence in the solid state means that we cannot rule out potential imaging utility in whole cell applications. Additionally, a number of strongly fluorescent JAS239 derivatives were synthesized with rational modifications to several parameters involved in pharmacokinetic behavior (e.g. hydrophobicity, structural rigidity, functional group replacement). While awaiting pure human ChoK α , a modified ChoK α activity assay was

developed to measure ^{14}C -choline phosphorylation in cytosolic preparations from MDA-MB-231 cells. Using this assay, remarkable activity was found for the MN58b derivative compounds, comparable to previously established inhibitors such as HC-3, MN58b, and TCD-717 (Fig. 7.2). Surprisingly little activity was found for any of the NIR fluorescent compounds. Most notably, 10 μM JAS239 induced only a 14% reduction in PC formation, despite our findings outlined in Chapter 4 using whole-cell radiotracing and cytosolic NMR assays.

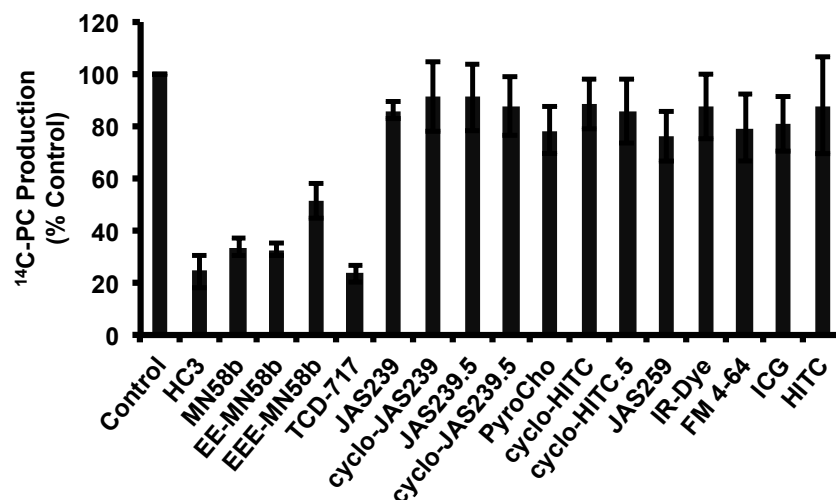


Figure 7.2. Screen of ChoK inhibition in cytosolic preparations. ^{14}C -PC production in cytosolic preparations was used as an indicator of ChoK activity in MDA-MB-231 cells. Dicationic compounds are the most effective ChoK inhibitors in the absence of cell membrane components. Fluorophore-derived compounds elicit minimal ChoK inhibition in the cytosol. Error bars represent \pm SEM of 3 separate experiments. Experiments were run with assistance from Michael Chiorazzo and Alejandro Arroyo of the Delikatny Lab.

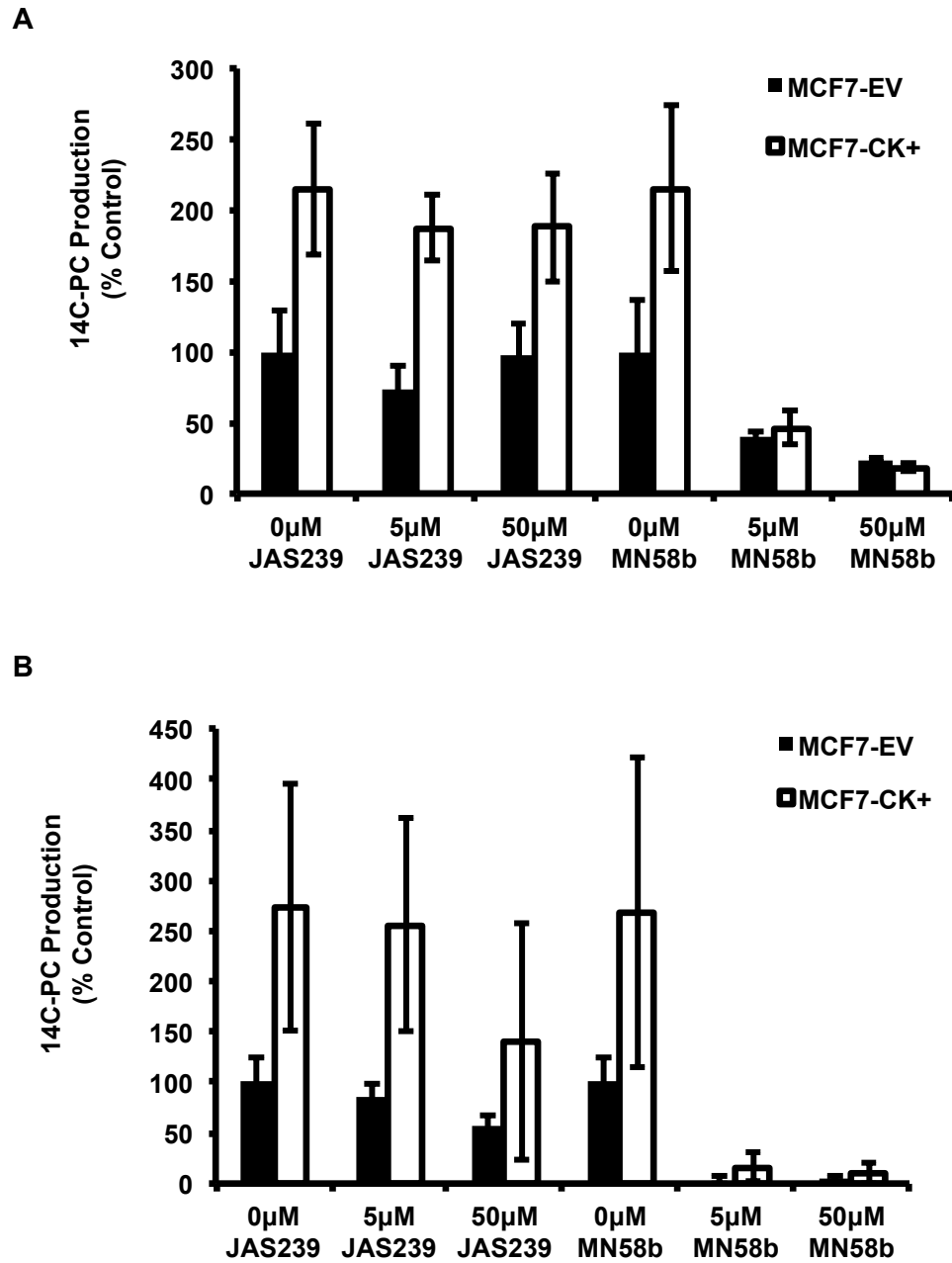


Figure 7.3. Comparison of JAS239 and MN58b in MCF7 cytosolic preparations. (A) ChoK inhibition in cytosolic preparations of MCF7-EV and MCF7-CK+ cells is only observed in the presence of MN58b. (B) In the absence of the reducing agent DTT, JAS239 more effectively inhibits ChoK, but high variability is found due to protease activity. MN58b is equally as effective in the absence of DTT. Error bars represent \pm SEM of 3 separate experiments.

To further explore JAS239 activity in the context of this membrane-free environment, we screened JAS239 and MN58b at 5 and 50 μM concentrations in MCF7-EV and MCF7-CK+ cytosolic preparations (Fig. 7.3A). JAS239 was again found to be ineffective in this assay, and the presence of dithiothreitol (DTT) became a concern. DTT is a reducing agent included in the lysis buffer to inactivate enzymes that have disulfide bonds critical to maintaining a catalytically-active structural conformation. As a reducing agent, however, it was not clear if JAS239 would remain pharmacologically active in this reducing environment, considering its conversion to a non-polar hydrocyanine state under strong reducing conditions (see Chapter 3, Section 6 on hydro-JAS239 synthesis). The same reaction conditions were followed as in Figure 7.3A, but without addition of the DTT and EDTA stock to the lysis buffer. These experiments demonstrated 44% reduction in ChoK α activity in the presence of 50 μM JAS239, but there was high experimental variability presumably due to the fact that denaturing proteases and counteracting phospholipases were no longer inactive in the absence of these crucial lysis buffer components (Fig. 7.3B). A logical step would be to add a protease inhibitor in an effort to minimize degradation of ChoK α during the reaction period. While DTT removal helped to restore JAS239 activity against ChoK α , it did not restore potency to levels observed in intact cells. Mass spectrometry analysis will be performed on JAS239 before and after DTT treatment to assess possible structural changes caused by this reducing agent.

7.3 Unexplored mechanisms of choline kinase inhibition

The data above indicate that JAS239 is more potent against ChoK α in intact cells, an unexpected result that may be due to several possibilities. The first possibility is that the

rapid uptake of JAS239 in intact cells observed using live-cell fluorescence microscopy (Fig. 4.13) caused higher local JAS239 concentrations within the cytosolic space and led to greater potency. Consistent with this hypothesis, MN58b is remarkably potent in cytosolic preparations, but the dicationic nature of this molecule causes the cell membrane to act as a greater barrier to MN58b entry, lowering its potency *in vitro*. The actual potency of MN58b against ChoK α in intact cells may be even less, considering our preliminary evidence which attributes some of MN58b's effect on ^{14}C - PC production to its inhibition of choline transport (Fig. 4.11). Choline phosphorylation by ChoK α is a mechanism cells use to trap this essential nutrient, in a manner similar to glucose phosphorylation by hexokinase. Its potential off-target effect on choline transporters has never previously been reported, although Rodríguez-González *et al.* observed reduced choline uptake in MN58b-treated cells; this effect was explained by citing a reduction in choline phosphorylation and, thus, cellular trapping (Rodríguez-González *et al.*, 2003). Interaction with choline transporters does help to explain the respiratory paralysis observed in mice treated with 4 mg/kg MN58b (Chapter 5) and in previous generation ChoK inhibitors.

The possibility for off-target effects of JAS239 cannot be ruled out, although the binding specificity demonstrated using immunohistochemistry techniques in fixed cells provides strong evidence against this. Off-target inhibition of choline transport would explain why JAS239 is most effective at reducing PC production in intact cells. Confocal microscopy and fluorimetry have detected no identifiable interaction with the plasma membrane or the choline transporters. An antagonistic effect on upstream regulators of ChoK α (such as Ras or RhoA) could also explain the inactivity in cell lysates, although

upstream growth signals are only known to cause changes in ChoK α expression, not activity. It is not likely that significant transcriptional changes could occur within the 1-hour treatment period used in radiotracing studies. For this same reason, JAS239's effect on PC accumulation cannot be due to an indirect action on the phospholipase enzymes due to the duration of time that would be required for the choline tracer to be incorporated into PtdCho. The quaternary ammonium group of JAS239 led to concerns that DNA intercalation or mitochondrial uncoupling may contribute to the molecule's antiproliferative effects. DNA intercalation was ruled out as a mode of antiproliferative activity when JAS239 was found to be excluded from the nucleus. Measurements of JAS239 viability (EC₅₀) were substantially lower in Trypan exclusion assays, which measure plasma membrane integrity, than in MTT assays, which measure mitochondrial integrity. This difference in potency between the two assays suggests that mitochondrial toxicity is not the driving factor in JAS239's antiproliferative effect.

It has recently been suggested that ChoK α 's contribution to tumorigenesis is through a non-catalytic mechanism, most likely related to its newly reported scaffolding function (Falcon *et al.*, 2013). For ChoK α to not be the direct target of JAS239, the probe would likely bind to a protein currently unknown to form a scaffolding complex with ChoK α . This possibility could explain the colocalization between JAS239 and ChoK α , but would not explain why exogenous choline addition rescues the inhibitory effect of JAS239, nor could it explain the reversal of JAS239 binding by a ChoK α antibody. We observed no evidence of ChoK α recruitment to the plasma membrane in our immunohistochemistry studies, but JAS239 may be a useful tool in the effort to characterize ChoK α 's binding partners.

7.4 Future studies

Screening for ChoK α inhibition and antiproliferative effects is currently under way for the JAS239 and MN58b derivatives. Identification of interesting candidates will then be co-crystallized with ChoK α and structure-activity relationships will then be assessed. Many molecular biology tools that were not available at the start of this project, such as ChoK α -specific antibodies, siRNA, and ELISA kits, are now commercially available. These offer new and specific strategies to explore ChoK α inhibitors at a level of detail that was not previously possible. We believe the most promising application for JAS239 derivatives is in NIRF-guided tumor resection. Use of an inducible orthotopic tumor model would allow small tumors to be resected from mice. Disease-free margins from animals with tumors resected by naked eye could be compared to those resected by NIRF-guidance; the result of such studies could provide further evidence to support the utility of these probes. For therapeutic assessment, studies of new dose formulations and treatment regimens may identify a strategy that stops or reverses tumor growth. Finally, testing synergistic effects with existing drugs that target compensatory pathways could validate ChoK α inhibition as a clinically viable treatment option.

In summary, JAS239 remains the most effective small molecule ChoK α -targeted theranostic. Its interaction with ChoK α is most likely at the choline binding site, although further studies with the pure enzyme are needed to understand this mechanism. The single cationic charge on JAS239 may be the reason it is only half as potent as the dicationic inhibitors such as MN58b. By removing one quaternary ammonium group, however, JAS239 shares less structural features with HC-3 and is better tolerated than

MN58b in mice. The single charge also appears critical for fluorescence in less rigid structures. With fluorescence in the NIR wavelength range, attenuation of the Kennedy pathway, and a low toxicity profile, JAS239 is a promising multi-functional small molecule for identification and treatment of cancer. The use of a dye as a signal transduction inhibitor represents a return to the paradigm of the therapeutic “magic bullet”, although our modernization of Ehrlich’s postulation more closely resembles a diagnostic beacon fired from a NIRF gun.

APPENDIX 1

Synthesis and characterization of E,E-conjMN58b (PTC1452-01)

Procedure for PTC1452-01

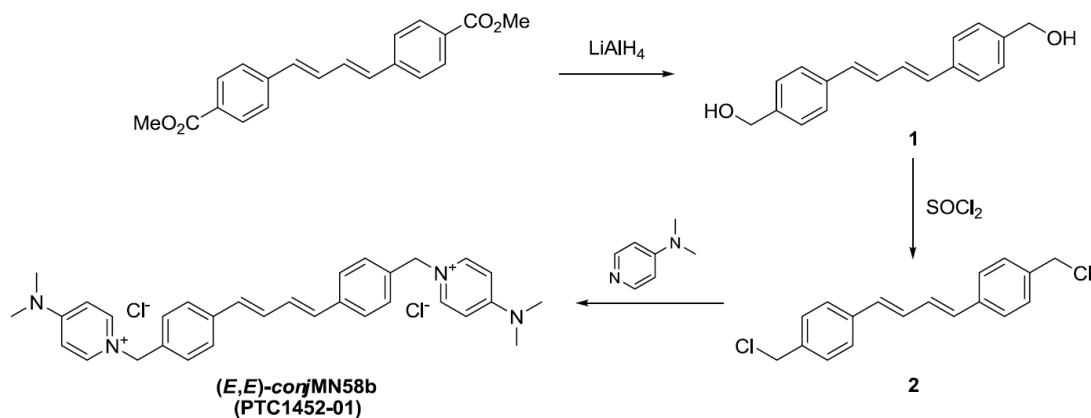
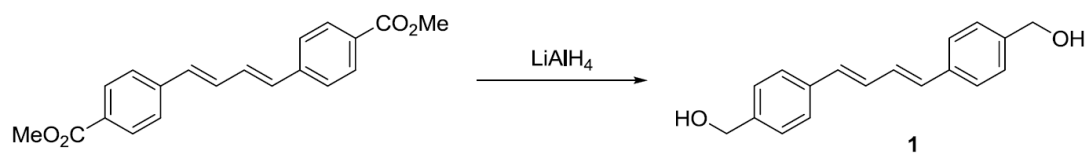
Prepared by: Haiming Wang 11/12/2014

PhD, Senior Scientist

Approved by: Xiaowen Sun 11/12/2014

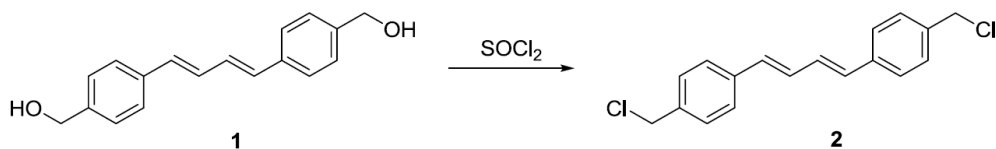
PhD, Director of Med. Chem.

PepTech Corporation
(Shanghai)

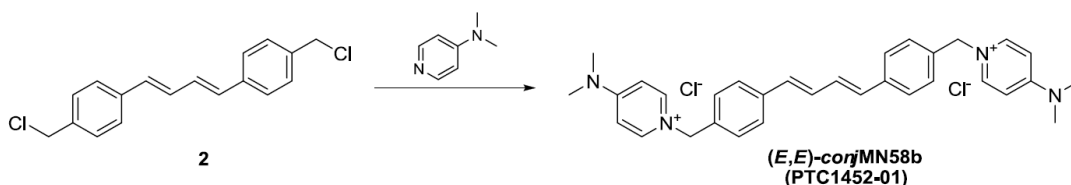
Scheme for PTC1452-01**Experiment Procedure****Preparation of compound 1**

To a suspension of LiAlH_4 (2.4 g, 62.0 mmol) in THF (300 mL) was added a solution of dimethyl 4,4'-((*1E,3E*)-buta-1,3-diene-1,4-diyl)dibenzoate (5.0 g, 15.5 mmol) in THF (100 mL) slowly at room temperature under N_2 atmosphere. The reaction mixture was stirred at room temperature for 1 h and then heated at 50°C overnight. The reaction was quenched with aqueous NaOH (4 *N*, 300 mL) carefully and the resulting mixture was extracted with EtOAc (200 mL \times 5). The combined organic layers were dried over anhydrous Na_2SO_4 and concentrated. The residue was purified by flash column chromatography on silica gel (EtOAc /Petroleum ether = 5:1) to afford compound **1** (3.4 g, 83% yield) as a brown solid.

$^1\text{H NMR}$ (400 MHz, DMSO-d_6): δ 7.46 (d, $J = 8.0$ Hz, 4H), 7.28 (d, $J = 8.0$ Hz, 4H), 7.03-7.13 (m, 2H), 6.68-6.78 (m, 2H), 4.50 (s, 4H).

Preparation of compound 2

To a solution of compound **1** (0.2 g, 0.75 mmol) in DCM (15 mL) was added SOCl_2 (2.0 mL, 27.6 mmol) under N_2 atmosphere at room temperature. The reaction mixture was stirred overnight at room temperature and then quenched with aqueous NaHCO_3 . The resulting mixture was extracted with DCM (50 mL \times 3). The combined organic layers were dried over anhydrous Na_2SO_4 and concentrated to afford compound **2**, which was used in the next step without further purification.

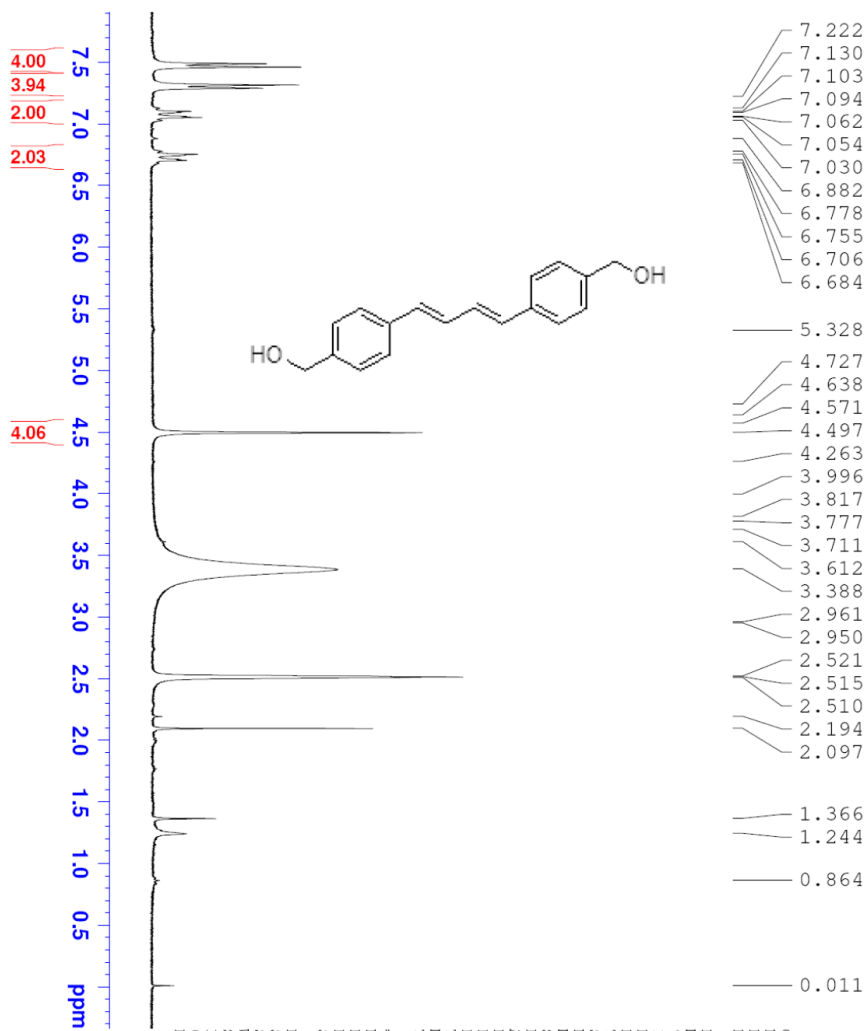
Preparation of compound PTC1452-01

To a solution of crude compound **2** (0.75 mmol) in 2-butanone (10 mL) was added DMAP (1.3 g, 10.6 mmol) under N_2 atmosphere at room temperature. The reaction mixture was heated under reflux for 4 h. The resulting precipitate was collected by filtration (in hot), washed with acetone and then purified by prep-HPLC to afford compound **PTC1452-01** (13 mg, 3.2% yield over two steps) as a yellow solid.

¹H NMR (400 MHz, CD_3OD): δ 8.50 (s, 1H), 8.22 (d, $J = 8.0$ Hz, 4H), 7.54 (d, $J = 8.0$ Hz, 4H), 7.34 (d, $J = 8.0$ Hz, 4H), 7.08 (dd, $J = 2.4, 12.4$ Hz, 2H), 7.00 (d, $J = 8.0$ Hz, 4H), 6.75 (d, $J = 14.0$ Hz, 2H), 5.35 (s, 4H), 3.13 (s, 12H).

NMR Spectra

¹H NMR of compound 1



PTC1452-PJT-1802P24-H-20140903

- 7.222
- 7.130
- 7.103
- 7.094
- 7.062
- 7.054
- 7.030
- 6.882
- 6.778
- 6.755
- 6.706
- 6.684
- 5.328
- 4.727
- 4.638
- 4.571
- 4.497
- 4.263
- 3.996
- 3.817
- 3.777
- 3.711
- 3.612
- 3.388
- 2.961
- 2.950
- 2.521
- 2.515
- 2.510
- 2.194
- 2.097
- 1.366
- 1.244
- 0.864
- 0.011



Current Data Parameters
 NAME PTC1452-FU0-1802P24
 EXPNO 1
 PROCNO 1

F2 - Acquisition Parameters
 Date_ 20140903
 Time_ 10.34
 INSTRUM spect
 PROBR0 5 mm PABBO BBO
 PULPROG zgpg30
 SOLVENT DMSO
 NS 12
 DS 2
 SWH 6172.838 Hz
 FIDRES 0.064190 Hz
 AQ 5.3084650 sec
 RG 512
 DW 812.600 usec
 DM 6.000 usec
 TE 295.1 K
 D1 1.00000000 sec
 TD0 1

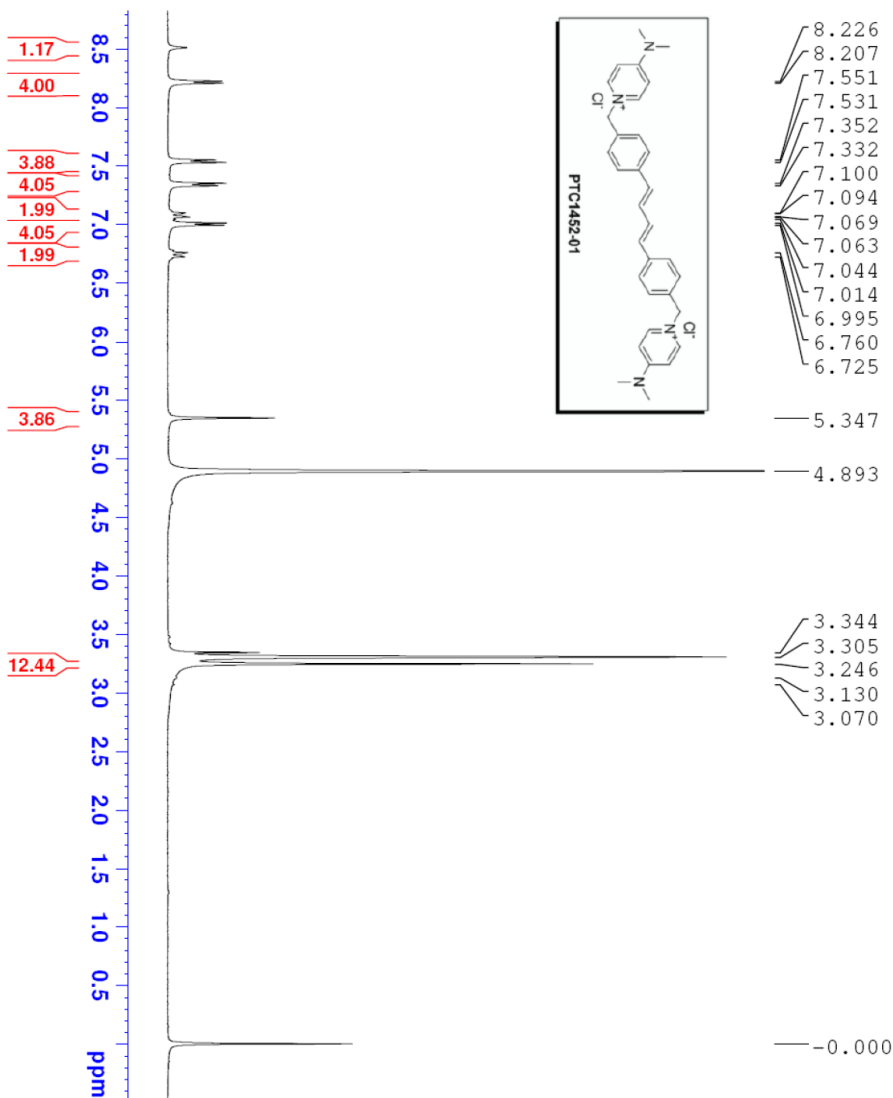
===== CHANNEL f1 =====
 NUCL1 1H
 P1 12.70 usec
 PL1 0.00 dB
 SFO1 300.1318534 MHz

F2 - Processing parameters
 SI 32768
 SF 300.1300000 MHz
 WDW no
 SSB 0
 LB 0.00 Hz
 GB 0
 PC 1.00

[Return](#)

PTC1452-01-PJT-1802P33-H-20140917

¹H NMR of compound PTC1452-01



- 8.226
- 8.207
- 7.551
- 7.531
- 7.352
- 7.332
- 7.100
- 7.094
- 7.069
- 7.063
- 7.044
- 7.014
- 6.995
- 6.760
- 6.725

- 5.347
- 4.893

- 3.344
- 3.305
- 3.246
- 3.130
- 3.070

-0.000



Current Data Parameters
 NAME PTC1452-01-PJT-1802P33
 EXPNO 1
 PROCNO 1

F2 - Acquisition Parameters
 Date_ 20140917
 Time 16.58
 INSTRUM spect
 PROBHD 5 mm PABBO BB/
 PULPROG zg30
 TD 65536
 SOLVENT MeOD
 NS 16
 DS 2
 SMH 8012.820 Hz
 FIDRES 0.122266 Hz
 AQ 4.089465 sec
 RG 116.94
 DW 62.400 usec
 DE 6.50 usec
 TE 293.6 K
 D1 1.00000000 sec
 TD0 1

==== CHANNEL f1 =====
 SFO1 400.1324710 MHz
 NUCL1 1H
 P1 10.00 usec
 PLW1 16.00000000 W

F2 - Processing parameters
 SI 65536
 SF 400.1300098 MHz
 MDM EM
 SSB 0
 LB 0.30 Hz
 GB 0
 PC 1.00

[Return](#)

APPENDIX 2

Synthesis and characterization of E,E,E-conjMN58b (PTC1452-02)

Procedure for PTC1452-02

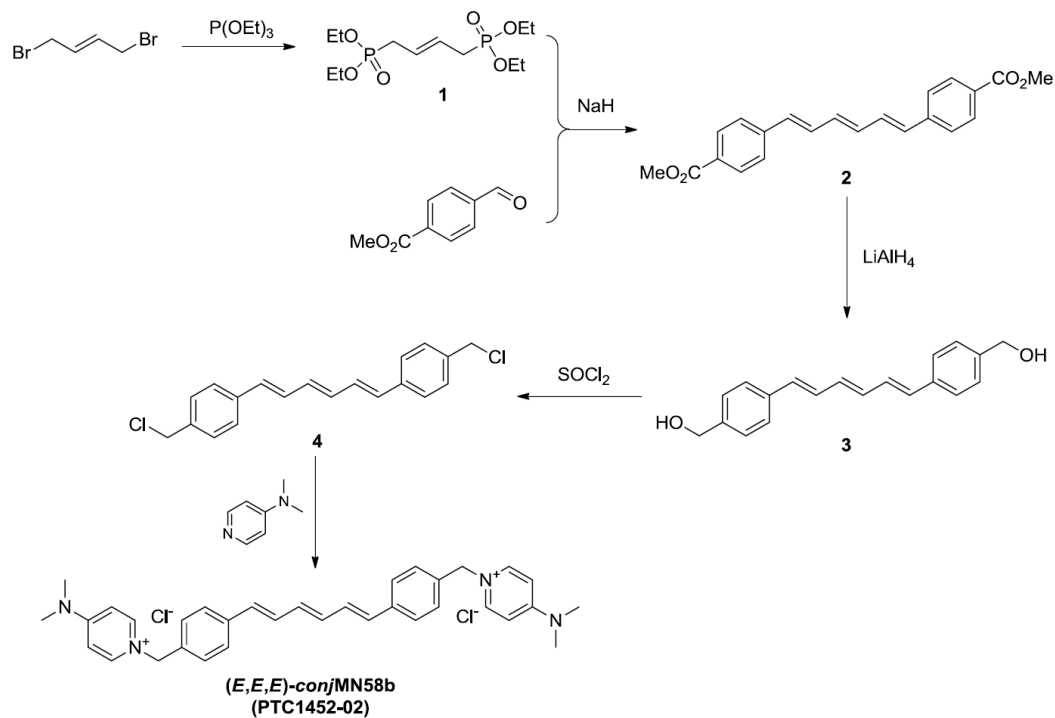
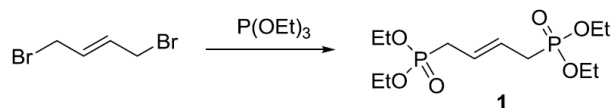
Prepared by: Haiming Wang 11/12/2014

PhD, Senior Scientist

Approved by: Xiaowen Sun 11/12/2014

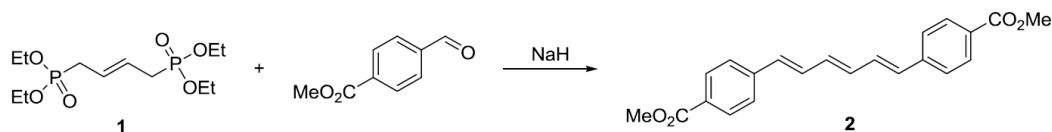
PhD, Director of Med. Chem.

PepTech Corporation
(Shanghai)

Scheme for PTC1452-02**Experiment Procedure****Preparation of compound 1**

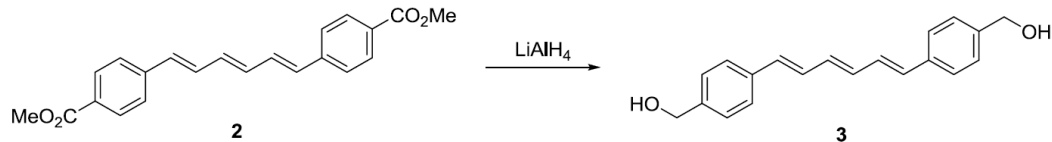
A mixture of 1,4-dibromo-2-buten (11.5 g, 53.7 mmol) and P(OEt)₃ (24 mL) was heated under reflux overnight and then cooled to room temperature. The volatiles were removed under vacuum to afford compound **1**, which was used in the next step without further purification.

¹H NMR (300 MHz, CDCl₃): δ 5.59 (s, 2H), 4.02-4.13 (m, 8H), 2.54-2.62 (m, 4H), 1.29 (t, *J* = 6.9 Hz, 12H).

Preparation of compound 2

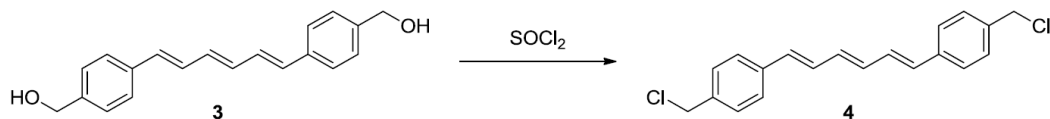
To a suspension of NaH (60%, 3.7 g, 91.5 mmol) in THF (100 mL) was added a solution of compound **1** (10.0 g, 30.5 mmol) in THF (100 mL) at room temperature under N₂ atmosphere. The mixture was stirred at room temperature for 1 h and a solution of methyl 4-formylbenzoate (10.0 g, 61 mmol) in THF (200 mL) was added slowly. The reaction mixture was stirred overnight at room temperature and then quenched with water (200 mL) carefully. The resulting mixture was extracted with EtOAc (100 mL × 3) and the combined organic layers were dried over anhydrous sodium sulfate and concentrated. The residue was washed with DCM several times to afford compound **2** (3.6 g, 33% yield) as a yellow solid.

¹H NMR (400 MHz, CDCl₃): δ 7.99 (d, *J* = 8.0 Hz, 4H), 7.47 (d, *J* = 8.0 Hz, 4H), 6.96-7.02 (m, 2H), 6.66 (d, *J* = 15.6 Hz, 2H), 6.59 (dd, *J* = 2.8, 9.2 Hz, 2H), 3.95 (s, 6H).

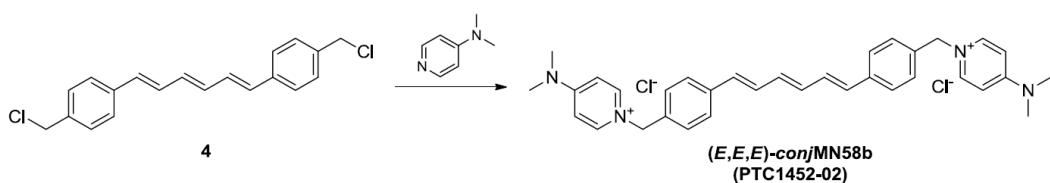
Preparation of compound 3

To a suspension of LiAlH₄ (0.43 g, 11.3 mmol) in THF (80 mL) was added a solution of compound **2** (2.6 g, 7.5 mmol) in THF (100 mL) slowly at room temperature under N₂ atmosphere. The reaction mixture was stirred at room temperature for 1 h and then heated at 50°C overnight. The reaction was quenched with aqueous NaOH (4*N*, 100 mL) carefully. The resulting mixture was extracted with EtOAc (100 mL × 3) and the combined organic layers were dried over anhydrous sodium sulfate and concentrated. The residue was purified by flash column chromatography on silica gel (EtOAc/Petroleum ether = 5:1) to afford compound **3** (1.1 g, 33% yield) as a yellow solid.

¹H NMR (400 MHz, DMSO-*d*₆): δ 7.45 (d, *J* = 8.0 Hz, 4H), 7.28 (d, *J* = 8.0 Hz, 4H), 6.98-7.03 (m, 2H), 6.65 (d, *J* = 15.6 Hz, 2H), 6.58 (dd, *J* = 2.4, 6.8 Hz, 2H), 5.17 (t, *J* = 5.6 Hz, 2H), 4.48 (d, *J* = 5.6 Hz, 4H).

Preparation of compound 4

To a solution of compound **3** (0.5 g, 1.7 mmol) in DCM (30 mL) was added SOCl_2 (1.6 mL, 22.0 mmol) under N_2 atmosphere at room temperature. The reaction mixture was stirred overnight at room temperature and then quenched with aqueous NaHCO_3 . The resulting mixture was extracted with DCM (50 mL \times 3). The combined organic layers were dried over anhydrous Na_2SO_4 and concentrated to afford compound **4**, which was used in the next step without further purification.

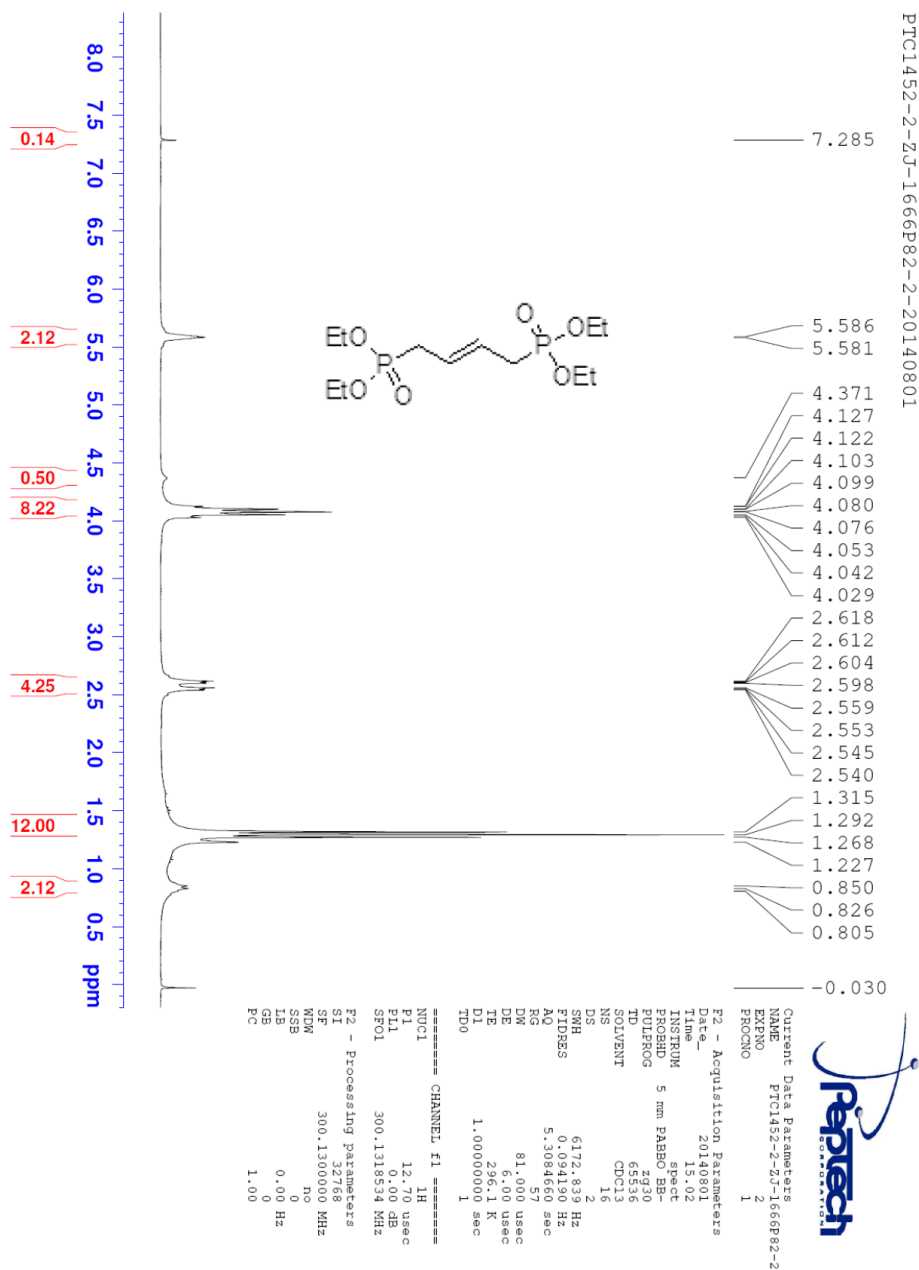
Preparation of compound PTC1452-02

To a solution of crude compound **4** (1.7 mmol) in 2-butanone (10 mL) was added DMAP (2.1 g, 17.4 mmol) under N_2 atmosphere at room temperature. The reaction mixture was heated under reflux for 4 h. The resulting precipitate was collected by filtration (in hot), washed with acetone and then purified by prep-HPLC to afford compound **PTC1452-02** (48 mg, 4.2% yield over two steps) as a yellow solid.

¹H NMR (400 MHz, CD₃OD): δ 8.49 (s, 2H), 8.21 (d, J = 8.0 Hz, 4H), 7.52 (d, J = 8.0 Hz, 4H), 7.33 (d, J = 8.0 Hz, 4H), 6.99-7.04 (m, 6H), 6.59-6.66 (m, 4H), 5.34 (s, 4H), 3.24 (s, 12H).

NMR Spectra

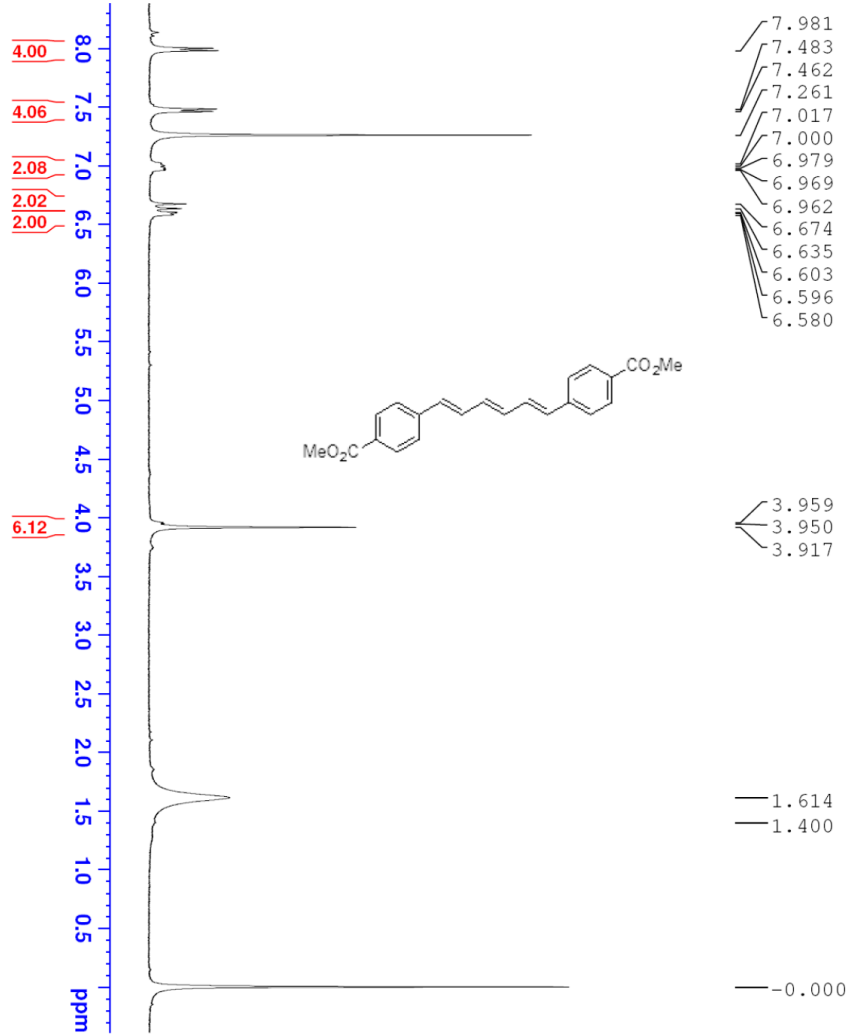
¹H NMR of compound 1



[Return](#)

¹H NMR of compound 2

PTC1452-2-2J-1666P96-1-H-20140821



7.981
7.483
7.462
7.261
7.017
7.000
6.979
6.969
6.962
6.674
6.635
6.603
6.596
6.580

3.959
3.950
3.917

1.614
1.400

-0.000



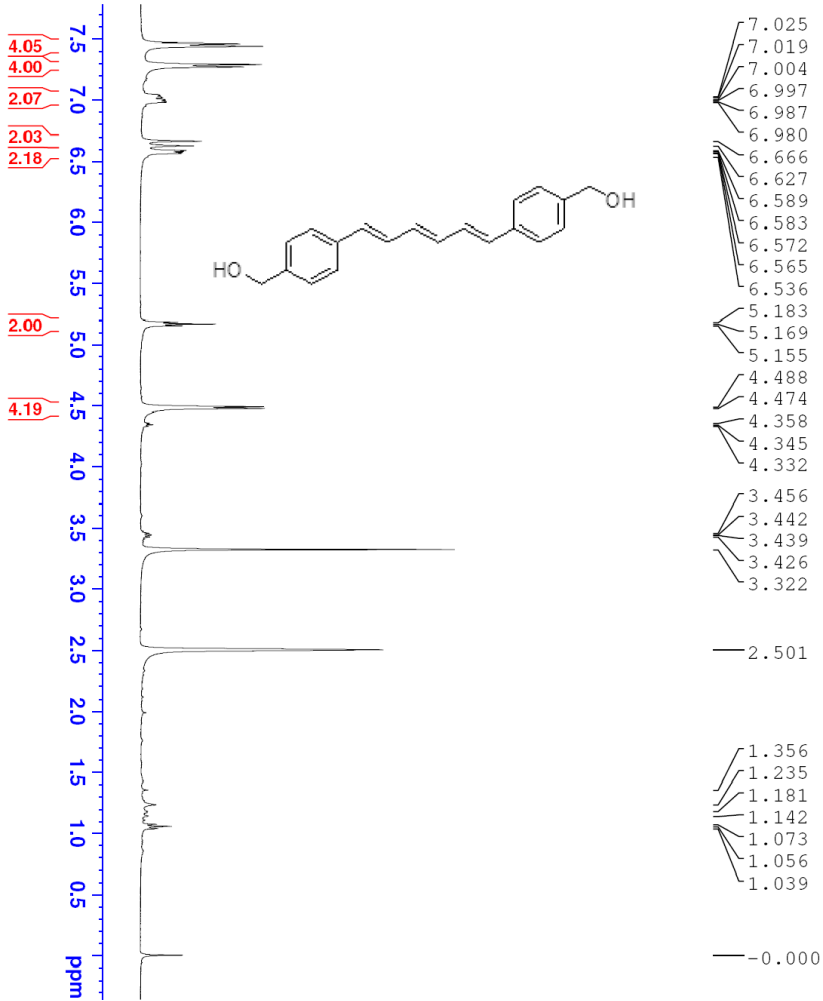
Current Data Parameters
NAME PTC1452-2-2J-1666P96-1
EXPNO 1
PROCNO 1

F2 - Acquisition Parameters
Date_ 20140821
Time 16.00
INSTRUM spect
PROBHD 5 mm PABBO BB/
PULPROG zg30
TD 65536
SOLVENT CDCl3
NS 16
DS 2
SWH 8012.820 Hz
FIDRES 0.122266 Hz
AQ 4.0894465 sec
RG 131.1
DW 62.400 usec
DE 6.50 usec
TE 298.0 K
D1 1.00000000 sec
TD0 1

==== CHANNEL f1 =====
SFO1 400.1324710 MHz
NUC1 1H
P1 10.00 usec
PLM1 16.00000000 W
F2 - Processing Parameters
SI 65536
SF 400.1300089 MHz
WDW EM
SSB 0
LB 0.30 Hz
GB 1.00
PC

PTC1452-2-ZJ-1666P99-A-H-20140827

¹H NMR of compound 3



7.025
7.019
7.004
6.997
6.987
6.980
6.666
6.627
6.589
6.583
6.572
6.565
6.536
5.183
5.169
5.155
4.488
4.474
4.358
4.345
4.332
3.456
3.442
3.439
3.426
3.322
2.501
1.356
1.235
1.181
1.142
1.073
1.056
1.039
0.000

Current Data Parameters
 NAME PTC1452-2-ZJ-1666P99-A
 EXPNO 1
 PROCNO 1

F2 - Acquisition Parameters
 Date_ 20140827
 Time 10.48
 INSTRUM spect
 PROBHD 5 mm PABBO BB/
 PULPROG zg30
 TD 2930
 FIDRES 0.122266 Hz
 RG 4.0894465 sec
 RW 116.94
 DM 62.400 usec
 DE 66.50 usec
 TE 296.0 K
 DF 1.00000000 sec
 TD 1

==== CHANNEL F1 =====
 SFO1 400.1324710 MHz
 NUC1 1H
 P1 10.00 usec
 PL1 16.00000000 W
 FLM1

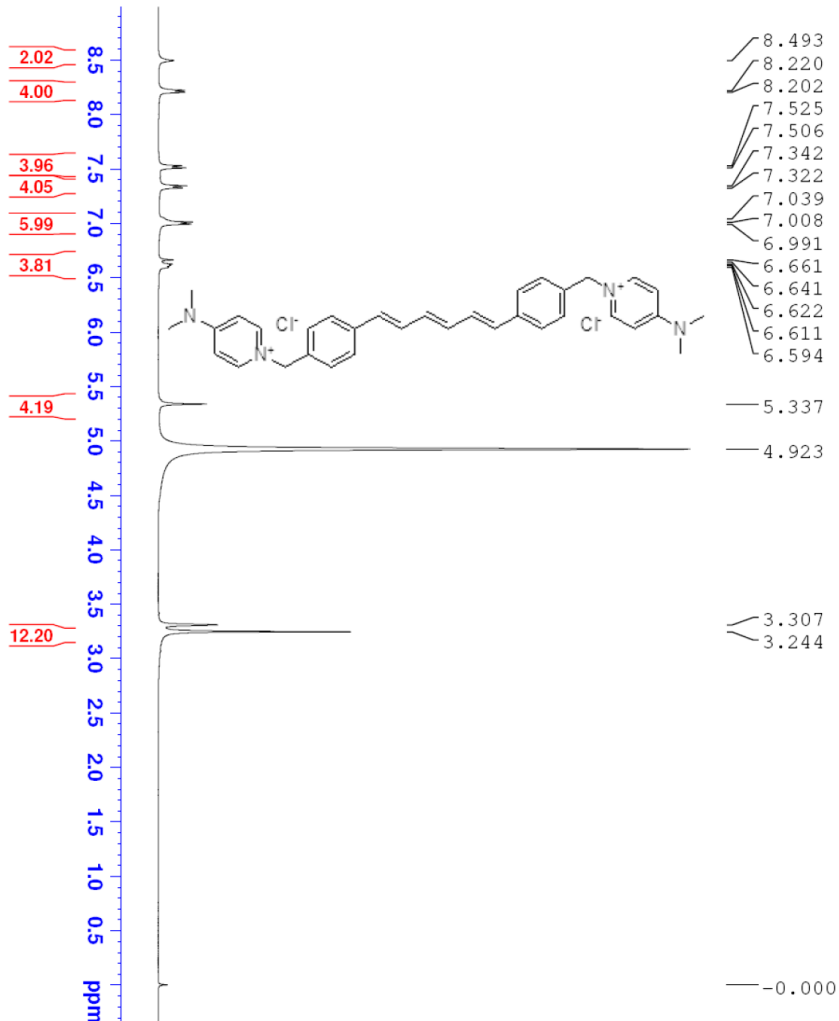
F2 - Processing parameters
 SI 65536
 SF 400.1300023 MHz
 MCM 0
 SSB 0
 LB 0
 GB 0
 PC 1.00



[Return](#)

¹H NMR of compound PTC1452-02

PTC1452-2-2J1861P6-H-20140923



Current Data Parameters
 NAME PTC1452-2-2J1861P6
 EXPNO 1
 PROCNO 1

F2 - Acquisition Parameters
 Date_ 20140923
 Time 8:46
 INSTRUM spect
 PROBHD 5 mm PABBO BB/
 PULPROG zg30
 TD 65536
 SOLVENT MeOD
 NS 16
 DS 2
 SMH 8012.820 Hz
 FIDRES 0.122266 Hz
 AQ 4.0894465 sec
 RG 32.27
 DW 62.400 usec
 DE 6.50 usec
 TE 291.4 K
 D1 1.00000000 sec
 TD0 1

==== CHANNEL f1 =====
 SFO1 400.1324710 MHz
 NUCL1 1H
 P1 10.00 usec
 PLW1 16.00000000 W

F2 - Processing parameters
 SI 65536
 SF 400.1300091 MHz
 MDW EM
 SSB 0
 LB 0
 GB 0
 PC 1.00



[Return](#)

APPENDIX 3

Synthesis and characterization of TCD-717 (PTC1452-07)

Procedure for PTC1452-07

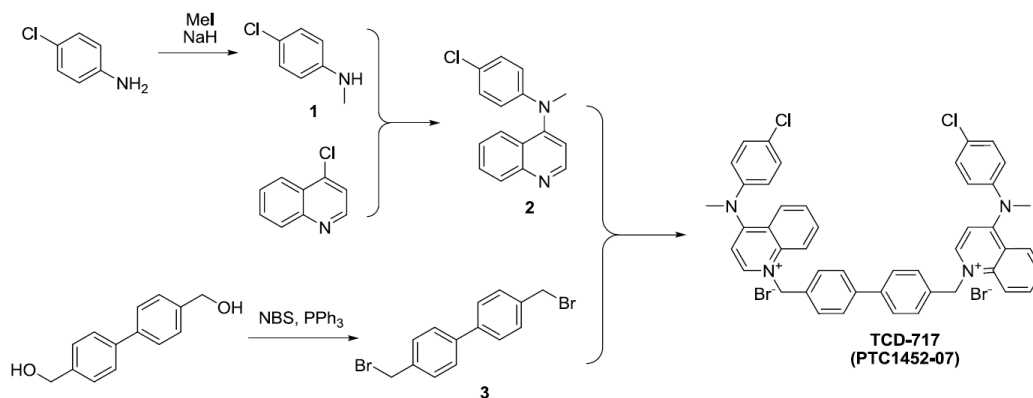
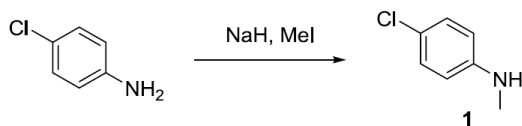
Prepared by: Haiming Wang 11/10/2014

PhD, Senior Scientist

Approved by: Xiaowen Sun 11/10/2014

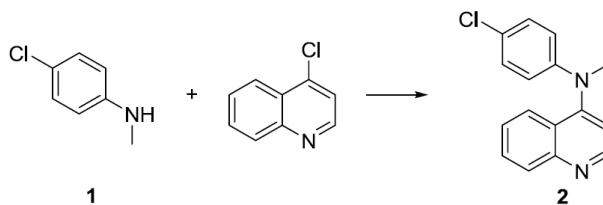
PhD, Director of Med. Chem.

PepTech Corporation
(Shanghai)

Scheme for PTC1452-07**Experiment Procedure****Preparation of compound 1**

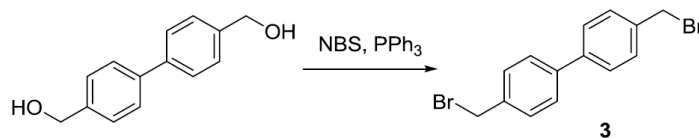
To a suspension of NaH (3.14 g, 78.5 mmol) in THF (80 mL) was added a solution of 4-chloroaniline (10.0 g, 78.4 mmol) slowly at 0°C. The mixture was stirred at 0°C for 1 h. MeI was added and the reaction mixture was allowed to warm to room temperature and stirred overnight. The reaction was quenched with water at 0°C and the resulting mixture was extracted with EtOAc (100 mL×3). The combined organic extracts were dried over anhydrous sodium sulfate and concentrated. The residue was purified by flash column chromatography on silica gel (petroleum ether/EtOAc = 100:1 to 50:1) to afford compound 1 (6.2 g, 55% yield) as a pale yellow oil.

¹H NMR (400 MHz, CDCl₃): δ 7.15 (d, *J* = 7.2 Hz, 2H), 6.57 (d, *J* = 7.2 Hz, 2H), 3.63 (br s, 1H), 2.84 (s, 3H).

Preparation of compound 2

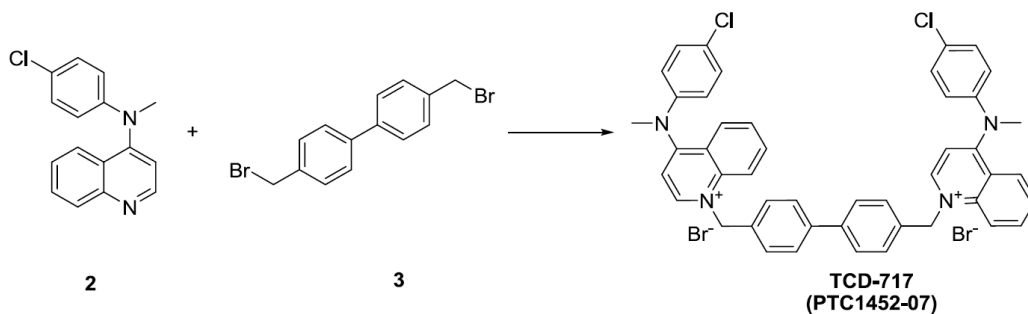
A mixture of compound **1** (1.0 g, 7.0 mmol) and 4-chloroquinoline (0.43 g, 2.6 mmol) was heated at 130°C for 12 h and then cooled to room temperature. The resulting red residue was purified by flash column chromatography on silica gel (petroleum ether/EtOAc = 100:1 to 50:1) to afford compound **2** (0.33 g, 47%) as a yellow solid.

¹H NMR (400 MHz, CDCl₃): δ 8.85 (d, *J* = 4.8 Hz, 1H), 8.10 (d, *J* = 8.4 Hz, 1H), 7.62-7.71 (m, 2H), 7.36 (t, *J* = 7.2 Hz, 2H), 7.13-7.18 (m, 3H), 6.76 (d, *J* = 8.8 Hz, 2H), 3.45 (s, 6H).

Preparation of compound 3

To a solution of [1,1'-biphenyl]-4,4'-diylmethanol (2.0 g, 9.3 mmol) in THF (30 mL) were added NBS (4.16 g, 23.4 mmol) and PPh₃ (6.33 g, 23.4 mmol) under N₂ atmosphere at room temperature. The reaction mixture was stirred overnight at room temperature and then quenched with saturated aqueous NaHCO₃ (30 mL). The resulting mixture was extracted with DCM (50 mL×3) and the combined organic layers were dried over anhydrous sodium sulfate and concentrated. The residue was purified by flash column chromatography on silica gel (Petroleum ether/EtOAc = 50:1) to afford compound **3** (1.0 g, 31% yield) as a white solid.

¹H NMR (400 MHz, CDCl₃): δ 7.56 (d, *J* = 8.0 Hz, 4H), 7.47 (d, *J* = 8.0 Hz, 4H), 4.55 (s, 4H).

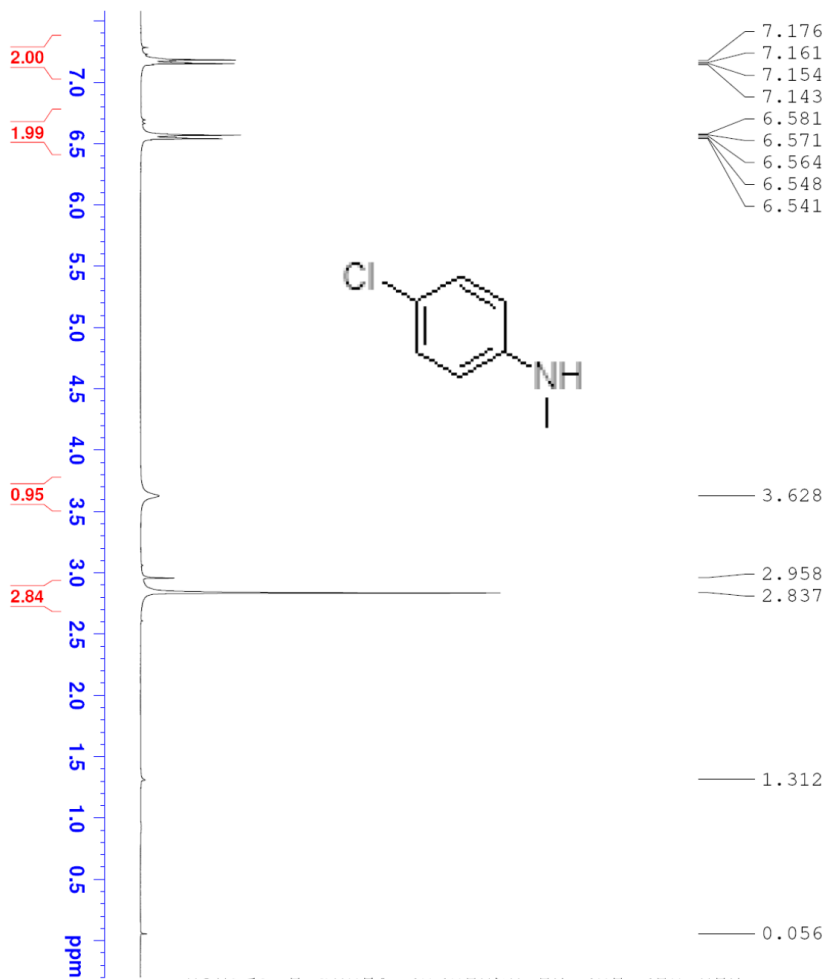
Preparation of compound PTC1452-07

To a solution of compound **2** (0.40 g, 1.5 mmol) in 2-butanone (5 mL) was added compound **3** (0.20 g, 0.74 mmol) under N₂ atmosphere at room temperature. The reaction mixture was heated under reflux overnight. The solvent was evaporated and the resulting residue was washed with acetone. The crude compound was purified by prep-HPLC to afford compound **PTC1452-07** (19.0 mg, 14% yield) as a yellow solid.

¹H NMR (300 MHz, CD₃OD): δ 8.96 (d, *J* = 8.4 Hz, 2H), 8.41 (m, 2H), 8.11 (d, *J* = 8.4 Hz, 2H), 7.82 (dt, *J* = 1.2, 8.4 Hz, 2H), 7.67 (d, *J* = 8.4 Hz, 6H), 7.53 (d, *J* = 7.8 Hz, 4H), 7.36-7.44 (m, 10H), 6.03 (s, 4H), 3.83 (s, 6H).

NMR Spectra

¹H NMR of compound 1



PTC1452-7-2J-1666P83-H-20140804

7.176
7.161
7.154
7.143
6.581
6.571
6.564
6.548
6.541
3.628
2.958
2.837
1.312
0.056



Current Data Parameters
NAME PTC1452-7-2J-1666P83
EXPNO 1
PROCNO 1

F2 - Acquisition Parameters

Date_ 20140804
Time 13.58
INSTRUM spect
PROBHD 5 mm PABBO BB-
PULPROG zgpg30
SOLVENT CDCl3
NS 16
DS 2
SWH 6172.839 Hz
FIDRES 0.094190 Hz
AQ 5.3084660 sec
RG 80.6
DE 81.000 usec
TE 296.9 K
D10 1.00000000 sec

----- CHANNEL f1 -----

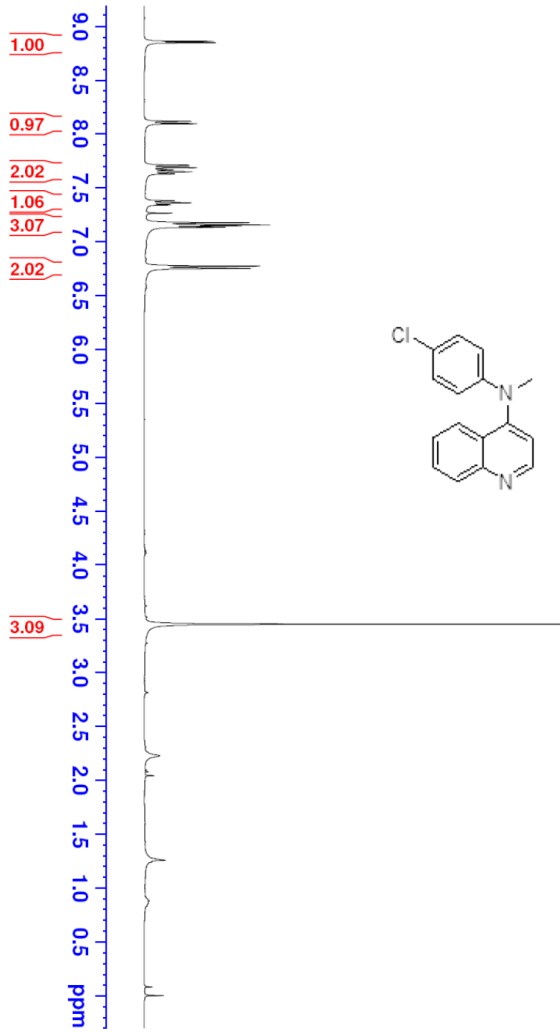
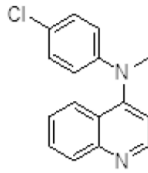
NUC1 1H
P1 12.70 usec
PL1 0.00 dB
SFO1 300.1318534 MHz
F2 - Processing parameters
SI 32768
SF 300.1300000 MHz
WDW no
SSB no
GB 0.00 Hz
PC 1.00

[Return](#)

¹H NMR of compound 2

PTC1452-CQG-1803P23-H-20140828

- 8.094
- 7.707
- 7.686
- 7.667
- 7.664
- 7.647
- 7.629
- 7.377
- 7.359
- 7.341
- 7.263
- 7.175
- 7.153
- 7.144
- 7.132
- 6.772
- 6.750



- 3.446
- 2.225
- 2.040
- 1.272
- 1.256
- 0.079
- 0.000



Current Data Parameters
 NAME PTC1452-CQG-1803P23
 EXPNO 1
 PROCNO 1

F2 - Acquisition Parameters
 Date_ 20140828
 Time 9.06

INSTRUM spect
 PROBHD 5 mm PABBO BB/
 PULPROG zg30
 TD 65536
 SOLVENT CDCl3

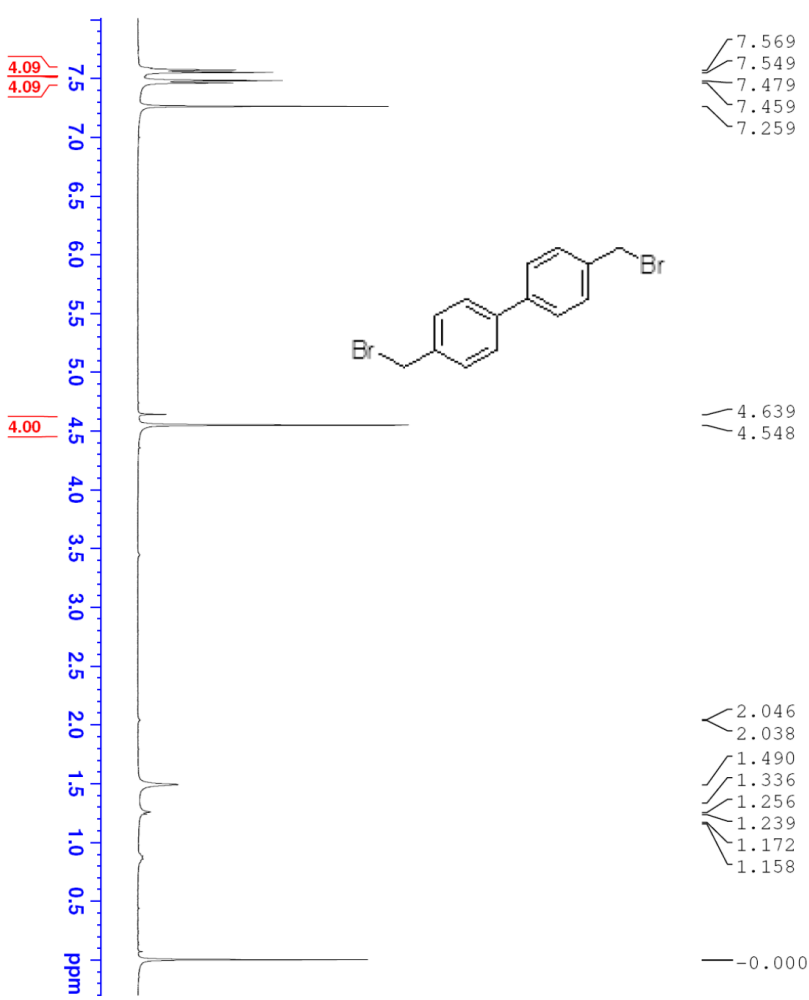
NS 16
 DS 2
 SMH 8012.820 Hz
 FIDRES 0.122266 Hz
 AQ 4.0894465 sec
 RG 50.71
 DW 62.400 usec
 DE 6.50 usec
 TE 298.0 K
 D1 1.00000000 sec
 TD0 1

===== CHANNEL f1 =====
 SFO1 400.1324710 MHz
 NUCl 1H
 P1 10.00 usec
 PLW1 16.000000000 W

F2 - Processing parameters
 SI 65536
 SF 400.1300083 MHz
 WDW EM
 SSB 0
 LB 0.30 Hz
 GB 0
 PC 1.00

[Return](#)

¹H NMR of compound 3



PTC1452-CQG-1803P22-H-20140826



Current Data Parameters
 NAME PTC1452-CQG-1803P22
 EXPNO 1
 PROCNO 1

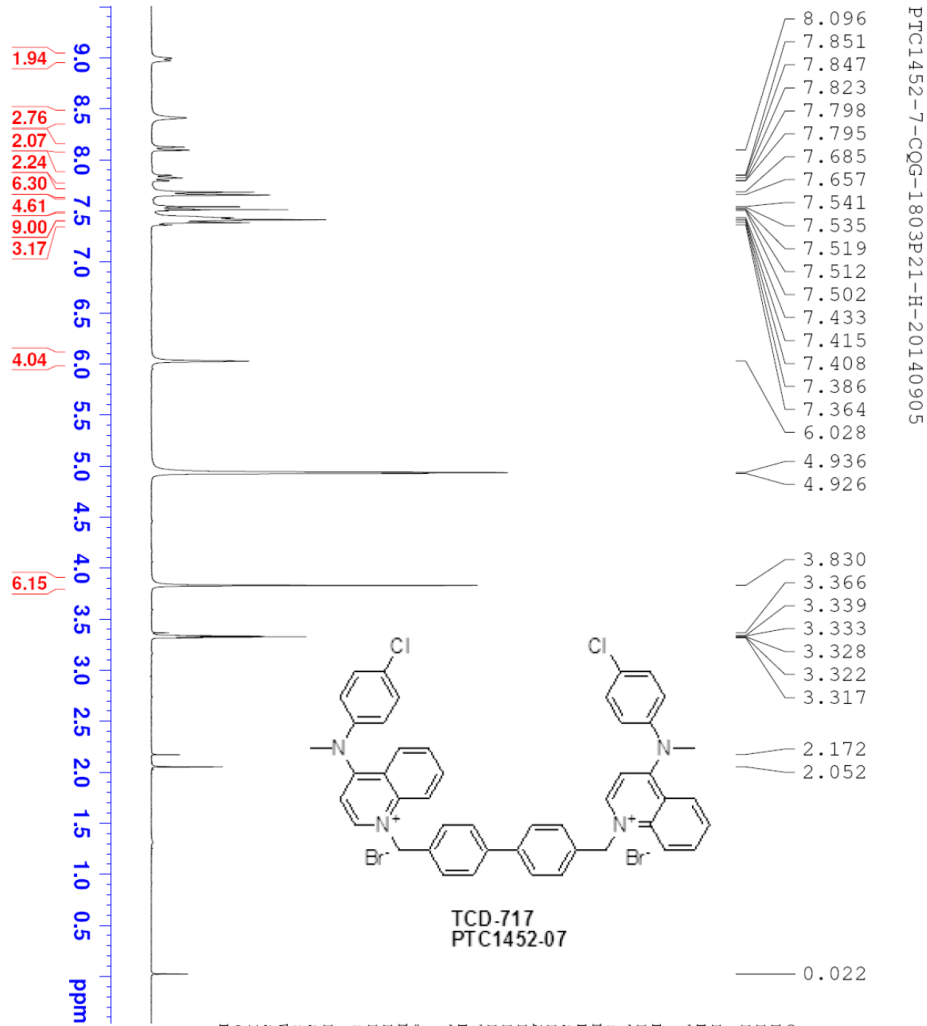
F2 - Acquisition Parameters
 Date_ 20140826
 Time 16.41
 INSTRUM spect
 PROBD 5 mm PABBO BB/
 PULPROG zg30
 TD 65536
 SOLVENT CDCl3
 NS 16
 DS 2
 SFO1 8012.820 HZ
 FIDPRES 0.122266 HZ
 AQ 4.089495 sec
 RG 147.75
 DW 62.400 usec
 DE 6.50 usec
 TE 298.0 K
 D1 1.00000000 sec
 TDO 1

===== CHANNEL f1 =====
 SFO1 400.1324710 MHz
 NUC1 1H
 P1 10.00 usec
 PLW1 16.00000000 W

F2 - Processing parameters
 SI 65536
 SF 400.1300928 MHz
 WDW EM
 SSB 0
 LB 0
 GE 0
 PC 1.00

[Return](#)

¹H NMR of compound PTC1452-07



Current Data Parameters
 NAME PTC1452-7-CQG-1803P21
 EXPNO 1
 PROCNO 1

F2 - Acquisition Parameters
 Date_ 20140905
 Time 12.14
 INSTRUM spect
 PROBHD 5 mm PABBO BB-
 PULPROG zg30
 TD 65536
 SOLVENT MeOD
 NS 19
 DS 2
 SFRH 6172.839 Hz
 FIDRES 0.094190 Hz
 AQ 5.3084660 sec
 RG 161.3
 DW 81.000 usec
 DE 6.00 usec
 TE 294.7 K
 D1 1.00000000 sec
 TD0 1

===== CHANNEL f1 =====
 NUCL1 1H
 P1 12.70 usec
 PL1 0.00 dB
 SF01 300.1318594 MHz

F2 - Processing Parameters
 SI 32768
 SF 300.1300000 MHz
 MDW no
 SSB 0
 LB 0.00 Hz
 GB 0
 PC 1.00



[Return](#)

APPENDIX 4

Synthesis and characterization of cycloJAS239 (PTC1452-08)

Procedure for PTC1452-08

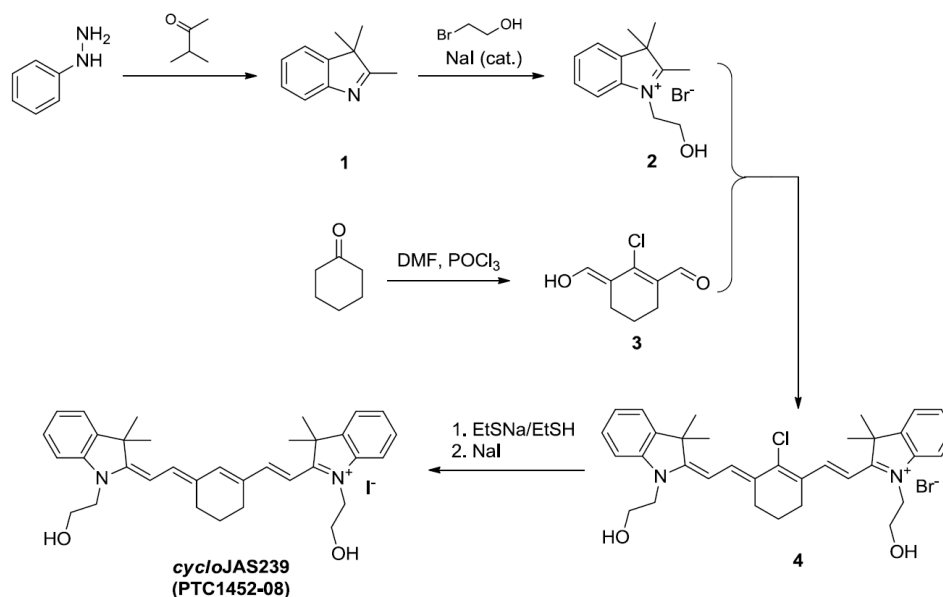
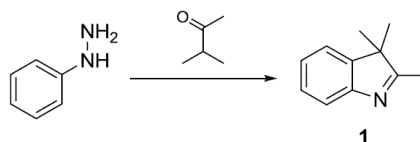
Prepared by: Haiming Wang 11/10/2014

PhD, Senior Scientist

Approved by: Xiaowen Sun 11/10/2014

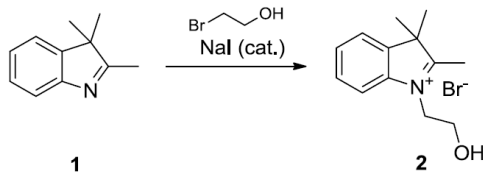
PhD, Director of Med. Chem.

PepTech Corporation
(Shanghai)

Scheme for PTC1452-08**Experiment Procedure****Preparation of compound 1**

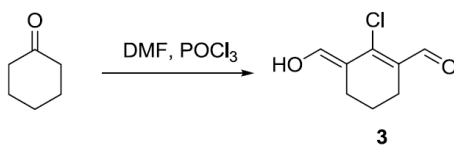
To a mixture of phenylhydrazine (5.5 g, 50 mmol) and glacial acetic acid (50 mL) was added 3-methylbutanone (4.4 g, 60 mmol). The reaction mixture was heated under reflux for 5 h and then cooled to room temperature. The volatiles were removed under vacuum and the residue was dissolved in EtOAc (100 mL). The resulting solution was washed with water (100 mL) and the aqueous phase was re-extracted with EtOAc (100 mL). The combined organic layers were dried over anhydrous sodium sulfate and concentrated to afford compound **1** (6.3 g, 80% yield), which was used directly in the next step without further purification.

¹H NMR (400 MHz, CDCl₃): δ 7.51 (d, *J* = 8.0 Hz, 1H), 7.22-7.30 (m, 2H), 7.17-7.22 (m, 1H), 2.28 (s, 3H), 1.30 (s, 6H).

Preparation of compound 2

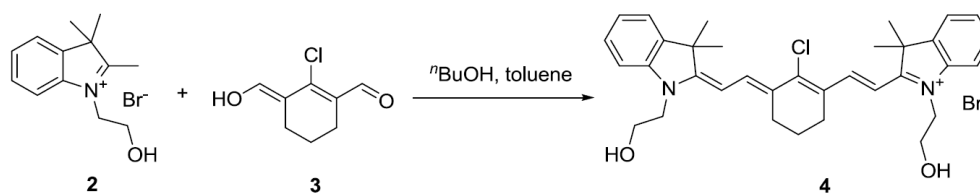
To a solution of 2,3,3-trimethylindolenine **1** (2.6 g, 16.0 mmol) in CH_3CN (20 mL) were added 2-bromoethanol (2.5 g, 20.0 mmol) and NaI (0.24 g, 1.6 mmol) at room temperature. The reaction mixture was heated at 110°C under microwave conditions for 2 h and then cooled to room temperature. The resulting precipitate was collected by filtration and washed with acetone to afford compound **2** (2.2 g, 73% yield) as a pale yellow solid.

$^1\text{H NMR}$ (400 MHz, D_2O): δ 7.67-7.72 (m, 2H), 7.53-7.58 (m, 2H), 4.58 (t, $J = 5.2$ Hz, 2H), 4.04 (t, $J = 5.2$ Hz, 2H), 2.73-2.77 (m, 3H), 1.52(s, 6H).

Preparation of compound 3

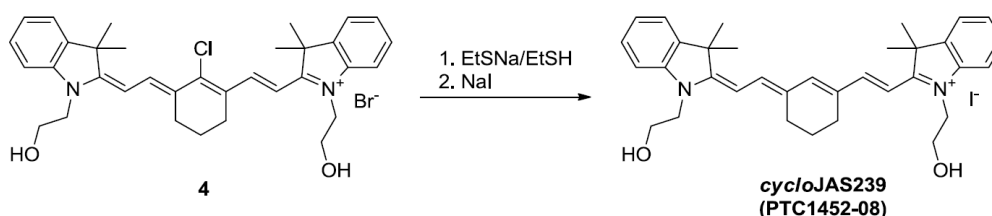
To a solution of *N,N*-dimethylformamide (20 mL, 273 mmol) in CH_2Cl_2 (80 mL) was added dropwise a solution of POCl_3 (17.5 ml, 115 mmol) in DCM (20 mL) under N_2 atmosphere at 0°C . The mixture was stirred for 30 min at 0°C and cyclohexanone (5 g, 50 mmol) was added. The reaction mixture was refluxed with vigorous stirring for 3 h and then poured into ice-water. The resulting mixture was kept overnight to afford compound **3** (6.5 g, 74% yield) as a yellow solid.

$^1\text{H NMR}$ (400 MHz, CDCl_3): δ 8.95 (br s, 1H), 2.47 (t, $J = 6.0$ Hz, 4H), 1.71 (quint, $J = 6.0$ Hz, 2H).

Preparation of compound 4

To a solution of compound **3** (0.17 g, 1.0 mmol) in *n*-butanol/toluene (7:3, 50 mL) was added compound **2** (0.57 g, 2.0 mmol) under N₂ atmosphere. The reaction mixture was refluxed at 150°C for 5 h with a Dean-Stark apparatus and then cooled to room temperature. The resulting precipitate was collected by filtration and washed with ether to afford compound **4** (0.46 g, 73% yield) as a green solid.

¹H NMR (400 MHz, CDCl₃): δ 8.35 (d, *J* = 13.6 Hz, 2H), 7.26-7.40 (m, 4H), 7.20- 6.27 (m, 4H), 6.55 (d, *J* = 13.6 Hz, 2H), 4.38 (m, 4H), 4.03-4.07 (m, 4H), 2.84 (m, 4H), 1.97-2.04 (m, 6H), 1.73 (s, 12H).

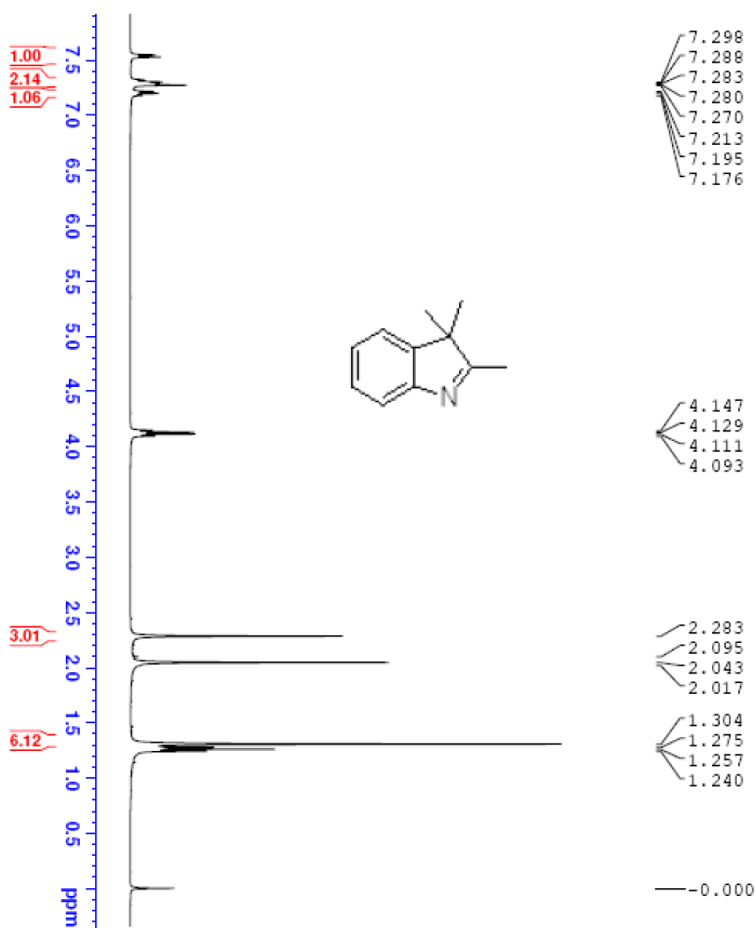
Preparation of compound PTC1452-08

To a solution of compound **4** (0.12 g, 0.19 mmol) in DMF (5 mL) were added Et₃SNa (0.26 g, 3.10 mmol) and EtSH (2 mL) at room temperature. The reaction mixture was stirred overnight at room temperature. The solvent was evaporated and the residue was dissolved in DCM. The resulting solution was washed with saturated aqueous NaI (20 mL × 2) and then concentrated under reduced pressure. The residue was purified by flash column chromatography on silica gel (DCM/MeOH = 50:1) in combination with prep-HPLC to afford compound **PTC1452-08** (50 mg, 10% yield) as a green solid.

¹H NMR (400 MHz, DMSO-*d*₆): δ 7.62-7.68 (m, 3H), 7.57 (d, *J* = 6.8 Hz, 2H), 7.35-7.40 (m, 4H), 7.20- 6.23 (m, 2H), 6.25 (d, *J* = 13.6 Hz, 2H), 5.03 (br s, 2H), 4.20 (m, 4H), 3.37 (m, 4H), 2.50 (m, 4H), 1.81 (m, 2H), 1.67 (s, 12H).

NMR Spectra

¹H NMR of compound 1



PTC1452-D52-P81-H-20140722



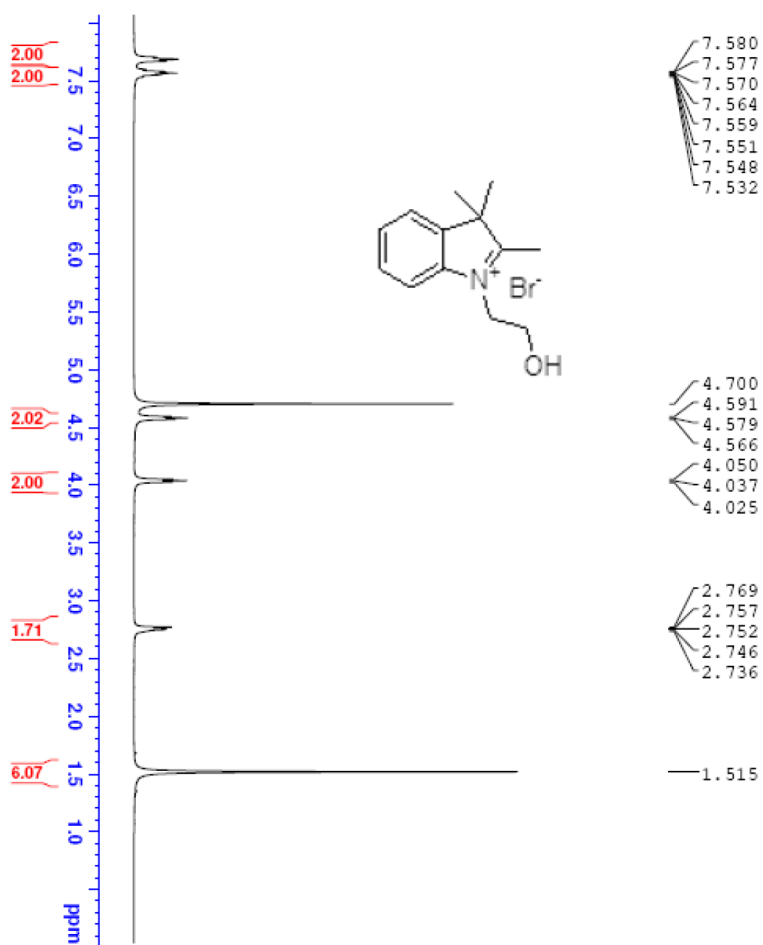
Current Data Parameters
 NAME PTC1452-D52-P81
 EXPNO 1
 PROCNO 1

F2 - Acquisition Parameters
 Date_ 20140722
 Time 11.27
 INSTRUM spect
 PROBRD 5 mm PABBO BB/
 PULPROS zq30
 TD 65536
 SOLVENT CDCl3
 NS 16
 DS 2
 SMF 8012.820 Hz
 FIDRES 0.122266 Hz
 AQ 4.089485 sec
 Rg 50.71
 DM 62.900 usec
 DE 6.50 usec
 TE 298.0 K
 D1 1.00000000 sec
 TD0 1

CHANNEL f1
 SFO1 400.1324710 MHz
 NUCL1 1H
 P1 10.00 usec
 PLW1 16.000000000 W
F2 - Processing parameters
 SI 65536
 SF 400.130056 MHz
 WDW EM
 SSB 0
 GB 0
 PC 1.00
 LB 0.30 Hz

[Return](#)

¹H NMR of compound 2



PTC1452-DGZ-P85-1-H-20140729



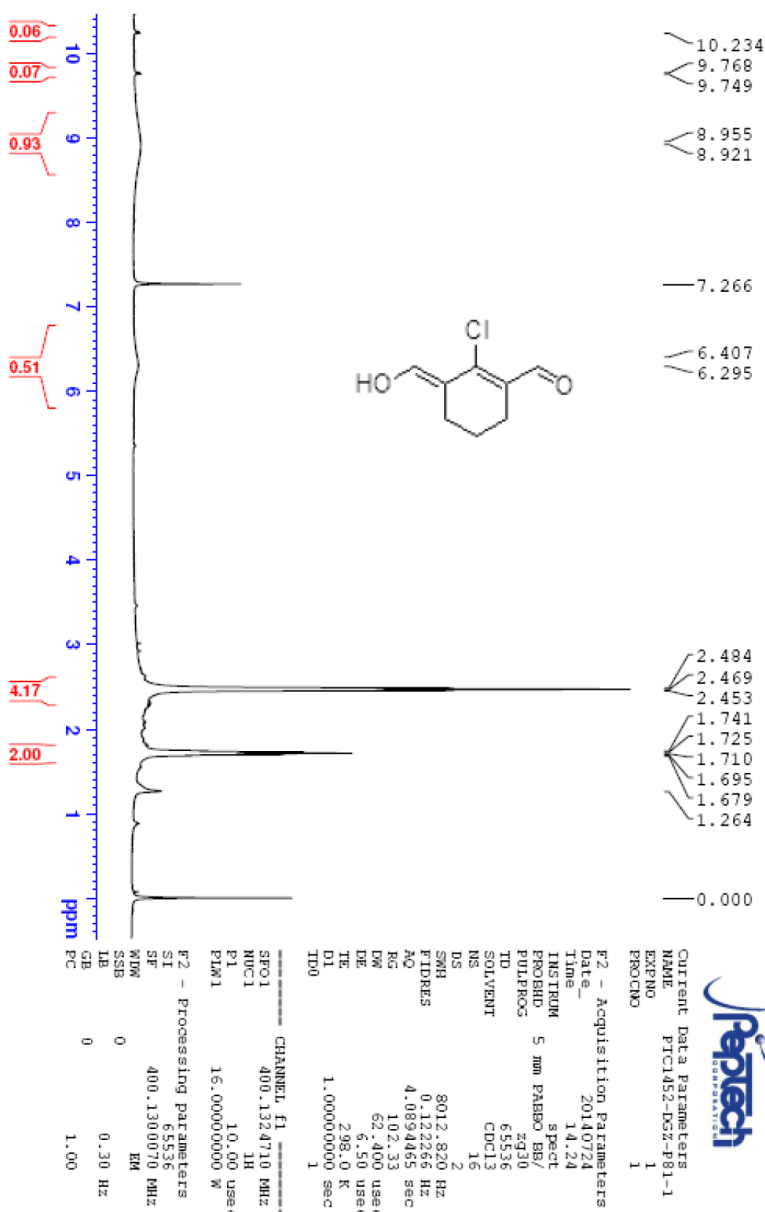
Current Data Parameters
 NAME PTC1452-DGZ-P85-1
 EXPNO 1
 PROCNO 1

F2 - Acquisition Parameters
 Date_ 20140729
 Time 12:51
 INSTRUM spect
 FPROBHD 5 mm PABBO BBO
 PULPROG zgpg30
 TD 65536
 SOLVENT D2O
 NS 15
 DS 2
 SWH 8012.820 Hz
 FIDRES 0.122286 Hz
 AQ 4.089485 sec
 RG 74.48
 DW 62.400 usec
 DE 6.50 usec
 TE 298.0 K
 D1 1.00000000 sec
 TD0 1

CHANNEL f1
 SFO1 400.1324710 MHz
 NUQC1 1H
 P1 10.00 usec
 PLM1 16.000000000 W
 F2 - Processing parameters
 SI 65536
 SF 400.1300000 MHz
 WDW EM
 SSB 0
 LB 0.30 Hz
 GB 0
 PC 1.00

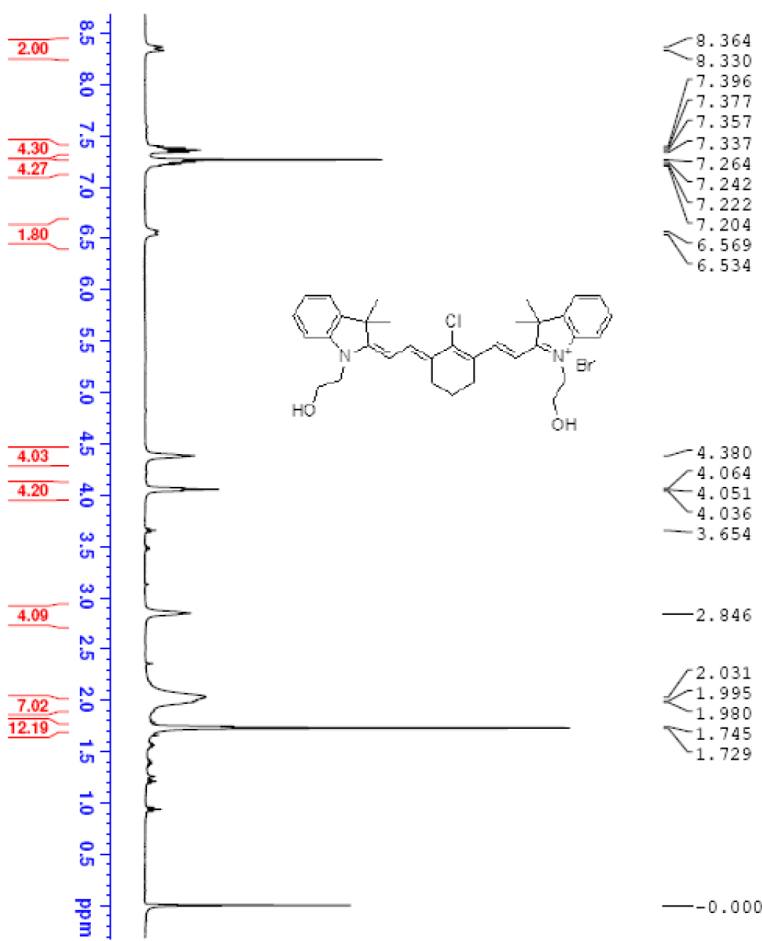
[Return](#)

¹H NMR of compound 3



[Return](#)

¹H NMR of compound 4



PTC1452-D52-P93-1-H-20140811

Current data Parameters
 NAME PTC1452-D52-P93-1
 EXTNO 1
 PROCNO 1



F2 - Acquisition Parameters
 Date_ 20140811
 Time 15:56
 INSTRUM spect
 PROBRD 5 mm EBB90 B8/
 PULPROG zg30
 TD 65536
 ID C0C13
 SOLVENT CDCl3
 NS 16
 DS 2
 SWH 8012.820 Hz
 FIDRES 0.124265 Hz
 AQ 4.089465 sec
 RG 116.94
 LW 62.400 usec
 DE 6.50 usec
 TE 298.0 K
 DI 1.000000000 sec
 ID0 1

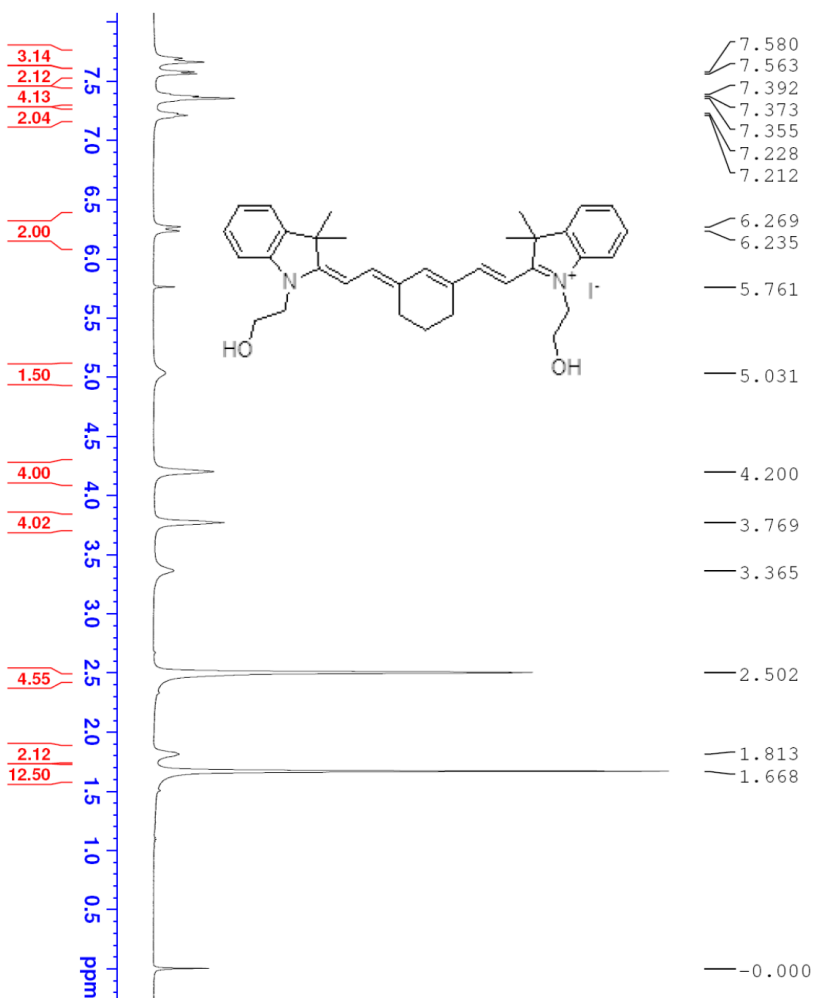
CHANNEL f1
 SFO1 400.1324710 MHz
 NUCL1 1H
 P1 10.00 usec
 PLW1 16.000000000 W

F2 - Processing parameters
 SI 65536
 SF 400.130086 MHz
 WDM EM
 SSB 0
 LB 0.30 Hz
 GB 0
 PC 1.00

[Return](#)

¹H NMR of compound PTC1452-08

PTC1452-08-DGZ-1863P01-2-H-20140915



Current Data Parameters
 NAME PTC1452-08-DGZ-1863P01-2
 EXPNO 1
 PROCNO 1

F2 - Acquisition Parameters
 Date_ 20140915
 Time 12.02
 INSTRUM spect
 PULPROG zgpg30
 FIDRES 0.122266 Hz
 AQ 4.0894465 sec
 RG 116.94
 DM 62.440 usec
 DE 295.2 K
 TE 295.2 K
 D1 1.00000000 sec
 TD0 1

CHANNEL F1
 SFO1 400.1324710 MHz
 NUCL1 1H
 P1 10.00 usec
 PLM1 16.00000000 W

F2 - Processing parameters
 SFO2 400.1300019 MHz
 SF 400.1300019 MHz
 EM
 SSB 0
 WBW 0
 GB 0
 PC 1.00



[Return](#)

APPENDIX 5

Synthesis and characterization of cycloJAS239.5 (PTC1452-09)

Procedure for PTC1452-09

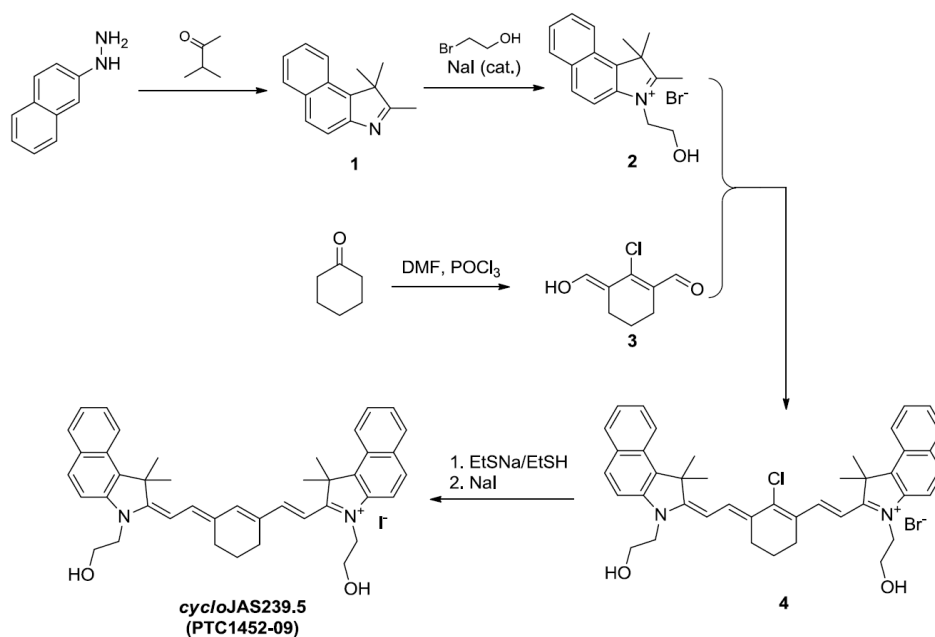
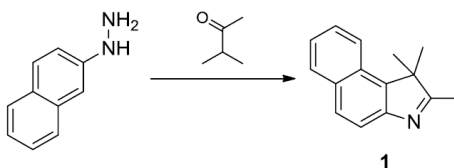
Prepared by: Haiming Wang 11/10/2014

PhD, Senior Scientist

Approved by: Xiaowen Sun 11/10/2014

PhD, Director of Med. Chem.

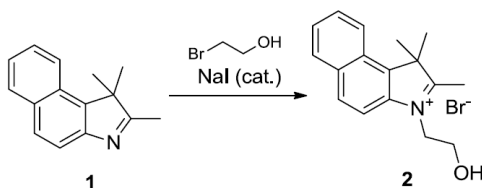
PepTech Corporation
(Shanghai)

Scheme for PTC1452-09**Experiment Procedure****Preparation of compound 1**

To a mixture of 2-naphthylhydrazine hydrochloride (5.0 g, 25.7 mmol) and glacial acetic acid (50 mL) was added 3-methylbutanone (4.4 g, 60 mmol). The reaction mixture was heated under reflux for 5 h and then cooled to room temperature. The volatiles were removed under vacuum and the residue was dissolved in EtOAc (100 mL). The resulting solution was washed with water (100 mL) and the aqueous phase was re-extracted with EtOAc (100 mL). The combined organic layers were dried over anhydrous sodium sulfate and concentrated to afford compound **1** (3.8 g, 71% yield) as a brown solid. The material was used directly in the next step without further purification.

¹H NMR (400 MHz, CDCl₃): δ 8.03 (d, *J* = 8.4 Hz, 1H), 7.94 (d, *J* = 8.4 Hz, 1H), 7.83 (d, *J* = 8.4 Hz, 1H), 7.78 (d, *J* = 8.4 Hz, 1H), 7.55 (dt, *J* = 1.2, 8.0 Hz, 1H), 7.44 (dt, *J* = 1.2, 8.0 Hz, 1H), 2.38 (s, 3H), 1.55 (s, 6H).

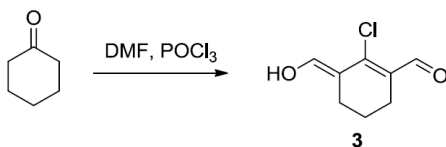
Preparation of compound 2



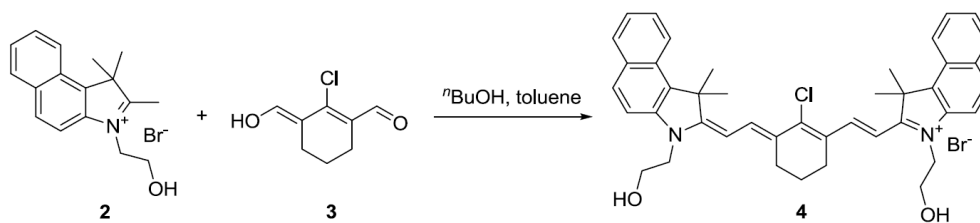
To a solution of compound **1** (5.9 g, 28.2 mmol) in CH₃CN (20 mL) were added 2-bromoethanol (7.1 g, 56.5 mmol) and NaI (0.9 g, 6.0 mmol) at room temperature. The reaction mixture was heated at 110°C under microwave conditions for 2 h and then cooled to room temperature. The resulting precipitate was collected by filtration and washed with ether to afford compound **2** (7.2 g, 76% yield) as a black solid.

¹H NMR (400 MHz, DMSO-*d*₆): δ 8.38 (d, *J* = 8.8 Hz, 1H), 8.28 (d, *J* = 8.8 Hz, 1H), 8.21 (d, *J* = 8.8 Hz, 1H), 8.15 (d, *J* = 8.8 Hz, 1H), 7.80 (t, *J* = 7.2 Hz, 1H), 7.73 (t, *J* = 7.2 Hz, 1H), 4.73 (t, *J* = 4.8 Hz, 1H), 3.94 (t, *J* = 4.8 Hz, 1H), 2.93 (s, 3H), 1.78 (s, 6H).

Preparation of compound 3

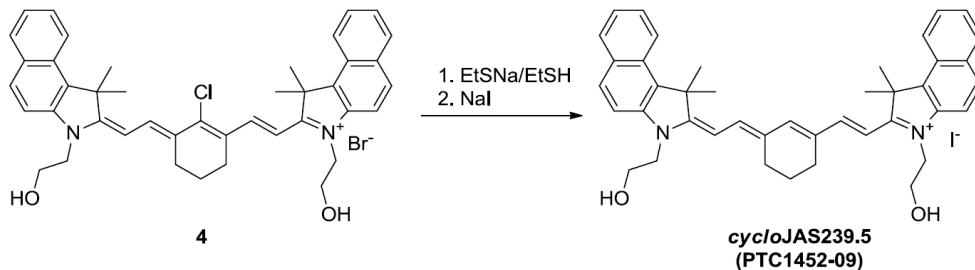


See its preparation in “*Procedure for PC1452-08*”.

Preparation of compound 4

To a solution of compound **3** (1.25 g, 7.2 mmol) in *n*-butanol/toluene (7:3, 200 mL) was added compound **2** (5.1 g, 14.5 mmol) under N₂ atmosphere. The reaction mixture was refluxed at 150°C for 5 h with a Dean-Stark apparatus and then cooled to room temperature. The resulting precipitate was collected by filtration and washed with ether to afford compound **4** as a green solid (4.3 g, 84% yield).

¹H NMR (400 MHz, DMSO-*d*₆): δ 8.38 (d, *J* = 14.0 Hz, 2H), 8.31 (d, *J* = 8.8 Hz, 2H), 8.05-8.10 (m, 4H), 7.78 (d, *J* = 9.2 Hz, 2H), 7.66 (t, *J* = 7.2 Hz, 2H), 7.53 (t, *J* = 7.2 Hz, 2H), 6.48 (d, *J* = 14.4 Hz, 2H), 5.12 (t, *J* = 4.8 Hz, 2H), 4.43 (m, 4H), 3.84-3.88 (m, 4H), 2.70-2.77 (m, 4H), 1.90-2.00 (m, 14H).

Preparation of compound PTC1452-09

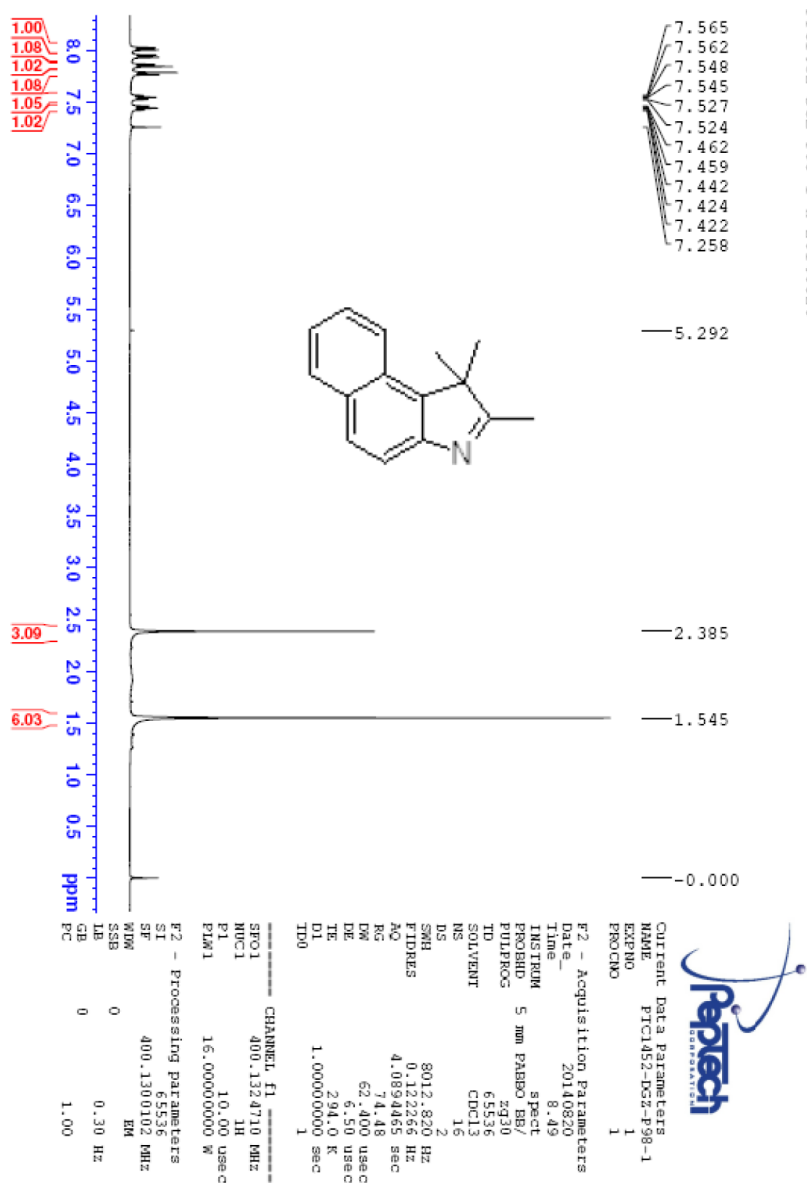
To a solution of compound **4** (0.5 g, 0.69 mmol) in DMF (20 mL) were added EtSNa (1.5 g, 17.8 mmol) and EtSH (20 mL) at room temperature. The reaction mixture was stirred at 40°C overnight. The solvent was evaporated and the residue was dissolved in DCM. The resulting solution was washed with saturated aqueous NaI (20 mL × 2) and then concentrated under reduced pressure. The residue was purified by flash column chromatography on silica gel (DCM/MeOH = 50:1) in combination with prep-HPLC to afford compound **PTC1452-09** (50 mg, 10% yield) as a green solid.

¹H NMR (400 MHz, CD₃OD): δ 8.23 (d, *J* = 8.0 Hz, 2H), 7.87 (d, *J* = 8.0 Hz, 4H), 7.87 (t, *J* = 13.6

Hz, 2H), 7.57-7.65 (m, 4H), 7.44-7.51 (m, 4H), 6.33 (d, $J = 14.0$ Hz, 2H), 4.35 (m, 4H), 4.00 (m, 4H), 2.60 (m, 4H), 2.04 (s, 12H), 1.95-2.02 (m, 2H).

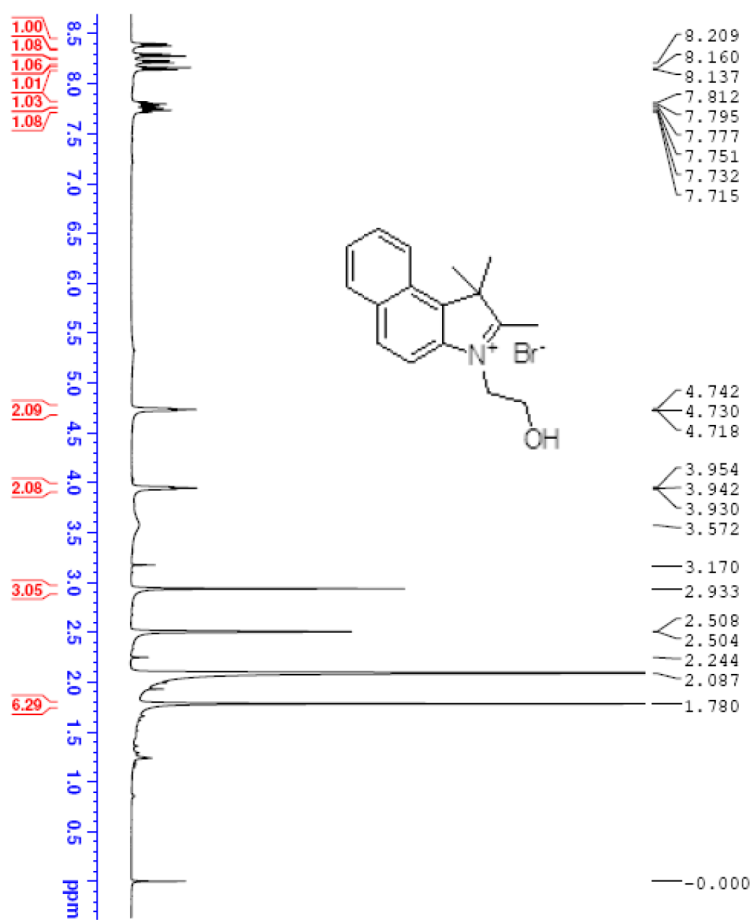
NMR Spectra

¹H NMR of compound 1



[Return](#)

¹H NMR of compound 2



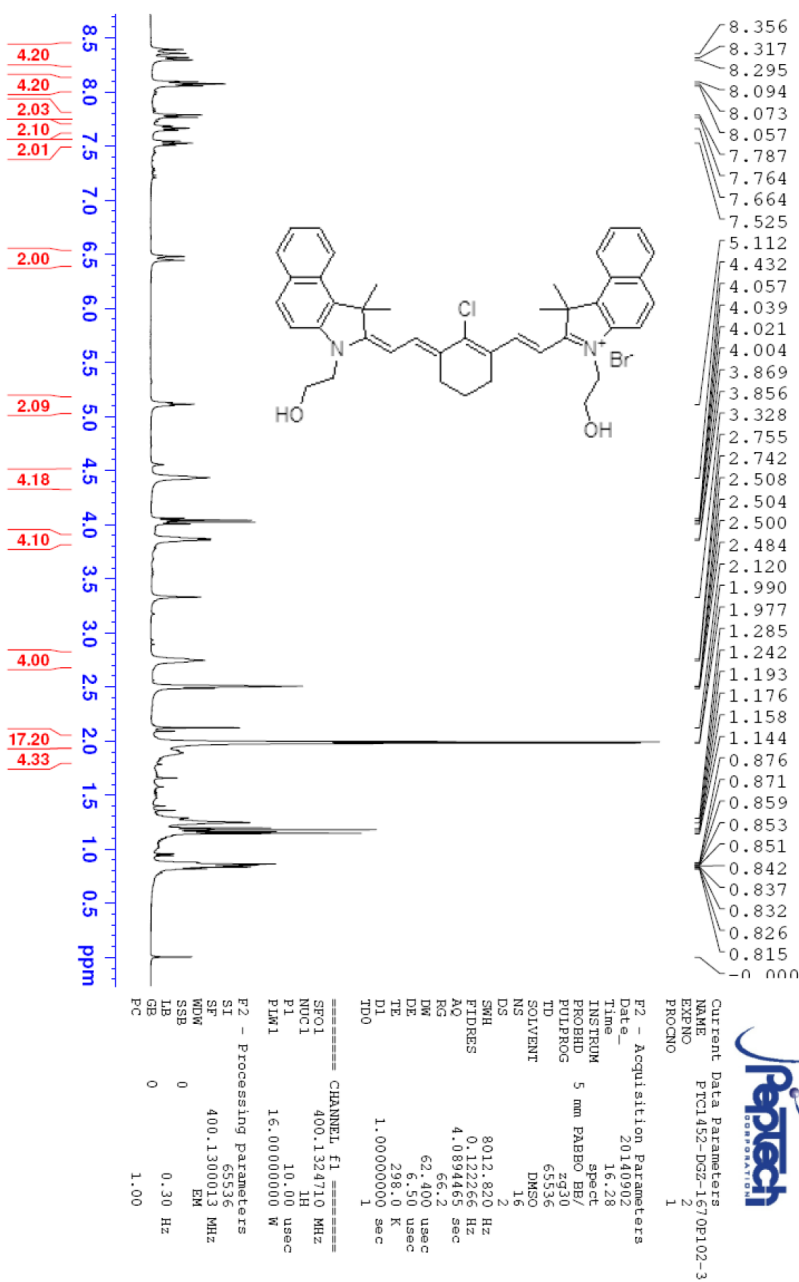
PTC1452-D5Z-1670P102-3-H-20140829

Current Data Parameters
 NAME PTC1452-D5Z-1670P102-3
 EXPNO 1
 PROCNO 1
 F2 - Acquisition Parameters
 Date_ 20140829
 Time 16.20
 INSTRUM spect
 PULPROG zgpg30
 PROBRD 5 mm PABBO BB/
 TD 65536
 SOLVENT DMSO
 NS 1
 DS 2
 SSB 8012.820 Hz
 FTIDRES 0.122216 Hz
 AQ 4.089465 sec
 RG 81.42
 DW 62.400 usec
 DE 6.50 usec
 TE 298.0 K
 TL 1.00000000 sec
 TDO 1
 ===== CHANNEL f1 =====
 SFO1 400.1324710 MHz
 NUCL1 1H
 P1 10.00 usec
 PL1 16.00000000 W
 FWH1
 F2 - Processing parameters
 SI 65536
 SF 400.1300012 MHz
 NIEM EM
 SSB 0
 LB 0
 GB 0
 PC 1.00



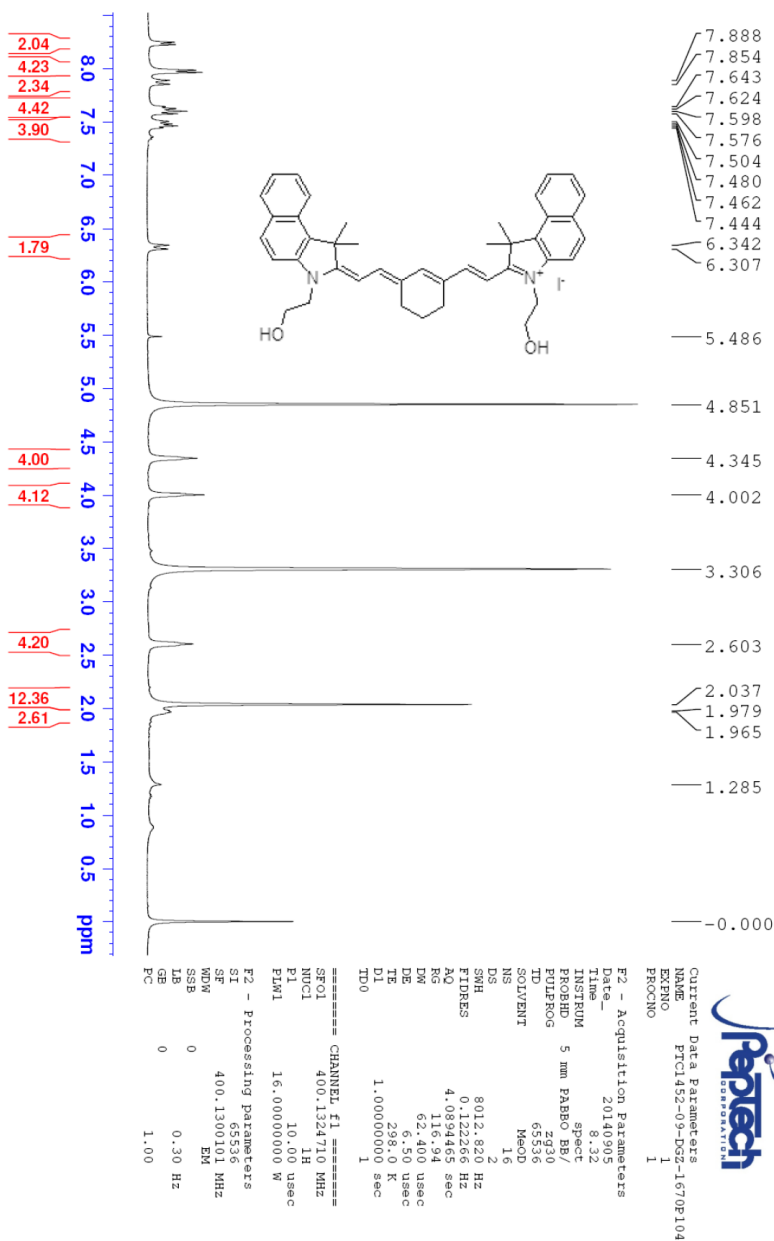
[Return](#)

¹H NMR of compound 4



[Return](#)

¹H NMR of compound PTC1452-09



[Return](#)

APPENDIX 6

Synthesis and characterization of cycloHITC (PTC1452-10)

Procedure for PTC1452-10

Prepared by: Haiming Wang 11/11/2014

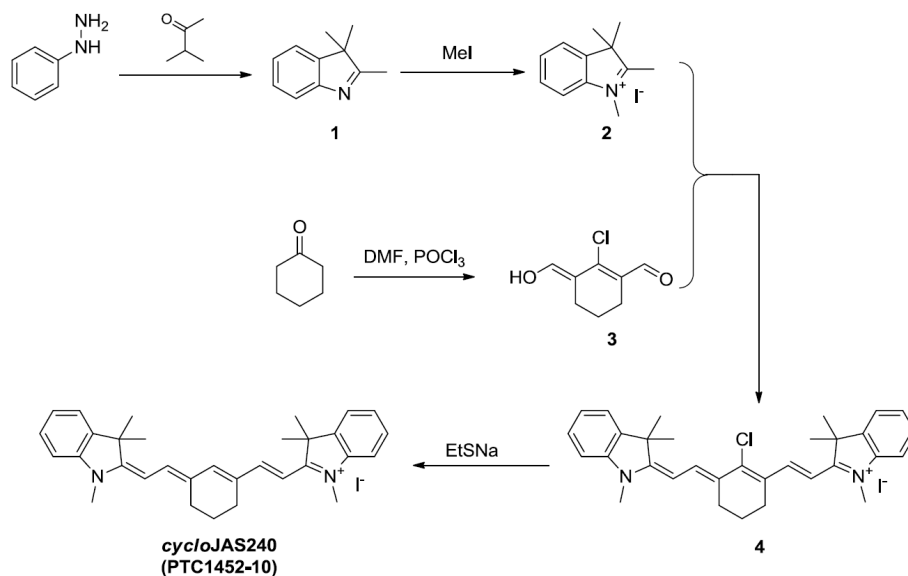
PhD, Senior Scientist

Approved by: Xiaowen Sun 11/11/2014

PhD, Director of Med. Chem.

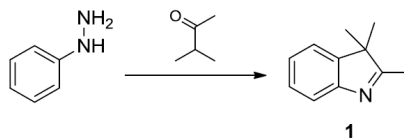
PepTech Corporation
(Shanghai)

Scheme for PTC1452-10



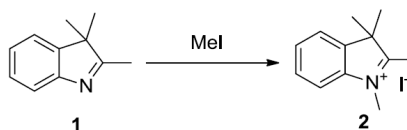
Experiment Procedure

Preparation of compound 1



See its preparation in “*Procedure for PC1452-08*”.

Preparation of compound 2

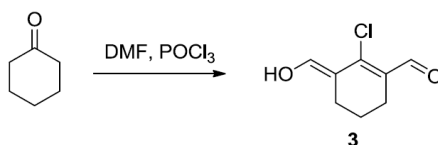


To a solution of compound **1** (1.6 g, 10.0 mmol) in CH₃CN (20 mL) was added methyl iodide (3.5 g, 25.0 mmol) at room temperature. The reaction mixture was heated at 80°C under microwave conditions for 30 min and then cooled to room temperature. The resulting precipitate was collected

by filtration and washed with ether to afford compound **2** (2.2 g, 73% yield) as a pale red powder.

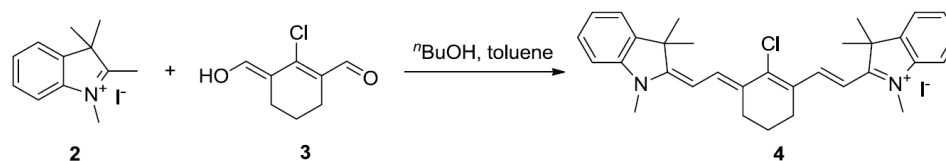
¹H NMR (400 MHz, D₂O): δ 7.63-7.65 (m, 2H), 7.53-7.57 (m, 2H), 3.93 (s, 3H), 2.69 (br s, 3H), 1.48 (s, 6H).

Preparation of compound **3**



See its preparation in “Procedure for PC1452-08”.

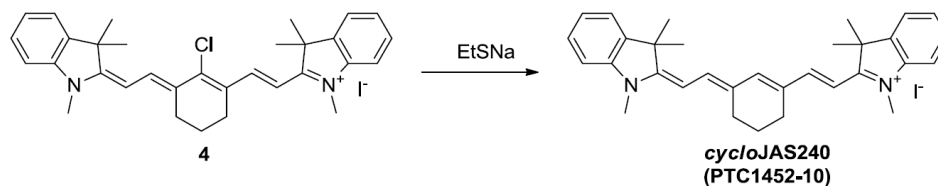
Preparation of compound **4**



To a solution of compound **3** (0.17 g, 1.0 mmol) in *n*-butanol/toluene (7/3, 50 mL) was added compound **2** (0.62 g, 2.0 mmol) under N₂ atmosphere. The reaction mixture was refluxed at 150°C for 5 h with a Dean-Stark apparatus and then cooled to room temperature. The resulting precipitate was collected by filtration and washed with ether to afford compound **4** (0.56 g, 92%) as a green solid.

¹H NMR (400 MHz, CDCl₃): δ 8.35 (d, *J* = 14.0 Hz, 2H), 7.36-7.43 (m, 4H), 7.25 (t, *J* = 7.2 Hz, 2H), 7.18 (d, *J* = 8.0 Hz, 2H), 6.26 (d, *J* = 14.0 Hz, 2H), 3.77 (s, 6H), 2.78 (t, *J* = 6.0 Hz, 4H), 1.93-2.01 (m, 2H), 1.73 (s, 12H).

Preparation of compound PTC1452-10

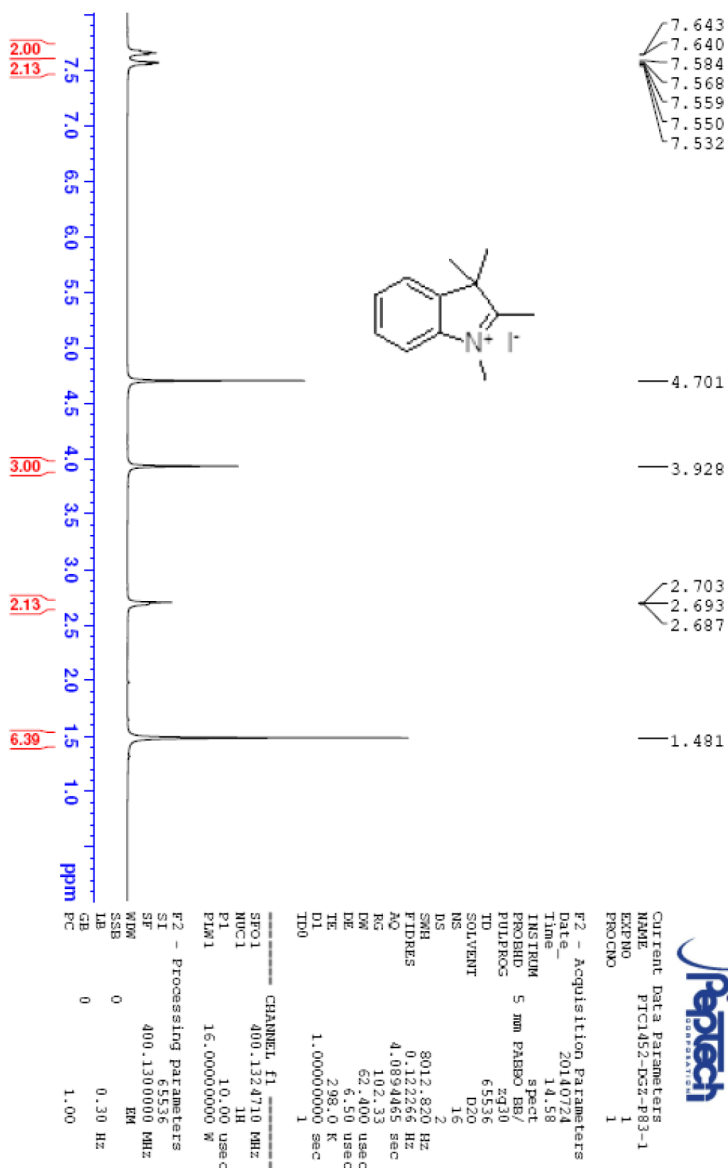


To a solution of compound **4** (1.0 g, 1.64 mmol) in DMF (20 mL) were added EtSNa (2.6 g, 31.0 mmol) and Ph₂PH (5.9 g, 31.5 mmol) at room temperature. The reaction mixture was stirred at room temperature overnight. The solvent was evaporated and the residue was purified by flash column chromatography on silica gel (DCM/MeOH = 50:1) in combination with prep-HPLC to afford compound **PTC1452-10** (34 mg, 3.6% yield) as a green solid.

¹H NMR (400 MHz, CDCl₃): δ 7.71 (br s, 3H), 7.33-7.36 (m, 4H), 7.20 (t, *J* = 7.2 Hz, 2H), 7.10 (d, *J* = 7.6 Hz, 2H), 6.03 (d, *J* = 13.6 Hz, 2H), 3.66 (s, 6H), 2.51-2.54 (m, 4H), 1.91-1.97 (m, 2H), 1.73 (s, 12H).

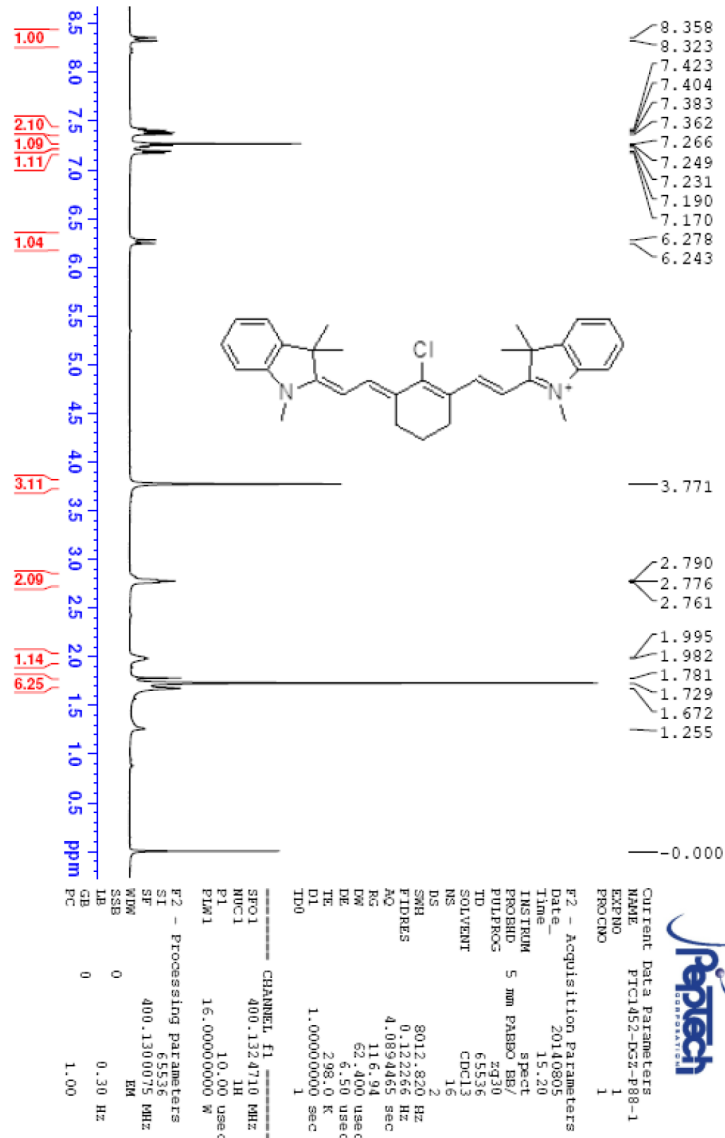
NMR Spectra

¹H NMR of compound 2



[Return](#)

¹H NMR of compound 4

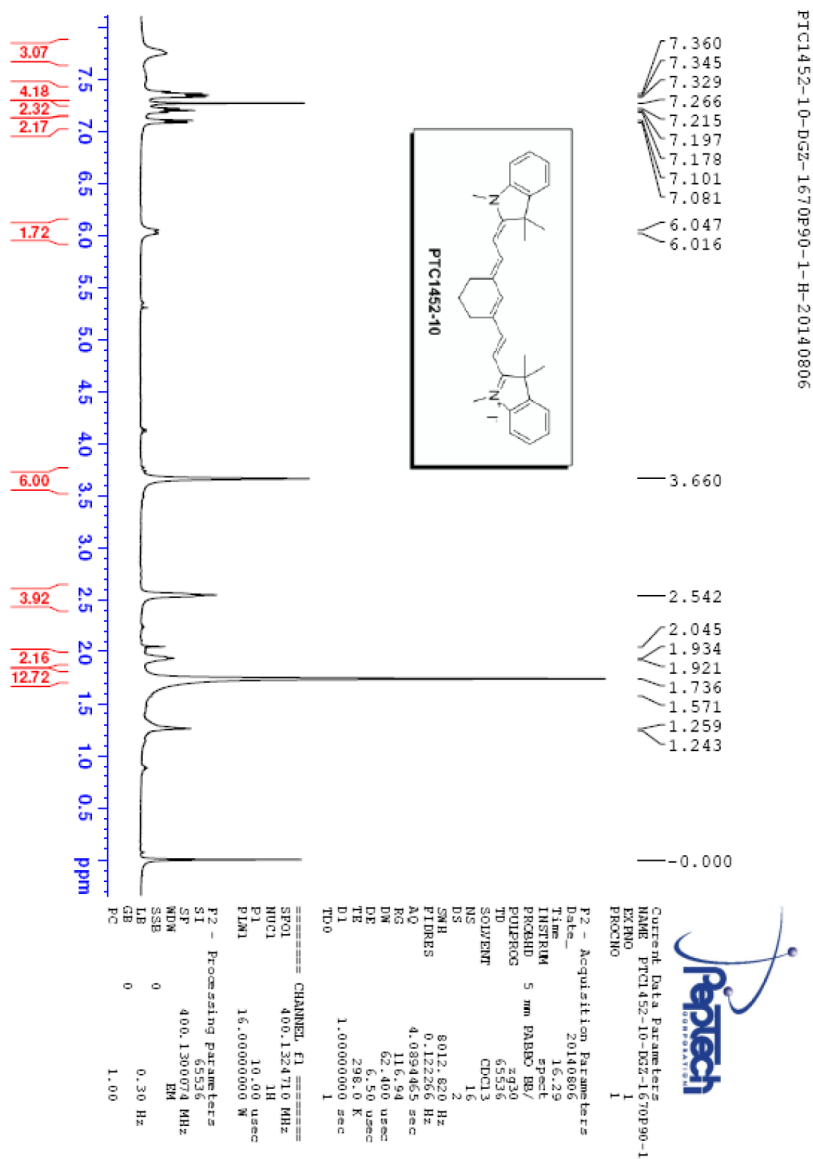


PTC1452-D52-P88-1-H-20140805



[Return](#)

¹H NMR of compound PTC1452-10



[Return](#)

APPENDIX 7

Synthesis and characterization of cycloHITC.5 (PTC1452-11)

Procedure for PTC1452-11

Prepared by: Haiming Wang 11/11/2014

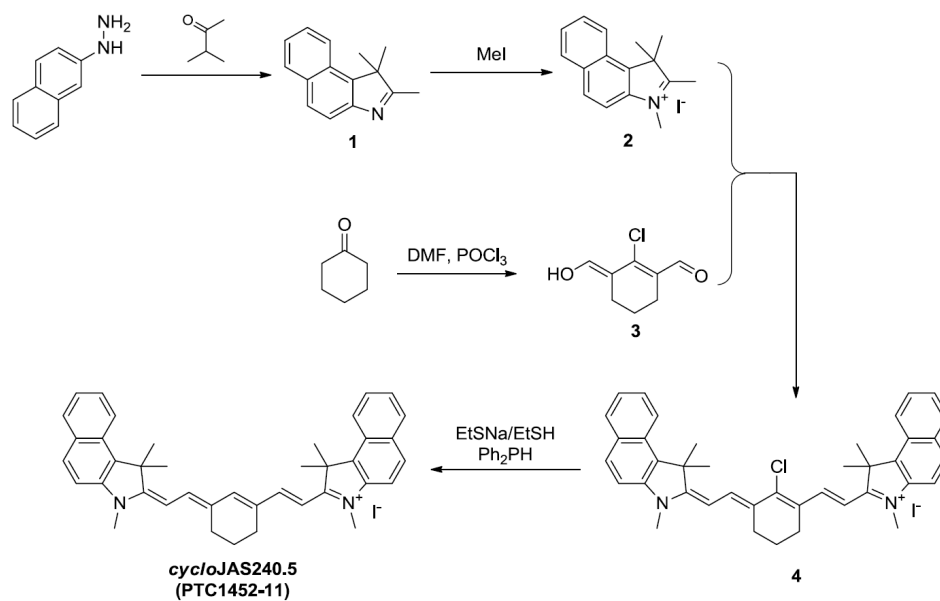
PhD, Senior Scientist

Approved by: Xiaowen Sun 11/11/2014

PhD, Director of Med. Chem.

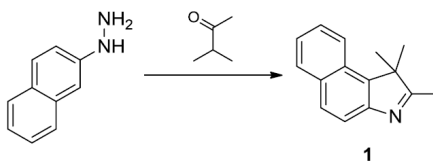
PepTech Corporation
(Shanghai)

Scheme for PTC1452-11



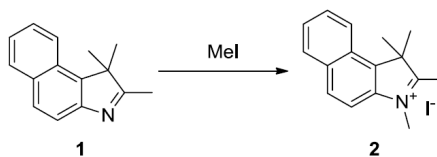
Experiment Procedure

Preparation of compound 1

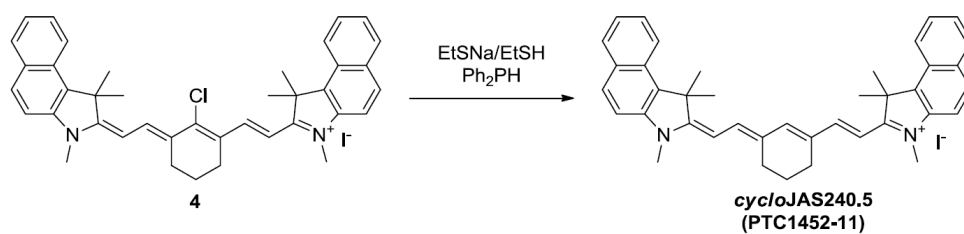


See its preparation in "Procedure for PC1452-09".

Preparation of compound 2



To a solution of compound **1** (2.0 g, 9.6 mmol) in CH₃CN (20 mL) was added methyl iodide (6.8 g,

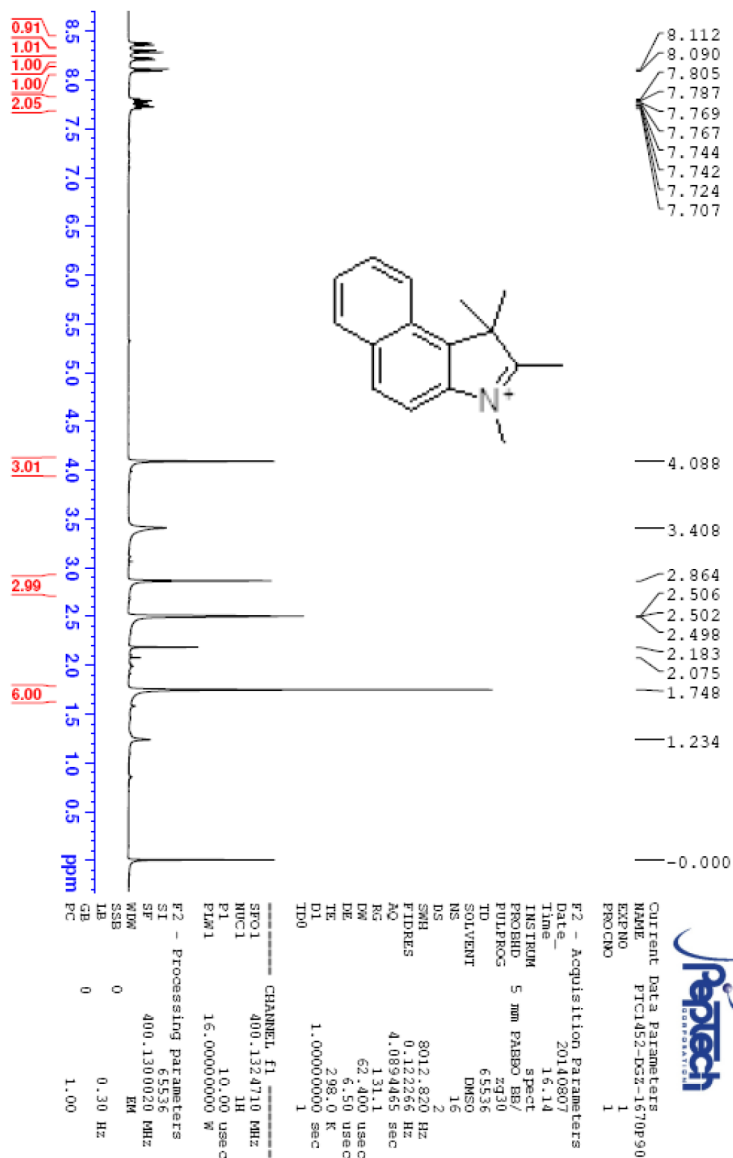
Preparation of compound PTC1452-11

To a solution of compound **4** (2.3 g, 3.0 mmol) in DMF (20 mL) were added EtSNa (5.2 g, 62.0 mmol), EtSH (5.0 g, 60.0 mmol) and Ph₂PH (11.8 g, 63.0 mmol) at room temperature. The reaction mixture was stirred at room temperature overnight. The solvent was evaporated and the residue was purified by flash column chromatography on silica gel (DCM/MeOH = 50:1) in combination with prep-HPLC to afford compound **PTC1452-11** (250 mg, 12% yield) as a green solid.

¹H NMR (400 MHz, CDCl₃): δ 8.15 (d, *J* = 8.4 Hz, 2H), 7.83-7.94 (m, 7H), 7.60 (t, *J* = 7.6 Hz, 2H), 7.45 (t, *J* = 7.6 Hz, 2H), 7.39 (d, *J* = 8.8 Hz, 2H), 6.06 (d, *J* = 12.4 Hz, 2H), 3.78 (s, 6H), 2.56 (br s, 4H), 2.04 (s, 12H), 1.93-1.99 (m, 2H).

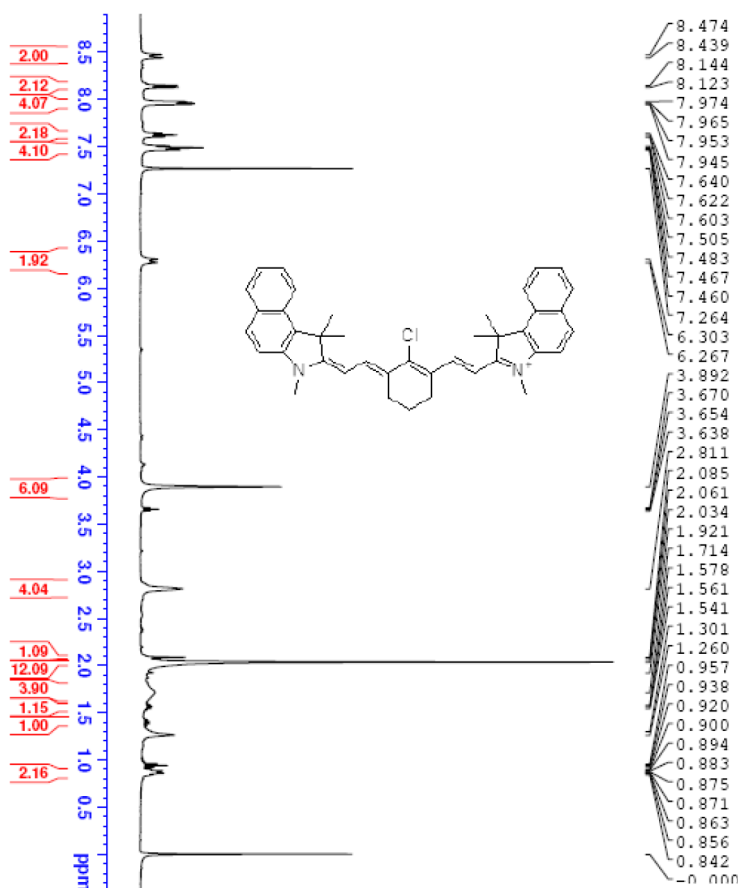
NMR Spectra

¹H NMR of compound 2



[Return](#)

¹H NMR of compound 4



PTC1452-D52-P93-2-H-20140811

8.474
8.439
8.144
8.123
7.974
7.965
7.953
7.945
7.640
7.622
7.603
7.505
7.493
7.467
7.460
7.264
6.303
6.267
3.892
3.670
3.654
3.638
2.811
2.085
2.061
2.034
1.921
1.714
1.578
1.561
1.541
1.301
1.260
0.957
0.938
0.920
0.900
0.894
0.883
0.875
0.971
0.863
0.856
0.842
0.000



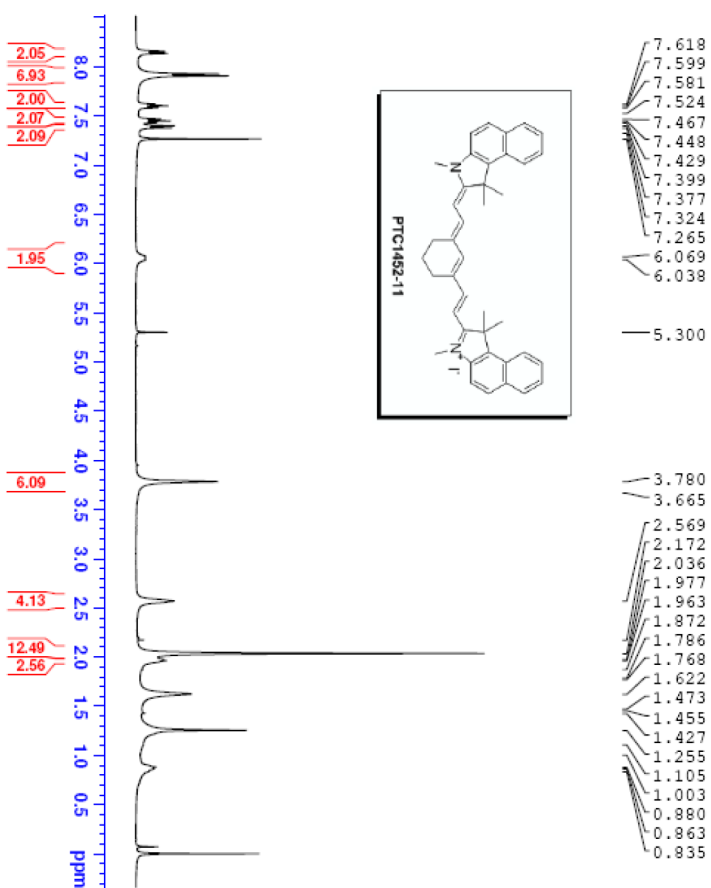
Current Data Parameters
NAME PTC1452-D52-P93-2
EXPNO 1
PROCNO 1

F2 - Acquisition Parameters
Date_ 20140811
Time 16:00
INSTRUM spect
PROBHD 5 mm PABBO BB/
PULPROG zg30
TD 65536
SOLVENT CDCl3
NS 16
DS 2
SWH 8012.820 Hz
FIDRES 0.122266 Hz
AQ 4.0894465 sec
RG 116.94
DM 62.400 usec
DE 6.50 usec
TE 298.0 K
D1 1.00000000 sec
ID0 1

CHANNEL f1
SFO1 400.1324710 MHz
NUC1 1H
PI 10.00 usec
PL1 15.000000000 W
F2 - Processing parameters
SI 65536
SF 400.1300081 MHz
WDW EM
SSB 0
LB 0
GB 0
PC 1.00

[Return](#)

¹H NMR of compound PTC1452-11



PTC1452-11-DG2-1670P98-H-20140822

- 7.618
- 7.599
- 7.581
- 7.524
- 7.467
- 7.448
- 7.429
- 7.399
- 7.377
- 7.324
- 7.265
- 6.069
- 6.038
- 5.300
- 3.780
- 3.665
- 2.569
- 2.172
- 2.036
- 1.977
- 1.963
- 1.872
- 1.786
- 1.768
- 1.622
- 1.473
- 1.455
- 1.427
- 1.255
- 1.105
- 1.003
- 0.880
- 0.863
- 0.835



Current Data Parameters
 NAME PTC1452-11-DG2-1670P98
 EXPRO 1
 PROCNO 1
 P2 - Acquisition Parameters
 Date_ 20140822
 Time 9:40
 INSTRUM spect
 PROBRD 5 mm BBOB 80/
 PULPROG zg30
 TD 65536
 SOLVDMT DC13
 DS 12
 SFO 801.2820 Hz
 FIDRES 0.122265 Hz
 AQ 4.0894465 sec
 RG 91.2
 DM 62.400 usec
 DE 3.20 usec
 TE 295.0 K
 D1 1.00000000 sec
 TDO 1

===== CHANNEL f1 =====
 SFO1 400.1324710 MHz
 PUL1 10.00 usec
 PL1 16.000000000 N

P2 - Processing parameters
 SI 65536
 SF 400.1300075 MHz
 SSB 0
 LB 0
 GB 0
 PC 1.00

[Return](#)

BIBLIOGRAPHY

- Aboagye EO, and Bhujwala ZM (1999) Malignant transformation alters membrane choline phospholipid metabolism of human mammary epithelial cells. *Cancer Research* **59**:80–84.
- Achilefu S, Dorshow RB, Bugaj JE, and Rajagopalan R (2000) Novel receptor-targeted fluorescent contrast agents for in vivo tumor imaging. *Invest Radiol* **35**:479–485.
- Ackerstaff E, Gimi B, Artemov D, and Bhujwala ZM (2007) Anti-inflammatory agent indomethacin reduces invasion and alters metabolism in a human breast cancer cell line. *Neoplasia* **9**:222–235.
- Ackerstaff E, Glunde K, and Bhujwala ZM (2003) Choline phospholipid metabolism: A target in cancer cells? *J Cell Biochem* **90**:525–533.
- Ackerstaff E, Pflug BR, Nelson JB, and Bhujwala ZM (2001) Detection of increased choline compounds with proton nuclear magnetic resonance spectroscopy subsequent to malignant transformation of human prostatic epithelial cells. *Cancer Research* **61**:3599–3603, American Association for Cancer Research.
- Adams EQ, and Haller HL (1920) Isocyanine Dyes from Lepidine and its Homologs. *J Am Chem Soc*, doi: 10.1021/ja01456a037.
- Agwu DE, McPhail LC, Chabot MC, Daniel LW, Wykle RL, and McCall CE (1989) Choline-linked phosphoglycerides. A source of phosphatidic acid and diglycerides in stimulated neutrophils. *Journal of Biological Chemistry* **264**:1405–1413.
- Al-Saffar NMS, Jackson LE, Raynaud FI, Clarke PA, Ramirez de Molina A, Lacal JC, Workman P, and Leach MO (2010) The Phosphoinositide 3-Kinase Inhibitor PI-103 Downregulates Choline Kinase Leading to Phosphocholine and Total Choline Decrease Detected by Magnetic Resonance Spectroscopy. *Cancer Research* **70**:5507–5517.
- Al-Saffar NMS, Troy H, Ramirez de Molina A, Jackson LE, Madhu B, Griffiths JR, Leach MO, Workman P, Lacal JC, Judson IR, and Chung Y (2006) Noninvasive magnetic resonance spectroscopic pharmacodynamic markers of the choline kinase inhibitor MN58b in human carcinoma models. *Cancer Research* **66**:427–434.
- Ansell GB, and Spanner SG (1974) The inhibition of brain choline kinase by hemicholinium-3. *J Neurochem* **22**:1153–1155.
- Aoyama C, Ishidate K, Sugimoto H, and Vance DE (2007) Induction of choline kinase alpha by carbon tetrachloride (CCl₄) occurs via increased binding of c-jun to an AP-1 element. *Biochimica et Biophysica Acta (BBA) - Molecular and Cell Biology of Lipids* **1771**:1148–1155.
- Aoyama C, Liao H, and Ishidate K (2004) Structure and function of choline kinase isoforms in mammalian cells. *Progress in Lipid Research* **43**:266–281.
- Aoyama C, Nakashima K, and Ishidate K (1998) Molecular cloning of mouse choline kinase and choline/ethanolamine kinase: their sequence comparison to the respective rat homologs. *Biochim Biophys Acta* **1393**:179–185.

- Aoyama C, Ohtani A, and Ishidate K (2002) Expression and characterization of the active molecular forms of choline/ethanolamine kinase- α and - β in mouse tissues, including carbon tetrachloride-induced liver. *Biochem J* **363**:777–784.
- Arlaukas SP, Popov AV, and Delikatny EJ (2014) Direct inhibition of choline kinase by a near-infrared fluorescent carbocyanine. *Mol Cancer Ther* **13**:2149–2158, American Association for Cancer Research.
- Autschbach J (2007) Why the particle-in-a-box model works well for cyanine dyes but not for conjugated polyenes. *Journal of Chemical Education*, doi: 10.1021/ed084p1840.
- Ballou B, Fisher GW, Hakala TR, and Farkas DL (1997) Tumor Detection and Visualization Using Cyanine Fluorochrome-Labeled Antibodies. *Biotechnol Prog* **13**:649–658.
- Ballou B, Fisher GW, Waggoner AS, Farkas DL, Reiland JM, Jaffe R, Mujumdar RB, Mujumdar SR, and Hakala TR (1995) Tumor Labeling in-Vivo Using Cyanine-Conjugated Monoclonal-Antibodies. *Cancer Immunol Immunother* **41**:257–263.
- Bansal A, Harris RA, and DeGrado TR (2011) Choline phosphorylation and regulation of transcription of choline kinase in hypoxia. *The Journal of Lipid Research* **53**:149–157.
- Bansal A, Shuyan W, Hara T, Harris RA, and DeGrado TR (2008) Biodisposition and metabolism of [18F]fluorocholine in 9L glioma cells and 9L glioma-bearing fisher rats. *Eur J Nucl Med Mol Imaging* **35**:1192–1203, Springer-Verlag.
- Baykal AT, Jain MR, and Li H (2008) Aberrant regulation of choline metabolism by mitochondrial electron transport system inhibition in neuroblastoma cells. *Metabolomics* **4**:347–356.
- Báñez-Coronel M, Ramírez de Molina A, Rodríguez-González A, Sarmentero J, Ramos MA, García-Cabezas MA, García-Oroz L, and Lacal JC (2008) Choline kinase α depletion selectively kills tumoral cells. *Curr Cancer Drug Targets* **8**:709–719.
- Becker A, Hassenius C, Licha K, Ebert B, Sukowski U, Semmler W, Wiedenmann B, and Grötzinger C (2001) Receptor-targeted optical imaging of tumors with near-infrared fluorescent ligands. *Nature Biotechnology* **19**:327–331.
- Becker A, Riefke B, Ebert B, Sukowski U, Rinneberg H, Semmler W, and Licha K (2000) Macromolecular contrast agents for optical imaging of tumors: Comparison of indotricarbocyanine-labeled human serum albumin and transferrin. *Photochem Photobiol* **72**:234–241.
- Belouche-Babari M, Chung Y-L, Al-Saffar NMS, Falck-Miniotis M, and Leach MO (2010) Metabolic assessment of the action of targeted cancer therapeutics using magnetic resonance spectroscopy. *Br J Cancer* **102**:1–7.
- Bernal SD, Lampidis TJ, McIsaac RM, and Chen LB (1983) Anticarcinoma activity in vivo of rhodamine 123, a mitochondrial-specific dye. *Science* **222**:169–172.
- Bhakoo KK, Williams SR, Florian CL, Land H, and Noble MD (1996) Immortalization and transformation are associated with specific alterations in choline metabolism. *Cancer Research* **56**:4630–4635.
- Bhattacharyya B, Sokoll MD, Cannon JG, and Long JP (1987) Pharmacologic evaluation and structure activity relationships of a series of hemicholinium-3 (HC-3) analogs. *Arch Int Pharmacodyn Ther* **288**:136–146.

- Boobis AR, Gibson A, and Stevenson RW (1975) Ethanol protection against hemicholinium toxicity in mice. *Biochem Pharmacol* **24**:485–488.
- Bremer C, Tung CH, and Weissleder R (2001) In vivo molecular target assessment of matrix metalloproteinase inhibition. *Nature Medicine* **7**:743–748.
- Brophy PJ, and Vance DE (1976) Copurification of choline kinase and ethanolamine kinase from rat liver by affinity chromatography. *FEBS Lett* **62**:123–125.
- Brostrom MA, and Browning ET (1973) Choline kinase from brewers' yeast. Partial purification, properties, and kinetic mechanism. *Journal of Biological Chemistry* **248**:2364–2371.
- Bryant MJ, Chuah TL, Luff J, Lavin MF, and Walker DG (2008) A novel rat model for glioblastoma multiforme using a bioluminescent F98 cell line. *J Clin Neurosci* **15**:545–551.
- Burk D, and Schade AL (1956) On respiratory impairment in cancer cells. *Science* **124**:270–272.
- Busch DR, Choe R, Durduran T, and Yodh AG (2013) Towards non-invasive characterization of breast cancer and cancer metabolism with diffuse optics. *PET Clin* **8**.
- Campos J, del Carmen Núñez M, Rodríguez V, Entrena A, Hernández-Alcoceba R, Fernández F, Lacal JC, Gallo MA, and Espinosa A (2001) LUMO energy of model compounds of bispyridinium compounds as an index for the inhibition of choline kinase. *European Journal of Medicinal Chemistry* **36**:215–225.
- Campos J, Núñez MC, and Conejo-García A (2003) QSAR-derived choline kinase inhibitors: how rational can antiproliferative drug design be? *Curr Med Chem*, doi: 10.2174/0929867033457539.
- Campos JM, Nunez MC, Sanchez RM, Gomez-Vidal JA, Rodríguez-González A, Banez M, Gallo MA, Lacal JC, and Espinosa A (2002) Quantitative structure-activity relationships for a series of symmetrical bisquaternary anticancer compounds. *Bioorg Med Chem* **10**:2215–2231.
- Campos JM, Sánchez-Martín RM, Conejo-García A, Entrena A, Gallo MA, and Espinosa A (2006) (Q)SAR studies to design new human choline kinase inhibitors as antiproliferative drugs. *Curr Med Chem* **13**:1231–1248.
- Candolfi M, Curtin JF, Nichols WS, Muhammad AG, King GD, Pluhar GE, McNiel EA, Ohlfest JR, Freese AB, Moore PF, Lerner J, Lowenstein PR, and Castro MG (2007) Intracranial glioblastoma models in preclinical neuro-oncology: neuropathological characterization and tumor progression. *J Neurooncol* **85**:133–148, Springer US.
- Cannon JG (1994) Structure-activity aspects of hemicholinium-3 (HC-3) and its analogs and congeners. *Med Res Rev* **14**:505–531.
- Cannon JG, Lee TM, Chang Y, Nyanda AM, Bhattacharyya B, Flynn JR, Chatterjee T, Bhatnagar RK, and Long JP (1988) Structure-activity relationship studies of hemicholinium (HC-3) congeners. *Pharm Res* **5**:359–364.
- Chabner BA, and Roberts TG (2005) Timeline: Chemotherapy and the war on cancer. *Nat Rev Cancer* **5**:65–72.
- Chen X, Gambhir SS, and Cheon J (2011) Theranostic Nanomedicine. *Acc Chem Res* **44**:841–841.

- Chua BT, Gallego-Ortega D, Ramírez de Molina A, Ullrich A, Lacal JC, and Downward J (2009) Regulation of Akt(ser473) phosphorylation by choline kinase in breast carcinoma cells. *Mol Cancer* **8**:131.
- Chung T, Crilly KS, Anderson WH, and Mukherjee JJ (1997) ATP-dependent Choline Phosphate-induced Mitogenesis in Fibroblasts Involves Activation of pp70 S6 Kinase and Phosphatidylinositol 3'-Kinase through an Extracellular Site. *Journal of Biological Chemistry*, doi: 10.1074/jbc.272.5.3064.
- Chung Y, Troy H, Kristeleit R, Aherne W, Jackson LE, Atadja P, Griffiths JR, Judson IR, Workman P, Leach MO, and Belouche-Babari M (2008) Noninvasive magnetic resonance spectroscopic pharmacodynamic markers of a novel histone deacetylase inhibitor, LAQ824, in human colon carcinoma cells and xenografts. *Neoplasia* **10**:303–313.
- Clem BF, Clem AL, Yalcin A, Goswami U, Arumugam S, Telang S, Trent JO, and Chesney J (2011) A novel small molecule antagonist of choline kinase- α that simultaneously suppresses MAPK and PI3K/AKT signaling. *Oncogene* **30**:3370–3380.
- Conejo-García A (2003) Choline kinase inhibitory effect and antiproliferative activity of new 1,1',1''-(benzene-1,3,5-triylmethylene)tris{4-[(disubstituted)amino]pyridinium} tribromides. *European Journal of Medicinal Chemistry* **38**:109–116.
- Conejo-García A, Báñez-Coronel M, Sánchez-Martín RM, Rodríguez-González A, Ramos A, Ramírez de Molina A, Espinosa A, Gallo MA, Campos JM, and Lacal JC (2004) Influence of the Linker in Bispyridinium Compounds on the Inhibition of Human Choline Kinase. *J Med Chem* **47**:5433–5440.
- Conejo-García A, Campos JM, Sánchez-Martín RM, Gallo MA, and Espinosa A (2003) Bispyridinium Cyclophanes: Novel Templates for Human Choline Kinase Inhibitors. *J Med Chem* **46**:3754–3757.
- Conejo-García A, Pisani L, Núñez MDC, Catto M, Nicolotti O, Leonetti F, Campos JM, Gallo MA, Espinosa A, and Carotti A (2011) Homodimeric bis-quaternary heterocyclic ammonium salts as potent acetyl- and butyrylcholinesterase inhibitors: a systematic investigation of the influence of linker and cationic heads over affinity and selectivity. *J Med Chem* **54**:2627–2645.
- Contractor K, Challapalli A, Barwick T, Winkler M, Hellowell G, Hazell S, Tomasi G, Al-Nahhas A, Mapelli P, Kenny LM, Tadrous P, Coombes RC, Aboagye EO, and Mangar S (2011) Use of [¹¹C]Choline PET-CT as a Noninvasive Method for Detecting Pelvic Lymph Node Status from Prostate Cancer and Relationship with Choline Kinase Expression. *Clinical Cancer Research* **17**:7673–7683.
- Cram DJ, and Steinberg H (1951) Macro rings. I. Preparation and spectra of the paracyclophanes. *J Am Chem Soc*, doi: 10.1021/ja01156a059.
- Crane LMA, Themelis G, Pleijhuis RG, Harlaar NJ, Sarantopoulos A, Arts HJG, van der Zee AGJ, Ntziachristos V, Vasilis N, and van Dam GM (2011) Intraoperative multispectral fluorescence imaging for the detection of the sentinel lymph node in cervical cancer: a novel concept. *Mol Imaging Biol* **13**:1043–1049.
- Cuadrado A, Carnero A, Dolfi F, Jiménez B, and Lacal JC (1993) Phosphorylcholine: a novel second messenger essential for mitogenic activity of growth factors. *Oncogene* **8**:2959–2968.
- Cui Z, and Vance DE (1996) Expression of phosphatidylethanolamine N-methyltransferase-2 is markedly enhanced in long term choline-deficient rats. *Journal of Biological Chemistry* **271**:2839–2843.

- Cunningham D, Humblet Y, Siena S, Khayat D, Bleiberg H, Santoro A, Bets D, Mueser M, Harstrick A, Verslype C, Chau I, and Van Cutsem E (2004) Cetuximab monotherapy and cetuximab plus irinotecan in irinotecan-refractory metastatic colorectal cancer. *N Engl J Med* **351**:337–345.
- Daly PF, and Cohen JS (1989) Magnetic Resonance Spectroscopy of Tumors and Potential in Vivo Clinical Applications: A Review. *Cancer Research* **49**:770–779, American Association for Cancer Research.
- Darwish TA, Evans RA, James M, Malic N, Triani G, and Hanley TL (2010) CO₂ triggering and controlling orthogonally multiresponsive photochromic systems. *J Am Chem Soc* **132**:10748–10755.
- de Certaines JD, Larsen VA, and Podo F (1993) In vivo ³¹P MRS of experimental tumours. *NMR Biomed* **6**:345–365.
- De Grand AM, and Frangioni JV (2003) An operational near-infrared fluorescence imaging system prototype for large animal surgery. *Technol Cancer Res Treat* **2**:553–562.
- Delikatny EJ, Chawla S, Leung D-J, and Poptani H (2011) MR-visible lipids and the tumor microenvironment. *NMR Biomed* **24**:592–611.
- Doja MQ (1932) The Cyanine Dyes. *Chem Rev*, doi: 10.1021/cr60040a001.
- Du J, Sun C, Hu Z, Yang Y, Zhu Y, Zheng D, Gu L, and Lu X (2010) Lysophosphatidic Acid Induces MDA-MB-231 Breast Cancer Cells Migration through Activation of PI3K/PAK1/ERK Signaling. *PLoS ONE* **5**:e15940.
- Dunn KW, Kamocka MM, and McDonald JH (2011) A practical guide to evaluating colocalization in biological microscopy. *AJP: Cell Physiology* **300**:C723–C742.
- Ehrlich P (1911) The Theory and Practice of Chemotherapy. *Folia Serologica* **7**:697–714.
- Eliyahu G, Kreizman T, and Degani H (2007) Phosphocholine as a biomarker of breast cancer: Molecular and biochemical studies. *Int J Cancer* **120**:1721–1730.
- Etzioni R, Urban N, Ramsey S, McIntosh M, Schwartz S, Reid B, Radich J, Anderson G, and Hartwell L (2003) The case for early detection. *Nat Rev Cancer* **3**:243–252.
- Evanochko WT, Ng TC, and Glickson JD (1984) Application of in vivo NMR spectroscopy to cancer. *Magn Reson Med* **1**:508–534.
- Falcon SC, Hudson CS, Huang Y, Mortimore M, Golec JM, Charlton PA, Weber P, and Sundaram H (2013) A non-catalytic role of choline kinase alpha is important in promoting cancer cell survival. *Oncogenesis* **2**:e38–4, Nature Publishing Group.
- Folli S, Westermann P, Braichotte D, Pelegrin A, Wagnieres G, van den Bergh H, and Mach JP (1994) Antibody-indocyanin conjugates for immunophotodetection of human squamous cell carcinoma in nude mice. *Cancer Research* **54**:2643–2649.
- Fox IJ, Brooker LG, Heseltine DW, Essex HE, and Wood EH (1957) A tricarbocyanine dye for continuous recording of dilution curves in whole blood independent of variations in blood oxygen saturation. *Proc Staff Meet Mayo Clin* **32**:478–484.
- Frangioni JV (2003) In vivo near-infrared fluorescence imaging. *Current opinion in chemical biology* **7**:626–634.

- Frangioni JV (2008) New technologies for human cancer imaging. *J Clin Oncol* **26**:4012–4021, American Society of Clinical Oncology.
- Fullerton MD, Wagner L, Yuan Z, and Bakovic M (2006) Impaired trafficking of choline transporter-like protein-1 at plasma membrane and inhibition of choline transport in THP-1 monocyte-derived macrophages. *AJP: Cell Physiology* **290**:C1230–8.
- Gabellieri C, Reynolds S, Lavie A, Payne GS, Leach MO, and Eykyn TR (2008) Therapeutic Target Metabolism Observed Using Hyperpolarized ¹⁵N Choline. *J Am Chem Soc* **130**:4598–4599.
- Gallego-Ortega D, Ramírez de Molina A, Ramos MA, Valdes-Mora F, Barderas MG, Sarmentero-Estrada J, and Lacal JC (2009) Differential Role of Human Choline Kinase α and β Enzymes in Lipid Metabolism: Implications in Cancer Onset and Treatment. *PLoS ONE* **4**:e7819.
- Gan HK, Cvrljevic AN, and Johns TG (2013) The epidermal growth factor receptor variant III (EGFRvIII): where wild things are altered. *FEBS J* **280**:5350–5370.
- Gardiner JE (1961) The inhibition of acetylcholine synthesis in brain by a hemicholinium. *Biochem J* **81**:297–303.
- Gatenby RA, and Gillies RJ (2004) Why do cancers have high aerobic glycolysis? *Nat Rev Cancer* **4**:891–899.
- Gibbs JB (2000) Mechanism-based target identification and drug discovery in cancer research. *Science* **287**:1969–1973.
- Gibbs SL (2012) Near infrared fluorescence for image-guided surgery. *Quant Imaging Med Surg* **2**:177–187.
- Gillies RJ, and Morse DL (2005) In vivo magnetic resonance spectroscopy in cancer. *Annu Rev Biomed Eng* **7**:287–326.
- Gillies RJ, Barry JA, and Ross BD (1994) In vitro and in vivo ¹³C and ³¹P NMR analyses of phosphocholine metabolism in rat glioma cells. *Magn Reson Med* **32**:310–318.
- Glunde K, and Serkova NJ (2006) Therapeutic targets and biomarkers identified in cancer choline phospholipid metabolism. *Pharmacogenomics* **7**:1109–1123.
- Glunde K, Artemov D, Penet M-F, Jacobs MA, and Bhujwala ZM (2010) Magnetic Resonance Spectroscopy in Metabolic and Molecular Imaging and Diagnosis of Cancer. *Chem Rev* **110**:3043–3059.
- Glunde K, Bhujwala ZM, and Ronen SM (2011) Choline metabolism in malignant transformation. *Nat Rev Cancer* **11**:835–848.
- Glunde K, Raman V, Mori N, and Bhujwala ZM (2005) RNA interference-mediated choline kinase suppression in breast cancer cells induces differentiation and reduces proliferation. *Cancer Research* **65**:11034–11043.
- Glunde K, Shah T, Winnard PT, Raman V, Takagi T, Vesuna F, Artemov D, and Bhujwala ZM (2008) Hypoxia Regulates Choline Kinase Expression through Hypoxia-Inducible Factor-1 Signaling in a Human Prostate Cancer Model. *Cancer Research* **68**:172–180.

- Gomez MV, Domino EF, and Sellinger OZ (1970) Effect of hemicholinium-3 on choline distribution *in vivo* in the canine caudate nucleus. *Biochem Pharmacol*, doi: 10.1016/0006-2952(70)90167-X.
- Gonzalez B, Pajares MA, Martinez-Ripoll M, Blundell TL, and Sanz-Aparicio J (2004) Crystal structure of rat liver betaine homocysteine s-methyltransferase reveals new oligomerization features and conformational changes upon substrate binding. *J Mol Biol* **338**:771–782.
- Goodson JA, and Goodwin LG (1948) The chemotherapy of amoebiasis; variants of bis(diamylamino)decane. *Br J Pharmacol Chemother* **3**:62–71.
- Gómez Pérez V, McSorley T, See Too WC, Konrad M, and Campos JM (2012) Novel 4-amino bis-pyridinium and bis-quinolinium derivatives as choline kinase inhibitors with antiproliferative activity against the human breast cancer SKBR-3 cell line. *ChemMedChem* **7**:663–669.
- Granata A, Nicoletti R, Tinaglia V, De Cecco L, Pisanu ME, Ricci A, Podo F, Canevari S, Iorio E, Bagnoli M, and Mezzanzanica D (2014) Choline kinase- α by regulating cell aggressiveness and drug sensitivity is a potential druggable target for ovarian cancer. *Br J Cancer* **110**:330–340.
- Gruber J, See Too WC, Wong MT, Lavie A, McSorley T, and Konrad M (2012) Balance of human choline kinase isoforms is critical for cell cycle regulation: implications for the development of choline kinase-targeted cancer therapy. *FEBS J* **279**:1915–1928.
- Guo M, Roman RJ, Fenstermacher JD, Brown SL, Falck JR, Arbab AS, Edwards PA, and Scicli AG (2006) 9L gliosarcoma cell proliferation and tumor growth in rats are suppressed by N-hydroxy-N'-(4-butyl-2-methylphenol) formamidine (HET0016), a selective inhibitor of CYP4A. *Journal of Pharmacology and Experimental Therapeutics* **317**:97–108.
- Guyenet P, Lefresne P, Rossier J, Beaujouan JC, and Glowinski J (1973) Inhibition by hemicholinium-3 of (^{14}C)acetylcholine synthesis and (^3H)choline high-affinity uptake in rat striatal synaptosomes. *Mol Pharmacol* **9**:630–639.
- Hakumäki JM, Poptani H, Sandmair AM, Ylä-Herttuala S, and Kauppinen RA (1999) ^1H MRS detects polyunsaturated fatty acid accumulation during gene therapy of glioma: implications for the *in vivo* detection of apoptosis. *Nature Medicine* **5**:1323–1327.
- Hale GM, and Querry MR (1973) Optical Constants of Water in the 200-nm to 200- μm Wavelength Region. *Appl Opt, AO* **12**:555–563, Optical Society of America.
- Hamza M, Lloveras J, Ribbes G, Soula G, and Douste-Blazy L (1983) An *in vitro* study of hemicholinium-3 on phospholipid metabolism of Krebs II ascites cells. *Biochem Pharmacol* **32**:1893–1897.
- Hanahan D, and Weinberg RA (2011) Hallmarks of cancer: the next generation. *Cell* **144**:646–674.
- Hanahan D, and Weinberg RA (2000) The hallmarks of cancer. *Cell* **100**:57–70.
- Hara T, Bansal A, and DeGrado TR (2006) Choline transporter as a novel target for molecular imaging of cancer. *Molecular ...*, doi: 10.2310/7290.2006.00032.
- Hara T, Kosaka N, Shinoura N, and Kondo T (1997) PET imaging of brain tumor with [methyl- ^{11}C]choline. *Journal of Nuclear Medicine* **38**:842–847.
- Hernando E, Sarmentero-Estrada J, Koppie T, Belda-Iniesta C, Ramírez de Molina V, Cejas P, Ozu C, Le C, Sánchez JJ, González-Barón M, Koutcher J, Córdón-Cardó C, Bochner BH, Lacal JC, and Ramirez

- de Molina A (2009) A critical role for choline kinase- α in the aggressiveness of bladder carcinomas. *Oncogene* **28**:2425–2435.
- Hernández-Alcoceba R, Fernández F, and Lacal JC (1999) In vivo antitumor activity of choline kinase inhibitors: a novel target for anticancer drug discovery. *Cancer Research* **59**:3112–3118.
- Hernández-Alcoceba R, Saniger L, Campos J, Núñez MC, Khaless F, Gallo MA, Espinosa A, and Lacal JC (1997) Choline kinase inhibitors as a novel approach for antiproliferative drug design. *Oncogene* **15**:2289–2301.
- Hoey RP, Sanderson C, Iddon J, Brady G, Bundred NJ, and Anderson NG (2003) The parathyroid hormone-related protein receptor is expressed in breast cancer bone metastases and promotes autocrine proliferation in breast carcinoma cells. *Br J Cancer* **88**:567–573.
- Hong BS, Allali-Hassani A, Tempel W, Finerty PJ, Mackenzie F, Dimov S, Vedadi M, and Park H-W (2010) Crystal structures of human choline kinase isoforms in complex with hemicholinium-3: single amino acid near the active site influences inhibitor sensitivity. *J Biol Chem* **285**:16330–16340.
- Honig MG, and Hume RI (1986) Fluorescent carbocyanine dyes allow living neurons of identified origin to be studied in long-term cultures. *J Cell Biol* **103**:171–187, Rockefeller Univ Press.
- Hoogerwerff S, and Van Dorp WA (1883). *Recueil des Travaux Chimiques des Pays-Bas* **2**.
- Horská A, and Barker PB (2010) Imaging of brain tumors: MR spectroscopy and metabolic imaging. *Neuroimaging Clin N Am* **20**:293–310.
- Hosaka K, Murakami T, Kodaki T, Nikawa J, and Yamashita S (1990) Repression of choline kinase by inositol and choline in *Saccharomyces cerevisiae*. *J Bacteriol* **172**:2005–2012.
- Huang C, Hydo LM, Liu S, and Miller RT (2009) Activation of choline kinase by extracellular Ca^{2+} is Ca^{2+} -sensing receptor, $\text{G}\alpha_{12}$ and Rho-dependent in breast cancer cells. *Cellular Signalling* **21**:1894–1900, Elsevier B.V.
- Hudson CS, Knechtel RM, Brown K, Charlton PA, and Pollard JR (2013) Kinetic and mechanistic characterisation of Choline Kinase- α . *Biochimica et Biophysica Acta (BBA) - Proteins and Proteomics* **1834**:1107–1116.
- Huszthy PC, Daphu I, Niclou SP, Stieber D, Nigro JM, Sakariassen PO, Miletic H, Thorsen F, and Bjerkvig R (2012) In vivo models of primary brain tumors: pitfalls and perspectives. *Neuro-oncology* **14**:979–993, Oxford University Press.
- Iorio E, Mezzananza D, Alberti P, Spadaro F, Ramoni C, D'Ascenzo S, Millimaggi D, Pavan A, Dolo V, Canevari S, and Podo F (2005) Alterations of choline phospholipid metabolism in ovarian tumor progression. *Cancer Research* **65**:9369–9376.
- Iorio E, Ricci A, Bagnoli M, Pisanu ME, Castellano G, Di Vito M, Venturini E, Glunde K, Bhujwala ZM, Mezzananza D, Canevari S, and Podo F (2010) Activation of Phosphatidylcholine Cycle Enzymes in Human Epithelial Ovarian Cancer Cells. *Cancer Research* **70**:2126–2135.
- Ishidate K (1989) Choline transport and choline kinase, in *Phosphatidylcholine Metabolism* (Vance DE ed) pp 9–32, CRC Press.
- Ishidate K, Tsuruoka M, and Nakazawa Y (1980) Induction of choline kinase by polycyclic aromatic

- hydrocarbon carcinogens in rat liver. *Biochemical and Biophysical Research Communications* **96**:946–952.
- Jaffe CC (2006) Measures of response: RECIST, WHO, and new alternatives. *J Clin Oncol* **24**:3245–3251, American Society of Clinical Oncology.
- Janardhan S, and Srivani P (2006) 2D and 3D Quantitative Structure–Activity Relationship Studies on a Series of bis-Pyridinium Compounds as Choline Kinase Inhibitors. *QSAR & Combinatorial Science* **25**:860–872.
- Jiménez B, del Peso L, Montaner S, Esteve P, and Lacal JC (1995) Generation of phosphorylcholine as an essential event in the activation of Raf-1 and MAP-kinases in growth factors–induced mitogenic stimulation. *J Cell Biochem* **57**:141–149, Wiley Subscription Services, Inc., A Wiley Company.
- Jobsis FF (1977) Noninvasive, infrared monitoring of cerebral and myocardial oxygen sufficiency and circulatory parameters. *Science*, doi: 10.1126/science.929199.
- Kachur AV, Popov AV, Karp JS, and Delikatny EJ (2013) Direct fluorination of phenolsulfonphthalein: a method for synthesis of positron-emitting indicators for in vivo pH measurement. *Cell Biochem Biophys* **66**:1–5, Springer-Verlag.
- Kapoor GS, Poptani H, Hsu O, Kim S, and ORourke DM (2007) In vivo analysis of EGFRvIII rat glioma growth and invasion by magnetic resonance imaging (MRI). *Society for Neuro-Oncology* **9**:573.
- Katz-Brull R, Lavin PT, and Lenkinski RE (2002) Clinical utility of proton magnetic resonance spectroscopy in characterizing breast lesions. *J Natl Cancer Inst* **94**:1197–1203.
- Katzenellenbogen JA, Welch MJ, and Dehdashti F (1997) The development of estrogen and progestin radiopharmaceuticals for imaging breast cancer. *Anticancer Res* **17**:1573–1576.
- Ke S, Wen X, Gurfinkel M, Charnsangavej C, Wallace S, Sevick-Muraca EM, and Li C (2003) Near-infrared optical imaging of epidermal growth factor receptor in breast cancer xenografts. *Cancer Research* **63**:7870–7875.
- Kelkar SS, and Reineke TM (2011) Theranostics: combining imaging and therapy. *Bioconjug Chem*, doi: 10.1021/bc200151q.
- Kennedy EP (1957) Metabolism of lipides. *Annual review of biochemistry* **26**:119–148.
- Kennedy EP, and Weiss SB (1956) The function of cytidine coenzymes in the biosynthesis of phospholipides. *Journal of Biological Chemistry* **222**:193–214.
- Kim D, Jun H, Lee H, Hong S-S, and Hong S (2010) Development of New Fluorescent Xanthines as Kinase Inhibitors. *Org Lett* **12**:1212–1215.
- Kim D, Lee H, Jun H, Hong S-S, and Hong S (2011) Fluorescent phosphoinositide 3-kinase inhibitors suitable for monitoring of intracellular distribution. *Bioorg Med Chem* **19**:2508–2516, Elsevier Ltd.
- Kitai T, Inomoto T, Miwa M, and Shikayama T (2005) Fluorescence navigation with indocyanine green for detecting sentinel lymph nodes in breast cancer. *Breast Cancer* **12**:211–215.
- Kodama M, Tagashira Y, and Nagata C (1966) The interaction of pinacyanol with nucleic acids. *Biochim Biophys Acta* **129**:638–640.

- Kolesnick R (2002) The therapeutic potential of modulating the ceramide/sphingomyelin pathway. *J Clin Invest* **110**:3–8, American Society for Clinical Investigation.
- Kouji H, Inazu M, Yamada T, Tajima H, Aoki T, and Matsumiya T (2009) Molecular and functional characterization of choline transporter in human colon carcinoma HT-29 cells. *Arch Biochem Biophys* **483**:90–98.
- Kris MG, Natale RB, Herbst RS, Lynch TJ, Prager D, Belani CP, Schiller JH, Kelly K, Spiridonidis H, Sandler A, Albain KS, Cella D, Wolf MK, Averbuch SD, Ochs JJ, and Kay AC (2003) Efficacy of gefitinib, an inhibitor of the epidermal growth factor receptor tyrosine kinase, in symptomatic patients with non-small cell lung cancer - A randomized trial. *JAMA* **290**:2149–2158, American Medical Association.
- Krishnamachary B, Glunde K, Wildes F, Mori N, Takagi T, Raman V, and Bhujwala ZM (2009) Noninvasive detection of lentiviral-mediated choline kinase targeting in a human breast cancer xenograft. *Cancer Research* **69**:3464–3471.
- Kroemer G, and Pouyssegur J (2008) Tumor cell metabolism: cancers Achilles heel. *Cancer Cell* **13**:472–482, Elsevier.
- Kumar M, Arlauckas SP, Saksena S, Verma G, Ittyerah R, Pickup S, Popov AV, Delikatny EJ, and Poptani H (2015) Magnetic resonance spectroscopy for detection of choline kinase inhibition in the treatment of brain tumors. *Mol Cancer Ther*.
- Kundu K, Knight SF, Willett N, Lee S, Taylor WR, and Murthy N (2009) Hydrocyanines: a class of fluorescent sensors that can image reactive oxygen species in cell culture, tissue, and in vivo. *Angew Chem Int Ed Engl* **48**:299–303.
- Lacal JC (2001) Choline kinase: a novel target for antitumor drugs. *IDrugs* **4**:419–426.
- Lacal JC, and Campos JM (2015) Preclinical Characterization of RSM-932A, a Novel Anticancer Drug Targeting the Human Choline Kinase Alpha, an Enzyme Involved in Increased Lipid Metabolism of Cancer Cells. *Mol Cancer Ther* **14**:31–39, American Association for Cancer Research.
- Landsman ML, Kwant G, Mook GA, and Zijlstra WG (1976) Light-absorbing properties, stability, and spectral stabilization of indocyanine green. *J Appl Physiol* **40**:575–583.
- Lewis JS, Achilefu S, Garbow JR, Laforest R, and Welch MJ (2002) Small animal imaging: current technology and perspectives for oncological imaging. *Eur J Cancer* **38**:2173–2188.
- Licha K, Riefke B, Ntziachristos V, Becker A, Chance B, and Semmler W (2000) Hydrophilic cyanine dyes as contrast agents for near-infrared tumor imaging: Synthesis, photophysical properties and spectroscopic in vivo characterization. *Photochem Photobiol* **72**:392–398.
- Lieberman BP, Ploessl K, Wang L, Qu W, Zha Z, Wise DR, Chodosh LA, Belka G, Thompson CB, and Kung HF (2011) PET imaging of glutaminolysis in tumors by ¹⁸F-(2S,4R)4-fluoroglutamine. *J Nucl Med* **52**:1947–1955.
- Lipinski CA (2003) Chris Lipinski discusses life and chemistry after the Rule of Five. *Drug Discov Today* **8**:12–16.
- Long JP, and Schueler FW (1954) A new series of cholinesterase inhibitors. *Journal of the American Pharmaceutical Association* **43**:79–86, Wiley Subscription Services, Inc., A Wiley Company.

- Los M, Roodhart JML, and Voest EE (2007) Target practice: lessons from phase III trials with bevacizumab and vatalanib in the treatment of advanced colorectal cancer. *Oncologist* **12**:443–450.
- Macintosh FC (1961) Effect of HC-3 on acetylcholine turnover. *Fed Proc* **20**:562–568.
- MacKeigan JP, Murphy LO, and Blenis J (2005) Sensitized RNAi screen of human kinases and phosphatases identifies new regulators of apoptosis and chemoresistance. *Nat Cell Biol* **7**:591–600.
- Madajewski B, Judy BF, Mouchli A, Kapoor V, Holt D, Wang MD, Nie S, and Singhal S (2012) Intraoperative near-infrared imaging of surgical wounds after tumor resections can detect residual disease. *Clinical Cancer Research* **18**:5741–5751, American Association for Cancer Research.
- Mahmood U, and Weissleder R (2003) Near-infrared optical imaging of proteases in cancer. *Mol Cancer Ther* **2**:489–496.
- Malito E, Sekulic N, Too WCS, Konrad M, and Lavie A (2006) Elucidation of human choline kinase crystal structures in complex with the products ADP or phosphocholine. *J Mol Biol* **364**:136–151.
- Mankoff DA, Eary JF, Link JM, Muzi M, Rajendran JG, Spence AM, and Krohn KA (2007) Tumor-specific positron emission tomography imaging in patients: [18F] fluorodeoxyglucose and beyond. *Clinical Cancer Research* **13**:3460–3469, American Association for Cancer Research.
- Mantovani A, and Sica A (2010) Macrophages, innate immunity and cancer: balance, tolerance, and diversity. *Curr Opin Immunol* **22**:231–237.
- Marshall MV, Rasmussen JC, Tan I-C, Aldrich MB, Adams KE, Wang X, Fife CE, Maus EA, Smith LA, and Sevcik-Muraca EM (2010) Near-Infrared Fluorescence Imaging in Humans with Indocyanine Green: A Review and Update. *Open Surg Oncol J* **2**:12–25.
- Marten K, Bremer C, Khazaie K, Sameni M, Sloane B, Tung C-H, and Weissleder R (2002) Detection of dysplastic intestinal adenomas using enzyme-sensing molecular beacons in mice. *Gastroenterology* **122**:406–414.
- Matsui A, Tanaka E, Choi HS, Kianzad V, Gioux S, Lomnes SJ, and Frangioni JV (2010) Real-time, near-infrared, fluorescence-guided identification of the ureters using methylene blue. *Surgery* **148**:78–86.
- Maude SL, Frey N, Shaw PA, Aplenc R, Barrett DM, Bunin NJ, Chew A, Gonzalez VE, Zheng Z, Lacey SF, Mahnke YD, Melenhorst JJ, Rheingold SR, Shen A, Teachey DT, Levine BL, June CH, Porter DL, and Grupp SA (2014) Chimeric antigen receptor T cells for sustained remissions in leukemia. *N Engl J Med* **371**:1507–1517.
- Mawn TM, Popov AV, Beardsley NJ, Stefflova K, Milkevitch M, Zheng G, and Delikatny EJ (2011) In vivo detection of phospholipase C by enzyme-activated near-infrared probes. *Bioconjug Chem* **22**:2434–2443.
- Mayer D, and Werner D (1974) Inhibition of choline kinase by selectively cytotoxic purinyl-6-histamine. *Biochem Pharmacol* **23**:1227–1230.
- Michel V, Yuan Z, Ramsubir S, and Bakovic M (2006) Choline transport for phospholipid synthesis. *Exp Biol Med (Maywood)* **231**:490–504.
- Minn AJ, Gupta GP, Siegel PM, Bos PD, Shu W, Giri DD, Viale A, Olshen AB, Gerald WL, and Massagué J (2005) Genes that mediate breast cancer metastasis to lung. *Nature* **436**:518–524.

- Mishra A, Behera RK, Behera PK, Mishra BK, and Behera GB (2000) Cyanines during the 1990s: A Review. *Chem Rev* **100**:1973–2012.
- Mitchell RH, and Iyer VS (1989) *An Improved Procedure for Bromomethylation of Aromatics Using Phase-Transfer Catalysis. Rapid Bis-haloalkylation*, Synlett.
- Miyake T, and Parsons SJ (2012) Functional interactions between Choline kinase α , epidermal growth factor receptor and c-Src in breast cancer cell proliferation. *Oncogene* **31**:1431–1441.
- Moeller BJ, Cao Y, Li CY, and Dewhirst MW (2004) Radiation activates HIF-1 to regulate vascular radiosensitivity in tumors: role of reoxygenation, free radicals, and stress granules. *Cancer Cell* **5**:429–441.
- Moolenaar WH (1999) Bioactive lysophospholipids and their G protein-coupled receptors. *Exp Cell Res* **253**:230–238.
- Mori N, Delsite R, Natarajan K, Kulawiec M, Bhujwalla ZM, and Singh KK (2004) Loss of p53 function in colon cancer cells results in increased phosphocholine and total choline. *Mol Imaging* **3**:319–323.
- Mori N, Glunde K, Takagi T, Raman V, and Bhujwalla ZM (2007) Choline Kinase Down-regulation Increases the Effect of 5-Fluorouracil in Breast Cancer Cells. *Cancer Research* **67**:11284–11290.
- Morrish F, Isern N, Sadilek M, Jeffrey M, and Hockenbery DM (2009) c-Myc activates multiple metabolic networks to generate substrates for cell-cycle entry. *Oncogene* **28**:2485–2491.
- Morrish F, Neretti N, Sedivy JM, and Hockenbery DM (2008) The oncogene c-Myc coordinates regulation of metabolic networks to enable rapid cell cycle entry. *Cell Cycle* **7**:1054–1066.
- Muller C (2013) Folate-based radiotracers for PET imaging--update and perspectives. *Molecules* **18**:5005–5031.
- Nakayama A, del Monte F, Hajjar RJ, and Frangioni JV (2002) Functional near-infrared fluorescence imaging for cardiac surgery and targeted gene therapy. *Mol Imaging* **1**:365–377.
- Negendank W (1992) Studies of human tumors by MRS: A review. *NMR Biomed* **5**:303–324, John Wiley & Sons, Ltd.
- Neri D, Carnemolla B, Nissim A, Leprini A, Querze G, Balza E, Pini A, Tarli L, Halin C, Neri P, Zardi L, and Winter G (1997) Targeting by affinity-matured recombinant antibody fragments of an angiogenesis associated fibronectin isoform. *Nature Biotechnology* **15**:1271–1275.
- Nioka S, Miwa M, Orel S, Shnall M, Haida M, Zhao S, and Chance B (1994) Optical imaging of human breast cancer. *Adv Exp Med Biol* **361**:171–179.
- Nishizuka Y (1992) Intracellular signaling by hydrolysis of phospholipids and activation of protein kinase C. *Science* **258**:607–614, American Association for the Advancement of Science.
- Okoh OA, Bisby RH, and Lawrence CL (2014) Promising near-infrared non-targeted probes: benzothiazole heptamethine cyanine dyes. *J of Sulfur Chem* **35**:42–56.
- Oseroff AR, Ohuoha D, Ara G, McAuliffe D, Foley J, and Cincotta L (1986) Intramitochondrial dyes allow selective in vitro photolysis of carcinoma cells. *Proceedings of the National Academy of Sciences* **83**:9729–9733.

- Packard BS, and Wolf DE (1985) Fluorescence lifetimes of carbocyanine lipid analogues in phospholipid bilayers. *Biochemistry* **24**:5176–5181.
- Peisach D, Gee P, Kent C, and Xu Z (2003) The crystal structure of choline kinase reveals a eukaryotic protein kinase fold. *Structure*, doi: 10.1016/S0969-2126(03)00094-7.
- Penet M-F, Shah T, Bharti S, Krishnamachary B, Artemov D, Mironchik Y, Wildes F, Maitra A, and Bhujwala ZM (2015) Metabolic imaging of pancreatic ductal adenocarcinoma detects altered choline metabolism. *Clinical Cancer Research* **21**:386–395.
- Podo F, Canevari S, Canese R, Pisanu ME, Ricci A, and Iorio E (2011) MR evaluation of response to targeted treatment in cancer cells. *NMR Biomed* **24**:648–672.
- Poptani H, Bansal N, Graham RA, Mancuso A, Nelson DS, and Glickson JD (2003) Detecting early response to cyclophosphamide treatment of RIF-1 tumors using selective multiple quantum spectroscopy (SelMQC) and dynamic contrast enhanced imaging. *NMR Biomed* **16**:102–111.
- Ramírez de Molina A, Báñez-Coronel M, Gutiérrez R, Rodríguez-González A, Olmeda D, Megías D, and Lacal JC (2004) Choline kinase activation is a critical requirement for the proliferation of primary human mammary epithelial cells and breast tumor progression. *Cancer Research* **64**:6732–6739, American Association for Cancer Research.
- Ramírez de Molina A, Gallego-Ortega D, Sarmentero J, Báñez-Coronel M, Martín-Cantalejo Y, and Lacal JC (2005) Choline kinase is a novel oncogene that potentiates RhoA-induced carcinogenesis. *Cancer Research* **65**:5647–5653.
- Ramírez de Molina A, Gutierrez R, Ramos MA, Silva JM, and Silva J (2002) Increased choline kinase activity in human breast carcinomas: clinical evidence for a potential novel antitumor strategy. *Oncogene* **21**:4317–4322.
- Ramírez de Molina A, Oroz LG, and Sanjuan JCL (2011) Methods and compositions for the treatment of cancer, Google Patents.
- Ramírez de Molina A, Penalva V, Lucas L, and Lacal JC (2002) Regulation of choline kinase activity by Ras proteins involves Ral-GDS and PI3K. *Oncogene* **21**:937–946.
- Ramírez de Molina A, Rodríguez-González A, and Lacal JC (2004) From Ras signalling to ChoK inhibitors: a further advance in anticancer drug design. *Cancer Lett* **206**:137–148.
- Ramírez de Molina A, Rodríguez-González A, Gutiérrez R, Martínez-Piñeiro L, Sánchez J, Bonilla F, Rosell R, and Lacal J (2002) Overexpression of choline kinase is a frequent feature in human tumor-derived cell lines and in lung, prostate, and colorectal human cancers. *Biochemical and Biophysical Research Communications* **296**:580–583.
- Ramírez de Molina A, Rodríguez-González A, Penalva V, Lucas L, and Lacal JC (2001) Inhibition of ChoK Is an Efficient Antitumor Strategy for Harvey-, Kirsten-, and N-ras-Transformed Cells. *Biochemical and Biophysical Research Communications* **285**:873–879.
- Ramírez de Molina A, Sarmentero-Estrada J, and Belda-Iniesta C (2007) Expression of choline kinase alpha to predict outcome in patients with early-stage non-small-cell lung cancer: a retrospective study. *The Lancet Oncology*, doi: 10.1016/S1470-2045(07)70279-6.
- Ramoni C, Spadaro F, Barletta B, Dupuis ML, and Podo F (2004) Phosphatidylcholine-specific

- phospholipase C in mitogen-stimulated fibroblasts. *Exp Cell Res* **299**:370–382.
- Rodríguez-González A, de Molina AR, Fernández F, Ramos MA, Núñez MDC, Campos J, and Lacal JC (2003) Inhibition of choline kinase as a specific cytotoxic strategy in oncogene-transformed cells. *Oncogene* **22**:8803–8812.
- Rodríguez-González A, Ramírez de Molina A, Báñez-Coronel M, Megías D, and Lacal JC (2005) Inhibition of choline kinase renders a highly selective cytotoxic effect in tumour cells through a mitochondrial independent mechanism. *Int J Oncol* **26**:999–1008.
- Rodríguez-González A, Ramírez de Molina A, Fernández F, and Lacal JC (2004) Choline kinase inhibition induces the increase in ceramides resulting in a highly specific and selective cytotoxic antitumoral strategy as a potential mechanism of action. *Oncogene* **23**:8247–8259.
- Rubio-Ruiz B, and Figuerola-Conchas A (2014) Discovery of a New Binding Site on Human Choline Kinase $\alpha 1$: Design, Synthesis, Crystallographic Studies, and Biological Evaluation of Asymmetrical Bispyridinium Derivatives. *J Med Chem* **57**:507–515.
- Rurack K, and Spieles M (2011) Fluorescence Quantum Yields of a Series of Red and Near-Infrared Dyes Emitting at 600– 1000 nm. *Analytical chemistry*, doi: 10.1021/ac101329h.
- Sanchez-Lopez E, Zimmerman T, del Pulgar TG, Moyer MP, Sanjuan JCL, and Cebrian A (2013) Choline kinase inhibition induces exacerbated endoplasmic reticulum stress and triggers apoptosis via CHOP in cancer cells. **4**:e933–11, Nature Publishing Group.
- Sankaranarayananpillai M, Tong WP, Maxwell DS, Pal A, Pang J, Bornmann WG, Gelovani JG, and Ronen SM (2006) Detection of histone deacetylase inhibition by noninvasive magnetic resonance spectroscopy. *Mol Cancer Ther* **5**:1325–1334.
- Sarkar R, Comment A, Vasos PR, Jannin S, Gruetter R, Bodenhausen G, Hall H, Kirik D, and Denisov VP (2009) Proton NMR of (15)N-choline metabolites enhanced by dynamic nuclear polarization. *J Am Chem Soc* **131**:16014–16015.
- Sawyers C (2004) Targeted cancer therapy. *Nature* **432**:294–297.
- Sánchez-Martín R, Campos JM, Conejo-García A, Cruz-López O, Báñez-Coronel M, Rodríguez-González A, Gallo MA, Lacal JC, and Espinosa A (2005) Symmetrical Bis-Quinolinium Compounds: New Human Choline Kinase Inhibitors with Antiproliferative Activity against the HT-29 Cell Line. *J Med Chem* **48**:3354–3363.
- Scheeff ED, and Bourne PE (2005) Structural evolution of the protein kinase-like superfamily. *PLoS Comput Biol* **1**:e49.
- Schiaffino-Ortega S, López-Cara LC, Ríos-Marco P, Carrasco-Jimenez MP, Gallo MA, Espinosa A, Marco C, and Entrena A (2013) New Non-symmetrical Choline Kinase Inhibitors. *Bioorg Med Chem* 1–29, Elsevier Ltd.
- Semenza GL (2003) Targeting HIF-1 for cancer therapy. *Nat Rev Cancer* **3**:721–732.
- Shah T, Wildes F, Penet M-F, Winnard PT Jr, Glunde K, Artemov D, Ackerstaff E, Gimi B, Kakkad S, Raman V, and Bhujwalla ZM (2010) Choline kinase overexpression increases invasiveness and drug resistance of human breast cancer cells. *NMR Biomed* **23**:633–642, John Wiley & Sons, Ltd.

- Sheff KY, Tedford CE, Flynn JR, Yorek MA, Cannon JG, and Long JP (1988) Stereoisomers of quaternary and tertiary 4-methyl piperidine analogs of hemicholinium-3. *Journal of Pharmacology and Experimental Therapeutics* **247**:640–644.
- Shelley RM, and Hodgson E (1970) Biosynthesis of phosphatidylcholine in the fat body of *Phormia regina* larvae. *J Insect Physiol* **16**:131–139.
- Shen D, Bai M, Tang R, Xu B, Ju X, Pestell RG, and Achilefu S (2013) Dual fluorescent molecular substrates selectively report the activation, sustainability and reversibility of cellular PKB/Akt activity. *Sci Rep* **3**:1697.
- Sher RB, Aoyama C, Huebsch KA, Ji S, Kerner J, Yang Y, Frankel WN, Hoppel CL, Wood PA, Vance DE, and Cox GA (2006) A rostrocaudal muscular dystrophy caused by a defect in choline kinase beta, the first enzyme in phosphatidylcholine biosynthesis. *Journal of Biological Chemistry* **281**:4938–4948.
- Shields AF, Grierson JR, Dohmen BM, Machulla HJ, Stayanoff JC, Lawhorn-Crews JM, Obradovich JE, Muzik O, and Mangner TJ (1998) Imaging proliferation in vivo with [F-18]FLT and positron emission tomography. *Nature Medicine* **4**:1334–1336.
- Shukla-Dave A, Poptani H, Loevner LA, Mancuso A, Serrai H, Rosenthal DI, Kilger AM, Nelson DS, Zakian KL, Arias-Mendoza F, Rijpkema M, Koutcher JA, Brown TR, Heerschap A, and Glickson JD (2002) Prediction of treatment response of head and neck cancers with P-31 MR spectroscopy from pretreatment relative phosphomonoester levels. *Acad Radiol* **9**:688–694.
- Silver IA, Murrills RJ, and Etherington DJ (1988) Microelectrode studies on the acid microenvironment beneath adherent macrophages and osteoclasts. *Exp Cell Res* **175**:266–276.
- Simons TJ (1976) Carbocyanine dyes inhibit Ca-dependent K efflux from human red cell ghosts. *Nature* **264**:467–469.
- Sims PJ, Waggoner AS, Wang CH, and Hoffman JF (1974) Studies on the mechanism by which cyanine dyes measure membrane potential in red blood cells and phosphatidylcholine vesicles. *Biochemistry* **13**:3315–3330.
- Sporn MB (1996) The war on cancer. *The Lancet* **347**:1377–1381.
- Strebhardt K, and Ullrich A (2008) Paul Ehrlich's magic bullet concept: 100 years of progress. *Nat Rev Cancer* **8**:473–480.
- Tedford CE, Reed D, Bhattacharyya B, Bhalla P, Cannon JG, and Long JP (1986) Evaluation of 4-methylpiperidine analogs of hemicholinium-3. *Eur J Pharmacol* **128**:231–239.
- Tichauer KM, Samkoe KS, Klubben WS, Hasan T, and Pogue BW (2012) Advantages of a dual-tracer model over reference tissue models for binding potential measurement in tumors. *Phys Med Biol* **57**:6647–6659, IOP Publishing.
- Tichauer KM, Samkoe KS, Sexton KJ, Hextrum SK, Yang HH, Klubben WS, Gunn JR, Hasan T, and Pogue BW (2012) In vivo quantification of tumor receptor binding potential with dual-reporter molecular imaging. *Mol Imaging Biol* **14**:584–592.
- Tkac I, Starcuk Z, Choi IY, and Gruetter R (1999) In vivo 1H NMR spectroscopy of rat brain at 1 ms echo time. *Magnetic Resonance in Medicine* **41**:649–656, John Wiley & Sons, Inc.

- Torosean S, Flynn B, Axelsson J, Gunn J, Samkoe KS, Hasan T, Doyley MM, and Pogue BW (2013) Nanoparticle uptake in tumors is mediated by the interplay of vascular and collagen density with interstitial pressure. *Nanomedicine: Nanotechnology, Biology, and Medicine* **9**:151–158.
- Toyoda M, Sakuragawa N, Arai Y, Yoshikawa H, Sugai K, Arima M, Hara T, Iio M, and Satoyoshi E (1989) Positron emission tomography using pyruvate-1-11C in two cases of mitochondrial encephalomyopathy. *Ann Nucl Med* **3**:103–109.
- Trousil S, Carroll L, Kalusa A, Aberg O, Kaliszczak M, and Aboagye EO (2013) Design of symmetrical and nonsymmetrical N,N-dimethylaminopyridine derivatives as highly potent choline kinase alpha inhibitors. *Med Chem Commun* **4**:693.
- Trousil S, Lee P, Pinato DJ, Ellis JK, Dina R, Aboagye EO, Keun HC, and Sharma R (2014) Alterations of Choline Phospholipid Metabolism in Endometrial Cancer Are Caused by Choline Kinase Alpha Overexpression and a Hyperactivated Deacylation Pathway. *Cancer Research* **74**:6867–6877.
- Troyan SL, Kianzad V, Gibbs-Strauss SL, Gioux S, Matsui A, Oketokoun R, Ngo L, Khamene A, Azar F, and Frangioni JV (2009) The FLARE intraoperative near-infrared fluorescence imaging system: a first-in-human clinical trial in breast cancer sentinel lymph node mapping. *Ann Surg Oncol* **16**:2943–2952, Springer-Verlag.
- Tung C-H, Lin Y, Moon WK, and Weissleder R (2002) A Receptor-Targeted Near-Infrared Fluorescence Probe for In Vivo Tumor Imaging. *ChemBioChem* **3**:784–786, WILEY-VCH Verlag.
- Tung CH, Mahmood U, Bredow S, and Weissleder R (2000) In vivo imaging of proteolytic enzyme activity using a novel molecular reporter. *Cancer Research* **60**:4953–4958.
- Tuttle TM (2004) Technical advances in sentinel lymph node biopsy for breast cancer. *Am Surg* **70**:407–413.
- Tyagi RK, Azrad A, Degani H, and Salomon Y (1996) Simultaneous extraction of cellular lipids and water-soluble metabolites: evaluation by NMR spectroscopy. *Magn Reson Med* **35**:194–200.
- Ullman MD, and Radin NS (1974) The enzymatic formation of sphingomyelin from ceramide and lecithin in mouse liver. *Journal of Biological Chemistry* **249**:1506–1512.
- van de Ven SMWY (2008) Optical imaging of the breast. *Cancer Imaging* **8**:206–215.
- van Veen RLP, Sterenborg HJCM, Pifferi A, Torricelli A, Chikoidze E, and Cubeddu R (2005) Determination of visible near-IR absorption coefficients of mammalian fat using time- and spatially resolved diffuse reflectance and transmission spectroscopy. *J Biomed Opt* **10**:054004–054004–6, International Society for Optics and Photonics.
- Vance DE (2013) Physiological roles of phosphatidylethanolamine N-methyltransferase. *Biochim Biophys Acta* **1831**:626–632.
- Vander Heiden MG, Cantley LC, and Thompson CB (2009) Understanding the Warburg effect: the metabolic requirements of cell proliferation. *Science* **324**:1029–1033.
- Vogel C-A, Galmiche MC, Westermann P, Sun L-Q, Pèlegri A, Folli S, Bischof Delaloye A, Slosman DO, Mach J-P, and Buchegger F (1996) Carcinoembryonic antigen expression, antibody localisation and immunophotodetection of human colon cancer liver metastases in nude mice: A model for radioimmunotherapy. *Int J Cancer* **67**:294–302.

- Wang T, Li J, Chen F, Zhao Y, He X, Wan D, and Gu J (2007) Choline transporters in human lung adenocarcinoma: expression and functional implications. *Acta Biochim Biophys Sin (Shanghai)* **39**:668–674.
- Warburg O (1956) On the origin of cancer cells. *Science*.
- Ward CS, Eriksson P, Izquierdo-Garcia JL, Brandes AH, and Ronen SM (2013) HDAC inhibition induces increased choline uptake and elevated phosphocholine levels in MCF7 breast cancer cells. *PLoS ONE* **8**:e62610.
- Warden CH, and Friedkin M (1984) Regulation of phosphatidylcholine biosynthesis by mitogenic growth factors. *Biochim Biophys Acta* **792**:270–280.
- Weiss SB, Smith SW, and Kennedy EP (1956) Net synthesis of lecithin in an isolated enzyme system. *Nature*, doi: 10.1038/178594a0.
- Weissleder R, and Ntziachristos V (2003) Shedding light onto live molecular targets. *Nature Medicine* **9**:123–128.
- Weissleder R, Tung CH, Mahmood U, and Bogdanov A (1999) In vivo imaging of tumors with protease-activated near-infrared fluorescent probes. *Nature Biotechnology* **17**:375–378.
- Wieprecht M, Wieder T, and Geilen CC (1994) N-[2-bromocinnamyl (amino) ethyl]-5-isoquinolinesulphonamide (H-89) inhibits incorporation of choline into phosphatidylcholine via inhibition of choline kinase and has no effect on the phosphorylation of CTP:phosphocholine cytidyltransferase. *Biochem J*.
- Williams CHG (1856). *Transactions of The Royal Society of Edinburgh* **21**.
- Wittenberg J, and Kornberg A (1953) Choline phosphokinase. *Journal of Biological Chemistry* **202**:431–444.
- Wu D, and Hersh LB (1994) Choline acetyltransferase: celebrating its fiftieth year. *J Neurochem* **62**:1653–1663.
- Wu G, Aoyama C, Young SG, and Vance DE (2008) Early embryonic lethality caused by disruption of the gene for choline kinase alpha, the first enzyme in phosphatidylcholine biosynthesis. *Journal of Biological Chemistry* **283**:1456–1462.
- Yalcin A, Clem B, Makoni S, Clem A, Nelson K, Thornburg J, Siow D, Lane AN, Brock SE, Goswami U, Eaton JW, Telang S, and Chesney J (2010) Selective inhibition of choline kinase simultaneously attenuates MAPK and PI3K/AKT signaling. *Oncogene* **29**:139–149.
- Yamamura HI, and Snyder SH (1973) High affinity transport of choline into synaptosomes of rat brain. *J Neurochem* **21**:1355–1374.
- Yang X, Shi C, Tong R, Qian W, Zhau HE, Wang R, Zhu G, Cheng J, Yang VW, Cheng T, Henry M, Strekowski L, and Chung LWK (2010) Near IR heptamethine cyanine dye-mediated cancer imaging. *Clinical Cancer Research* **16**:2833–2844, American Association for Cancer Research.
- Ye Y, Li WP, Anderson CJ, Kao J, Nikiforovich GV, and Achilefu S (2003) Synthesis and characterization of a macrocyclic near-infrared optical scaffold. *J Am Chem Soc* **125**:7766–7767.

- Yenugonda VM, Deb TB, Grindrod SC, Dakshanamurthy S, Yang Y, Paige M, and Brown ML (2011) Fluorescent cyclin-dependent kinase inhibitors block the proliferation of human breast cancer cells. *Bioorg Med Chem* **19**:2714–2725, Elsevier Ltd.
- Yu Y, Sreenivas A, Ostrander DB, and Carman GM (2002) Phosphorylation of *Saccharomyces cerevisiae* Choline Kinase on Ser30 and Ser85 by Protein Kinase A Regulates Phosphatidylcholine Synthesis by the CDP-choline Pathway. *Journal of Biological Chemistry* **277**:34978–34986.
- Zheng Q-H, Gao M, Mock BH, Wang S, Hara T, Nazih R, Miller MA, Receveur TJ, Lopshire JC, Groh WJ, Zipes DP, Hutchins GD, and DeGrado TR (2007) Synthesis and biodistribution of new radiolabeled high-affinity choline transporter inhibitors [¹¹C]hemicholinium-3 and [¹⁸F]hemicholinium-3. *Bioorg Med Chem* **17**:2220–2224.